Novel PVDF Ultrafiltration Membranes with Tailor-made Zwitterionic Copolymer Additives

by

Miao Li
Xinjiang, China

Thesis submitted to the Department of Chemistry of

Universität Duisburg-Essen, in partial fulfillment

of the requirements of the degree of

Dr. rer. nat.

Approved by the examining committee on Oct. 05. 2017

Chair : Prof. Dr. Maik Walpuski

Advisor : Prof. Dr. Mathias Ulbricht

Reviewer : Prof. Dr. Jochen S. Gutmann

Essen, 2017

Abstract

Adsorptive fouling and “trade-off” relationship between membrane permeability and selectivity largely limit the long-term application of polymer ultrafiltration (UF) membrane in industrial area, especially in the water treatment for clean drinking water. The work of this dissertation is a part of NANOPUR project, targeting preparation of UF membrane with high throughput, high selectivity and low fouling. A number of Polyvinylidenfluorid (PVDF) UF membranes containing synthesized zwitterionic additive $PMMA_m$-*co*-$PSPE_n$ and $PMMA_m$-*b*-$PSPE_n$ were prepared via nonsolvent induced phase separation (NIPS) in order to research their performance improvement on the fouling resistance as well as “trade-off” phenomenon. PMMA is polymethylmethacrylate. PSPE is poly (sulfobetaine methacrylate).

Additive $PMMA_m$-*co*-$PSPE_n$ was directly synthesized via free radical copolymerization of monomer MMA and SPE. Macroinitiator PMMA-Br with various molecular weights were synthesized via Atom transfer radical polymerization (ATRP). The molecular weights of PMMA-Br were designed as ~10 kg/mol, ~14 kg/mol, 30 kg/mol and ~53 kg/mol in order to examine the various effects arisen from different PMMA lengths. Then they were used to reinitiate the N, N-dimethylaminoethyl methacrylate (DMAEMA) to synthesize a number of $PMMA_m$-*b*-$PDMAEMA_n$ with diverse molecular weights and various ratios of PMMA/PDMAEMA under different conditions for sequential ATRP. Finally after the post-treatment, $PMMA_m$-*b*-$PDMAEMA_n$ were readily converted to zwitterionic $PMMA_m$-*b*-$PSPE_n$. The additive $PMMA_m$-*b*-$PSPE_n$ with precise control of molecular weight as well as polydispersity plus tailor-made ratios of PMMA/PSPE can be achieved in this manner.

By comparison of three UF PVDF membranes which were prepared by dope solutions containing 17.5 wt.% PVDF and respective 2 wt.% $PMMA_m$-*co*-$PSPE_n$, $PMMA_m$-*b*-$PSPE_n$ and commercial Polyvinylpyrrolidon (PVP) via NIPS, zwitterionic $PMMA_m$-*co*-$PSPE_n$ and $PMMA_m$-*b*-$PSPE_n$ largely improved the bovine serum albumin (BSA) sieving performance as well as BSA fouling resistance for the corresponding PVDF membranes. However $PMMA_m$-*b*-$PSPE_n$ remarkably reduced water permeability due to its strong facilitation effect on the precipitation rate of PVDF matrix polymer.

A series of UF PVDF membranes were prepared by dope solutions possessing 16 wt.%PVDF and 0.5-1.5 wt.% $PMMA_m$-*b*-$PSPE_n$ respectively with different molecular weights and various ratios of PMMA/PSPE via NIPS. These PVDF membranes showed distinct properties and performance from reference PVDF membranes with single $PMMA_m$-*b*-$PDMAEMA_n$ or PVP. The additional $PMMA_m$-*b*-$PSPE_n$ apparently also improved the BSA sieving performance of all the

corresponding PVDF membranes. Some selected PVDF membranes also displayed much lower BSA fouling than reference membrane. The PVDF membrane containing $PMMA_m$-*b*-$PSPE_n$ with higher ratios of PMMA/PSPE generally showed better fouling resistantce. Water permeability for all the PVDF membranes with $PMMA_m$-*b*-$PSPE_n$ were generally still low. The higher precipitation rate of PVDF matrix resulted from $PMMA_m$-*b*-$PSPE_n$ can be supported firmly.

Another series of UF PVDF membranes were prepared with dope solutions containing 16 wt.% PVDF and combination of 1 wt.% PVP and 1-2 wt.% $PMMA_m$-*b*-$PSPE_n$ with different molecular weights and various ratios of PMMA/PSPE via NIPS. The combination of PVP and $PMMA_m$-*b*-$PSPE_n$ originated apparent synergy effect on the performance of corresponding PVDF membranes, the high water permeability and high BSA rejection being achieved at the same time. The "trade-off" phenomenon was overcome for all the PVDF UF membranes. The additional PVP properly offset part of the increased precipitation rate which brought by $PMMA_m$-*b*-$PSPE_n$ so that a balanced water permeability and sieving performance was achieved. Compared with reference PVDF membranes with commercial PVP, selected PVDF membrane with combination of PVP and $PMMA_m$-*b*-$PSPE_n$ also displayed stronger BSA fouling resistance and higher BSA sieving performance. One prepared UF PVDF membrane with combination of additives that showed performances meeting the target values of NANOPUR project was selected as prototype membrane.

PVDF UF membranes which were prepared by dope solutions containing 16 wt.% PVDF and combination of $PMMA_m$-*b*-$PSPE_n$ and respective PEG, glycol and PMMA via NIPS were also characterized and compared. The above combination of additives didn't show satisfying effect on performance of corresponding PVDF membranes.

Two UF PVDF membranes were prepared by dope solutions possessing 17.5 wt.% PVDF and 2 wt.% $PMMA_m$-*b*-$PDMAEMA_n$ with different molecular weights and various ratios of PMMA/PDMAEMA via NIPS. Then through the surface modification the PDMAEMA groups exposing on PVDF membrane surface were converted to PSPE groups. The surface modification can be available but the complete conversion was difficult. These PVDF membranes after surface modification showed decreased water permeability but improved BSA sieving performance in contrast to ones before surface modification.

Overall, synergy effect of PVP and $PMMA_m$-*b*-$PSPE_n$ with high ratio of PMMA/PSPE exhibited strong potential to improve PVDF membrane performance. The largely enhanced fouling

resistance to protein and properly controlled porosity can be readily donated to PVDF membranes via practical NIPS of the blending solution which involved $PMMA_m$-*b*-$PSPE_n$, PVP and PVDF.

This work was performed during the period from August 2012 to August 2015 at the Institute of Technical Chemistry (Lehrstuhl für Technische Chemie II), Department of Chemistry, Universität Duisburg Essen, under the supervision of Prof. Mathias Ulbricht.

I declare that this dissertation represents my own work, except where due acknowledgement is made.

_____

Miao Li

Acknowledgements

After the intensive period for writing, the moment of finishing touch on my dissertation comes finally. During this adventure of my Ph.D study full of various exciting and discouraging stories with grind, I have harvested plenty of learning, not only in scientific skills, but also on personal level. Here I would like to acknowledge all the invaluable helps with kindness from people who support me to follow through the memorable Ph.D experience.

First of all, I would like to heartily express my profound gratitude to my advisor Prof. Dr. Mathias Ulbricht for providing me the opportunity to study in his outstanding research team. I also would like to present my sincere thanks for his continuous support and valuable help, for his patience, kindness and motivation. His insightful guidance based on immense knowledge helped me throughout my whole Ph.D research and writing of this dissertation. I could not have imagined finding a better advisor and mentor for my Ph.D study.

I am also deeply grateful to the reviewer Prof. Dr. Jochen S. Gutmann for his support and comment.

I wish to greatly thank Dr. Robert Sulc for his beneficial help and discussion. I would like to sincerely thank Dipl.-Ing. Danielzik Inge, Dipl.-Ing. Kallweit Tobias and Claudia Schenk for their technical support during my Ph.D work. My great thanks also go to Frau Roswitha Nordmann for her kind helps. I really appreciate Dr. Jackelyn Aragon-Gomez and Dieter Jacobi for performing GPC analysis. Dipl.-Ing. Smail Boukercha is acknowledged for conducting SEM and EDX analysis. I also would like to thank Qianhui Xu and Jieqing Huang for some experiments which they contributed to this dissertation.

I quite enjoy the open and warm atmosphere in Prof. Dr. Mathias Ulbricht's working group. It is my great pleasure to work with all the excellent group members. I am also grateful to Anne, Thorsten, Jens (Meyer), Marc, Nkem, Dongxu, Xi, Ahmed, Ibrahim, Kevin, Wieczorek, Clemens, Inga, Sarah, Dominic for their often advantageous discussions. I also would like to thank the entire group members of the Ulbricht group for their kind helps and cooperations.

Last but not the least, I would love to present my great thankfulness to my grandparents, my parents, my wife and all my whole family members for their earnest prayers, enduring understanding, consistent support and permanent love. My great gratefulness goes to our Lord Jesus Christ for the blessing and endless grace.

Dedication

It is my genuine gratefulness and deep love that

I dedicate this thesis to my grandparents, my parents and my wife

for their wholehearted support, inspiration, sacrifice, tolerance

and endless love.

Contents

1. Introduction

1.1. Background and motivation

According to the demographic data from the United Nations in 2016, the world population has already exceeded 7.4 billion and will reach 10 billion by 2050. At that time, the requirement of clean water perhaps is predicted to increase sevenfold at least. With the world population as well as correspondingly economical development rapidly expanding, water demand in industry, domestic & public using, agriculture, commercial using, and energy supply etc. are growing largely. However, at present over 2.6 billion people around their world are sufferring from water scarcity at least one month out of each year. Aside from the worldwide water shortage, nowadays the global water pollution also brings about the damages to populations, individual species and natural biological communities. Around 2.2 billion people in the world are short of proper drinking water and sanitations.[1][2] Globally, water for various industry processes and domestic use, which are mostly drawn from ground water, accounts for respectively 20% and 10% of the total water consumption. Especially, in industrialized countries, the industrial water consumption mostly accounts for over 50% of local water consumption.[3][4] In order to protect the limited worldwide fresh water resources (surface water and ground water) and relieve the global fresh water withdrawing, treatment of discharged water from industrial processes and waste waters from domestic demand to reuse can supply the most sustainable and promising option.[5]

Compared with traditional water treatment methods such as coagulation, sand filtration, disinfection, biological treatment and distillation, the pressure-driven membrane technology, including microfiltration (MF), ultrafiltration (UF), nanofiltration (NF), reverse osmosis (RO), exhibits a number of quite promising advantages to meet the growing challenges in water treatment area. The membrane separation processes can be easily carried out continuously with relatively low energy consumption and at large industrial scale. The implementation of membrane processes also can be conveniently combined with other separation processes under mild conditions, no any additive being needed. In addition, membrane properties such as shapes, hydrophilicity etc. can be variable and adjusted for the different separation targets. To date, pressure-driven membrane processes are already widely applied in the worldwide water treatment area and many other industries such as food and beverage, pulp and paper, textile, biotechnology, pharmaceutical, chemical manufacture, metallurgy etc.[6][7] Pressure-driven membrane processes can be applied to remove a number of common components, ranging from suspended particles to organic compounds and ions. In contrast to NF and RO, UF gains more wide popularization in drinking water manufacturers due to its relatively low cost, low driving

pressure, facilitation of compactness and automation.[8] Effective removal of most organic macromolecules, microorganism such as bacteria and Giardia and various viruses can be easily realized via UF process and the water-related diseases can be decreased with a satisfied drinking water quality.[9] The global membrane market is predicted to grow at a CAGR (compound annual growth rate) of 9.47% from 2016 to reach 32.14 billion USD by 2020.[10] The global market for UF membranes has grown to nearly 3.3 billion USD in 2016 from 3.1 billion USD in 2015. This market is expected to grow continuously at a CAGR of 6.9% from 2016 to reach nearly 4.6 billion USD in 2021.[10]

As a main existing problem, the susceptibility to fouling largely limits the industrial applications of pressure-driven membrane processes, in particular in membrane processes for water treatment where the concentrated components cause fouling quite seriously.[11] To properly combine the high permeability and high separation selectivity is another prevailed difficulty for most of membrane manufacture due to the trade-off relationship existing between the two key parameters.[11][12] Better membrane separation selectivity is always achieved at the cost of low permeability and *vice versa*. In the work of this dissertation, a number of efforts were made to not only elevate fouling resistance of PVDF UF membrane but also overcome the trade-off relationship beween selectivity and permeability. A series of novel zwitterionic polymer additives $PMMA_m$-*co*-$PSPE_n$ and $PMMA_m$-*b*-$PSPE_n$ were synthesized through free radical polymerization (FRP) and atom transfer radical polymerization (ATRP). And then the additives were introduced in PVDF ultrafiltration membrane during nonsolvent induced phase separation in order to improve anti-fouling ability and the “trade-off”. The performance of the prepared UF membranes were fully characterized and the interesting results were carefully demonstrated and analyzed.

1.2. NANOPUR project

The work of this disseratation was affiliated to NANOPUR project of EU Nano4water cluster, funding from EU Seventh Framework Programme (FP7/2007-2013) with grant agreement No. : 280595.

The NANOPUR project aimed at leveraging on promising bottom-up technologies to develop intensified water treatment concepts based on nano-structured and nano-functionalized membranes as well as nanofilm deposition for micropollutants and virus removal. Major research included preparation of membranes with selective properties at nanoscale able to maintain high permeability with relatively low driving force. The main task of work in this dissertation for project

was development of nanostructured, low-fouling ultra-filtration (UF) membranes with high throughput as well as improved selective sieving performance.

2. Fundamentals

The fundamental knowledge including polymer synthesis as well as membrane technology concerning the work of this dissertation was briefly introduced as following.

2.1. Radical polymerization

2.1.1. Free radical polymerization

Conventional free radical polymerization (FRP), accounting for over 50% worldwide commercial polymers, is still significantly important in global chemical industry. Most of the necessary polymer materials can be produced via FRP, including low density polyethylene, polyacrylate, poly(methylacrylate), polyacrylamide, polyacrylonitrile, poly(vinyl acetate), polystyrene, poly(vinyl chloride), etc.[13]

FRP, as a course of chain polymerization, consists of four essential reactions: initiation, propagation, chain transfer, and termination. The sketched process of FRP is shown in **Fig. 1**. Normal homolytic cleavage of initiator resulted from thermal, photochemical or redox process generates primary free radicals (active center) that initiate polymerization. Addition of primary radicals to C=C of monomer gives birth to propagating radicals for further chain propagation of desired polymer (**Fig. 1**). Because $k_d << k_i$, rate of initiation is slower about 1000 times than rate of polymerization (homolytic cleavage of initiator is controlling step for rate of initiation).[13][14] Therefore it is necessary to select initiator with long half lifetime and keep it at quite low concentration during polymerization.[15] Propagating radicals initiated by primary radicals lead to a succession of exothermic propagation with fast rate of propagation ($k_p \sim 10^3$ $M^{-1}s^{-1}$) to build polymer chains (**Fig. 1**).[15][16] Since the course of chain growing (propagating) only last ~1 s, during which ~1000 acts of radical addition occur with a frequency of ~1 ms, it is no chance to perform synthetic manipulation for preparation of block copolymer in the life range of polymer chain propagation.[16] Chain transfer is the course of radical center transferring from propagating radical to transfer agent via unpaired electron transfer and followed formation of a dead polymer chain and another new radical center of small molecule. Since transfer shows higher energy barrier than propagation, it is normally only taken into account in the case of FRP with high temperature.[16] Termination is defined as the bimolecular coupling of propagating radicals via combination (k_{td}) or disproportionation that terminate polymer chain propagation (k_{tc}) (**Fig. 1**). In order to retard the diffusion-controlled fast bimolecular coupling ($k_t \sim 10^8$ $M^{-1}s^{-1} >> k_p$) and gain polymer with high molecular weight, the slower rate of termination, compared with rate of

propagation, must be reached via remaining very low concentration of radicals (normally ranging from ppb to ppm) throughout polymerization. As a 2nd order reaction with respect to radical concentration, termination rate decreases more than rate of propagation that is 1st order reaction in the case of lower radical concentration.[17]

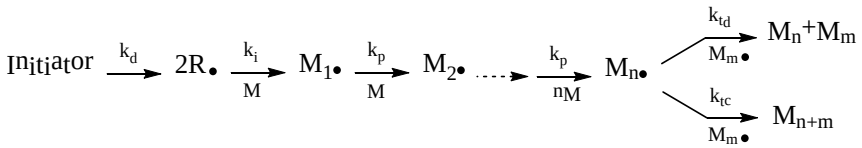

Fig. 1 General process of FRP. k_d, k_i, k_p, k_{td}, k_{tc} are respectively the rate constant of initiator decomposition, initiation, propagation, termination by disproportionation, termination by coupling. M is monomer.

FRP not only can be applied for a wide variety of monomer via convenient process but shows good reproducibility in scale of industrial production. However, in addition to impossibility of producing pure block copolymer or copolymer with special molecular architecture, no control of polymer molecular weight and polydispersity are accessible via FRP because of the short lifetime of growing polymer chains (~1 s) during production.[17]

2.1.2. Atom transfer radical polymerization

Atom transfer radical polymerization (ATRP) is a versatile and powerful technique for synthesis of polymer with precisely controlled molecular weight, low polydispersity (ideally $M_w/M_n<1.1$) and controlled molecular architecture in the forms of different composition (block, graft, alternating copolymers etc.), diverse chain topology (stars, combs, circle, brushes etc.) and various end functionality.[17] It is basically impossible to prepare polymer with precise control via conventional free radical polymerization due to the inevitable fast termination between radicals.

The general mechanism of ATRP can be outlined as shown in **Fig. 2**. As a catalytic process, ATRP is indeed controlled by the involved redox-active transition metal complexes (Mt^m/L and X-Mt^{m+1}/L; Cu^I/L and X-Cu^{II}/L are frequently used). Under the active action of transition metal complex Mt^m/L (activator), P_nX, namely alkyl halides or macromolecular dormant species, undergoes the homolytic cleavage on the alkyl halogen bond (P-X) and orginates the radical P_n·, the active species, followed by concomitant leaving of halogen atom X. In the meantime, transition metal halide complex X-Mt^{m+1}/L (deactivator) with higher oxidation state is formed through an one-electron oxidation of Mt^m/L that resulted from the coordination of X with Mt^m/L (with a rate constant k_{act}). The formed radical P_n· also can be reversibly re-formed from the dormant species P_nX under the deactivation of X-Mt^{m+1}/L with a rate contant of k_{deact}. The

equilibrium of whole ATRP process (K_{ATRP}= k_{act}/k_{deact}) normally should strongly shift towards the formation of dormant species (P_nX) for the precise control of polymerization ($k_{act}<<k_{deact}$).[18][19] Intermittently formed $P_n\cdot$ can propagate continuously to form growing polymer chains by the addition of $P_n\cdot$ to monomer in a way like FRP with a propagation rate constant k_p. The ocurrance of termination with rate constant k_t in ATRP also mainly arised from radical coupling and disproportionation as process in FRP. Generally no more than 5% growing polymer chains undergo termination in a well organized ATRP, and most of the termination occurs during the initial period of ATRP. As the build-up of persistent radical effect by the increasing concentration of deactivator X-Mt^{m+1}/L, the termination become minimized during the following period of ATRP. The fast initiation and rapid reversible exchange between activator and deactivator during ATRP can effectively reduce the termination and give uniform growth of all polymer chains.[20]

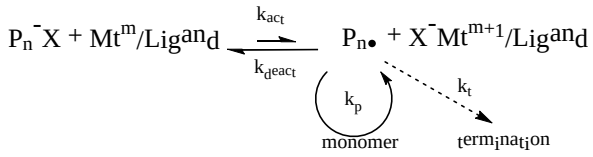

Fig. 2 Process of ATRP equilibrium. P_nX is alkyl halides or macromolecular dormant species. X is halogen atom. Mt^m and Mt^{m+1} are the transition metal species with low and high oxidation number.

The rate of ATRP is highly correlated to propagation rate k_p and concentration of monomer and radical. In addition, the structure of ligand (L), properties of transition metal ion, monomer and initiator P_nX, the reaction conditions such as solvent, temperature, pressure, time etc. also can largely influence the rate constant of ATRP (**Equation 1**). The rate of deactiviation contributes much to the narrow polydispersity (M_w/M_n) (**Equation 2**).[19][21] A well controlled ATRP normally needs completely balanced consideration on all involvement of factors.

$$R_p = k_p K_{ATRP} \left(\frac{[I]_0[Cu^I/L][M]}{[X-Cu^{II}/L]}\right) \qquad \textbf{(Equation 1)}[21]$$

R_p	Rate of ATRP
k_p	Rate constant of propagation
K_{ATRP}	Constant of ATRP equilibrium
$[I]_0$	Concentration of initiator
$[Cu^I/L]$	Concentration of activator
[M]	Concentration of monomer
$[X\text{-}Cu^{II}/L]$	Concentration of deactivator

$$\frac{M_w}{M_n} = 1 + \frac{1}{DP_n} + \left(\frac{k_p[I]_0}{k_{deact}[X-Cu^{II}/L]}\right)\left(\frac{2}{p} - 1\right)$$ (**Equation 2**)[21]

DP_n	Ratio of consumed monomer and initiator ($\Delta[M]/[I]_0$)
k_{deact}	Rate constant of deactivation
p	Conversion of monomer

The constant for equilibrium of whole ATRP process (K_{ATRP}) upscales in inverse proportion to the electrochemical activity of Cu(II)Br_2/Ligand complexes with various ligands shown in **Fig. 3**. The structural activity of ligands plays crucial role to determine the proper rate constant of ATRP.

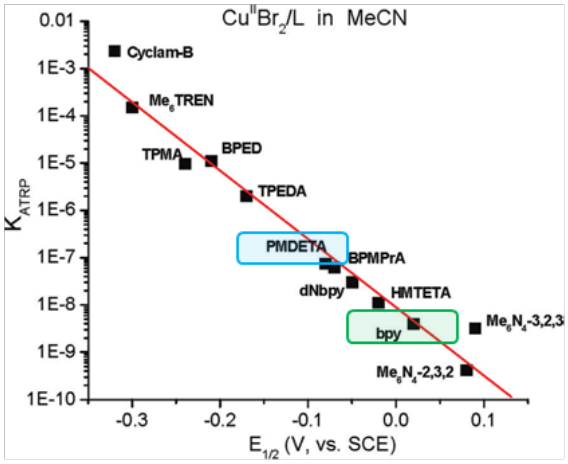

Fig. 3 Correlation between K_{ATRP} and redox potentials ($E_{1/2}$) of different ATRP active Cu(II)Br_2/L complexes in MeCN at 25°C.[21]

2.2. Membranes

2.2.1. Overview of membrane technology and ultrafiltration membranes

After the well-known breakthrough of the first anisotropic membrane invented by Loeb and Sourirajan in 1960s, the application of membrane technology in industry at large scale became available.[6] As a rapidly developing technology inspired by nature of biological membranes, synthetic membranes are normally defined as a permselective barrier or interphase between two adjacent phases, organizing the mass-transport between the two compartments of different phases actively or passively.[11][22][23][24] Nowadays a number of membrane processes were already well established based on different separation principles or mechanisms, but all the membrane processes can still be briefly characterized as the division of the feed stream into retentate or concentrate stream as well as permeate stream. Depending on the purposes of

different membrane process, the concentrate (retentate) or permeate stream is the final product.[6] Based on various mechanisms of membrane transports which facilitate different components in feed mixture, desired membrane separation can be achieved. A given membrane performance generally is evaluated by two parameters: selectivity and permeation rate through membrane. The definition of permeate rate is the volume flowing through the membrane per unit area and time, which is normally expressed as $L \cdot h^{-1} \cdot m^{-2}$. The selectivity of a membrane for filtration of solute in solvent (mostly water) is usually characterized in terms of the retention (rejection, R%) towards specific solute.[6][24] The expression of selectivity for gas separation membrane is beyond the scope of this dissertation. The selectivity and permeate rate are mainly governed by driving force and membrane nature (structure and material). Mass transport through the membrane occurs as a result of driving force, which acts on solute in feed and is typically correlated with a gradient of concentration, pressure, temperature and electric potential etc..[25] The structure (morphology) of membrane and the interaction between membrane material and feed give the dominant contribution to the membrane separation performance.

In present day a number of membrane processes are already employed in a wide range of industrial applications, including microfiltration (MF), ultrafiltration (UF), nanofiltration (NF), reverse osmosis (RO), membrane electrolysis (ME), dialysis (D), gas separation (GS), vapour permeation (VP), pervaporation (PV), membrane distillation (MD) and membrane contactor (MC) etc.[6][26] Membrane separation processes that are technically and commercially established in large scale include D for medical device(artificial kidney), RO for ultrapure water, UF for water treatment, MF for particle removal and GS for air separation.[26]

Solid synthetic polymers are widely applied in preparation of synthetic membranes due to the adaptability of polymers on designing membranes with varied structures and properties. The morphology of synthetic membranes can be classified as non-porous and porous membrane based on their porous characterization (**Fig. 4**). Non-porous membranes normally are characterized as dense film, which are usually applied in membrane processes of RO, GS etc.. The permeation across the membrane can be described by the solute/diffusion mechanism.[25][27] Non-porous membrane should minimize the thickness of dense film as thin as possible due to the inverse proportionality between flux and thickness of dense layer.[6][24] Porous membranes have numerous tiny pores with average size distribution ranging from 1-2nm to 10μm on membrane surface that served for porous barrier. Regularly MF, UF and NF process can be assigned to typical application of porous membrane. The mass transport and selectivity of porous membrane are primarily influenced by viscous flow and size exclusion.[28] The porous membranes can be further distinguished into symmetric (isotropic) and asymmetric (anisotropic) membrane according

to the different morphology of membrane cross section (**Fig. 4**). Symmetric membrane possesses a uniform morphology throughout the whole membrane thickness, which is generally applied in MF process or membrane surpporter due to the big average pore size (0.05-10 μm) and quite high flux. The mostly typical symmetric porous membrane morphologys include sponge- and web-like pore structures in membrane cross section.[6][24][29] Asymmetric membrane have a gradient structure that consists of a very thin skin layer on the top (<1 μm) and a highly porous sublayer with pronounced macrovoids and the skin layer plays the role of selective barrier. Asymmetric membrane whose skin layer and sublayer are from same material is defined as integrally-skinned asymmetric membrane, whereas thin-film composite membrane denotes the asymmetric membrane with skin layer and sublayer from different materials.[25][30] Commonly, dialysis, UF and some of MF membranes that characterized as porous skin layer where a number of tiny pores are distributed are typically integrally-skinned asymmetric membrane. The skin layer of asymmetric membranes should remain a minimum barrier thickness so that the resistance for mass transfer through the membrane can be minimized. The thin-film composite membrane mostly with heterogeous dense skin layer and porous support membrane mainly focuses on the applications of RO and part of NF.[24][30]

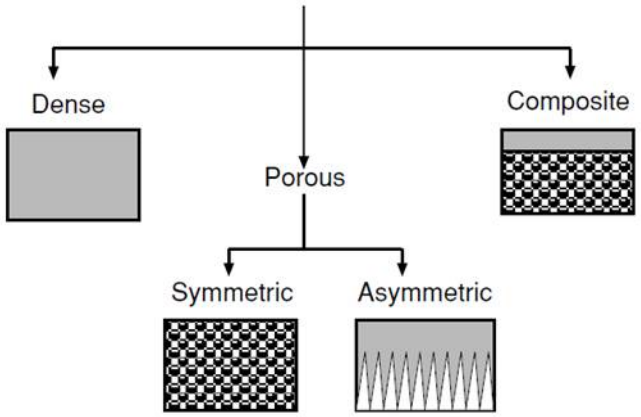

Fig. 4 Classification of synthetic membrane according to membrane morphology.[29]

For further understanding the work in this dissertation, some more detail about ultrafiltration membrane is given as following. Ultrafiltration process is normally specialized to retain the colloids and macromolecules with a minimum molecular weight as low as a few kg/mol from aqueous solution. As aforementioned, asymmetric UF membrane that has porous skin top layer generally shows relatively small pore size ranging from 1 nm to 100 nm so that the pressure defference for UF usually is ranging over 1-10 bar in order to obtain ideal rate of permeating flux. UF membrane with lower driven pressure is always pursued by scientists and this is also

regarded as one objective for this dissertation. The selectivity (rejection) of UF membrane is primarily determined by the size or shape (correlated with size of solute) of solute in feed solution, namely the size-exclusion. Difference on the molecular weights of macromolecules with various molecular weights is highly correlative to the different retention of these macromolecules in UF process. Therefore the norminal separation performance of a given UF membrane can be characterized by molecular weight cut-off, which is a concept to evaluate UF membrane discrimination towards solutes by the retention behavior of globular (normally is protein, such as BSA) or linear molecules (normally dextran) with varied molecular weights.[6][8] UF membrane with ability to separate high molecular weight components from low molecular weight components are already applied over wide fields such as water treatment, food and diary industry, pharmaceutical industry, chemical industry, textile industry and paper industry etc..[7]

2.2.2. Polymer material for synthetic membrane

To date basically all the synthetic membranes applied in industrial processes are made from organic or inorganic materials and the organic polymer membrane accounts for considerably major portions in worldwide market of commercial membrane. In practice, in consideration of the different physical and chemical properties with respect to the operational practicability, merely a limited number of polymers can be employed to prepare membrane. With respect to open porous membranes such as MF and UF membranes, the polymer selection is mainly on the principle of processing requirements for industrial manufacture, fouling tendency, chemical and thermal stability, because the selectivity and flux of porous membrane merely depends on the pore size and porosity. In contrast, regarding the dense nonporous membrane for gas separation and pervaporation, the nature of polymer material can largely influence the membrane performance (selectiveity and flux). A large number of organic polymer are frequently applied for industrial membrane manufacture, typically including polysulfone (PSF), polyacrylonitrile (PAN), polyamide (PA), poly(ether- sulfone) (PES), polyimide (PI) and poly(vinylidene fluoride) (PVDF) etc..[6][25]

Compared with other commercial membrane polymers, PVDF gains remarkable attention and wildely application on industrial UF and MF membrane fields in recent years. Commercial PVDF is a semicrystalline homopolymer with repeating units of $–(CH_2CF_2)_n–$. Generally commercialized PVDF membranes with proper crystallinity is capable of exhibiting quite outstanding mechanical strength property and impact resistance. The high bond dissociation energy of C–F that arises from the high electronnegativity of fluorine atom in PVDF chains donates the extraordinary stability to PVDF polymer, such as the much stronger thermal stability than normal hydrocarbon polymer, the excellent chemical resistance to most harsh chemicals.[34] The better thermal

stability and chemical resistance are quite essential for industrial polymer membrane used in water treatment. UF and MF PVDF membranes can be easily produced at large scale via NIPS due to the excellent solubility of PVDF in the frequently-used organic solvents for industrial manufacture of membrane such as DMF, DMSO, NMP and DMAc.[35](cf. **4.3.**) The proper solubility of PVDF also donates notable processing ability to PVDF for preparation of various membrane geometries, e.g. flat sheet, tubular, hollow fiber. Different from other crystalline polymers, PVDF displays proper thermodynamic compatibility with a number of other polymers such as PMMA, PVP and PEG etc., which supplys versatile selectivity to improve the properties of PVDF membrane. (cf. **6.**) The chemical characteristic of PVDF also allows some chemical modification to give some exral functional group in PVDF chains, which is quite important for modification of PVDF membrane with the purpose of higher performance. PVDF is also suitable for bio-separation area due to the low content of extractables after synthesis. Nevertheless, due to the hydrophobic nature of PVDF, PVDF membrane always encounters great difficulty of wetting by water and the serious adsorptive fouling during filtration, which results in the raised operation cost of PVDF membrane system.[36] To relieve these problems, effective hydrophilic modification of PVDF membrane attracts a large number of researchers' attention nowadays.

As an effective pore-forming additive, PVP is widely used in industrialized membrane manufacture. Since the work of this dissertation also involved some PVDF membranes with PVP additive, the influence of PVP on the mechanism of PVDF membrane formation during NIPS was briefly introduced. When casting film of membrane dope solution contacted with water nonsolvent, the doped hydrophilic PVP additive with low molecular weight tended to move towards the interfacial boundary between casting film of dope solution and nonsolvent water in order to diminish the interface energy.[51] In-diffusion rate of nonsolvent water that was largely enhanced by hydrophilic PVP was much higher than out-diffusion rate of solvent on interface of casting film / nonsolvent water.[79] Thus additional PVP thermodynamically improved demixing on interface of casting film / nonsolvent water (occurrence of instantaneous demixing). Consequently the sudden and rapid mutual diffusion of solvent and nonsolvent in interface region resulted in rapid solidification process in the interface between casting film and nonsolvent coagulation bath. In some cases, accompanying the strongly increased interfacial polymer concentration, spinodal demixing occurred instead of binodal demixing in the interface of casting film, which led to quite rapid precipitation and nodular morphology of membrane surface,[81] The overall enhanced interfacial demixing rate brought about the rapid re-organization of spherical polymer molecules mainly composed of matrix polymer molecular chains in the interface region.[82] And the solvent-filled gaps which were surrounded by the collapsed coils of interfacial matrix polymer chains or between aggregates of agglomeration of individual matrix polymer spherical coils formed

interfacial pores on membrane skin top layer.[83] These interfacial pores also can be attributed to the combination of polymer-lean phase which contained part of out-diffused PVP molecular chains during the liquid-liquid demixing process before the rapid solidification of polymer-rich phase in the interfacial region.[6][83][84] Because of the hydrophilic PVP diffusion-out caused by the low entropy of PVP-PVDF mixing[85][86], the nuclei of polymer-lean phase which contained PVP in the interface region tended to form big pores.

In the sublayer underneath the interface region of casting film of PVP/PVDF dope solution, the liquid-liquid demixing occurred meanwhile. However the rapidly solidified top layer of casting film formed a mass-transfer resistant barrier which strongly decreased the in-flow diffusion of nonsolvent water.[87] Consequently the limited in-diffused nonslovent water induced some short nucleated droplets (nuclei) which started the polymer-lean phase during the liquid-liquid demixing in sublayer of casting film. Additionally, the out-diffused PVP from matrix polymer-rich phase were also helpful to formation of nuclei and trapped in matrix polymer-lean phase.[88] The distance from interface of casting film to the initial development region of nuclei in matrix polymer-lean phase, namely the thickness of top skin layer in asymmetric membrane, highly depends on the extent of interconnective porosity in skin layer, because the in-diffused nonsolvent via porous top surface was crucial to the variation of precipitation kinetic of matrix polymer in the sublayer below.[84][87]

When the mutual solvent-nonsolvent diffusion between the formed nuclei layer (matrix polymer-lean phase) in sublayer and the matrix polymer-rich phase went further, the diffusion flow of solvent out of matrix polymer solution (matrix polymer-rich phase) in sublayer was much larger than the nonsolvent flow from formed nuclei (matrix polymer-lean phase) into the matrix polymer-rich phase due to the limited in-flow of non-solvent through the solidified interface (top skin layer).[87] As a consequence, the initial instantaneous demixing process prevailed in the interfacial region transited gradually to the delayed demixing locally with further movement of the diffusion front of nuclei layer (matrix polymer-lean phase) towards the deeper region of casting film sublayer where local solvent/nonsolvent composition was higher and higher.[81][89] If there were no induced new nuclei formation in front of the formed nuclei layer of matrix polymer-lean phase, the freshly originated nuclei droplets of matrix polymer-lean phase would expand (grow) further with stably diffusion-induced composition along the interfacial boundary to finally create the macrovoid structure in sublayer of casting film. Generally the process of growing macrovoids can be disturbed by the newly formed nucleated droplets of matrix polymer-lean phase in front of the existing ones, which resulted in the sponge-like structure composed of closed matrix polymer cell with poor interconnectivity.[6][89] Growth of macrovoid actually was convective flow of matrix polymer-lean phase with respect to matrix polymer-rich phase. The variation of precipitation rate

and viscosity of dope solution are also key factor for macrovoid formation. During the growth process, the coalescence of smaller droplets of matrix polymer-lean phase occurred via coarsening process to form the larger structure based on the mechanism of minimization of interfacial free energy between droplets of polymer-lean phase.[81] After coarsening and growth, accompanied by precipitation of polymer chains, eventually the fully separated layers of polymer-rich and polymer-lean phase generated.[89] High mass transfer resistance from the rapidly solidified top layer led to the extended time for evolution of liquid-liquid demixing (delayed demixing) and decreased the driving force for out-diffusion of solvent in casting film sublayer. Accordingly the excess solvent in polymer-lean droplets brought about the obviously decreased precipitation rate of matrix polymer and retarded solidification of matrix polymer-rich phase which also favored the expanding of matrix polymer-lean droplets for formation of macrovoids morphology.

As above mentioned coagulation process of casting film, via polymer-polymer demixing, hydrophilic PVP can diffuse out from the PVDF matrix of polymer-rich phase and went into polymer-lean phase. Besides, PVP also tended to move towards nonsolvent in-flow near interface region and sublayer of casting film. During the out-diffusion course, hydrophilic PVP molecular chains strongly interfered with the nonsolvent-induced (water-induced) re-organization and arrangement of PVDF molecular chains in polymer-rich phase for PVDF solidification process.[82][83] Consequently, the PVDF precipitation rate was remarkably decreased, and thus, compared with normal coagulation process without PVP additive, the polymer-lean phase in interface region and in sublayer of casting film obtained relatively more time to grow further enough for the largely enhanced porous morphology in both top layer and sublayer region of formed membrane. The PVP which were trapped in polymer-lean phase can be leached out during filtration as well as coagulation process and formed extra pores in top layer and sublayer region.[88] In addition, the hydrophilic PVP in polymer-rich phase was also regarded as non-solvent which resulted in some enhancement of local viscosity that gave negative effect on precipitation rate of PVDF molecular chains in polymer-rich phase via the reduction of diffusion exchange rate between solvent and nonsolvent.[84] As an integrated consequence, the water permeability of PVP/PVDF membrane was also accordingly and highly increased.

2.2.3. Preparation of synthetic asymmetric polymer membrane via phase separation

Commercial polymeric membrane gains a dominant application through the range of industrial synthetic membrane due to its proper cost and strong variability on barrier morphology and properties. A broad variety of commercially polymeric membranes can be prepared via phase

inversion that covers a wide range of versatile procedures available for basically all kinds of membrane morphology.[6][22][24] Phase inversion can be briefly described as a transformation of polymer solution from liquid to solid state in a controlled manner.[22] Membrane prepared via nonsolvent induced phase separation (NIPS) dominates the majority of commercial membranes that are manufatured through implementation of processes based on phase separation in industrial fields. In particular, asymmetric polymer membrane such as NF, UF and some MF polymer membrane, which prevails as most of presently commercialized membrane due to the high permeating flow and proper selectivity provided by the combination of thin top layer and underlying porous macrovoids, can be readily prepared via NIPS with consistant quality at large scale in industrial fields.[24][29]

NIPS is normally performed isothermally and can be shortly described as a phase separation process that is led by exchange between solvent and nonsolvent of polymer solute.[23] The main mechanism and parameters of NIPS can be clearly explained on the basis of ternary phase diagrams of the three main components (polymer, solvent, nonsolvent). A pronounced miscibility gap (unstable region) should be the prerequisite of NIPS occurrence. After immersion of a homogeneous polymer solution with single or mixed solvents into a nonsolvent coagulation bath (in most of cases water is nonsolvent), due to the strong exchange of solvent and nonsolvent, the initially thermodynamical stable single-phase polymer solution system moves into the miscibility gap (unstable region) of the according ternary phase diagram where the minimum Gibbs free energy is reached. Consequently, as the liquid-liquid demixing (or solid-liquid demixing sometimes) takes place according to the specific unstable region in ternary phase diagram that is attained, the single liquid phase of immersed polymer solution film separates into two liquid phases, the polymer-rich phase and the polymer-lean phase. After that, with the solidification of polymer-rich phase, the final morphology of the prepared membrane is determined, namely, the membrane structure is built up via NIPS.[6][24]

As shown in **Fig. 5**, generally two different kinds of paths are often traveled when the composition of polymer solution film contacts with nonsolvent and comes into the unstable region in ternary phase diagram. The liquid-liquid demixing occurs rapidly and the droplets of polymer-lean phase that are dispersed in polymer-rich phase form nuclei to grow further in size until the solidification of polymer-rich phase or the thermodynamic equilibrium is reached as soon as the polymer system enters unstable region via Path A. If the polymer system directly goes through the critical point into unstable region as Path B, solid-liquid demixing occurs and results in the spinodal decomposition phenomenon. The growth and coalescence of nuclei of polymer-lean phase droplets forms the pores on the top surface of polymer solution film after the solidification of

polymer-rich phase, that is the well-known nucleation growth mechanism, whereas spinodal decomposition leads to two co-continuous phases and generates pores by fast solidification.[6][29][27]

Aside from thermodynamic effect, the precipitation kinetics of polymer-rich phase is another important factor that should be taken into account for the formation of expected morphology in NIPS. Keeping pace with demixing, as the decreasing of ratio of solvent/nonsolvent in polymer solution system, in polymer-rich phase the polymer chains that gradually lose their mobility due to the diluting solvent concentration by nonsolvent inflow undergoes the more physical collapse and re-arrangement so that the gelation, vitrification or crystallization of polymer-rich phase occur with varied precipitation rate. Consequently the interconnected porous structure arisen from the growth of polymer-lean phase nucleation is solidified and preserved as the final porous membrane morphology. Different from nucleation growth mechanism of liquid-liquid demixing, spinodal decomposition can give rise to the interconnected porous structure from the onset of solid-liquid demixing (**Fig. 5**).[6][29][31]

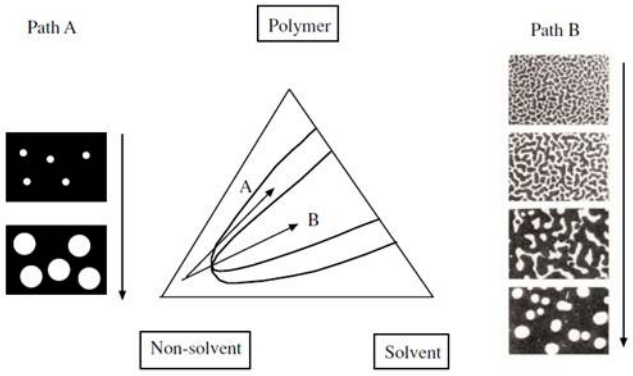

Fig. 5 Liquid-liquid demixing (Path A) and solid-liquid demixing (Path B)[29]

The precipitation kinetics of polymer-rich phase is decreasing from the top surface where the first contact with nonsolvent occurs to the bottom side of the polymer film during NIPS, whereas the resulted pore size is increasing from the top to the bottom. The reason can be mainly attributed to the barrier resistance of the solidified top layer which solidifies quite rapidly due to the fast exchanging of solvent and nonsolvent as soon as the contact with large amount of nonsolvent is at the onset. The solidified top layer consequently allows merely limited nonsolvent inflow to go through the formed pores into the region of polymer system underlying the top layer so that induced nuclei of polymer-lean phase droplets gains a relatively stable circumstance with less disturbance and more time for further growth and coalescence to develop the more porous

structure in sublayer, namely macrovoids. As a result, the asymmetric membrane that consists of the top layer with proper selectivity (pore size) and a finger-liked porous sublayer corresponding to high permeating flux can be available successfully. If the nuclei of polymer-lean phase stops growth due to the unstable circumstance caused by disturbance (e.g. additive effects, viscosity etc.), the sponge-like sublayer that is characterized as a suppressed macrovoids with a number of small closed cells and less interconnectivity between porous structure is formed and bring about the poor permeability.[29][32]

In practice of NIPS, except the abovementioned rapid liquid-liquid demixing (instantaneous demixing), another kind of delayed demixing also exists. After immersion in nonsolvent, if the polymer solution film takes a relatively long period to demix, the delayed demixing occurs, by which the polymer concentration and according viscosity reaches a high degree when the composition of polymer solution system enters the unstable region of ternary phase diagram. Consequently highly concentrated polymer chains are already difficult to re-arrange for pore-forming and rapidly solidified as soon as the demixing occurred. Therefore delayed demixing always creates a nonporous skin layer and sponge-like sublayer with quite low water permeability.[6][33]

Some other factors such as miscibility of sovent/nonsolvent, additive, properties of nonsolvent bath and polymer solution etc. also have strong influences on the morphology of prepared membrane via NIPS. In particular, additives, such as cosolvent, nonsolvent, pore-forming agent, crosslinking agents and anti-fouling agent etc., are frequently involved in polymer solution for NIPS as modifier for expected enhancement on performance of prepared membrane.[6][24] The anti-fouling zwitterionic copolymer additives that were applied in the work of this dissertation was discussed in detail in the following parts of this dissertation.

2.2.4. Concentration polarization and membrane fouling

During the practical separation, when pure water is replaced by feed, the transmembrane flux in various isothermal membrane processes regularly experiences an apparent decline to different extent within seconds. In particular, in the case of pressure-driven membrane such as MF, UF and RO membranes, the flux decline during performing separation is usually quite severe. The initial cause for this immediate flux drop can be attributed to the phenomenon of concentration polarization. Taking UF membrane as an example for explaination, during UF filtration, the gradual accumulation of retained solutes on the membrane surface build up an increased concentration of solutes there, which originates a diffusive flow back to the bulk of feed. Due to

the balance between feed flow towards membrane surface and diffusive back flow plus solute flow through membrane, it is difficult for the accumulated solutes on the membrane surface to flow back to bulk feed solution. Therefore a boundary layer of accumulated solutes can be established with concentration gradient and the maximum concentration of solutes is found at the membrane surface that is typically 20-50 times higher than the concentration of feed bulk. Consequently the concentrated solutes (normally macromolecular and colloidal for UF) fabricates a gel layer to largely and negatively influence flux through the membrane as a second barrier, which is one of the crucial factors responsible for further membrane fouling. Transmembrane pressure during separation processes is quite critical for minimization of effect from concentration polarization. In principle the higher transmembrane pressure intensifies the concentration polarization and thus the gel layer barrier.[6][8] The improved hydrophilicity of membrane surface and the turbulent eddies originated by the filtration module are quite helpful against the formation of gel layer.

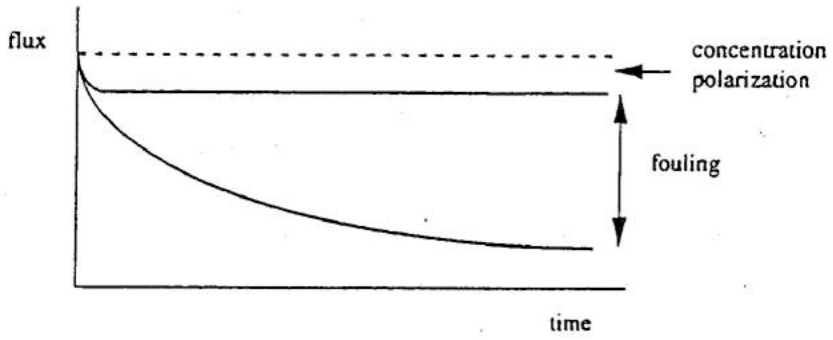

Fig. 6 Influence flux by concentration polarization and fouling as a function of time.[6]

Although theoretically the flux decline caused by concentration polarization should be a constant (steady state) as a function of filtration time, in practice, with respect to pressure-driven membrane, especially MF and UF membrane, an even further continuous decline in flux over a prolonged period of membrane operation can be often observed (**Fig. 6**), which is normally regarded as the result of membrane fouling that is an integral influence of various surface and internal fouling caused by the irreversible and reversible adsorptive deposition of retained solutes, such as macromolecules, biological substances, colloids, particles, salts etc. on or in the membrane.[37] (**Fig. 7**)

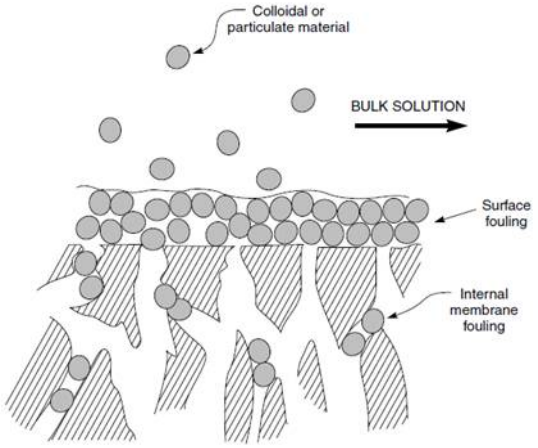

Fig. 7 Surface fouling and internal fouling of solutes for porous membrane.[8]

Part of surface fouling including the loosely consolidated gel layer (initialized by concentration polarization) and some initial adsorptive deposition of solutes on the membrane surface are regularly considered as the reversible fouling due to the feasibility of removal for these fouling through mechanical cleaning, e,g, backwashing. The irreversible fouling consists of cake layer formed by highly densified gel layer on membrane surface and the internal fouling such as adsorptive deposition of permeated solutes on the pore inner walls and the pore-plugging caused by the accumulated deposition of permeated solutes on pore inner walls. The irreversible fouling is impossible to be removed completely via regular membrane cleaning procedures and usually results in a slow and permanent flux loss of membrane. During industrial applications, chemical cleaning is frequently utilized to relieve the irreversible foulants on/in membranes. Indeed the porous membranes with relatively narrower average pore size more tend to provide sustainable flux during filtration due to the improved resistance to internal fouling.[6]

The membrane fouling largely elevates the operation cost of industrial membrane processes, highly decreases the lifetime of membrane system and limits the application of membrane system at large scale. In principle, membrane fouling can be alleviated to different extents via the following methods, including pretreatment of the feed solution, rational design of membrane module and process conditions, regular cleaning (incl. hydraulic, mechanic and chemical cleaning) and improved membrane properties.[6][8][38] Novel porous membrane with high sieving performance and improved anti-fouling ability have been paid more attentions by researchers in recent two decades. On one hand, the narrower pore size can prohibit the inner membrane fouling to some extent. On the other hand, the membrane with improved anti-fouling nature, such as membrane with neutralized charge, pre-adsorption and hydrophilic modification of membrane

etc., can more effectively diminish the membrane fouling from the early stage compared with those external methods. Especially, various hydrophilic modification of membrane are regarded as the most effective way against membrane fouling and extensively applied nowadays, because the hydrophobic interaction between solute and hydrophobic membrane surface as well as inner pore walls dominates the occurance of adsorptive deposition. The dispersion of water molecules on the hydrophobic membrane surface can be described as “less dense” so that there is no adequate hydration layer formed on the membrane surface to further decrease the membrane/water interfacial energy. Consequently, the approaching macromolecule solutes, such as protein, are spontaneously driven by the excess of interfacial free energy to repulse theose water molecules and expose their internal hydrophobic residues to adhere to the hydrophobic surface tightly. The advantageous enhancement of configuration entropy of protein also is a plus for the hydrophobic protein/membrane adsorption.[39]

2.2.5. Hydrophilic modification of PVDF membrane

As aforementioned, the hydrophobic nature and poor water wettability of PVDF membrane largely limit its potential application, in particular the application areas of water treatment and biological product separation. Poor wettability normally results in the low water flux of PVDF membrane, whereas the PVDF membrane fouling arisen from the hydrophobicity highly decrease the lifetime of PVDF membrane and accordingly enhances the operational cost. Besides the improvement of surface wettability by elevated surface energy, the hydrophilic surface of membrane usually also forms more accumulation of water molecules around the membrane surface and inner pore walls, which can effectively prevent the approaching permeated macro molecules (such as protein) from adsorption on membrane surface and thus reduces the resultant membrane fouling.[40][41] To promote the surface hydrophilicity, numerous efforts have already been made towards hydrophilic modification of PVDF membrane in recent years. In general, surface modification of already prepared PVDF membrane and modification via blending during manufacturing are two main methods to effectively realize the hydrophilic modification of PVDF membrane.[42]

Surface modification of prepared PVDF membrane can be subdivided into surface coating and surface grafting. A number of hydrophilic commercial polymer and amphiphilic copolymer such as PVA, chitosan etc. can be easily coated on PVDF membrane surfaces via physical noncovalent bonding to build up hydrophilic layer against irreversible fouling.[43] However, due to the relatively weak physical interaction, the coating layer is normally unstable and susceptible to be leached out from the PVDF matrix membrane during the long-term practical application. In addition, another inevitable problem brought by coating layer is the loss of permeability for coated PVDF

membrane to different extents as a result of extra permeation resistance and membrane pore-blocking caused by the coating material. Various monomers and some polymers can be successfully grafted on PVDF membrane surface to form fouling resistance via UV photoirradiation, plasma treatment, high energy electron beam and living/controlled surface polymerization etc.. In contrast to surface coating, grafted hydrophilic layer gains more long-term stability due to the chemical covalent bonding between grafted polymer chains and PVDF membrane surface. Nevertheless, apparent flux decline due to pore-blocking still can be observed in surface grafing. Besides, undesirable degradation on original morphology of PVDF membrane and employment of caustic chemicals as well as specific equipments always accompany the process of surface grafting, whereby limiting the accordingly industrial applications.[42] Overall, surface modification technique can effectively establish the functional hydrophilic layer on the both surface of PVDF membrane.

Modification of PVDF membrane via blending is widely applied in industrial manufacture at large scale, because the pursued properties including hydrophilicity can be donated to PVDF membrane simultaneously via NIPS within single-step process.[44] In this method, PVDF polymer and hydrophilic additive were simply blended together as homogeneous blend and processed via phase separation (mostly NIPS) to fabricate hydrophilic PVDF membrane, by which hydrophilic additive can be readily entrapped or exposed on/in PVDF membrane surface without any extral pretreatment or post-treatment. More practically, through blending modification, the modified hydrophilic layer can be achieved not only on the surfaces but also along the inner pore walls of PVDF membrane due to the thermodynamic-driven surface migration of hydrophilic additive during NIPS.[44][45] Blending modification procedure can be employed for preparation of flat sheet as well as hollow fibre membranes.

Regularly, hydrophilic homopolymer, inorganic nanoparticles and amphiphilic copolymer are often used as hydrophilic additive in blending modification of PVDF membrane. Hydrophilic PVP and PEG are extensively used to blend with PVDF and fabricate modified PVDF membrane via NIPS. (cf. **2.2.2.**) The unstability of these water soluble homopolyer in PVDF matrix always results in the basically complete loss of additive during the long-term filtration process. It should be mentioned that PMMA, also commonly being used as hydrophilic additive in PVDF blend, displayed excellent thermodynamic miscibility with PVDF.[46][47][48] In the case of amphiphilic copolymer as blending additive with PVDF, during the NIPS, thermodynamically driven by the minimization of water/PVDF interface free energy of whole system, the hydrophilic block (segments) of amphiphilic copolymer in blend can migrate and enrich on the membrane surface and along the inner pore walls with adequate coverage. Meanwhile, the hydrophobic block (segment) of

amphiphilic copolymer, which usually consist of the polymer with better PVDF compatibility such as PMMA or even PVDF backbone, can still steadily anchor in PVDF matrix by entanglement so that the exposed hydrophilic part of amphiphilic copolymer are also fixed on the surface to form stable hydrophilic layer with durable long-term stability.[49][50][51] (**Fig. 8**) The single-step operation of blending modification largely decreases the manufacture cost and is in favor of industrial application. It also should be noted that the property of bulk PVDF membrane can be remained completely without any negative influence during blending modification.[42][44] In the work of this dissertation, the blending modification is also adopted to prepare novel hydrophilic PVDF membranes with tailored surface engineering. Incorporation of inorganic nanoparticle via blending modification has also already been studied and proves the improvement of PVDF membrane hydrophilicity and mechanical strength, which is beyond the scope of this dissertation and are described in many other relevant publications.[52][53]

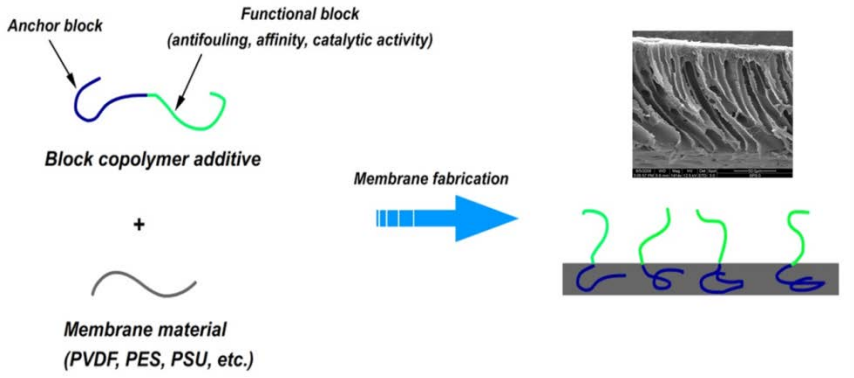

Fig. 8 Through NIPS of PVDF solution bleding with amphiphilic copolymer additive, the functional block (hydrophilic block) of additive can expose on the PVDF membrane surface (incl. inner pore walls) and the anchor block (hydrophobic block) can be thermodymically accommodated in PVDF membrane matrix.

2.3. Anti-fouling mechanism of zwitterionic polymers

Urged by the practical challenge from nonspecific adsorption fouling of microorganism and bio-macromolecules, the development of anti-fouling material with nonspecific protein resistance is attracting considerable attentions in relevant chemical and biological area. The most widely applied polymer material against fouling, in the presence of oxygen and transition metal ions, poly(ethylene glycol) (PEG) is quite susceptible to be decomposed and loses the anti-fouling function.[54][55][56] Inspired by the nonthrombogenic zwitterionic phospholipids that enriched in the outside surface of mammalian cell membrane, numerous exploring efforts are already invested

on the development of novel anti-fouling polymer material with zwitterions in recent decades. Three types of typical zwitterionic polymers can be seen in **Fig. 9**.

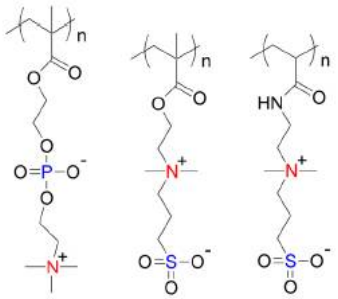

Fig. 9 Three types of typical zwitterionic polymers. Poly(methacryloyloxylethyl phosphorylcholine) (left); Poly(sulfobetaine methylacrylate) or PolySPE, (middle); Poly(sulfobetaine acrylamide) (right).[57]

In principle, anti-fouling material should possess neutral- or slightly negative-charged surface and well hydration layer.[57] The strong hydrogen bonding interaction between hydrophilic PEG polymer chains and water molecules originates the hydration layer, whereas zwitterionic polymer, in which the cationic and anionic groups are generated in same repeating unit and give an electric neutrality, can even more strongly bind more water molecules via ionic solvation (hydration) as well as the existing osmotic pressure. It has already been strongly evidenced that zwitterions can not interrupt the hydrogen bonding connection among water molecules that are attracted around zwitterions, even including the water molecules that are directly hydrated to the zwitterion charges.[54][57][58][59] The fixed polarity orientation and the specific proximity distance of the opposite zwitterions charges are capable of forming a field to accomodate and remain the original polarity orientation of water molecules without any structural rearrangement of hydrogen bonding network of water molecules. In other words, there is no structural difference between water around zwitterions and natural water in bulk.[57][60] The structural comparison between the bound water around zwitterionic charges and single charge can give more details (**Fig. 10**).

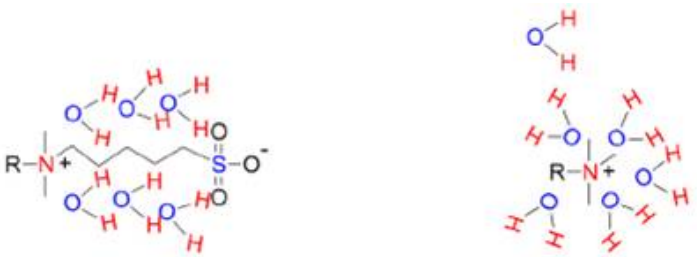

Fig. 10 Comparison of water molecules orientation around zwitterion charges (left) and single positive charges (right).[57]

As shown in **Fig. 10**, it is quite clear to see that, water molecules between zwitterions can be arranged in order without discruption towards hydrogen bonding network of water molecules, which is basically same as the manner of water molecules in bulk liquid water, while the arrangement of hydrogen bonding orientation are in disorder and deform seriously around only charged polar group.[57] Due to the large cohesive energy density of water molecules that remain undisrupted hydrogen bonding network, it is almost impossible for approaching proteins to repulse the water molecules in the field between zwitterions and generate the adsorption on the polymer interface.[57][61] In addition, adsorption of protein also needs to overcome the entropy penalty resulted from the reordering of disordered water hydrogen bonds around zwitterions. It should be mentioned that polySPE normally shows the minimal disruption on the bound water structure, which indicates that polySPE has great potential to be applied against nonspecific protein fouling. In contrast to PEG that makes use of the steric repulsion resulted from flexible polymer chains as well as physical water barrier to prevent protein from adsorption, the hydration layer around zwitterions can be regarded as an energy barrer which itself is capable of playing the role of excluded volume against protein adsorption.[57][62][63] In the work of this dissertation, polySPE are introduced as anti-fouling functional groups on PVDF membrane surface for detailed characterization.

3. Objectives and concepts

3.1. Objectives

Technologies for preparation of polymer membranes based on pressure-driven size-selectivity in widely applied fields are well known and established. The expensive energy consumption and the inpredictable separation performance as well as decreased lifetime caused by the high driven pressure and the membrane fouling are still challenging the improvement of industrial membrane process. A great number of efforts are invested to improve membrane performance with respect to enhancement of permeability as well as separation selectivity and alleviation of membrane fouling propensity. The narrower pore size distribution at high porosity is always pursued in current membrane development.[22]

Rooting in “promising bottom-up technologies to develop intensified water treatment concepts based on nano-structured and nano-functionalized membranes”, as NANOPUR project aims, the research objectives of this dissertation focused on bottom-up development of nanostructured ultrafiltration membranes characterized by high flow rate, high separation selectivity and low fouling properties. Introduction of proper amphiphilic additive during membrane manufacturing normally can offer effective control of porosity, pore size, pore size distribution and surface energy to prepared membrane. Membranes with integration of desired properties arisen from rational utilization of additives can be expected to meet various challenges in scientific and industrial fields, e.g. “trade-off” and fouling.

As requirements of NANOPUR project, the detailed main targeting parameter values for the optimized prototype ultrafiltration membrane included, water permeability $\geqq 500$ $L \cdot h^{-1} \cdot m^{-2} \cdot bar^{-1}$, molecular weight cut-off (MWCO) $\leqq$ 100,000 g/mol, water contact angle of top membrane surface $\leqq 40^{o}$.

3.2. Concepts

PVDF was selected as matrix polymer material to fulfill the bottom-up preparation of UF membranes with above targeted performance parameters in consideration of the prevailing merits of PVDF that were detailed introduced in **2.2.3.**. To overcome the severe fouling susceptibility caused by hydrophobic nature of PVDF material, in the work of this dissertation the carefully tailored amphiphilic block copolymers was established and introduced in PVDF membranes as surface-segregating additive to improve the hydrophilicity as well as fouling resistance of surface

and inner pore walls.[44][57][64] In addition, improvement of trade-off relationship between water permeability and sieving selectivity (pore size) was also pursued for the targeted PVDF UF membrane.

Amphiphilic $PMMA_m$-*b*-$PSPE_n$ was rationally designed for the main purpose of enhancing hydrophilicity and anti-fouling ability of PVDF membranes (**Fig. 11**). On one hand, the PMMA worked as anchoring block to root the whole additive chains in matrix PVDF depending on the excellent thermodynamic compatibility and miscibility between PMMA and PVDF.[46][47][48] On the other hand, zwitterionic PSPE supplied super hydrophilicity and remarkable fouling resistance by means of the energy barrier of strong hydration layer (hydrogen-bonding network of water molecules) via strong ionic hydration and electrostatic interaction between negative charged sulfo-betaine groups and positive charged ammonium groups in the pendent side chains of PSPE backbones.[57] $PMMA_m$-*b*-$PSPE_n$ with various molecular weights were designed to be synthesized via sequential atom transfer radical polymerization (ATRP) and both the chain lengths of PMMA and PSPE can be well controlled and accurately adjusted for the most optimized membrane performance. Amphiphilic $PMMA_m$-*co*-$PSPE_n$ (**Fig. 11**) also was utilized to compare with $PMMA_m$-*b*-$PSPE_n$ in order to figure out the influence of different polymer architecture on its additive function.

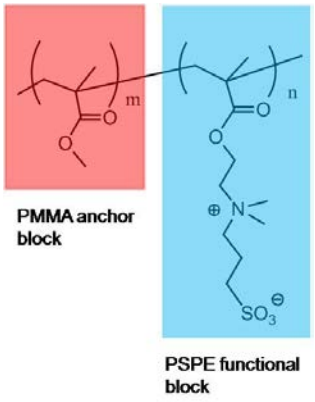

Fig. 11 Schematic chemical structure of $PMMA_m$-*b*-$PSPE_n$ and $PMMA_m$-*co*-$PSPE_n$. PMMA is anchor block (left). PSPE is functional block (right).

The blend solution films of $PMMA_m$-*b*-$PSPE_n$ and PVDF were cast into water coagulation bath and formed the nanostructured membranes with expected asymmetric structure via nonsolvent induced phase separation (NIPS) process. During the coagulation PSPE blocks were capable of enriching (segregating) on the PVDF membrane surface and inner pore walls due to the strong tendency of hydrophilic PSPE to migrate towards membrane surface for minimization of

interphase energy (**Fig. 12**).[42][44] Tailor-made $PMMA_m$-*b*-$PSPE_n$ with different design parameters, such as molecular weight, ratio of PMMA/PSPE, showed effects on performance and morphology of prepared membranes to different extents. Generally, higher molecular weight of $PMMA_m$-*b*-$PSPE_n$ signified less surface enrichment due to its enlargement of configuration entropy penalty, whereas higher ratio of PMMA/PSPE exhibitedd improved solubility in membrane dope solution and more typical effect of zwitterionic additive, i.e. quite low water permeability and high anti-fouling ability.

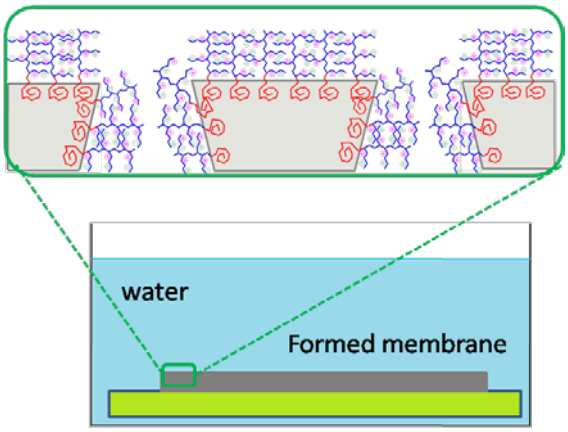

Fig. 12 During coagulation the $PMMA_m$-*b*-$PSPE_n$ migrated towards membrane suface. The hydrophilic PSPE blocks segregated on the surface and inner pore walls of the formed membrane. The PMMA block anchored in the bulk PVDF.

The exposed PSPE blocks that were tethered by PMMA block in bulk PVDF formed tight hydration shell with similar nature to natural bualk water and offered strong resistance against approaching organic and micropollutants during filtration. Consequently the irreversible adsorptive fouling on PVDF membrane was largely relieved and the difficulties for PVDF membrane cleaning was also decreased remarkably (**Fig. 13**).[40][54]

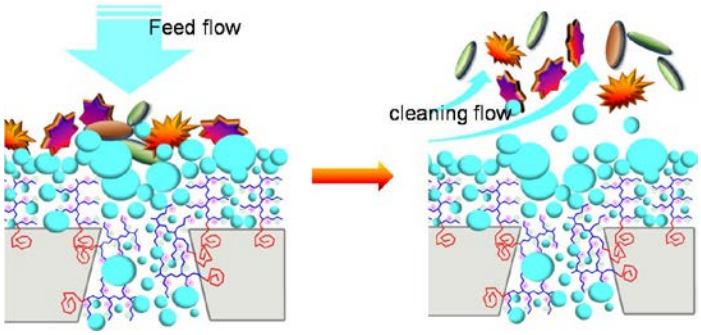

Fig. 13 Stable hydration layer was fixed by PSPE via ionic hydration on surface and inner pore walls of membrane. Organic (e.g. proteins) and microbial foulants can not contact with hydrophobic PVDF membrane directly due to the energy barrier. Deposites was readily removed by simple cleaning of membrane.

In addition, other homopolymer hydrophilic additives such as PVP, PEG etc. also were introduced as single additive or second additive in combination with $PMMA_m$-*b*-$PSPE_n$ to further improve the trade-off relationship between membrane permeability and selectivity.

4. Experiments

4.1. Materials

Methylmethacrylate (MMA, ≧ 99%), 1,3-propane sultone (≧ 98%), ethyl 2-bromopropionate (EBrP, ≧ 99%), 2,2′-bipyridine (BiPy, ≧ 97%), 4,4'-dinonyl-2,2′-bipyridine (Dinonyl-BiPy, ≧ 97%), N-(2-methacryloyl-oxyethyl)-N,N-dimethyl-N-(3-sulfopropyl) ammonium betaine (sulfobetaine methacrylate, SPE, ≧ 97%), d-Chloroform ($CDCl_3$, ≧ 99.8%), d_6-Dimethylsulfoxid ($(CD_3)_2SO$, ≧ 99.9%), d_3-Acetonitrile (CD_3CN, ≧ 99.8%), ethylene glycol (anhydrous, ≧ 99.8%), N-methyl-2-pyrrolidon (NMP), remover for stablizer MeHQ (≧ 99%), toluene (anhydrous, ≧ 99.8%), tetrahydrofuran (THF, anhydrous, ≧ 99.9%), n-Hexane (anhydrous, ≧ 95%), dimethylformamid (DMF, ACS reagent, ≧ 99.8%), sodium chloride (NaCl, ≧ 99%), sodium azide (≧ 99.99%), potassium dihydrogenphosphate (KH_2PO_4, ACS reagent), sodium hydrogen phosphate (Na_2HPO_4, ≧ 99.95%) were purchased from Sigma-Aldrich and utilized as received. N,N,N',N'',N''-pentamethyldiethylenetriamine (PMDETA, ≧ 99%), Copper(I) bromide (≧99%), Copper(II) bromide (≧ 99%) were purchased from Acros and utilized as received. Ethanol (laboratory reagent, ≧ 96%), iso-propanol (ACS reagent, ≧ 99.5%) were purchased from VWR and utilized as received. N,N-dimethylaminoethyl methacrylate (DMAEMA,≧ 99%) was purchased from Polyscience Inc. and utilized as received. Azobis(isobutyronitril) (AIBN, ≧ 98%) was purchased from AppliChem and utilized as received. Polyvinylidenfluorid (PVDF, M_w= 48.1 KDa, ≧ 99.9%) was purchased from SOLVAY and utilized as received. Polyvinylpyrrolidon (PVP K30, PVP K17, ≧ 99.9%) was purchased from BASF and utilized as received. Polyethylenglycol (PEG, ≧ 99.9%) was purchased from Fluka and utilized as received. Bovine Serum Albumin (BSA, ≧ 99.7%) was purchased from ICN Biomedicals Inc. and utilized as received. Dextran (≧ 99.9%) was purchased from CARL ROTH and utilized as received. NaOH solution (0.1M, ≧ 99.9%) was purchased from Merck and utilized as received. Water deionized with MilliQ system (Millipore) was utilized for all the relevant experiments.

4.2. Synthesis

4.2.1. Synthesis of $PMMA_m$-*co*-$PSPE_n$ via free radical polymerization

MMA (3 g, 0.03 mol) and SPE (0.95 g, 0.0035 mol) were dissolved in 70 ml DMSO and then the mixture was degassed by Ar for about 30 min. Meanwhile, AIBN (0.219 g, 0.0013 mol) was dissolved in 5 ml DMSO and degassed by Ar for about 15 min. Subsequently above two degassed solutions were mixed and stirred under protection of Ar at 60°C for about 24h. $PMMA_m$-

co-PSPE$_n$ was precipitated after transfering the reaction solution into ethanol. After filtration and dryness, 3.38 g off-white solid was obtained.

[MMA]:[SPE]:[AIBN] = 23.1 : 2.7 : 1

C_{MMA} = 0.4 mol/L, C_{SPE} = 0.047 mol/L, C_{AIBN} = 0.017 mol/L.

4.2.2. Synthesis of PMMA$_m$-*b*-PSPE$_n$ via atom transfer radical polymerization

4.2.2.1. Synthesis of PMMA$_m$-*b*-PSPE$_n$ with $M_{n\ PMMA}$= 13.9 kg/mol

Synthesis of PMMA$_m$-Br macroinitiator ($M_{n\ PMMA}$= 13.9 kg/mol)

MMA (treated by Remover in advance for removal of stablizer MeHQ) was dissolved in toluene and degassed by Ar for 15 min. After addition of Copper(I)bromide and PMDETA, the mixture was stirred for 5min at r.t.. Then degassed EBrP/toluene solution was transferred into above mixture. Subsequently the whole mixture was kept stirring about 4h at 85°C. After removal of complex catalysts, macroinitiator PMMA$_m$-Br was precipitated in ethanol and dried by vaccum oven.

[MMA]:[EBrP]:[Cu(I)Br]:[PMDETA]= 120: 1: 1.5: 1.5,

C_{MMA}= 5 mol/L, C_{EBrP}= 0.042 mol/L, $C_{Cu(I)Br}$= 0.063 mol/L, C_{PMDETA}= 0.063 mol/L.

Synthesis of PMMA$_m$-*b*-PDMAEMA$_n$ with $M_{n\ PMMA}$= 13.9 kg/mol

DMAEMA (treated by Remover in advance for removal of stablizor MeHQ) was dissolved in toluene and degassed by Ar for 15min. After addition of PMDETA and Copper(I) bromide, the mixture was stirred for 5min at r.t.. Then the degassed PMMA$_m$-Br/toluene solution was transferred into above misture. Subsequently the whole mixture was kept stirring for 20 min at 85°C. After removal of complex catalysts, diblock copolymer PMMA$_m$-*b*-PDMAEMA$_n$ was precipitated in n-Hexane and dried by vaccum oven.

[DMAEMA]:[PMMA$_m$-Br]:[Cu(I)Br]:[PMDETA]= 30: 1: 2: 2,

C_{DMAEMA}=0.3 mol/L, $C_{PMMA\text{-}Br}$= 0.01mol/L, $C_{Cu(I)Br}$= 0.02 mol/L, C_{PMDETA}= 0.02 mol/L.

Synthesis of PMMA$_m$-*b*-PSPE$_n$ with $M_{n\ PMMA}$= 13.9 kg/mol

PMMA$_m$-*b*-PDMAEMA$_n$ (precursor) was dissolved in THF. Then after addition of 1,3-propane sultone, the whole solution was kept stirring for 24h at 40°C under protection of Ar. (PMMA)$_m$-*b*-(PSPE)$_n$ was precipitated in ethanol and dried in vaccum oven.

[precursor]: [sultone]= 1: 10.19,

$C_{precursor}$= 5 g/L.

4.2.2.2. Synthesis of $PMMA_m$-*b*-$PSPE_n$ with $M_{n\ PMMA}$= 30 kg/mol

Synthesis of $PMMA_m$-Br macroinitiator ($M_{n\ PMMA}$= 30 kg/mol)

MMA (treated by Remover in advance for removal of stablizor MeHQ) was dissolved in toluene and degassed by Ar for 15 min. After addition of Copper(I) bromide and Bipyridine (BiPy), the mixture was stirred for 5 min at r.t.. Then degassed EBrP/toluene solution was transferred into above mixture. Subsequently the whole mixture was kept stirring about 3h at 50°C. After removal of complex catalysts, macroinitiator $PMMA_m$-Br was precipitated in ethanol and dried by vaccum oven.

[MMA]:[EBrP]:[Cu(I)Br]:[BiPy]= 50:1: 1: 2,

C_{MMA}=3 mol/L, C_{EBrP}=0.06 mol/L, $C_{Cu(I)Br}$=0.06 mol/L, C_{BiPy}=0.12 mol/L.

Synthesis of $PMMA_m$-*b*-$PDMAEMA_n$ with $M_{n\ PMMA}$= 30 kg/mol

DMAEMA (treated by Remover in advance for removal of stablizor MeHQ) was dissolved in toluene and degassed by Ar for 15 min. After addition of PMDETA and Copper(I) bromide, the mixture was stirred for 5 min at r.t.. Then the degassed $PMMA_m$-Br/toluene solution was transferred into above misture. Subsequently the whole mixture was kept stirring for different time span respectively at 50°C and r.t.. After removal of complex catalysts, diblock copolymer $PMMA_m$-*b*-$PDMAEMA_n$ was precipitated in n-Hexane and dried by vaccum oven. 13 $PMMA_m$-*b*-$PDMAEMA_n$ with defferent ratios of PMMA versus PDMAEMA (m/n) were synthesized under various conditions. The details of conditions can be seen in **5.2.2.2.**.

Synthesis of $PMMA_m$-*b*-$PSPE_n$ with $M_{n\ PMMA}$= 30 kg/mol

$PMMA_m$-*b*-$PDMAEMA_n$ (precursor) was dissolved in THF under protection of Ar. Then after addition of 1,3-propane sultone, the whole solution was kept stirring for 24h at 40°C. $(PMMA)_m$-*b*-$(PSPE)_n$ was precipitated in Ethanol and dried in vaccum oven.

[precursor]: [sultone]= 1: 10.87×m (m is number of MMA repeating units),

$C_{precursor}$= 5 g/L.

4.2.2.3. Synthesis of $PMMA_m$-*b*-$PSPE_n$ with $M_{n\ PMMA}$= ~10 kg/mol

Synthesis of $PMMA_m$-Br macroinitiator ($M_{n\ PMMA}$= ~10 kg/mol)

MMA (treated by Remover in advance for removal of stablizor MeHQ) was dissolved in toluene and degassed by Ar for 15 min. After addition of Copper(I) bromide and dinonyl-Bipyridine(dN-Bipy), the mixture was stirred for 5min at r.t.. Then the degassed EBrP/toluene solution was transferred into above mixture. Subsequently the whole mixture was kept stirring about 2h at

40°C. After removal of complex catalysts, macroinitiator $PMMA_m$-Br was precipitated in ethanol/n-Hexane (2/1, v/v) and dried by vaccum oven.

[MMA]:[EBrP]:[Cu(I)Br]:[dN-BiPy]= 50:1: 1: 2,

C_{MMA}=3 mol/L, C_{EBrP}= 0.06 mol/L, $C_{Cu(I)Br}$=0.06 mol/L, $C_{dN\text{-}BiPy}$=0.12 mol/L.

Synthesis of $PMMA_m$-*b*-$PDMAEMA_n$ with $M_{n\ PMMA}$= ~10 kg/mol

DMAEMA (treated by Remover in advance for removal of stablizor MeHQ) was dissolved in toluene and degassed by Ar for 15 min. After addition of PMDETA and Copper(I) bromide, the mixture was stirred for 5min at r.t.. Then the degassed $PMMA_m$-Br/toluene solution was transferred into above misture. Subsequently the whole mixture was kept stirring for different time span respectively at 60°C or below. After removal of complex catalysts, diblock copolymer $PMMA_m$-*b*-$PDMAEMA_n$ was precipitated in n-Hexane and dried by vaccum oven. Five $PMMA_m$-*b*-$PDMAEMA_n$ with defferent ratios of PMMA versus PDMAEMA (m/n) were synthesized under various conditions. The details of conditions can be seen in **5.2.2.5.**.

Synthesis of $PMMA_m$-*b*-$PSPE_n$ with $M_{n\ PMMA}$= ~10 kg/mol

$PMMA_m$-*b*-$PDMAEMA_n$ (precursor) was dissolved in THF under protection of Ar. Then after addition of 1,3-propane sultone, the whole solution was kept stirring for 24h at 40°C. $(PMMA)_m$-*b*-$(PSPE)_n$ was precipitated in ethanol and dried in vaccum oven.

[precursor]: [sultone]= 1: 10.87×m (m is number of MMA repeating units),

$C_{precursor}$= 5 g/L.

4.3. Membrane preparation

Target UF membranes were prepared respectively via non-solvent induced phase separation (NIPS) and surface modification.

4.3.1. Brief procedure of normal NIPS

By NIPS, generally, quantified matrix material PVDF and additives were dissolved in solvent and form homogeneous dope solution with different viscosity. And then the dope solution was cast on supporter as viscous film and subsequently coagulated in non-solvent bath to form asymmetric membrane with porous skin layer and macrovoids structure.

By surface aggregation of amphiphilic copolymer additives, hydrophilic PSPE segments of additives were dispersed homogeneously on the surface and inert pore walls of formed membrane.

4.3.2. Preparation of PVDF membrane from dope solutions with single additive

Materials

Additives: Polyvinylpyrrolidon (PVP, K30), $PMMA_m$-*b*-$PSPE_n$, $PMMA_m$-*co*-$PSPE_n$;

Matrix membrane material: Polyvinylidenfluoride (PVDF, M_w= 48.1 kg/mol);

Solvent: NMP; Others: Sodium azide solution (0.01mol/L), Deionized water.

Procedure

Quantified single additive was dissolved in NMP and stirred for about 24h at 60ºC. Then quantified PVDF was added into the solution and the whole solution was stirred for about 48h at 60ºC. After filtration under Ar pressure (5 bar, Filter 3500T) and releasing bubble by vaccum pump for about 30 min, the homogeneous solution was spread on a smooth glass plate (substrate supporter) through a steel casting knife (gate size 200 µm) at casting speed 5 mm/s (or 50 mm/s) under controlled relative humidity between 19-21% at 20-21ºC. Subsequently, formed film was immersed into coagulation bath of deionized water (DI water) ASAP. After 24h immersion, the formed membrane was peeled off and re-immersed in clean DI water bath for rinse. Then wet membrane was cut into round sample pieces (25 mm diameter) and stored in solution of sodium azide (0.01M) for further characterizations.

4.3.3. Preparation of PVDF membrane from dope solutions with two additives

Materials

Additives: $PMMA_m$-*b*-$PSPE_n$, Polyvinylpyrrolidon (PVP, K30, M_n=14 kg/mol), Polyvinylpyrrolidon (PVP, K17, M_n=2 kg/mol), Polyethylenglycol (PEG, M_n= 12 kg/mol), PMMA (M_n=68.2 kg/mol), Ethylenglycol.

Matrix membrane material: Polyvinylidenfluoride (PVDF, M_w= 48.1 kg/mol);

Solvent: NMP; Others: Sodium azide solution (0.01 mol/L), DI water.

Procedure

Quantified $PMMA_m$-*b*-$PSPE_n$ or PMMA was dissolved in NMP and stirred for about 24h at 60ºC. Then quantified PVDF and respective PVP or PEG or ethylenglycol as second additive were added into the solution. The whole solution was stirred for about 24-48h at 60ºC. After filtration by Ar (5 bar, Filter 3500T) and releasing bubbles by vaccum pump for about 30min, the homogeneous dope solution was spread on a smooth glass plate by steel casting knife (gate size 200 µm) at casting speed 5mm/s under controlled relative humdity between 19-21% at 20-21ºC.

Subsequently, formed dope solution film was immersed into coagulation bath of deionized water at r.t. ASAP. After 24h immersion, the formed membane was peeled off and re-immersed in DI water bath for rinse. Then wet membrane were cut into round pieces (25 mm diameter) and stored in solution of sodium azide (0.01M) for further characterizations.

4.3.4. Surface modification of PVDF membrane with precursor additives

Diblock copolymer $PMMA_m$-*b*-$PDMAEMA_n$ (precursor) were dissolved as additives with PVDF in NMP and then processed via NIPS to form original membranes. Then hydrophilic PDMAEMA blocks exposed on the sueface and inner pore walls of PVDF membrane were converted to PSPE block via surface modification.

4.3.4.1. Preparation of PVDF membranes with precursor additives

Materials

Polyvinylidenfluoride (PVDF, M_w= 48.1 kg/mol), $PMMA_m$-*b*-$PDMAEMA_n$, NMP, DI water.

Procedure

Quantified $PMMA_m$-*b*-$PDMAEMA_n$ and PVDF were dissolved in NMP and stirred for about 48h at r.t.. After filtration by Ar (5bar, Filter 3500T) and releasing bubbles by vaccum pump for about 30min, the homogenious solution was spread on a smooth glass plate by steel casting knife (gate size 200 µm) at casting speed 50mm/s under uncontrolled humdity (over 50%) at r.t.. Subsequently, formed films were immersed into coagulation bath of deionized water ASAP at r.t.. After 24h, the formed membanes were peeled off and rinsed in DI water bath. Then wet membrane was cut into round pieces (25 mm diameter) and stored in sodium azide solution (0.01M) for further characterizations.

4.3.4.2. Surface modification

PDMAEMA blocks dispersed on sueface of PVDF membrane were converted to PSPE block via surface modification in Isopropanol.

Materials

Prepared PVDF membranes with $PMMA_m$-*b*-$PDMAEMA_n$, Isopropanol, 1,3-propane sultone.

Procedure

Round pieces (25 mm diameter) of previously prepared PVDF membranes with $PMMA_m$-*b*-$PDMAEMA_n$ was immersed in isopropanol. And then quantified 1,3-propane sultone was added and dissolved. Subsequently the whole mixture was shaked for about 24h at r.t.. Modified membranes were picked out and rinsed by DI water for further characterizations.

4.4. Characterizations

4.4.1. Polymer

4.4.1.1. ^{1}H-NMR

All ^{1}H-NMR spectra of PMMA-Br, $PMMA_m$-*b*-$PDMAEMA_n$, $PMMA_m$-*co*-$PSPE_n$ were recorded with a Bruker DMX-300 (300 MHz) or Bruker DMX-500 (500 MHz) at 25°C (r.t.). $CDCl_3$, d_6-DMSO or d_3-Acetonitrile were employed respectively as solvents.

The spectra obtained could quantitatively determine the functional groups of prepared polymer. Integrated areas of hydrogen signals from spectra correspond to the specific amount of hydrogen atoms of individual groups. By calculation of ratios from integrals, the average ratios between amount of repeating units in prepared copolymers (m/n) and the mole ratios between rest unpolymerized and polymerized monomer in reaction solution can be determined. The conversion of monomer could be calculated with the latter ratios.

4.4.1.2. GPC

As one type of liquid chromatography, Gel permeation chromatography (GPC) is widely employed to determine molecular weight of polymer. The chromatographic separation mechanism of GPC is based on size of polymer molecular chains in solution. The stationary phase is composed of heterogeneous porous medium filled with inert liquid. The mobile phase carrying dissolved polymer flows between porous medium. By accumulated different interaction between dissolved polymer molecular chains with various hydrodynamic radius and micropores, polymer chains with different lengths reaches the exit at eluted shift rate, by which the small polymer takes more time than big polymer to pass through the whole GPC column.

The GPC measurements were performed with DMF or DMAc as eluent and LiBr (0.01 mol/L) as an additive at 23°C or 60°C. The HPLC system used is based on a pump (PU-2080 Plus, Jasco),

a Refractive index detector (ETA-2020) and columns (2 columns GRAM analytical linear (8 x 300 mm) 10 µm + precolumn GRAM) in the range of 100- 100,000,000 g/mol. The flow rate was 1 mL/min. The evaluation was performed using the software PSS WinGPC 6.2. Calibration polymer was poly (methyl methacrylate) for all molecular weights given as classic calibration. All indicated PDI values were also based on the GPC measurement and the classical calibration.

4.4.1.3. Elemental Analysis

The proportion of carbon, hydrogen, nitrogen, oxygen and sulfur in each molecule can be determined with elemental analysis. In the work of this dissertation only proportion of nitrogen and sulfur were employed for characterization of copolymer. The sample was burned with additional V_2O_5 in oxygen, and the produced gases were analyzed by EURO-EA from Euro Vector company. Ratio of blocks for copolymer can be calculated via proportion of nitrogen and sulfur.

4.4.1.4. Attenuated total reflection infrared spectroscopy

Infrared spectroscopy (IR) indicates the absorbance of specific frequencies in the infrared region which matches the transition energy of the vibrating bond or group from chemicals. The determined absorbance and frequency can be utilized for quantitative or qualitative characterization of the functional groups as chemical structure identification. Both Solid and liquid samples can be directly examined without any pretreatment via conjunction of IR and Attenuated total reflection (ATR), the latter can control the path of incident radiation length via total internal reflection to avoid strong attenuation of the IR signal in highly absorbing media. In the work of this dissertation, S=O and C=O were mainly confirmed qualitatively with ATR-IR.
All IR spectra were examined via 3100 FT-IR Excalibur with MCT detector of Ge crystal and ATR attachment Miracle (Pike) (from Varian company) at room temperature.

4.4.2. Membranes

4.4.2.1. Rheology

As a crucial parameter, viscosity of membrane dope solution has strong relation with indication on mass transfer rates during phase separation, precipitation dynamics and membrane morphology. Rheology behavior of membrane dope solutions were researched via rheometer (Physica MCR 301, Anton Paar). The geometry for measurements was CP50-1-SN25123 with conic plate (d=

0.101 mm). The most measurements were performed in rotation mode with incremental shear rate from 0.1 [1/s] to 1000 [1/s] at 25ºC.

4.4.2.2. Scanning Electron Microscopy

Scanning Electron Microscopy (SEM) scans test samples via focused electron beams and produces images which offer information about sample composition and morphology of sample surface and inner structure by means of processing signals from interaction of electrons and atoms of samples. The high resolution and resulted high magnification (up to 2,000,000x) of SEM facilitates the detailed investigation of membrane surfaces and cross sections.

Predried membrane samples were fixed on testing plates and sputtered with 7nm Au/Pd layer by a K550 sputter coater (Emitech, UK) after vaccum-drying. The scanning and recording was performed via Quanta 400 FEG (FEI, Czech Republic) environmental scanning electron microscope (ESEM).

4.4.2.3. Contact angle

Contact angle can be employed to indicate the interaction of testing surface and specific liquid, e.g. water wettability of membrane surface. Contact angle geometrically measured with tangent line through contact point along liquid-vapor interface around the droplets or air bubble outline. The device for measurement was OCA 15 Plus from Data Physics GmbH (Filderstadt, Germany). The analysis was performed with the software SCA20 Version 2.0.
All of samples was measured with captive bubble method at r.t..

Captive bubble method

A membrane sample with 25 mm diameter was fixed on plastic plate with double-faced adhesive tape and cut into rectangle shape. The selected surface of membrane sample was exposed and immersed into deionized water bath. Then after the air bubbles of 5 µL were discharged one by one via special syringe, contact angles can be measured and calculated with device program. The final value for each membrane sample was the average value from 5-10 measurement points.

4.4.2.4. Attenuated total reflection infrared spectroscopy

In the case of membrane samples, different C=O signals from ester groups or amide groups were identified qualitatively with ATR-FTIR.
Double faces of all membrane samples were measured. All ATR-FTIR spectra were examined via 3100 FT-IR Excalibur with MCT detector of GE crystal and ATR attachment Miracle (Pike) (from Varian company) at room temperature.

4.4.2.5. X-ray Photoelectron Spectroscopy

As a surface-sensitive quantitative spectroscopic technique, X-ray Photoelectron Spectroscopy (XPS) can analyze the elemental composition, chemical state and electronic state of elements in depth of 0-10nm from surface of testing materials.

A Physical Electron 5800 ultrahigh vacuum XPS-Auger spectrometer was utilized for the measurement at 45° takeoff angle. Twenty high-resolution scans that focused on the nitrogen (395 – 405 eV), the carbon (282 - 292eV), and sulfur (155 - 175eV) regions were carried out to identify the PSPE functional block of additive which exposed on membrane surface. Charge compensation was achieved by using double beam neutralizer.

4.4.2.6. Water permeability, BSA rejection and relative water flux reduction

Water permeability and BSA rejection were measured for each prepared PVDF membrane as preliminary membrane performance characterizations. 25mm diameter membrane samples with effective filtration area of 4.15mm^2 were utilized for deionized water (DI water) permeability and BSA rejection via dead-end filtration setting-up connected with stirred 25ml Amicon cell (Amicon8010, Millipore). The stirring rate was fixed at 300 rpm. Nitrogen gas was employed as driven-pressure for ultrafiltration examinations.

Under the transmembrane pressure of 0.5 bar the masses of permeated water through each tested membrane sample was recorded within 5 minutes for once. Then the tested membrane sample was compacted under 1.5 bar for 30 minutes in order to stabilize the flux of permeated water. Subsequently the masses of permeated water was recorded every 5 minutes for 3 times under 0.5 bar. Afterward, the Amicon cell was emptied and refilled with 1mg/mL BSA buffer solution (PBS buffer, pH=7.0) for BSA rejection examination. Under the transmembrane pressure corresponding to initial DI water flux$\leqq$ 20 or 50 $L \cdot h^{-1} \cdot m^{-2}$, the BSA filtration was performed. After

discarding the first 1-2g permeated solution, the subsequent 5-6g permeated solution was collected and scanned via UV-vis spectrometer (λ= 280 nm) for confirmation of BSA concentration and calculation of BSA rejection. For each prepared membrane, more than 3 random samples were examined. After that, the Amicon cell was emptied and filled with deionized water again. Under the transmembrane pressure of 0.5bar, the masses of permeated water were recorded again every 5 minutes for 3 times for the same membrena sample which was already utilized for BSA filtration.

The water permeability was calculated with the following equation:

Water permeability (WP)= $\frac{(\mathrm{m}/\mathrm{d})}{\mathrm{A_{eff}} \cdot p \cdot t}$ [L/(m²·bar·h)] (**Equation 3**)

m= mass of permeated water ; d= density of pure water at r.t.; A_{eff}= effective area of membrane top surface; *p*= transmembrane pressure; *t*= time.

The BSA rejection percentage was calculated with the following equation:

BSA rejection (R)= $(1 - \frac{C_p}{C_f}) \cdot 100\%$ (**Equation 4**)

C_p= concentration of permeated BSA solution; C_f = concentration of feed BSA solution.

The relative water flux reduction was calculated with the following equation:

Relative water flux reduction(RFR) = $(\frac{J_0 - J_1}{J_0}) \cdot 100\%$ (**Equation 5**)

J_0= initial pure water flux; J_1= water flux after BSA filtration.

4.4.2.7. Molecular weight cut-off

Molecular weight cut-off (MWCO) analysis were performed only for optimized prototype of membrane as further performance characterizations. 25 mm diameter membrane samples with effective filtration area of 4.15 cm² were utilized for MWCO via dead-end filtration setting-up connected with stirred 25 ml Amicon cell (Amicon8010, Millipore). The stirring rate was fixed at 300 rpm. Nitrogen gas was employed as pressure for ultrafiltration examinations.

The water permeability before and after compaction were recorded firstly. After 30 min compaction process of membrane under 1.5 bar, the Amicon cell was emptied and refilled with 1 mg/ml dextran mixture solution (nominal dextran molecular weight and concentration: 100 KDa, 0.2 g/L; 70 KDa, 0.4 g/L; 35 KDa, 0.4 g/L; all dextran was dissolved in 0.01 mol/L NaN_3 solution)

for MWCO examination. Under the pressure to initial DI water flux ≦h20 $L \cdot h^{-1} \cdot m^{-2}$, the dextran filtration was performed. After discarding the first 1-2g permeated solution, the subsequent 2g permeated solution was collected. Then the feed, retentate and permeate were analyzed via GPC (GPC column SUPREMA, linear, 10 µm, 600/8 mm, 100-100,000,000 g/mol, PSS, Germany) coupled with a refractive index detector for confirmation of permeated solute molecular weight distribution. After calculation with professional software the MWCO can be obtained. The MWCO is defined as the molar mass of a tested dextran molecular that was rejected to 90% by the membrane.

4.4.2.8. Dynamic fouling test

Dynamic fouling investigation was carried out via membrane filtration process. 1 mg/ml BSA buffer solution (PBS buffer, pH= 7.0) was still employed as model solute solution. Water permeability of membrane sample (25 mm diameter) was measured firstly as above mentioned procedure with a dead-end setting-up (25 ml, Amicon 8010 cell). Then the cell was emptied and refilled with 25 mL BSA solution. Under the pressure to initial DI water flux= 120 $L \cdot h^{-1} \cdot m^{-2}$, the BSA filtration was performed with stirring rate 300 rpm. After discarding the first 1-2g permeated solution, the subsequent 5-6g permeated solution was collected and scanned via UV-vis spectrometer (λ= 280 nm) for confirmation of permeated BSA concentration and calculation of BSA rejection.

After filtration, the Amicon cell was emptied and refilled with DI water. Then the tested membrane sample was rinsed with stirring DI water in Amincon cell at about 100 rpm for 30 seconds. Subsequently the water permeability was re-meausred at 0.5 bar. For each prepared membrane, more than 3 random samples were examined.

.

5. Results and discussion of copolymer synthesis

5.1. Synthesis of $PMMA_m$-*co*-$PSPE_n$

5.1.1. Modification of synthesis route for $PMMA_m$-*co*-$PSPE_n$

$PMMA_m$-*co*-$PSPE_n$ was synthesized with MMA and SPE monomer via free radical polymerization (FRP). In consideration of the economic and environmental factor, ethanol was selected as the solvent for polymerization (**Fig. 14**). Due to the lower solubility of polySPE segments in ethanol, during the propagation, copolymerized chains of $PMMA_m$-*co*-$PSPE_n$ became heterogeneous in ethanol. In reaction solution, SPE monomers preferentially approached around propagating copolymer chains due to the electrostatic interaction between SPE monomer and PSPE segments. Therefore the propagating radical sites which were surrounded by precipitating copolymer chains had more probability to copolymerize with SPE monomer which was richer in the comonomer composition around propagating radical sites.[13][17] Then excess of copolymerized SPE repeating units in copolymer chains caused the massive precipitation of copolymer with over expected incorporation of PSPE segments. Consequently more additions of SPE units in the propagating copolymer chains were facilitated further. Finally, the $PMMA_m$-*co*-$PSPE_n$ copolymer prepared in ethanol had no solubility basically in DMF or DMSO even after long-term ultrasonic treatment because of the excess proportion of copolymerized PSPE segments.

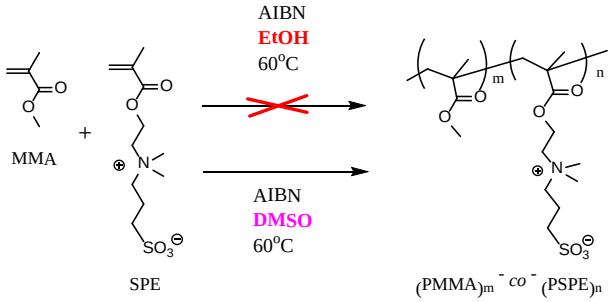

Fig. 14 Routes for synthesis of $PMMA_m$-*co*-$PSPE_n$.

After changing the solvent from ethanol to DMSO (**Fig. 14**), during the whole course of copolymerization, the reaction system remained homogeneous and no precipitation formed, which indicated that the the synthesis of $PMMA_m$-*co*-$PSPE_n$ escaped from the unfavorable excess of PSPE segments.

5.1.2. Synthesis and characterizations of $PMMA_m$-*co*-$PSPE_n$

Synthesis route of $PMMA_m$-*co*-$PSPE_n$ via FRP can be seen in **Fig. 14**.

Synthesis conditions: [MMA]:[SPE]:[AIBN] = 23.1 : 2.7 : 1. C_{MMA} = 0.4 mol/L. Reaction time was 24h.

The detailed characterizations can be seen as following.

The chemical structure of synthesized $PMMA_m$-*co*-$PSPE_n$ can be confirmed as shown in **Fig. 15**. The proton signals at 0.74 ppm, 0.93 ppm (d) corresponded to $–CH_3$ from **1** and **a** collectively. The proton signals at 1.74 ppm, 1.82 ppm (d) corresponded to $–CH_2–$ from **2** and **b** collectively. The proton signals at 4.37 ppm (s) and 2.06 ppm (s) can be attributed to $O–CH_2–$ and $–CH_2–$ from **3** and **8** respectively. The proton signals at 3.13ppm (s) corresponded to $N–CH_3$ from **5** and **6** collectively. The proton signals of $–CH_2–$ from **4**, **7** and **9** were screened by other proton signals. The proton signals at 3.55 ppm (s) can be distinctly identified and attributed to $O–CH_3$ from **c**.

The integral area value of proton signals **c** ($O–CH_3$ from PMMA side chains, δ=3.55 ppm, s) and **3** ($–CH_2–$ from PSPE side chains, δ=4.37 ppm, s) were utilized to calculate the ratio of PMMA versus PSPE (m/n) in $PMMA_m$-*co*-$PSPE_n$ with the following equation.

$$\frac{I_{(c)}}{I_{(3)}} = \frac{3m}{2n} \qquad \textbf{(Equation 6)}$$

The calculated PMMA versus PSPE (m/n) in $PMMA_m$-*co*-$PSPE_n$ was 11.4.

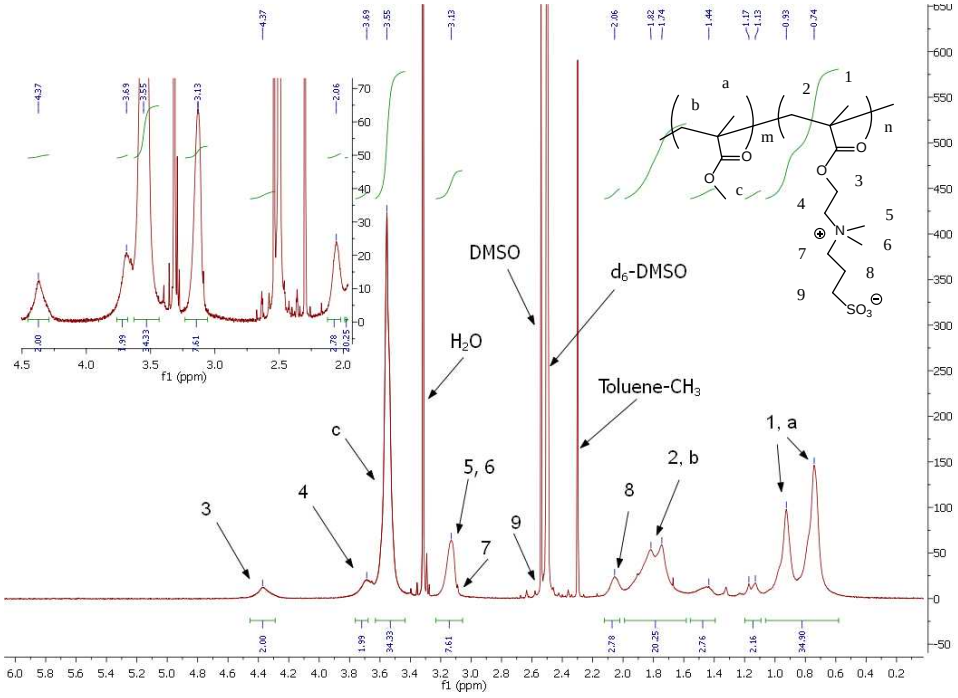

Fig. 15 ^{1}H-NMR (500 MHz) of PMMA$_m$-*co*-PSPE$_n$. Solvent: d$_6$-DMSO@298K (r.t.).

As shown in **Fig. 16**, the molecular weight distribution of synthesized PMMA$_m$-*co*-PSPE$_n$ exhibited single peak.

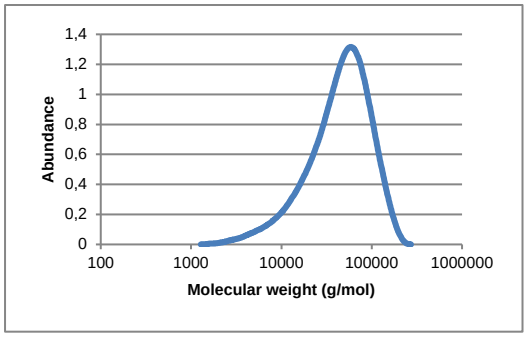

Fig. 16 GPC molecular weight distribution of synthesized PMMA$_m$-*co*-PSPE$_n$.

The GPC molecular weight (M_n) and polydispersity (M_w/M_n, PDI) of synthesized PMMA$_m$-*co*-PSPE$_n$ can be seen in **Table 1**.

Code	Ratio (PMMA/ PSPE) (^{1}H-NMR)	(PMMA)$_m$-*co*-(PSPE)$_n$ (^{1}H-NMR)	[a]Ratio (PMMA/ PSPE) (EAs)	(PMMA)$_m$-*co*-(PSPE)$_n$ (EAs)	M_w/M_n (PDI)	M_n (g/mol) (GPC)	Yield (%)
RCP1	11.4	(PMMA)$_{188}$-*co*-(PSPE)$_{16.5}$	9.1	(PMMA)$_{179}$-*co*-(PSPE)$_{20}$	1.93	23400	68.9

Table 1 Characterized PMMA$_m$-*co*-PSPE$_n$. EAs was elemental analysis. [a]The results of EAs were directly used to calculate the ratio of PMMA versus PSPE here.

Ratios of PMMA/PSPE (m/n) in PMMA$_m$-*co*-PSPE$_n$ which were calculated repectively from ^{1}H-NMR and EAs were shown in **Table 1**. Ratio of PMMA/PSPE from ^{1}H-NMR was bigger than the ratio from EAs, which can be attributed to the slightly overlapped proton signals from O–CH_3 of PMMA and –CH_2– of PSPE as shown in ^{1}H-NMR (**Fig. 14**). The broad molecular weight distribution (M_w/M_n=1.93) can be regarded as a result of normal uncontrol of free radical polymerization.

5.2. Synthesis of PMMA$_m$-*b*-PSPE$_n$

5.2.1. Different synthesis routes for PMMA$_m$-*b*-PSPE$_n$

In Route 1 (**Fig. 17**), PMMA-Br was successfully prepared as macroinitiator with proper molecular weight (M_n) and polydispersity (PDI) (cf. **Table 5**). However, after reinitiation of monomer SPE, the polymerization rate was too fast to be controlled. The prepared copolymer contained excess proportion of PSPE block which caused the insolubility of synthesized copolymer in most of organic solvents. In Route 2 (**Fig. 17**), PSPE-Br macroinitiator merely can be prepared in strong polar solvents (e.g., water, TFE) with high dielectric constants because polySPE and SPE monomer can merely be dissolved completely in these solvents. The prepared PSPE-Br macroinitiator showed uncontrolled M_n and quite poor solubility in normal organic solvents so that it was quite difficult to effectively implement the further reinitiation of monomer MMA.

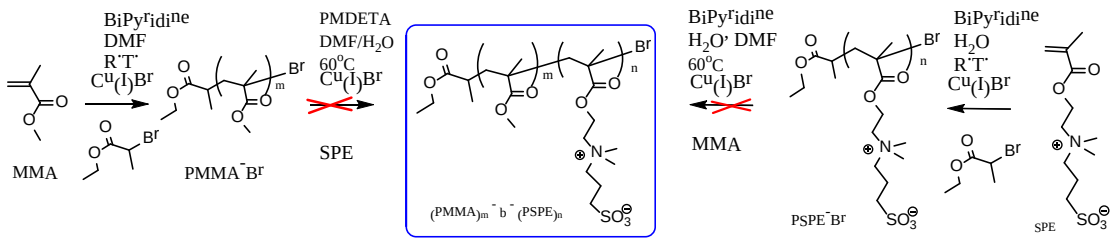

Fig. 17 Unsuccessful synthesis routes for PMMA-*b*-PSPE. Route 1 (left), Route 2 (right).

The reason of uncontrolled polymerization of SPE monomer can be mainly attributed to the largely increased rate of ATRP during the synthesis of polySPE in strong polar solvents. [19][21] The polar and aqueous solvents that were employed for synthesis of polySPE can highly accelerate the rate of ATRP.[65] The most likely explanation for this phenomenon was based on the fact that the structure of catalytic complexes Cu(I)/Ligand and Cu(II)/Ligand changed in solvents with different polarity which were employed in ATRP.[19][66] Mononuclear $[Cu(I)/(Ligand)]^{+}Br^{-}$ is the valid catalytic species (activator) in conventional ATRP process due to the tetrahedral environment from d^{10} electronic configuration of Cu(I).[66] However, after oxidation of Cu(I) to Cu(II), dicationic tetrahedral Cu(II)/Ligand complex and dimer of Cu(II)/Ligand complex with bridging halides (**Fig. 18**) were formed at the same time.[67] The former complex is the more active catalytic species. In other word, compared with dimer of Cu(II)/Ligand complex, the dicationic tetrahedral Cu(II)/Ligand complex had less deactivating action on the formed radical species in ATRP.[19][66] In non-polar or non-aqueous solvent system, the formation of bridged dimeric Cu(II)/Ligand complex was more possible.[66][68] As a result, the dominant dicationic tetrahedral Cu(II)/Ligand complex in polar organic solvents or aqueous medium was responsible for the acceleration or even uncontrol of ATRP for polySPE. Water and polar DMF are even capable of acting as coordinating coligands to further stabilize the dicationic tetrahedral Cu(II)/Ligand complex. [20]

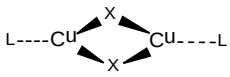

Fig. 18 Dimer of Cu(II) complex with bridging halides. X was Cl or Br. L was Ligand.

Overall, the Route1 and Route 2 were not suitable for synthesis of tailored $PMMA_m$-*b*-$PSPE_n$ via ATRP in precise control. Therefore another synthesis route of sequential ATRP was adopted and presented in following part of this dissertation.

5.2.2. Synthesis and characterizations of $PMMA_m$-*b*-$PSPE_n$

The adopted synthesis route of $PMMA_m$-*b*-$PSPE_n$ was shown in **Fig. 19**. $PMMA_m$-*b*-$PSPE_n$ was still synthesized via sequential ATRP. PMMA-Br was firstly synthesized as macroinitiator. And then monomer DMAEMA were reinitiated with prepared PMMA-Br to synthesize the block copolymer $PMMA_m$-*b*-$PDMAEMA_n$ as the precursor. Finally, $PMMA_m$-*b*-$PSPE_n$ was formed through the post-treatment with 1,3-propane sultone.[69][70] In this procedure, the different ligands were utilized for synthesis of macro initiator PMMA-Br with different molecular weights. The

involved solvents for this three-step route were low polar toluene and THF, which avoided the aforementioned undesirable acceleration of ATRP rate caused by the polar solvent.

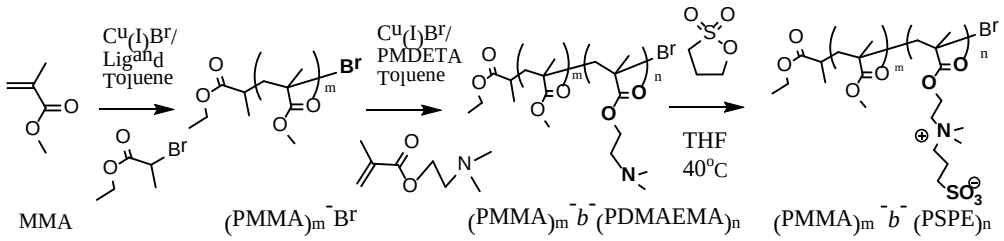

Fig. 19 Synthesis route of $PMMA_m$-*b*-$PSPE_n$.

5.2.2.1. Establishment of ATRP conditions for synthesis of macroinitiator PMMA-Br

The synthesis of macro initiator PMMA-Br with precise control was quite critical to the synthesis of final product $PMMA_m$-*b*-$PSPE_n$ with desired additive function. Therefore the establishment of synthesis conditions for macroinitiator PMMA-Br is introduced in detail. Reasonable ligands play main role in successful ATRP. Multidentate nitrogen ligands with higher k_{act} and k_{deact} (cf. **2.1.2.**) are frequently applied in Cu-mediated ATRP to solubilize copper salt and adjust its redox potential.[19] Cu(I)Br/PMDETA and Cu(I)Br/bipyridine were selected as catalysts system for synthesis of PMMA-Br macro initiator, since PMDETA and bipyridine (**Fig. 20**) have multi-coordinating sites (N3 of alky amine, N2 of pyridine), and suitable linking units of carbon between nitrogen binding sites (C2) with proper coordinating angles.[18][19]

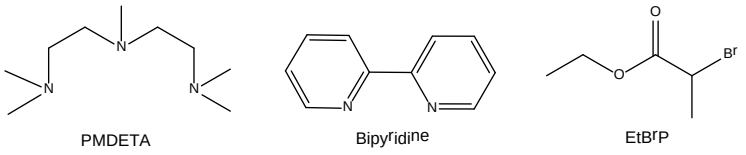

Fig. 20 Chemical structures of PMDETA, bipyridine and EtBrP.

In MeCN at 22ºC, K_{ATRP} of Cu(I)Br/PMDETA and k_{ATRP} of Cu(I)Br/bipyridine were respectively 7.46×10^{-8} and 3.93×10^{-9} ($K_{ATRP}= k_{act}/k_{deact}$), which accompanied by that, PMDETA gives bigger rate of polymerization than bipyridine, and the according $Cu(II)Br_2$/PMDETA shows more negative redox potential than $Cu(II)Br_2$/$bipyridine_2$.[21] EBrP (**Fig. 20**) was selected as initiator for ATRP of PMMA-Br. The better leaving group –Br on secondary carbon and an electron-withdrawing group of –C(O)OR at adjacent position facilitate the faster initiation of EBrP in ATRP. In principle, the

structure similarity between EBrP and PMMA dormant species monomer also was a plus for better control of ATRP.[20]

Reaction **MIni.1** and **MIni.2** (**Fig. 21**) were examined for the first exploration of rational catalyst system towards best control of PMMA-Br synthesis. With the increased concentration of Cu(I)Br and bipyridine, M_n of synthesized PMMA-Br from **MIni.2** ($M_{n(\mathbf{MIni.2})}$) became higher than M_n of PMMA-Br from **MIni.1** ($M_{n(\mathbf{MIni.1})}$), whereas the value of M_w/M_n (PDI) from **MIni.2** ($PDI_{(\mathbf{MIni.2})}$) also went higher than that from **MIni.1** ($PDI_{(\mathbf{MIni.1})}$). Referring to the **Equation 4** and **5**, in contrast to **MIni.1**, increased concentration of Cu(I)Br/ bypridine$_2$ in **MIni.2** raised the ratio of [Cu(I)Br/ bipyridine$_2$]/ [Cu(II)Br$_2$/ bipyridine$_2$], which accelerated the rate of ATRP(R_p) for **MIni.2** and thus resulted in a increased $M_{n(\mathbf{MIni.2})}$ (**Fig. 21**). Too fast initiation rate caused by the increased concentration of Cu(I)Br/ bypridine$_2$ and low concentration of MMA led to the higher $PDI_{(\mathbf{MIni.2})}$ and $PDI_{(\mathbf{MIni.1})}$ (**Fig. 21**) due to the increased probability of termination in ATRP.

Ligands were changed from bipyridine to PMDETA in reaction **MIni.3** and **MIni.4** in order to improve the ATRP rate (R_p) by higher K_{ATRP} of PMDETA in contrast to bipyridine. Concentration of MMA and reaction temperature in **MIni.3** and **MIni.4** were also increased for intention of enhancing R_P of ATRP. In order to gain better control of ATRP (narrower PDI, unity of polymer chains growing), concentration of Cu(I)Br/ PMDETA in **MIni.3** and **MIni.4** were decreased in contrast to **MIni.2**, whereas the solvent were changed to DMF in **MIni.3** and toluene in **MIni.4** respectively. According to **Equation 2** (cf. **2.1.2.**), decreased PDI were obtained via increased k_{deact} which resulted from not only the enhanced homogeneity of catalyst system brought by DMF in **MIni.3** but also the low polarity of toluene in **MIni.4**. Compared with **MIni.3**, higher reaction temperature (85ºC), higher concentration of MMA (5 mol/L) and employment of non-polar solvent toluene generated improved M_n and narrow PDI in **MIni.4**.

To explore the possibility to modify the condition of **MIni.4** for preparing smaller M_n of PMMA-Br, reactions **MIni.5**, **MIni.6**, **MIni.7**, **MIni.8** were examined (**Fig. 21**).

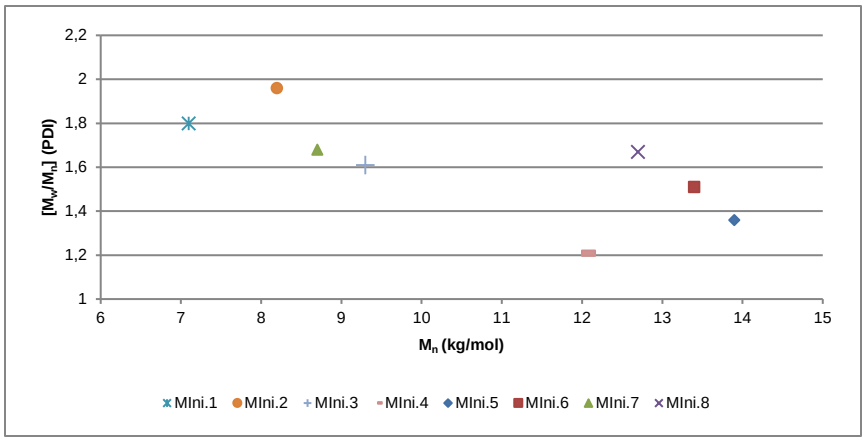

Fig. 21 M_n of final product PMMA-Br *vs.* M_w/M_n (PDI) for reaction **MIni.1**, **MIni.2**, **MIni.3**, **MIni.4**, **MIni.5**, **MIni.6**, **MIni.7**, **MIni.8**.

(**MIni.1**) [MMA]:[EtBrP]: [Cu(I)Br]:[Bipyridine]=150:1:1.5:2 in MeOH for 4h at r.t., $C_{(MMA)}$ = 0.36 mol/L;

(**MIni.2**) [MMA]:[EtBrP]: [Cu(I)Br]:[Bipyridine]=150:1:2:4 in MeOH for 4h at r.t., $C_{(MMA)}$ = 0.36 mol/L;

(**MIni.3**) [MMA]:[EBrP]:[Cu(I)Br]:[PMDETA] =150:1:1.5:1,5 in DMF for 4h at 50ºC, $C_{(MMA)}$ = 3 mol/L;

(**MIni.4**) [MMA]:[EBrP]:[Cu(I)Br]:[PMDETA] =120:1:1.5:1.5 in toluene for 4h at 85ºC, $C_{(MMA)}$ = 5 mol/L,

(**MIni.5**) [MMA]:[EBrP]:[Cu(I)Br]:[PMDETA] =120:1:1.5:1.5 in toluene for 4h at 85ºC, $C_{(MMA)}$ = 5 mol/L;

(**MIni.6**) [MMA]:[EBrP]:[Cu(I)Br]:[PMDETA] =80:1:1.5:1.5 in toluene for 4h at 85ºC, $C_{(MMA)}$ = 5 mol/L;

(**MIni.7**) [MMA]:[EBrP]:[Cu(I)Br]:[PMDETA] =47:1:1.5:1.5 in toluene for 4h at 70ºC, $C_{(MMA)}$ = 5 mol/L;

(**MIni.8**) [MMA]:[EBrP]:[Cu(I)Br]:[PMDETA] =94:1:1.5:1.5 in toluene for 4h at 70ºC, $C_{(MMA)}$ = 5 mol/L.

MIni.5 repeated the conditions of **MIni.4** and generated PMMA-Br with the similar M_n and PDI to that synthesized from **MIni.4**. In **MIni.6** the equivalents of initiator EBrP and Cu(I)Br/ PMDETA were increased but the concentration of MMA kept same as **MIni.5**. As a result, the $M_{n(\textbf{MIni.6})}$ reduced but $PDI_{(\textbf{MIni.6})}$ enlarged in contrast to the ones in **MIni.5**. The increased concentration of initiator and catalysts in **MIni.6** brought about not only the enhanced R_p (cf. **Equation 1**) of ATRP but also the faster initiation and more initiated radical species, which tended to form more irreversible terminations at the beginning of ATRP and led to bigger $PDI_{(\textbf{MIni.6})}$. Shorter PMMA chains (with smaller M_n) resulted from increasing initiated species gave rise to the decreased $M_{n(\textbf{MIni.6})}$ and bigger $PDI_{(\textbf{MIni.6})}$ in **MIni.6**, compared with **MIni.5**. Furthermore, the increased concentration of initiator and Cu(I)Br/ PMDETA as well as the reduced reaction temperature in **MIni.7**and **MIni.8**, according to above mentioned elaboration, also yielded decreased M_n and raised PDI. The conditions of **MIni.4** and **MIni.5** were utilized for next step due to the resultant PMMA-Br with proper M_n and narrow PDI.

5.2.2.2. Synthesis of $PMMA_m$-*b*-$PSPE_n$ with $M_{n\ PMMA}$=13.9 kg/mol

The conditions of **MIni.4** and **MIni.5** were employed here and PMMA-Br with M_n= 13.9 kg/mol was synthesized (**Fig. 22**).

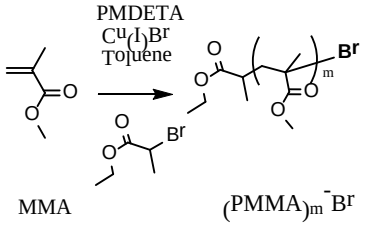

Fig. 22 Synthesis of macro initiator PMMA-Br (M_n= 13.9 kg/mol). [MMA]:[EBrP]:[Cu(I)Br]:[PMDETA] =120:1:1.5:1.5 in toluene for 4h at 85ºC, $C_{(MMA)}$ = 5 mol/L.

The chemical structure of synthesized $PMMA_m$-Br was confirmed by ^{1}H-NMR (cf. **10.2.1.**). The detailed characterizations of prepared $PMMA_m$-Br were described in **Table 2**.

Code	M_w/M_n (PDI)	M_n (g/mol) (GPC)	$(PMMA)_m$-Br (GPC)	Yield (%)
MI14k	1.36	13900	$(PMMA)_{139}$-Br	76

Table 2 Characterized PMMA-Br (M_n = 13.9 kg/mol) macroinitiator.

The molecular weight (M_n) of synthesized $PMMA_m$-Br were determined by GPC. The PDI of PMMA-Br was narrow. The value for average number of repeating MMA units (m) in $PMMA_m$-Br was calculated by the following equation.

$$m = \frac{M_n}{M_{monomer}} \qquad \textbf{(Equation 7)}$$

M_n was the GPC molecular weight of homopolymer or the block of copolymer (here M_n was molecular weight of $PMMA_m$-Br); $M_{monomer}$ was the molecular weight of monomer (here $M_{monomer}$ was molecular weight of MMA monomer, 100 g/mol). The calculated m was 139.

Synthesis of $PMMA_m$-*b*-$PDMAEMA_n$ with $M_{n\ PMMA}$=13.9 kg/mol

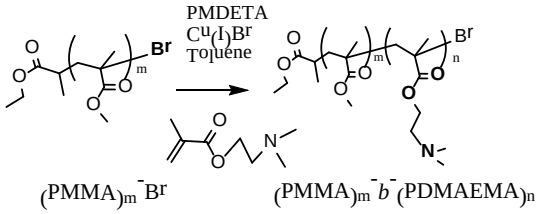

Fig. 23 Synthesis of precursor $PMMA_m$-*b*-$PDMAEMA_n$. [DMAEMA]:[PMMA-Br]:[Cu(I)Br]:[PMDETA] =30:1:2:2 in toluene for 20min at 85ºC, $C_{(DMAEMA)}$=0.3 mol/L. $PMMA_{139}$-Br was employed as macro initiator.

Conditions for synthesis of $PMMA_m$-*b*-$PDMAEMA_n$ with PMMA-Br (M_n=13.9 kg/mol) was shown in **Fig. 23**. Cu(I)Br/ PMDETA was still utilized as the catalyst system for reinitiation of sequential block PDMAEMA here, because the more reducing complex of Cu(I)Br/ PMDETA may offset the tendency of coordination effect between tertiary amine of DMAEMA and Cu(I). In order to synthesize DMAEMA block with shorter length, concentration of monomer DMAEMA was kept at low level (0.3 mol/L).

The chemical structure of synthesized $PMMA_m$-*b*-$PDMAEMA_n$ can be confirmed as shown in **Fig. 24**. The proton signals at 0.85 ppm, 1.02 ppm (d) corresponded to $–CH_3$ from **1** and **a** collectively. The proton signals at 1.82 ppm, 1.90 ppm (d) corresponded to $–CH_2–$ from **2** and **b** collectively. The proton signal at 4.07 ppm (s) can be attributed to $O–CH_2–$ from **3**. The proton signal at 2.56 ppm (s) can be attributed to $N–CH_2–$ from **4**. The proton signals at 2.28 ppm (s) corresponded to $N–CH_3$ from **5** and **6** collectively. The proton signals at 3.60 ppm (s) can be distinctly identified and attributed to $O–CH_3$ from **c**.

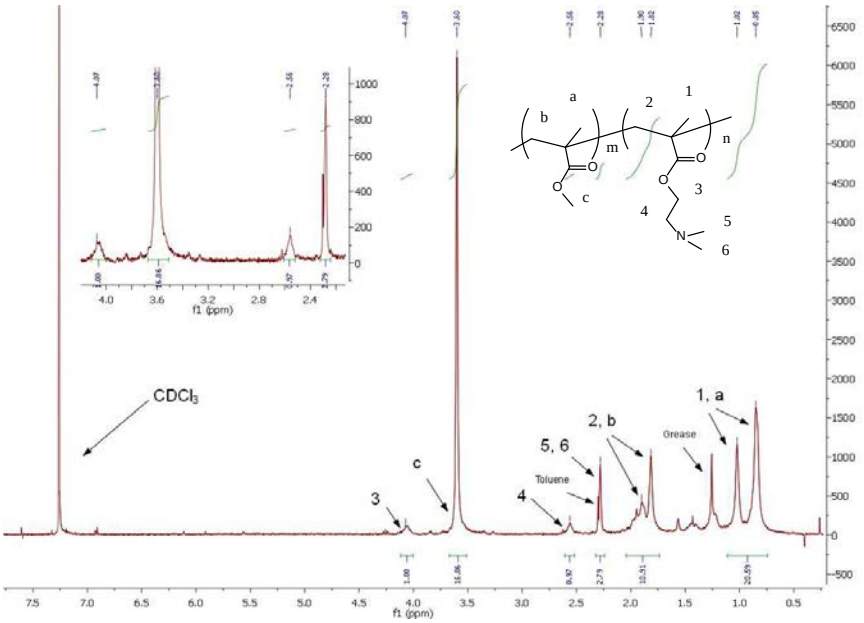

Fig. 24 ^{1}H-NMR (300 MHz) of PMMA$_m$-*b*-PDMAEMA$_n$ (PMMA M_n=13.9 kg/mol). Solvent: d_1-$CDCl_3$ @298K (r.t.).

The integral area value of proton signals **c** (O–CH_3 from PMMA side chains, δ=3.60 ppm, s) and **3** (O–CH_2– from PDMAEMA side chains, δ=4.07 ppm, s) were utilized to calculate the ratio of PMMA/PDMAEMA (m/n) in PMMA$_m$-*b*-PDMAEMA$_n$ with **Equation 6** (cf. **5.1.2.**). The calculated ratio of PMMA/PDMAEMA (m/n) in PMMA$_m$-*b*-PDMAEMA$_n$ was 11.2.

As shown in **Table 3**, the molecular weight (M_n) of PMMA$_m$-*b*-PDMAEMA$_n$ from GPC was quite similar to the M_n that was calculated by m/n ratio from ^{1}H-NMR, which indicated that the ATRP process for synthesis of PMMA$_m$-*b*-PDMAEMA$_n$ was controlled well. The displayed PDI was proper, which signified the uniform growth of polymer chains during ATRP.

Code	(PMMA)$_m$-*b*-(PDMAEMA)$_n$ (^{1}H-NMR)	Ratio (PMMA/ PDMAEMA) (^{1}H-NMR)	M_n(g/mol) (^{1}H-NMR)	M_n(g/mol) (GPC)	M_w/M_n (PDI)	Yield (%)
BP14k	(PMMA)$_{139}$-*b*-(PDMAEMA)$_{12.5}$	11.2	15900	14400	1.41	49

Table 3 Characterized PMMA$_m$-*b*-PDMAEMA$_n$ (PMMA M_n = 13.9 kg/mol).

The value of m (number of MMA repeating units in PMMA block) was 139 as calculated before. Therefore the value of n (number of DMAEMA repeating units in PDMAEMA block) can be calculated through the known ratio of PMMA/PDMAEMA (m/n) in PMMA$_m$-*b*-PDMAEMA$_n$ (11.2). The calculated value of n was 12.5. Then PMMA$_{139}$-*b*-PDMAEMA$_{12.5}$ was adopted to represent the synthesized PMMA$_m$-*b*-PDMAEMA$_n$ here.

Synthesis of $PMMA_m$-*b*-$PSPE_n$ with $M_{n\ PMMA}$=13.9 kg/mol

As shown in **Fig. 25**, the prepared precursor ($PMMA_{139}$-*b*-$PDMAEMA_{12.5}$) can be readily and completely converted to zwitterionic $PMMA_{139}$-*b*-$PSPE_{12.5}$ with 1,3-propane sultone.[69][71]

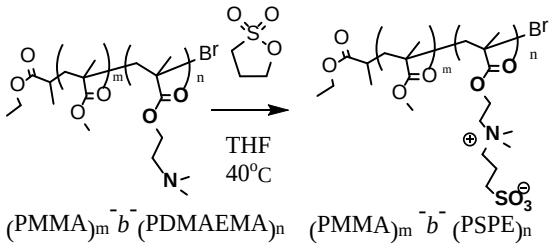

Fig. 25 Synthesis of $PMMA_m$-*b*-$PSPE_n$ with PMMA (M_n=13.9 kg/mol) via the post-treatment of precursor. [precursor]: [sultone]= 1: 10.19 in THF for 24h at 40 ºC, $C_{precursor}$ = 5 g/L.

As shown in **Fig. 26**, GPC distribution of $PMMA_{139}$-Br (M_n= 13.9 kg/mol), $PMMA_{139}$-*b*-$PDMAEMA_{12.5}$, $PMMA_{139}$-*b*-$PSPE_{12.5}$ were different and displayed the tendency of gradually increasing molecular weights, which strongly evidenced the successful sequential ATRP and post-treatment. The connected PDMAEMA block and formed zwitterionic betaine groups in side chains of PSPE were responsible for the increasing of according molecular weight in **Fig. 26**.

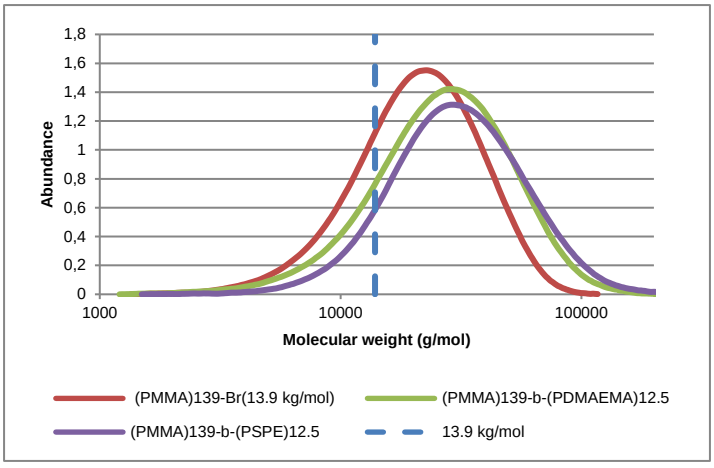

Fig. 26 Comparison among GPC molecular weight distribution of $PMMA_{139}$-Br (M_n= 13.9 kg/mol), $PMMA_{139}$-*b*-$PDMAEMA_{12.5}$, $PMMA_{139}$-*b*-$PSPE_{12.5}$.

It is quite clear to see in **Table 4**, the ratio of PMMA/PSPE which was calculated from EAs results was basically same as the ratio of PMMA/ PDMAEMA which was calculated from ^{1}H-NMR result.

This strongly implied the the complete conversion of PDMAEMA side chains to zwitterionic PSPE side chains after post-treatment step. The M_n of $PMMA_{139}$-*b*-$PSPE_{12.5}$ that was calculated respectively from the ^{1}H-NMR ratio and EAs ratio were also nearly same. And the two M_n also were quite close to M_n from GPC. All the M_n that were characterized with different ways were consistent. The PDI of prepared $PMMA_{139}$-*b*-$PSPE_{12.5}$ was pretty low and signified the better unity of polymer chain lengths.

Code	$(PMMA)_m$-*b*-$(PSPE)_n$ (^{1}H-NMR)	[a]Ratio (PMMA/ PSPE) (^{1}H-NMR)	[a]M_n(g/mol) (by ^{1}H-NMR of precursor)	[b]Ratio (PMMA/ PSPE) (EAs)	[b]M_n(g/mol) (EAs)	M_n(g/mol) (GPC)	M_w/M_n (PDI)	Yield (%)
ZBP14k	$(PMMA)_{139}$-*b*-$(PSPE)_{12.5}$	11.2	17400	11.0	17400	17000	1.25	100

Table 4 Characterized $PMMA_m$-*b*-$PSPE_n$ (PMMA M_n=13.9 kg/mol). [a]The ratio of PMMA/ PDMAEMA that calculated by ^{1}H-NMR was still used here as the ratio of PMMA/ PSPE to calculate the according M_n. EAs is elemental assay. [b]The results of EAs were directly used to calculate the ratio of PMMA / PSPE and according M_n here.

5.2.2.3. Modified ATRP condition for improving end functional activity of PMMA-Br

Although macro initiator $(PMMA)_{139}$-Br (**MI14k**, cf. **5.2.2.2.**) was prepared and utilized to successfully synthesize $PMMA_{139}$-*b*-$PSPE_{12.5}$ with narrow PDI, in further exploration, it was found that the bromine end functional activity of PMMA-Br which was synthesized with same procedure as $(PMMA)_{139}$-Br showed absence of reliable reproducibility for the sequential re-initiation to the monomer for second block. At the higher reaction temperature, such as 85ºC ($PMMA_{139}$-Br was prepared at 85ºC), both the ATRP rate and chain transfer rate were elevated. With the growing conversion of MMA and the slowdown of chain propagation in ATRP, side reactions, especially the possible PMMA radical chains transfer to the linear aliphatic amine ligand (PMDETA), became pronounced.[17][19] Another more possible assumption was the nucleophilic substitution and subsequential elimination reaction between PMDETA ligand and bromine end of PMMA chains, which resulted in the elimination of HBr and inactive PMMA chains (**Fig. 27**).[72][73][74]

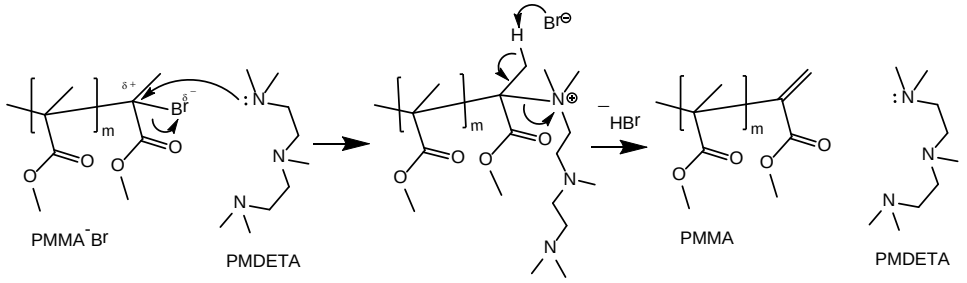

Fig. 27 Nucleophilic substitution to the end bromine and further elimination of HBr during ATRP. (left) Electron pair of tertiary amine of PMDETA attacked the terminal quaternary carbon of PMMA-Br substrate (electrophilic center). (middle) New C-N bond formed whereas bromine anion departed as leaving group; meanwhile subsequential Hoffman elimination occurred and resulted in the loss of HBr and recovery of quaternary amine cation to tertiary amine. (right) Inactive PMMA chains without end bromine function.

In contrast to $Cu(II)Br_2$/ PMDETA, $Cu(II)Br_2$/ $bipyridine_2$ shows less rate constant of activation and higher rate constant of deactivation in ATRP process.[18][21] In view of electrochemical activity (**Fig. 3**, cf. **2.1.2.**), the negative redox potential of $Cu(II)Br_2$/PMDETA and positive redox potential of $Cu(II)Br_2$/$bipyridine_2$ (in MeCN at 25°C) were respectively consistent in the high and low K_{ATRP}, which signify that less reducing complex of Cu(I)/$bipyridine_2$ had weak favor for electron transfer activation of dormant polymer chains whereas the according complex of Cu(II)/$bipyridine_2$ showed lability of Br–Cu(II) and the consequent facilitation on faster deactivation of growing polymer chains to dormant species accompanying low radical concentration during ATRP and better control on polymerization.

To avoid above mentioned side reaction and better retain the end functional bromine group, active ligand PMDETA was replaced with bipyridine which showed less reactivity with end functional bromine and the stronger redox potential for deactivation of propagation in ATRP.[19] And in another alternative way for protection of end function, $Cu(II)Br_2$ was applied as additive at the beginning stage of ATRP in order to build ATRP equilibrium rapidly.[20]

To improve the ATRP conditions for better retaining the end functional bromine, reaction **MIni.9**, **MIni.10**, **MIni.11**, **MIni.12** were explored as shown in **Fig. 28**. The proportion of terminated polymer chains were diminished by the initially added $Cu(II)Br_2$ in reaction **MIni.9**, thereafter ATRP equilibrium was built up rapidly and lower PDI was available. As indication of **Equation 1** and **Equation 2**, increased concentration of $Cu(II)Br_2$/PMDETA (deactivator) in **MIni.9** can brought about narrower PDI at a cost of slower ATRP rate (**Fig. 28**).

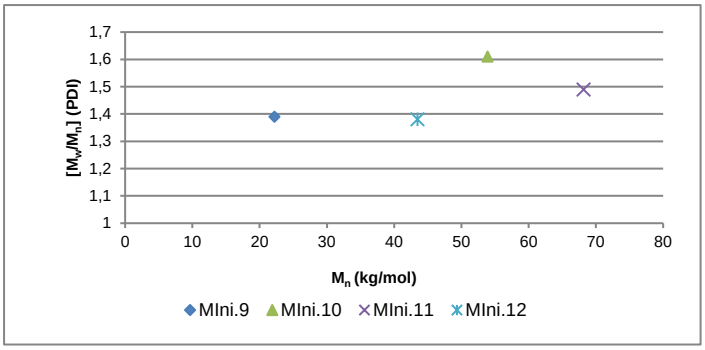

Fig. 28 M_n of final product PMMA-Br *vs.* M_w/M_n (PDI) for reaction **MIni.9**, **MIni.10**, **MIni.11**, **MIni.12**.

(**MIni.9**) [MMA]:[EBrP]:[Cu(I)Br]:[Cu(II)Br_2]:[PMDETA] =150:1:1.5:0.15:1.5 in toluene for 7h at 50ºC, $C_{(MMA)}$= 3 mol/L;

(**MIni.10**) [MMA]:[EBrP]:[Cu(I)Br]:[Bipyridine]=100:1:1:2 in toluene for 7h at 50ºC, $C_{(MMA)}$= 3 mol/L;

(**MIni.11**) [MMA]:[EBrP]:[Cu(I)Br]:[Bipyridine]=100:1:1:2 in toluene for 17h at 50ºC, $C_{(MMA)}$= 3 mol/L;

(**MIni.12**) [MMA]:[EBrP]:[Cu(I)Br]:[Bipyridine] =50:1:1:2 in toluene for 6h at 50ºC, $C_{(MMA)}$= 3 mol/L.

To further indentify the effect of additional Cu(II)Br_2 on control of ATRP rate, the comparison of MMA conversion between reaction **Ref.1** and **MIni.9** was showed in **Fig. 29**. Compared with reaction **Ref.1** where no Cu(II)Br_2 involved, MMA conversion at all the comparable time points in reaction **MIni.9** were apparently lower, which also suggested that the stably controlled ATRP rate resulted from the improved deactivation by additional Cu(II)Br_2. (**Fig. 29**)

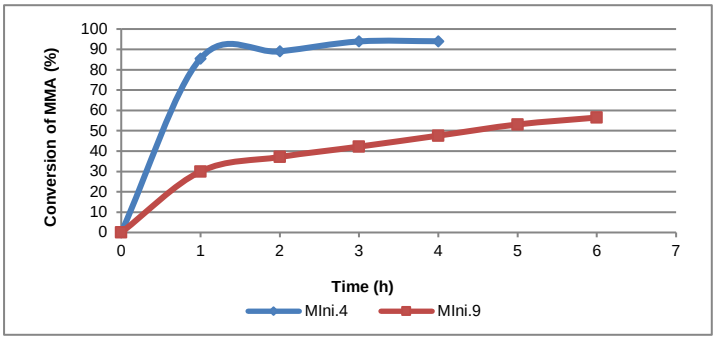

Fig. 29 Comparison of MMA conversion as a function of time in reaction **Ref.1** and **MIni.9**.

(**Ref.1**) [MMA]:[EBrP]:[Cu(I)Br]:[PMDETA]=150:1:1.5:1.5 in toluene for 4h at 50ºC, $C_{(MMA)}$=3 mol/L;

(**MIni.9**) [MMA]:[EBrP]:[Cu(I)Br]:[Cu(II)Br_2]:[PMDETA] =150:1:1.5:0.15:1.5 in toluene for 7h at 50ºC, $C_{(MMA)}$= 3 mol/L.

In **Fig. 28**, it was clear to see that, even after long reaction time (7h and 17h) for reaction **MIni.10**, **MIni.11**, PMMA molecular weight grew high enough for further application while the PDI were still kept below 1.6. In particular for **MIni.12**, within 6h that is less than reaction time of **MIni.9**, enough high molecular weight and narrow PDI was both reached with lower MMA consumption at lower temperature (50°C). Evidently, Cu(I)Br/bipyridine$_2$ brought about better control to ATRP.

In comparison with **MIni.11**, conversion of MMA at all the comparable time points for reaction **MIni.12** were higher because of the raised concentration of initiator and catalysts. The conversion at first hour was kept at lower level (<3.5%) for **MIni.12** and **MIni.11**, which strongly indicated that the ATRP equilibrium can be built up rapidly at the beginning stage with catalyst system of Cu(I)Br/ bipyridine$_2$ (**Fig. 30**). After 5h reaction the 39% conversion of MMA in **MIni.12** also can be regarded as a collateral evidence for reservation of end bromine function, because the too high conversion of monomer usually caused the low local concentration of monomer which always led to the terminations of radical species.

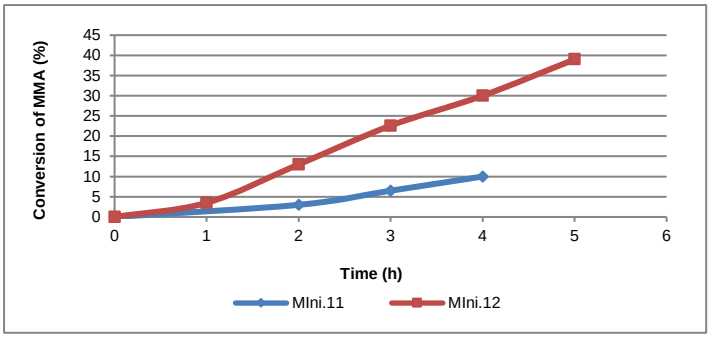

Fig. 30 Comparison of MMA conversion as a function of time in reaction **Mini.11*** and **Mini.12**. *Only the conversion data for 2h, 3h, 4h in reaction **Mini.11** were shown.

(**MIni.11**) [MMA]:[EBrP]:[Cu(I)Br]:[Bipyridine] =100:1:1:2 in toluene for 17h at 50ºC, $C_{(MMA)}$= 3 mol/L;

(**MIni.12**) [MMA]:[EBrP]:[Cu(I)Br]:[Bipyridine] =50:1:1:2 in toluene for 5h at 50ºC, $C_{(MMA)}$= 3 mol/L.

As shown in **Fig. 31**, as a result of strong deactivation of Cu(I)Br/ bipyridine$_2$ and suitable concentration of dormant growing chains in **MIni.12**, rate of PMMA chains growing (rate of M_n increasing) slowed down with time, while PDI also increased slowly but still stayed in rational range of ATRP (1.0~1.5) within 5 hours for. Based on the ATRP conditions of **MIni.12**, macro initiator PMMA-Br with desired M_n= 30 kg/mol and PDI=1.44 was synthesized in enlarged scale during the shorter reaction time (3h) than time of **MIni.12** (5h). The details can be seen in the next following parts.

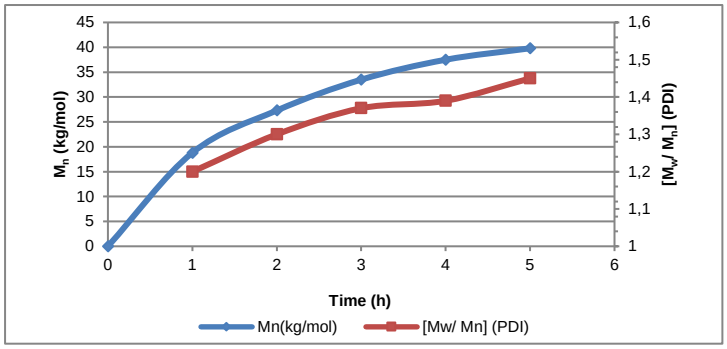

Fig. 31 Evolution of M_n and PDI as functions of time for synthesis of PMMA-Br in reaction **MIni.12**. *M_n values were gained via GPC, PMMA calibration.

(**MIni.12**) [MMA]:[EBrP]:[Cu(I)Br]:[Bipyridine] =50:1:1:2 in toluene for 5h at 50ºC, $C_{(MMA)}$= 3 mol/L.

5.2.2.4. Synthesis of $PMMA_m$-*b*-$PSPE_n$ with $M_{n\ PMMA}$=30 kg/mol

As shown in **Fig.32**, the conditions for synthesis of macro initiator PMMA-Br (M_n= 30 kg/mol) was basically same as conditions in reaction **MIni.12**. The reaction time was decreased to 3h for desired molecular weight of PMMA-Br. Cu(I)Br/ $Bipyriding_2$ was adopted as catalyst system in order to improve the retaining of end functional bromine and control the rate of ATRP more precisely.

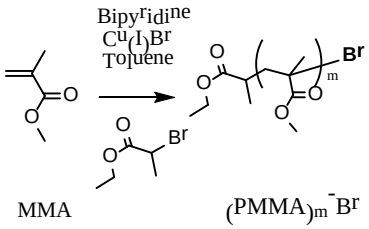

Fig. 32 Synthesis of macro initiator PMMA-Br(M_n=30kDa). [MMA]:[EBrP]:[Cu(I)Br]:[Bipyridine] =50:1:1:2 in toluene for 3h at 50ºC, $C_{(MMA)}$= 3 mol/L.

The chemical structure of synthesized $PMMA_m$-Br was confirmed by ^{1}H-NMR (cf. **10.2.2.**). The detailed characterizations of prepared $PMMA_m$-Br were described in **Table 5**.

Code	M_w/M_n (PDI)	M_n (g/mol) (GPC)	$(PMMA)_m$-Br (GPC)	Yield (%)
MI30k	1.44	30000	$(PMMA)_{300}$-Br	16.9

Table 5 Characterized PMMA-Br (M_n = 30 kg/mol) macroinitiator.

The molecular weight (M_n) of synthesized $PMMA_m$-Br were determined by GPC. The calculation process for value of m was same as aforementioned description (cf. **5.2.2.2.**, **Equition 7**). The calculated m was 300.

Synthesis of $PMMA_m$-*b*-$PDMAEMA_n$ with $M_{n\ PMMA}$=30 kg/mol

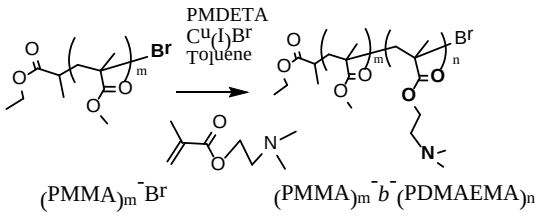

Fig. 33 Synthesis of precursor $PMMA_m$-*b*-$PDMAEMA_n$ (PMMA M_n = 30 kg/mol).

As shown in **Fig. 33**, Cu(I)Br/PMDETA catalyst system was used to synthesize $PMMA_m$-*b*-$PDMAEMA_n$ with PMMA (M_n= 30 kg/mol). Cu(I)Br/PMDETA was considered as the catalyst system for reinitiation of sequential block PDMAEMA, because the more reducing complex of Cu(I)Br/PMDETA may compete with the tendency of coordination between tertiary amine of DMAEMA and Cu(I). For the sake of preparation of $PMMA_m$-*b*-$PDMAEMA_n$ with diverse ratios of PMMA versus PDMAEMA, the rate of ATRP for synthesis of second block PDMAEMA, as aforementioned ATRP rate for synthesis of PMMA-Br, can also be regulated conveniently via several direct parameters (i.e. concentrations of monomer and catalysts, reaction temperature, reaction time).

To find the proper ATRP conditions for synthesis of $PMMA_m$-*b*-$PDMAEMA_n$ with expected ratio of m/n, many exploring reactions were performed and the conversion of DMAEMA for three typical reactions **BlockP.2**, **BlockP.13**, **BlockP.14** with proper conditions were selected to compare in **Fig. 34**. The lowest conversion of DMAEMA at all the comparable time points were shown in reaction **BlockP.2** which was performed at 26ºC, while the raised conversion of DMAEMA were found in reaction **BlockP.13** and **BlockP.14** which were performed at 50ºC. This can be explained by the increased ATRP rate at increased reaction temperature. In contrast to **BlockP.2** and **BlockP.13**, the DMAEMA conversions at all time points for reaction **BlockP.14** remained the highest values and was persistently increasing, as a reward for the enhanced concentration of Cu(I)Br/ PMDETA and consequent accelerated ATRP rate (**Fig. 34**). Therefore, it was crucial to synthesize the relatively long PDMAEMA block that the catalyst concentration and temperature should be kept higher.

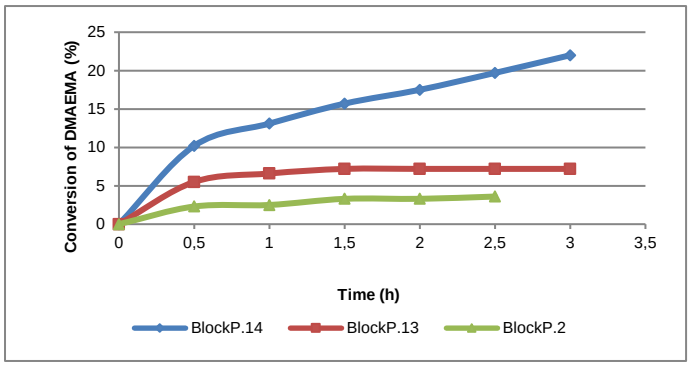

Fig. 34 Comparison of DMAEMA conversion as a function of time in reaction **BlockP.2**, **BlockP.13**, **BlockP.14**. (**BlockP.2**) [DMAEMA]:[PMMA-Br]:[Cu(I)Br]:[PMDETA] =1600:1:1.5:1.5 in toluene for 2.5h at 26ºC, $C_{(DMAEMA)}$= 1.46 mol/L, M_n of PMMA-Br=30 kg/mol;

(**BlockP.13**) [DMAEMA]:[PMMA-Br]:[Cu(I)Br]:[PMDETA] =1600:1:1.5:1.5 in toluene for 3h at 50ºC, $C_{(DMAEMA)}$= 1.46 mol/L, M_n of PMMA-Br= 30 kg/mol;

(**BlockP.14**) [DMAEMA]:[PMMA-Br]:[Cu(I)Br]:[PMDETA] =1600:1:10:10 in toluene for 3h at 50ºC, $C_{(DMAEMA)}$= 1.46 mol/L, M_n of PMMA=30 kg/mol.

The equilibrium of ATRP were basically build up during the first 30min in **BlockP.2** (**Fig. 35**), **BlockP.13** (cf. **10.2.3.**) and **BlockP.14** (cf. **10.2.3.**), whereas in the case of PDI, most stable and narrow PDI evolution was reached in **BlockP.2** due to low ATRP rate brought by the lowest temperature (**Fig. 35**). The high PDI at the beginning of reaction **BlockP.14** can be mainly ascribed to the termination caused by the faster initial ATRP rate resulted from the high employed concentration of complex of Cu(I)Br/PMDETA (cf. **10.2.3.**).

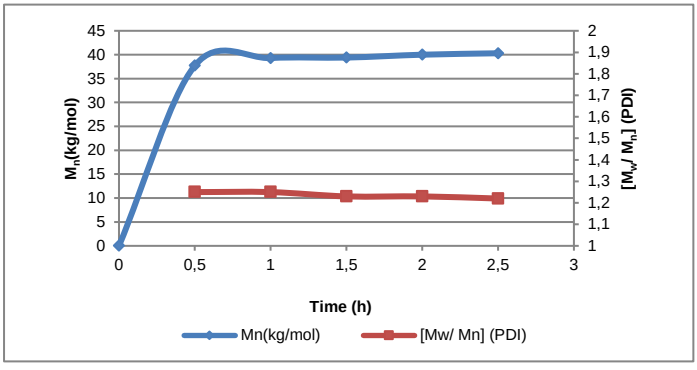

Fig. 35 Evolution of M_n and PDI as functions of time for synthesis of $PMMA_m$-*b*-$PDMAEMA_n$ in reaction **BlockP.2**. (**BlockP.2**) [DMAEMA]:[PMMA-Br]:[Cu(I)Br]:[PMDETA] =1600:1:1.5:1.5 in toluene for 2.5h at 26ºC, $C_{(DMAEMA)}$= 1.46 mol/L, M_n of PMMA-Br=30 kg/mol.

In consideration of the parameters as above discussed, the various ATRP conditions were employed to achieve the desired m/n ratio in prepared $PMMA_m$-*b*-$PDMAEMA_n$. All the used ATRP conditions for synthesis of $PMMA_m$-*b*-$PDMAEMA_n$ (PMMA M_n= 30 kg/mol) can be seen in **Table 6**. The prepared $PMMA_m$-*b*-$PDMAEMA_n$ with calculated specific value of m and n were also displayed.

[DMAEMA]:[$PMMA_m$Br]:[Cu(I)Br]:[PMDETA]	C_{DMAEMA} (mol/L)	Temperatures (°C)	Time (h)	$PMMA_m$-*b*-$PDMAEMA_n$ (^{1}H-NMR)
1600: 1: 1.5: 1.5	1.46	26	2.5	$(PMMA)_{300}$-*b*-$(PDMAEMA)_{45.6}$
1600: 1: 1.5: 1.5	1.46	26	1	$(PMMA)_{300}$-*b*-$(PDMAEMA)_{36.2}$
1600: 1: 1.5: 1.5	1.46	26	0.7	$(PMMA)_{300}$-*b*-$(PDMAEMA)_{33.9}$
1600: 1: 1.5: 1.5	1.46	20	1.2	$(PMMA)_{300}$-*b*-$(PDMAEMA)_{33.5}$
1600: 1: 1.5: 1.5	1.46	22	0.5	$(PMMA)_{300}$-*b*-$(PDMAEMA)_{15.8}$
1600: 1: 1.5: 1.5	1.46	20	0.8	$(PMMA)_{300}$-*b*-$(PDMAEMA)_{24.7}$
1600: 1: 1.5: 1.5	1.46	26	0.75	$(PMMA)_{300}$-*b*-$(PDMAEMA)_{38.9}$
1600: 1: 1.5: 1.5	1.46	23	1	$(PMMA)_{300}$-*b*-$(PDMAEMA)_{38.1}$
1600: 1: 1.5: 1.5	1.46	24	0.7	$(PMMA)_{300}$-*b*-$(PDMAEMA)_{36.4}$
1600: 1: 1.5: 1.5	1.46	50	3	$(PMMA)_{300}$-*b*-$(PDMAEMA)_{83.6}$
1600: 1: 10: 10	1.86	50	3	$(PMMA)_{300}$-*b*-$(PDMAEMA)_{291.3}$
1600: 1: 10: 10	1.86	50	7	$(PMMA)_{300}$-*b*-$(PDMAEMA)_{566}$
1600: 1: 1.5: 1.5	1.46	26	0.5	$(PMMA)_{317}$-*b*-$(PDMAEMA)_{25.3}$

Table 6 All the synthesized $PMMA_m$-*b*-$PDMAEMA_n$ (PMMA M_n= 30 kg/mol) and the corresponding ATRP conditions. Cu(I)Br/PMDETA catalyst system was used in all the reaciotns. The specific value of m and n in $PMMA_m$-*b*-$PDMAEMA_n$ were calculated by results of ^{1}H-NMR.

As shown in **Table 7**, most of the molecular weight (M_n) of $PMMA_m$-*b*-$PDMAEMA_n$ from GPC were similar to the M_n that was calculated by m/n ratio from ^{1}H-NMR, which indicated that the ATRP process for synthesis of $PMMA_m$-*b*-$PDMAEMA_n$ was controlled well. Except prepared $PMMA_m$-*b*-$PDMAEMA_n$ with low ratio of m/n (**BP30k-10**, **BP30k-11**, **BP30k-12**), all the rest $PMMA_m$-*b*-$PDMAEMA_n$ displayed narrow PDI, which signified the uniform growth of PDMAEMA chains during ATRP. The chemical structures of synthesized $PMMA_m$-*b*-$PDMAEMA_n$ were confirmed by ^{1}H-NMR (cf. **10.2.4.**).

The value of m (number of MMA repeatin units in PMMA block) was 300 as calculated before. Calculation processes for all the values of ratio (m/n, by ^{1}H-NMR) and n (number of DMAEMA repeating units in PDMAEMA block) were same as aforementioned description (cf. **5.2.2.2.**).

Code	$(PMMA)_m$-*b*-$(PDMAEMA)_n$ (^{1}H-NMR)	Ratio (PMMA/ PDMAEMA) (^{1}H-NMR)	M_n(g/mol) (^{1}H-NMR)	M_n(g/mol) (GPC)	M_w/M_n (PDI)	Yield (%)
BP30k-1	$(PMMA)_{300}$-*b*-$(PDMAEMA)_{45.6}$	6.7	37200	37800	1.47	[a]37.3
BP30k-2	$(PMMA)_{300}$-*b*-$(PDMAEMA)_{36.2}$	8.3	35700	37200	1.23	53.3
BP30k-3	$(PMMA)_{300}$-*b*-$(PDMAEMA)_{33.9}$	9.1	35300	34300	1.29	74.0
BP30k-4	$(PMMA)_{300}$-*b*-$(PDMAEMA)_{33.5}$	9.1	35300	36500	1.30	82.2
BP30k-5	$(PMMA)_{300}$-*b*-$(PDMAEMA)_{15.8}$	20	32500	30600	1.41	78.0
BP30k-6	$(PMMA)_{300}$-*b*-$(PDMAEMA)_{24.7}$	12.5	33900	32100	1.32	75.1
BP30k-7	$(PMMA)_{300}$-*b*-$(PDMAEMA)_{38.9}$	7.7	36100	35000	1.36	83.6
BP30k-8	$(PMMA)_{300}$-*b*-$(PDMAEMA)_{38.1}$	7.7	36000	34000	1.35	92.7
BP30k-9	$(PMMA)_{300}$-*b*-$(PDMAEMA)_{36.4}$	8.3	35700	35000	1.33	98.1
BP30k-10	$(PMMA)_{300}$-*b*-$(PDMAEMA)_{83.6}$	3.6	43100	38300	1.36	[a]29.6
BP30k-11	$(PMMA)_{300}$-*b*-$(PDMAEMA)_{291.3}$	1.0	75800	60800	1.58	[a]40.2
BP30k-12	$(PMMA)_{300}$-*b*-$(PDMAEMA)_{566}$	0.5	119000	86400	1.79	72.6
BP30k-13	$(PMMA)_{317}$-*b*-$(PDMAEMA)_{25.3}$	12.5	34000	31700	1.52	82.0

Table 7 Characterized $PMMA_m$-*b*-$PDMAEMA_n$ (PMMA M_n=30 kg/mol). [a]Yields of **BP30k-1**, **BP30k-10** and **BP30k-11** were lower than others because trace samples were taken during the respective synthesis.

As shown in **Fig. 36**, GPC distribution of PMMA-Br (M_n=30 kg/mol) and all the derived $PMMA_m$-*b*-$PDMAEMA_n$, were different depending on the various corresponding molecular weights resulted from the different lengths of formed DMAEMA block, which also strongly evidenced the precise control on the architechture of $PMMA_m$-*b*-$PDMAEMA_n$ via optimized ATRP conditions.

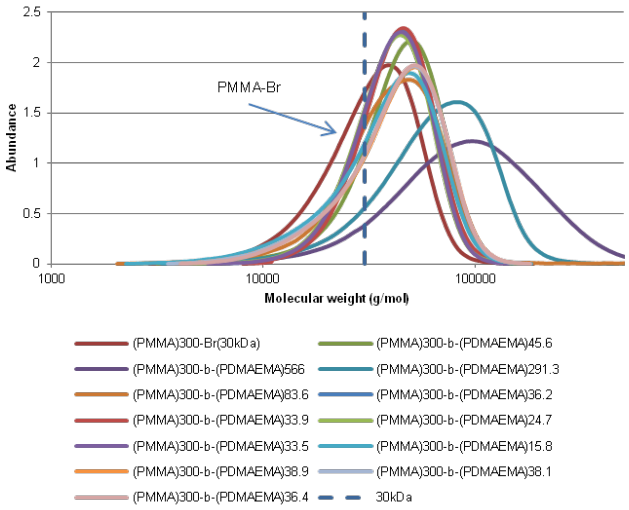

Fig. 36 GPC molecular weight distribution of all the $PMMA_m$-*b*-$PDMAEMA_n$ (PMMA M_n=30 kg/mol) and PMMA-Br (M_n=30 kg/mol).

Synthesis of $PMMA_m$-*b*-$PSPE_n$ with $M_{n\ PMMA}$= 30 kg/mol

As shown in **Fig. 37**, all the prepared precursors ($PMMA_m$-*b*-$PDMAEMA_n$) can be readily converted to zwitterionic $PMMA_m$-*b*-$PSPE_n$ completely with 1,3-propane sultone.

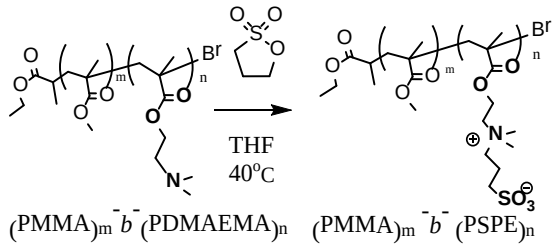

Fig. 37 Synthesis of $PMMA_m$-*b*-$PSPE_n$ with PMMA (M_n= 30 kg/mol) via the post-treatment of precursor. [precursor]: [sultone]= 1: 10.87×m (m is number of MMA repeating units) in THF for 24h at 40 ºC, $C_{precursor}$= 5 g/L.

The synthesized $PMMA_m$-*b*-$PSPE_n$ (PMMA M_n= 30 kg/mol) in **Table 8** were difficult to dissolve completely in solvent for GPC elution. Therefore the PDI of precursors were still used here. For most of $PMMA_m$-*b*-$PSPE_n$ (PMMA M_n=30 kg/mol), their M_n that were calculated repectively from the ^{1}H-NMR ratio and EAs ratio were nearly similar, except the prepared $PMMA_m$-*b*-$PSPE_n$ with low ratio of m/n (**ZBP30k-10**, **ZBP30k-11**, **ZBP30k-12**).

Code	[c](PMMA)m-b-(PSPE)n (^{1}H-NMR)	[c]Ratio (PMMA/ PSPE) (^{1}H-NMR)	[a]Mn(g/mol) (by ^{1}H-NMR of precursor)	[b]Mn(g/mol) (EAs)	[c]Mw/Mn (PDI of precursor)	Yield (%)
ZBP30k-1	$(PMMA)_{300}$-*b*-$(PSPE)_{45.6}$	6.7	42700	40000	1.47	100
ZBP30k-2	$(PMMA)_{300}$-*b*-$(PSPE)_{36.2}$	8.3	40100	40300	1.23	100
ZBP30k-3	$(PMMA)_{300}$-*b*-$(PSPE)_{33.9}$	9.1	39500	41900	1.29	93.3
ZBP30k-4	$(PMMA)_{300}$-*b*-$(PSPE)_{33.5}$	9.1	39300	41100	1.30	100
ZBP30k-5	$(PMMA)_{300}$-*b*-$(PSPE)_{15.8}$	20	34400	36500	1.41	100
ZBP30k-6	$(PMMA)_{300}$-*b*-$(PSPE)_{24.7}$	12.5	36900	38600	1.32	83.0
ZBP30k-7	$(PMMA)_{300}$-*b*-$(PSPE)_{38.9}$	7.7	40900	43700	1.36	82.7
ZBP30k-8	$(PMMA)_{300}$-*b*-$(PSPE)_{38.1}$	7.7	40600	39200	1.35	100
ZBP30k-9	$(PMMA)_{300}$-*b*-$(PSPE)_{36.4}$	8.3	40200	44700	1.33	100
ZBP30k-10	$(PMMA)_{300}$-*b*-$(PSPE)_{83.6}$	3.6	53300	63700	1.36	53.9
ZBP30k-11	$(PMMA)_{300}$-*b*-$(PSPE)_{291.3}$	1.0	111300	120100	1.58	55.3
ZBP30k-12	$(PMMA)_{300}$-*b*-$(PSPE)_{566}$	0.5	188000	233300	1.79	87.6
ZBP30k-13	$(PMMA)_{317}$-*b*-$(PSPE)_{25.3}$	12.5	38800	36500	1.52	96.9

Table 8 Characterized $PMMA_m$-*b*-$PSPE_n$ (PMMA M_n = 30 kg/mol). [a]The ratio of PMMA/ PDMAEMA that calculated by ^{1}H-NMR was still used here as the ratio of PMMA/PSPE to calculate the according M_n. EAs is elemental assay. [b]The results of EAs were directly used to calculate the ratio of PMMA/PSPE and according M_n here. [c]Ratios of PMMA/PSPE, M_w/M_n

(PDI) of $PMMA_m$-*b*-$PSPE_n$ and values of m, n directly followed the corresponding values from the $PMMA_m$-*b*-$PDMAEMA_n$ precursors.

5.2.2.5. Synthesis of $PMMA_m$-*b*-$PSPE_n$ with $M_{n\ PMMA}$= ~10 kg/mol

As shown in **Fig. 38**, to further improve the homogeneity of ATRP catalyst in toluene solvent, Cu(I)Br/ [dinonyl bipyridine]$_2$ was selected as catalyst system for synthesis of PMMA-Br with molecular weight approximate 10 kg/mol.

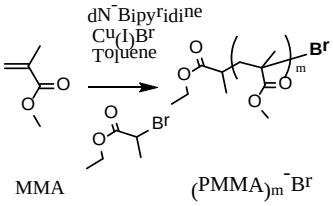

Fig. 38 Synthesis of macroinitiator PMMA-Br (M_n=30 kg/mol). [MMA]:[EBrP]:[Cu(I)Br]:[dN-bipyridine] =50:1:1:2 in toluene for for 2h at 40ºC, $C_{(MMA)}$= 3 mol/L.

Depending on the two linear aliphatic branches of normal nonyl groups in dinonyl bipyridine (**Fig. 39**), better homogeneity of catalytic system in low polar toluene solvent can be available by use of Cu(I)Br/[dinonyl bipyridine]$_2$ for ATRP, in contrast of Cu(I)Br/bipyridine$_2$. In addition, complex of Cu(II)Br/[dinonyl bipyridine]$_2$ showed lower redox potential than Cu(II)Br/ bipyridine$_2$, but higher redox potential than Cu(II)Br/PMDETA in MeCN at 25°C (**Fig. 3,** cf. **2.1.2.**).[21] Correspondingly, complex of Cu(I)Br/ [dinonyl bipyridine]$_2$ brought about higher K_{ATRP} than Cu(I)Br/bipyridine$_2$ but lower K_{ATRP} than Cu(I)Br/PMDETA in MeCN at 25°C (**Fig. 3**).[21] Therefore, the proper rate of deactivation still can be obtained by use of Cu(I)Br/[dinonyl bipyridine]$_2$ as catalyst, which was also largely favorable to preserve the end functional bromine of macro initiator PMMA-Br.

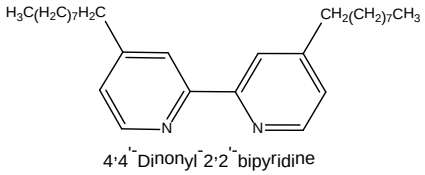

Fig. 39 4,4'-dinonyl-2,2'-bipyridine.

To optimize the ATRP conditions for synthesis of PMMA-Br with expected molecular weight by use of Cu(I)Br/[dinonyl bipyridine]$_2$, many exploring reactions were performed. Here, the

conversion of MMA for three typical reactions **MIni.14**, **MIni.15**, **MIni.16** with proper conditions were selected to compare with **MIni.12** where Cu(I)Br/[dinonyl bipyridine]$_2$ was used (**Fig. 40**).

As shown in **Fig. 40**, conversion of MMA at all the comparable time points for reaction **MIni.14**, **MIni.15**, **MIni.16** were higher than their counterparts in reaction **MIni.12** due to the improved rate of ATRP (higher K_{ATRP}) by relatively faster activation of Cu(I)Br/[dinonyl bipyridine]$_2$. Especially the higher conversion compared with **MIni.12** were also obtained in **MIni.16** where the much lower concentration of Cu(I)Br/[dinonyl bipyridine]$_2$ was employed. This was well in agreement with the fact that the complex of Cu(I)Br/ [dinonyl bipyridine]$_2$ brought about higher K_{ATRP} than Cu(I)Br/ bipyridine$_2$. The basically reproducible conversion of MMA can be observed in reaction **MIni.14** and **MIni.15** which were performed under same reaction conditions.

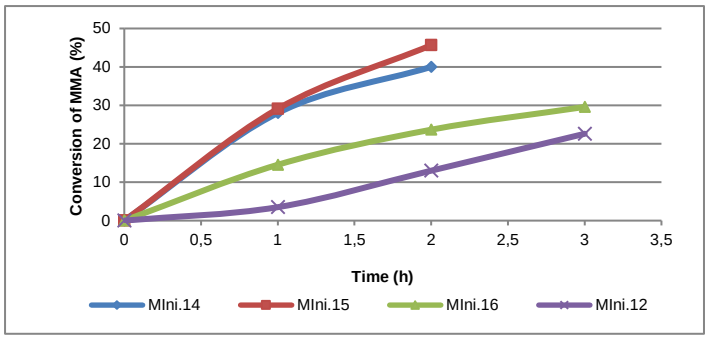

Fig. 40 Comparison of MMA conversion as a function of time in reaction **MIni.14**, **MIni.15**, **MIni.16** and **MIni.12***. *Only the conversion data for 1h, 2h, 3h in reaction **MIni.12** were showed here.

(**MIni.14**) [MMA]:[EtBrP]:[Cu(I)Br]:[dinonyl bipyridine] =50:1:1:2 in toluene for 2h at 40ºC, $C_{(MMA)}$= 3 mol/L;

(**MIni.15**) [MMA]:[EtBrP]:[Cu(I)Br]:[dinonyl bipyridine] =50:1:1:2 in toluene for 2h at 40ºC, $C_{(MMA)}$= 3 mol/L;

(**MIni.16**) [MMA]:[EtBrP]:[Cu(I)Br]:[dinonyl bipyridine] =200:1:1:2 in toluene for 3h at 40ºC, $C_{(MMA)}$= 3 mol/L;

(**MIni.12**) [MMA]:[EBrP]:[Cu(I)Br]:[bipyridine] =50:1:1:2 in toluene for 5h at 50ºC, $C_{(MMA)}$= 3 mol/L.

In **MIni.14** and **MIni.15**, rate of PMMA chains growing (rate of M_n increasing) slowed down with time progressing, while PDI also increased slowly but still stayed in rational range of ATRP (1.0~1.5) within 2 hours (cf. **10.2.5.**).

Based on the ATRP conditions of **MIni.14** and **MIni.15**, macroinitiator PMMA-Br with desired M_n approximate 10 kg/mol and according narrow PDI were available. As shown in **Table 9**, two prepared macro initiator PMMA-Br were characterized by quite similar M_n and narrow PDI, as a result of proper control from optimized ATRP conditions. The two macro initiator $(PMMA)_{94}$-Br and $(PMMA)_{98}$-Br with similar M_n ~10 kg/mol were respectively synthesized in reaction **MIni.14** and **MIni.15** where same ATRP conditions were used. This strongly suggested the stable

reproducibility of the employed ATRP conditions and resultant precise control on ATRP process for **MIni.14** and **MIni.15**. The chemical structure of synthesized $PMMA_m$-Br was confirmed by ^{1}H-NMR (cf. **10.2.6.**).

Code	M_w/M_n (PDI)	M_n (g/mol) (GPC)	$(PMMA)_m$-Br (GPC)	Yield (%)
MI10k-1	1.18	9400	$(PMMA)_{94}$-Br	27.0
MI10k-2	1.25	9800	$(PMMA)_{98}$-Br	28.3

Table 9 Characterized PMMA-Br (M_n= ~10 kg/mol) macroinitiator. ***MI10k-1** and **MI10k-2** had similar M_n (GPC), so these two PMMA-Br macro intiator were classified as PMMA-Br with M_n= ~10 kg/mol.

The molecular weight (M_n) of synthesized $PMMA_m$-Br were determined by GPC. The calculation process for values of m were same as aforementioned description (cf. **5.2.2.2.**, **Equation 7**). The calculated m were 94 and 98 respectively.

Synthesis of $PMMA_m$-*b*-$PDMAEMA_n$ with $M_{n\ PMMA}$= ~10 kg/mol

As shown in **Fig. 41**, Cu(I)Br/PMDETA catalyst system was still used to synthesize $PMMA_m$-*b*-$PDMAEMA_n$ with PMMA (M_n= ~10 kg/mol). For the sake of preparation of $PMMA_m$-*b*-$PDMAEMA_n$ with diverse ratios of PMMA versus PDMAEMA, the rate of ATRP for synthesis of second block PDMAEMA, as aforementioned ATRP rate for synthesis of PMMA-Br (cf. **2.1.2.**), can also be regulated via different ATRP parameters (i.e. concentrations of monomer and catalysts, reaction temperature, reaction time).

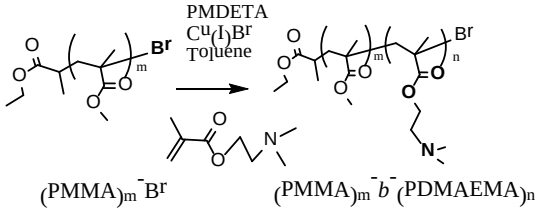

Fig. 41 Synthesis of precursor $PMMA_m$-*b*-$PDMAEMA_n$($PMMA\ M_n$= ~10 kg/mol).

To find the proper ATRP conditions for synthesis of $PMMA_m$-*b*-$PDMAEMA_n$ ($PMMA\ M_n$= ~10 kg/mol) with expected ratio of m/n, some exploring reactions were performed. As shown in **Fig. 42**, evolution of M_n with progressing time for two selected exploring reaction **BlockP.20** and **BlockP.22** were compared. Compared with reaction **BlockP.20**, higher rate of PDMAEMA chains growing (rate of M_n increasing) with time progressing was observed in reaction **BlockP.22** where higher concentration of DMAEMA monomer was applied. This was quite consistent with

Equation 1, which indicated that the raised concentration of monomer was favorable to ATRP rate. As above discussion, synthesis of $PMMA_m$-*b*-$PDMAEMA_n$ with various ratios of PMMA/PDMAEMA can still be available through regulation of ATRP rate via reaction parameters.

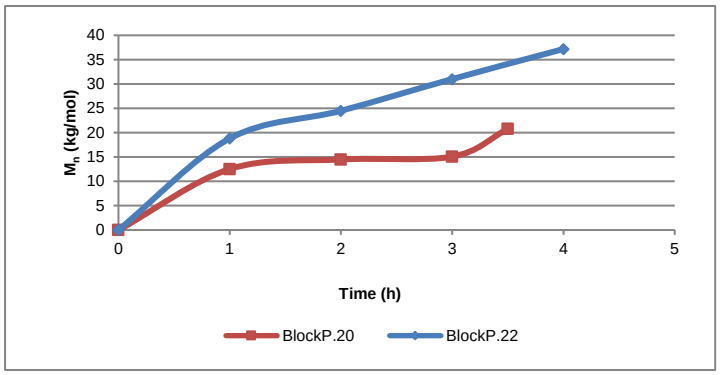

Fig. 42 Evolution of M_n as a function of time for synthesis of $PMMA_m$-*b*-$PDMAEMA_n$ in reaction **BlockP.20** and **BlockP.22**. (**BlockP.20**) [DMAEMA]:[PMMA-Br]:[Cu(I)Br]:[PMDETA] =1600:1:10:10 in toluene for 3.5h at 60ºC, $C_{(DMAEMA)}$= 1.46 mol/L, $M_{n\ (PMMA\text{-}Br)}$=10 kg/mol;
(**BlockP.22**) [DMAEMA]:[PMMA-Br]:[Cu(I)Br]:[PMDETA] =3323:1:10:10 in toluene for 4h at 60ºC, $C_{(DMAEMA)}$= 2.97 mol/L, $M_{n\ (PMMA\text{-}Br)}$=10 kg/mol.

All the used ATRP conditions for synthesis of $PMMA_m$-*b*-$PDMAEMA_n$ (PMMA M_n=~10 kg/mol) can be seen in **Table 10**. The various ATRP conditions were employed to achieve the desired m/n ratio in prepared $PMMA_m$-*b*-$PDMAEMA_n$. The prepared $PMMA_m$-*b*-$PDMAEMA_n$ with calculated specific values of m and n were also displayed.

[DMAEMA]:[$PMMA_m$Br]:[Cu(I)Br]:[PMDETA]	C_{DMAEMA} (mol/L)	Temperatures (°C)	Time (h)	$PMMA_m$-Br	$PMMA_m$-*b*-$PDMAEMA_n$ (GPC)
1600: 1: 1.5: 1.5	1.46	60	3.5	$(PMMA)_{94}$-Br	$(PMMA)_{94}$-*b*-$(PDMAEMA)_{366}$
1600: 1: 1.5: 1.5	1.46	23	2	$(PMMA)_{98}$-Br	$(PMMA)_{98}$-*b*-$(PDMAEMA)_5$
1600: 1: 1.5: 1.5	1.46	50	1	$(PMMA)_{98}$-Br	$(PMMA)_{98}$-*b*-$(PDMAEMA)_{187}$
1600: 1: 10: 10	1.46	60	1.5	$(PMMA)_{98}$-Br	$(PMMA)_{98}$-*b*-$(PDMAEMA)_{416}$
1600: 1: 1.5: 1.5	1.46	50	4	$(PMMA)_{98}$-Br	$(PMMA)_{98}$-*b*-$(PDMAEMA)_{243}$

Table 10 All the synthesized $PMMA_m$-*b*-$PDMAEMA_n$ (PMMA M_n=~10 kg/mol) and the corresponding ATRP conditions. Cu(I)Br/ PMDETA catalyst system was used in all the reaciotns. The specific values of m and n in $PMMA_m$-*b*-$PDMAEMA_n$ were calculated by results of GPC.

As shown in **Table 11**, all the ratios of PMMA/PDMAEMA (m/n) were calculated by GPC results. All the listed $PMMA_m$-*b*-$PDMAEMA_n$ displayed narrow PDI, which signified the uniform growth of

PDMAEMA chains during ATRP. The chemical structures of synthesized $PMMA_m$-*b*-$PDMAEMA_n$ were confirmed by ^{1}H-NMR (cf. **10.2.7.**).

Code	[b](PMMA)$_m$-*b*-(PDMAEMA)$_n$ (GPC)	[a]Ratio (PMMA/ PDMAEMA) (GPC)	M_w/M_n (PDI)	M_n (g/mol) (GPC)	Yield (%)
BP10k-1	$(PMMA)_{94}$-*b*-$(PDMAEMA)_{366}$	0.3	1.41	67100	92
BP10k-2	$(PMMA)_{98}$-*b*-$(PDMAEMA)_5$	19.6	1.22	10500	30.9
BP10k-3	$(PMMA)_{98}$-*b*-$(PDMAEMA)_{187}$	0.5	1.04	39300	86
BP10k-4	$(PMMA)_{98}$-*b*-$(PDMAEMA)_{416}$	0.3	1.19	75300	30.8
BP10k-5	$(PMMA)_{98}$-*b*-$(PDMAEMA)_{243}$	0.4	1.06	48100	75

Table 11 Characterized $PMMA_m$-*b*-$PDMAEMA_n$ (PMMA M_n= ~10 kg/mol). [a]All the ratios of PMMA/PDMAEMA were calculated with GPC results. [b]Values of m and n were calculated with ratio of PMMA / PDMAEMA from GPC results.

The value of m (number of MMA repeatin units in PMMA block) was 94 or 98 as aforementioned calculation. All the values of n (number of DMAEMA repeating units in PDMAEMA block) can be calculated with following **Equation 8**.

$$\frac{M_n(\text{precursor}) - M_n(\text{PMMA})}{157} = m \qquad \textbf{(Equation 8)}$$

M_n (precursor) was the GPC M_n of prepared $PMMA_m$-*b*-$PDMAEMA_n$. M_n (PMMA) was the GPC M_n of macroinitiatior PMMA-Br. Molecular weight of monomer DMAEMA was 157.

As shown in **Fig. 43**, GPC distribution of PMMA-Br (M_n= 9.4 kg/mol) and the derived $PMMA_m$-*b*-$PDMAEMA_n$ were different depending on gradually increasing molecular weights, which strongly evidenced the successful sequential ATRP and post-treatment.

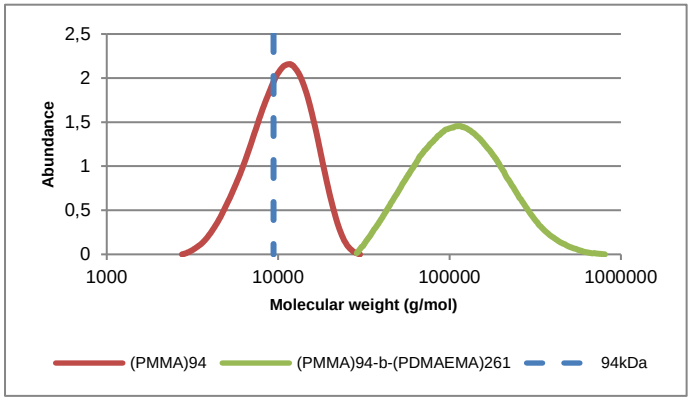

Fig. 43 GPC molecular weight distribution of PMMA-Br (M_n= 9.4 kg/mol) and derived $PMMA_m$-*b*-$PDMAEMA_n$ ($M_{n\,(PMMA)}$= 9.4 kg/mol).

As shown in **Fig. 44**, GPC distribution of PMMA-Br (M_n=9.8 kg/mol) and the derived PMMA$_m$-*b*-PDMAEMA$_n$ were different depending on the various corresponding molecular weights resulted from the different lengths of formed DMAEMA block, which also strongly evidenced the effective control on the architechture of PMMA$_m$-*b*-PDMAEMA$_n$ via optimized ATRP conditions.

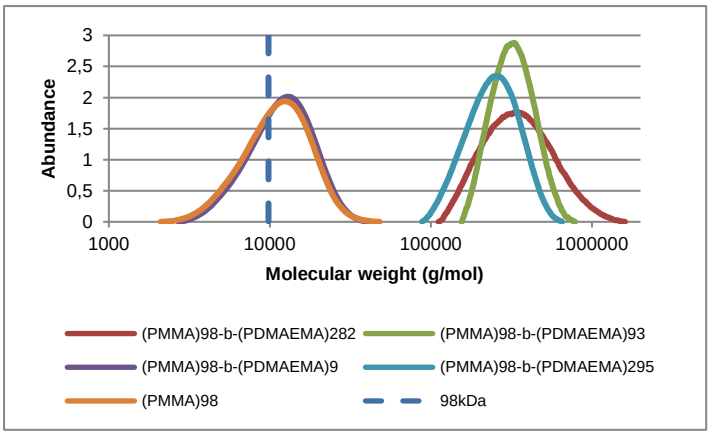

Fig. 44 GPC molecular weight distribution of PMMA-Br (M_n= 9.8 kg/mol) and derived PMMA$_m$-*b*-PDMAEMA$_n$ ($M_{n\ (PMMA)}$ = 9.8 kg/mol).

Synthesis of PMMA$_m$-*b*-PSPE$_n$ with $M_{n\ PMMA}$= ~10 kg/mol

As shown in **Fig. 45**, all the prepared precursors (PMMA$_m$-*b*-PDMAEMA$_n$) can be readily converted to zwitterionic PMMA$_m$-*b*-PSPE$_n$ completely with 1,3-propane sultone.

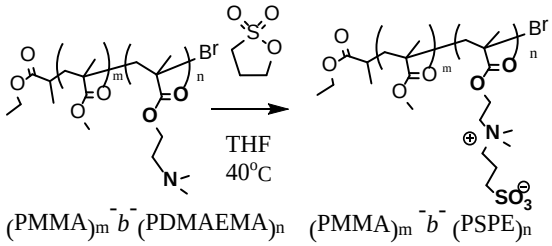

Fig. 45 Synthesis of PMMA$_m$-*b*-PSPE$_n$ with PMMA (M_n= ~10 kg/mol) via the post-treatment of precursor. [precursor]: [sultone]= 1: 10.87×m (m is number of MMA repeating units) in THF for 24h at 40 ºC, $C_{precursor}$= 5 g/L.

The synthesized PMMA$_m$-*b*-PSPE$_n$ (PMMA M_n= ~10 kg/mol) in **Table 12** were difficult to dissolve completely in solvent for GPC elution. Therefore the PDI of precursors were still used here. The ratios of m/n and the specific values of m and n for all the prepared PMMA$_m$-*b*-PSPE$_n$ (PMMA M_n= ~10 kg/mol) were calculated by the according elemental assay results.

Code	[a](PMMA)$_m$-*b*-(PSPE)$_n$ (EAs)	[a]Ratio (PMMA/ PSPE) (EAs)	[b]M_n (g/mol) (EAs)	[c]M_w/M_n (PDI of precursor)	Yield (%)
ZBP10k-1	(PMMA)$_{94}$-*b*-(PSPE)$_{261}$	0.4	82300	1.41	62.1
ZBP10k-2	(PMMA)$_{98}$-*b*-(PSPE)$_9$	11.4	12200	1.22	98.0
ZBP10k-3	(PMMA)$_{98}$-*b*-(PSPE)$_{93}$	1.1	35900	1.04	56.0
ZBP10k-4	(PMMA)$_{98}$-*b*-(PSPE)$_{282}$	0.4	88600	1.19	66.7
ZBP10k-5	(PMMA)$_{98}$-*b*-(PSPE)$_{295}$	0.3	92200	1.06	70.2

Table 12 Characterized PMMA$_m$-*b*-PSPE$_n$ (PMMA M_n=~10kDa). [a]Ratios of PMMA to PSPE and values of m&n were calculated with sulfur contents (wt.%) from elemental analysis results. [b]M_n were calculated with elemental analysis results. [c]M_w/M_n followed GPC results of precursors.

5.2.2.6. Synthesis of PMMA$_m$-*b*-PDMAEMA$_n$ with $M_{n\ PMMA}$= 53.9 kg/mol

As shown in **Table 13**, two PMMA$_m$-*b*-PDMAEMA$_n$ were prepared with macroinitiator PMMA-Br (M_n= 53.9 kg/mol). The detailed synthesis process can be seen in **10.2.8.** and **10.2.9.**.

Code	(PMMA)$_m$-*b*-(PDMAEMA)$_n$ (^{1}H-NMR)	Ratio (PMMA/ PDMAEMA) (^{1}H-NMR)	M_n(g/mol) (^{1}H-NMR)	M_n(g/mol) (GPC)	M_w/M_n (PDI)	Yield (%)
BP53k-1	(PMMA)$_{539}$-*b*-(PDMAEMA)$_{350}$	1.5	108200	77100	1.93	67,7
BP53k-2	(PMMA)$_{539}$-*b*-(PDMAEMA)$_{173}$	3.1	80700	75000	1.53	72,9

Table 13 Characterizaed PMMA$_m$-*b*-PDMAEMA$_n$ (PMMA M_n= 53.9 kg/mol). The reaction time was respectively 9h and 6h for synthesis of **BP53k-1** and **BP53k-2**.

5.2.2.7. Comparison of ATR-FTIR spectra

As shown in **Fig. 46**, the ATR-FTIR spectra for selected different samples of PMMA-Br, PMMA$_m$-*b*-PDMAEMA$_n$, PMMA$_m$-*b*-PSPE$_n$ and PMMA$_m$-*co*-PSPE$_n$ were compared to identify the feature difference of chemical structure in beween. All the examined samples in **Fig. 46** showed clear absorption at 1715-1730 cm^{-1}, which can be attributed to the stretching vibration of C=O from carboxylate groups in pendent side chains of PMMA, PDMAEMA and PSPE. Absorption from stretching vibration of C-O at 1163-1210 cm^{-1} also can be identified easily in all the four ATR-FTIR spectra, which also strongly supported the existing carboxylate groups in pendent side chains of PMMA, PDMAEMA and PSPE. The absorption at 1024-1034 cm^{-1} corresponding to the stretching vibration of S=O can be merely identified in ATR-FTIR of PMMA$_m$-*b*-PSPE$_n$ and PMMA$_m$-*co*-PSPE$_n$, which strongly verified the existence of PSPE with SO_3^- groups. Overall, through the comparison of ATR-FTIR, the successful synthesis of PMMA$_m$-*b*-PSPE$_n$ and PMMA$_m$-*co*-PSPE$_n$ can be confirmed undoubtedly.

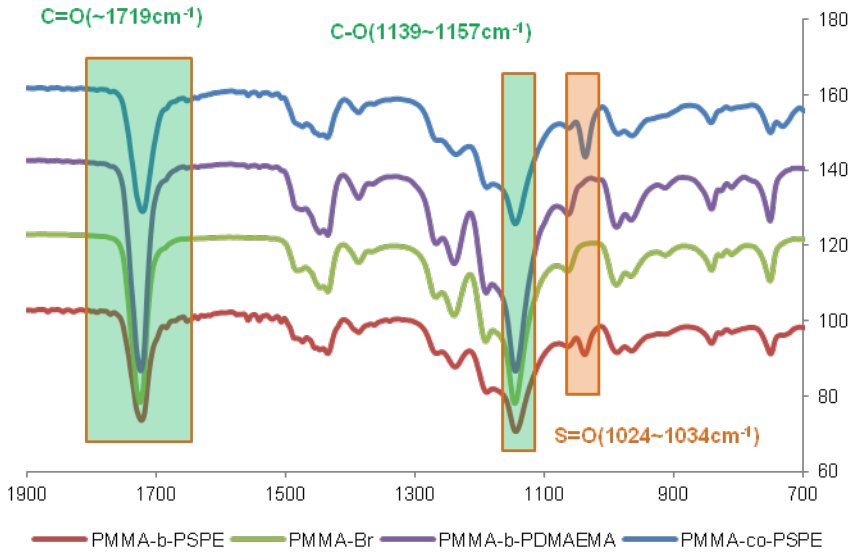

Fig. 46 Comparison of different typical ATR-FTIR spectra for PMMA-Br, $PMMA_m$-*b*-$PDMAEMA_n$, $PMMA_m$-*b*-$PSPE_n$ and $PMMA_m$-*co*-$PSPE_n$. Typical ATR-FTIR spectra were from selected samples of **MI30k**, **BP53k-1**, **ZBP14k** and **RCP1**.

6. Results and discussion of prepared PVDF membranes

6.1. PVDF membranes with single type of additive

$PMMA_m$-*co*-$PSPE_n$, $PMMA_m$-*b*-$PSPE_n$ (with $M_{n\ PMMA}$= 30 kg/mol, 13.9 kg/mol, 10 kg/mol and various ratios of PMMA/PSPE), PVP (K30) and $PMMA_m$-*b*-$PDMAEMA_n$ were applied respectively as single additive to prepare PVDF membranes in different NIPS conditions.

Empirically, $PMMA_m$-*b*-$PSPE_n$ or $PMMA_m$-*co*-$PSPE_n$ with higher ratio of PMMA/PSPE (> 6.7, cf. **Table 14**) were more easily dissolved in PVDF dope solution due to the less intensive interwinding between zwitterionic molecular chains. On the other hand, $PMMA_m$-*b*-$PSPE_n$ with lower ratio of PMMA/PSPE (< 1, cf. **Table 14**) were quite difficult to be dissolved in PVDF dope solution completely.

6.1.1. PVDF membranes with single additive

Only one kind of additives were doped in PVDF membrane, including self-synthesized $PMMA_m$-*co*-$PSPE_n$, various $PMMA_m$-*b*-$PSPE_n$, $PMMA_m$-*b*-$PDMAEMA_n$, and commercial PVP (K30), as shown in **Table 14**. The employed content (wt.%) for doped additives were various. The employed content (wt.%) of PVDF were respectively 17.5 wt.% and 16 wt.%. Except **M1.9**, only one type of additive was doped with PVDF in membrane dope solution. In the case of **M1.9**, two types of $PMMA_m$-*b*-$PSPE_n$ with different M_n were doped together with PVDF in one dope solution to prepare membrane. The procedure of NIPS for membrane **M1.1**, **M1.2**, **Rf1** had different parameters of casting speed and humidity in NIPS from the according parameters in NIPS for the rest other membrane. All the details regarding NIPS of membranes in **Table 14** can be seen in **4.3.2.**. The viscosity data for dope solutions of PVDF membrane with single additive were also tabulated in **Table 14** and further discussed in **6.1.2.**.

Code	Add. wt.%	Add. M_n(g/mol)	Ratio (PMMA/ PSPE)	PVDF Wt.%	[a]Viscosity (Pa.s)
M1.1	$(PMMA)_{188}$-*co*-$(PSPE)_{16.5}$ 2	23400	11.4	17.5	N/A
M1.2	$(PMMA)_{139}$-*b*-$(PSPE)_{12.5}$ 2	17000	11.1	17.5	N/A
Rf1	PVP(K30) 2	14000	N/A	17.5	N/A
M1.3	$(PMMA)_{300}$-*b*-$(PSPE)_{36.2}$ 0.5	40100	8.3	16	2.05±0.04
M1.4	$(PMMA)_{300}$-*b*-$(PSPE)_{36.4}$ 1	40200	8.3	16	2.20±0.05
M1.5	$(PMMA)_{317}$-*b*-($PSPE)_{25.3}$ 1	36900	12.5	16	2.42±0.06
M1.6	$(PMMA)_{300}$-*b*-$(PSPE)_{45.6}$ 1	42700	6.7	16	2.42±0.25
M1.7	$(PMMA)_{300}$-*b*-($PSPE)_{291.3}$ 1.5	111300	1.0	16	1.62±0.03
M1.8	$(PMMA)_{300}$-*b*-($PSPE)_{566}$ 1.5	188000	0.5	16	2.00±0.05
M1.9	$(PMMA)_{300}$-*b*-($PSPE)_{291.3}$ 1.5 $(PMMA)_{300}$-*b*-($PSPE)_{33.5}$ 1	111300 39300	1.0 9.1	16	2.50±0.18
M1.10	$(PMMA)_{94}$-*b*-$(PSPE)_{261}$ 1	82300	0.4	16	1.82±0.03
M1.11	$(PMMA)_{94}$-*b*-$(PSPE)_{261}$ 2	82300	0.4	16	1.82±0.02
M1.12	$(PMMA)_{98}$-*b*-$(PSPE)_{295}$ 1	92200	0.3	16	2.06±0.09
Rf2	$(PMMA)_{98}$-*b*-$(PDMAEMA)_{93}$ 1	24500	1.1	16	1.95±0.06
Rf3	PVP(K30) 0.5	14000	N/A	16	0.99±0.03
Rf4	PVP(K30) 1	14000	N/A	16	1.97±0.07
Rf5	PVP(K30) 1	14000	N/A	16	2.25±0.06
Rf6	PVP(K30) 1	14000	N/A	16	2.30±0.09
Rf7	PVP(K30) 1.5	14000	N/A	16	2.42±0.11
Rf8	PVP(K30) 3	14000	N/A	16	2.51±0.08

Table 14 Dope solutions for preparation of according PVDF membranes containing PVP, $PMMA_m$-*b*-$PDMAEMA_n$, $PMMA_m$-*co*-$PSPE_n$ or various $PMMA_m$-*b*-$PSPE_n$ respectively as single additive. Membrane matrix material was PVDF (M_w= 48.1 kg/mol). Solvent was NMP. Coagulation bath was deionized water. Temperature of casting plate and coagulation were r.t.. For membrane **M1.1**, **M1.2**, **Rf1**, the speed of casting knife were 50mm/s and humidity were 31.8% during casting. For the preparation of rest membranes, the speed of casting knife were 5mm/s and humidity were less than 20.0% during casting process. [a]Viscosity (@r.t.) of the listed PVDF membrane dope solutions with additives were also tabulated. Shear rate fixed to 25 [1/s]. Viscosity of dope solutions of **M1.1**, **M1.2**, **Rf1** were not be examined. Parameter details on measurement of rheology can be seen in **4.4.2.2.**.

6.1.2. Rheology

Rheology behavior of PVDF membrane dope solutions were characterized by viscosity measurement. The exchanging rate between solvent and nonsolvent during the liquid-liquid

demixing of membrane casting film, which was highly related to the viscosity of dope solution, played a key factor on precipitation kinetics of polymer and thus phase separation of casting film in coagulation bath (cf. **2.2.3.**).[75] Theoretically, the increment of polymer fraction in polymer solutions can render more intensified entanglement between polymer molecular chains and hence give rise to the more enhancement on the viscosity of polymer solution.[76]

Because there were no viscosity data for membrane dope solutions with 17.5 wt.% PVDF (**M1.1**, **M1.2** and **Rf1**) in **Table 14**, the discussion regarding viscosity here merely focused on the membrane dope solutions with 16 wt.% PVDF. In the following discussion, $PMMA_m$-*b*-$PSPE_n$ was used to represent the zwitterionic block copolymer additives in **Table 14**. For the dope solutions which contained $PMMA_m$-*b*-$PSPE_n$ with long PMMA block (m= 300) and relatively short PSPE block (PMMA/PSPE= m/n= 6.7-12.5, **M1.3**-**M1.6**), the **M1.3** dope solution that involved 0.5 wt.% $PMMA_m$-*b*-$PSPE_n$ apparently displayed lower viscosity than that of **M1.4**, **M1.5** and **M1.6** that had 1 wt.% $PMMA_m$-*b*-$PSPE_n$, which indicated that the content of $PMMA_m$-*b*-$PSPE_n$ with relatively short PSPE block dominated the viscosity of **M1.3**-**M1.6** dope solutions due to the better homogeneity of dope solutions. Dope solutions of **M1.7** and **M1.8** that involved 1.5wt.% $PMMA_m$-*b*-$PSPE_n$ with same PMMA block (m= 300) but relatively long PSPE block (PMMA/PSPE= m/n= 1.0, 0.5), showed apparently decreased viscosity compared with **M1.3**-**M1.6**, which perhaps arose from the degraded solubility of $PMMA_m$-*b*-$PSPE_n$ with relatively long PSPE block or less flexibility of long PSPE block due to the reinforced entanglement of zwitterionic side chains along the long PSPE block.[77]

In another case of dope solutions that contained additive 1-2 wt.% $PMMA_m$-*b*-$PSPE_n$ with shorter PMMA block (m=94 and 98) but relatively longer PSPE block (PMMA/PSPE= m/n= 0.4 and 0.3, **M1.10**-**M1.12**), all the viscosity of **M1.10**-**M1.12** were lower than **M1.4**-**M1.6** that involved 1 wt.% $PMMA_m$-*b*-$PSPE_n$ with long PMMA block (m=300) and relatively short PSPE block (PMMA/PSPE= m/n= 6.7-12.5), whereas **M1.7** and **M1.8** that had 1.5 wt.% $PMMA_m$-*b*-$PSPE_n$ with PMMA block (m= 300) but relatively long PSPE block (PMMA/PSPE= m/n= 1.0, 0.5) exhibited comparably lower viscosity in contrast to that of **M1.10**-**M1.12**. The rheology behavior of **M1.10**-**M1.12** were in agreement with **M1.7** and **M1.8**, which also can support the aforementioned conclusion concerning the negative influence of relatively long PSPE block on viscosity of dope solution.

Dope solution of **M1.9** that contained 1 wt.% $PMMA_{300}$-*b*-$PSPE_{33.5}$ and 1.5wt.% $PMMA_{300}$-*b*-$PSPE_{291.3}$, presented the highest viscosity, which signified that perhaps the $PMMA_m$-*b*-$PSPE_n$ with

short PSPE block contributed more to the viscosity and homogeneity of dope solution, than that of $PMMA_m$-*b*-$PSPE_n$ with relatively long PSPE block.

Dope solutions of **Rf4**-**Rf6**, which had same fraction of PVP (K30) (1 wt.%) and showed similar viscosity, revealed higher viscosity than that of **Rf3** which had 0.5wt.% PVP (K30). The bigger PVP fraction brought about enhanced viscosity of dope solution due to the improvement of entanglement between the molecular chains of PVDF and PVP depending on the good miscibility between them. Naturally, dope solution of **Rf8** that contained 3 wt.% PVP (K30) gained the higher viscosity than that of **Rf7** with 1.5 wt.% PVP, and both of **Rf7** and **Rf8** showed higher viscosity than **Rf4**-**Rf6**. It should be noted that the dope solutions of **M1.4**, **M1.5** and **M1.6** had 1 wt.% $PMMA_m$-*b*-$PSPE_n$ (PMMA/PSPE= m/n= 6.7-12.5) with better solubility in dope solution (cf. **6.1.**) apparently showed the relatively higher viscosity than that of **Rf4**-**Rf6** with 1 wt.% PVP (K30).

6.1.3. Typical SEM morphologies

Cross section, top surface, detailed top surface, and back surface of some selected typical PVDF membranes which contained one additive were imaged with SEM and shown in this part. Membrane **M1.1**, **M1.2** and **Rf1** were composed of 17.5 wt.% PVDF and respectively 2 wt.% $(PMMA)_{188}$-*co*-$(PSPE)_{16.5}$, 2 wt.% $(PMMA)_{139}$-*b*-$(PSPE)_{12.5}$, 2 wt.% PVP (K30) (cf. **6.1.1.**). Therefore morphology of **M1.1**, **M1.2** and **Rf1** were put together for comparison and discussion in detail.

The SEM morphology of membrane **Rf1**, **M1.1** and **M1.2** were presented in **Fig. 47**, **Fig. 48** and **Fig. 49**. In principle, the improved polymer concentration tends to drive the miscibility gap (or the nonsolvent amount needed for reaching cloud points) of polymer solutions (e.g. membrane dope solutions) approaching the polymer-solvent axis in ternary phase diagram (polymer-solvent-nonsolvent).[78][79] Additional 2 wt.% $(PMMA)_{188}$-*co*-$(PSPE)_{16.5}$, 2 wt.% $(PMMA)_{139}$-*b*-$(PSPE)_{12.5}$ and 2 wt.% PVP can significantly decrease the thermodynamic stability of the according dope solutions of **Rf1**, **M1.1** and **M1.2**. As shown in **Fig. 47**, **Fig. 48** and **Fig. 49**, all the three membranes **Rf1**, **M1.1** and **M1.2** showed asymmetric cross sections which can be clearly identified as top skin layer and supporting sublayer with macrovoids via onset of initial instantaneous liquid-liquid demixing.[6]

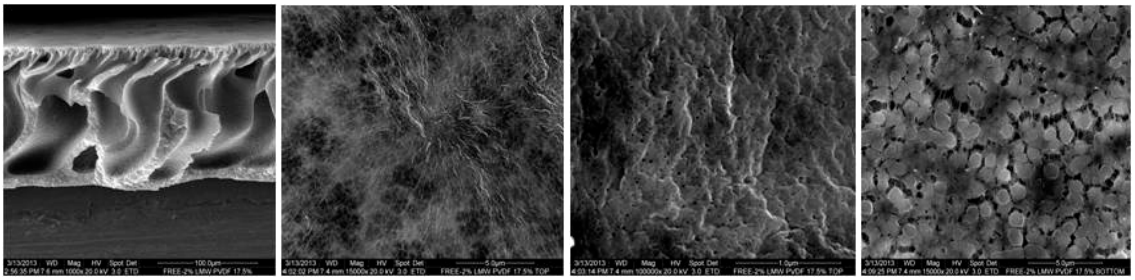

Fig. 47 Membrane **Rf1** (PVP K30 2 wt.%, PVDF 17.5 wt.%). From left to right: Cross section (Mag.1k), top surface (Mag.15k), top surface (Mag.100k), back surface (Mag.15k)

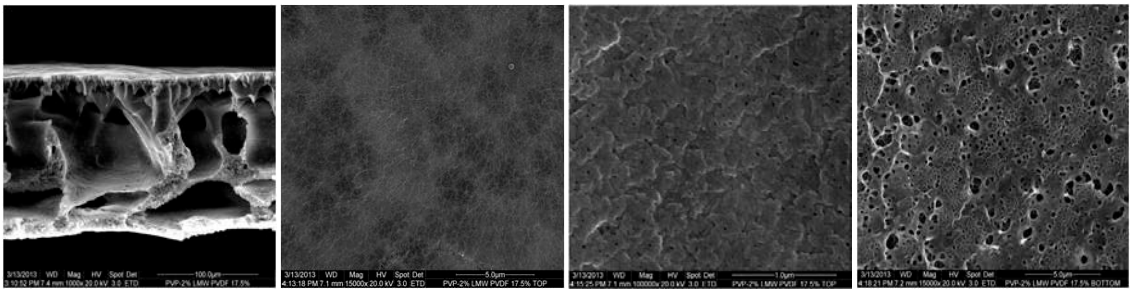

Fig. 48 Membrane **M1.1** ($PMMA_{188}$-*co*-$PSPE_{16.5}$ 2 wt.%, PVDF 17.5 wt.%). From left to right: Cross section (Mag.1k), top surface (Mag.15k), top surface (Mag.100k), back surface (Mag.15k).

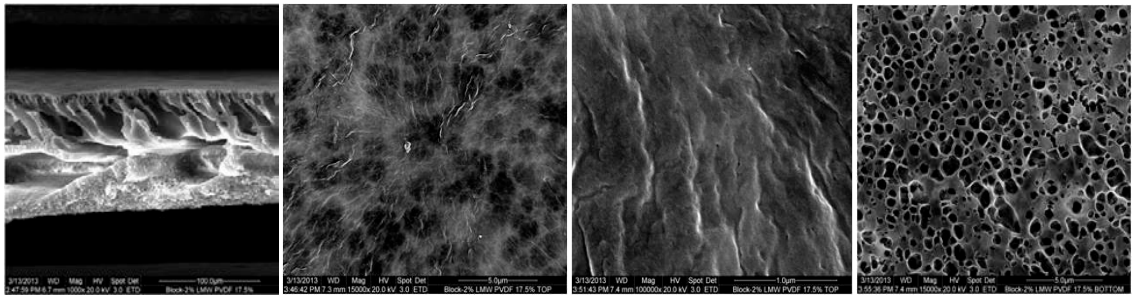

Fig. 49 Membrane **M1.2** ($PMMA_{139}$-*b*-$PSPE_{12.5}$ 2 wt.%, PVDF 17.5 wt.%). From left to right: Cross section (Mag.1k), top surface (Mag.15k), top surface (Mag.100k), back surface (Mag.15k).

For the clear illumination and better insight into morphologies of above membranes, the brief introduction on hypothetical mechanisms of **M1.1** and **M1.2** formation during NIPS was quite necessary to describe as following (formation mechanism of **Rf1**, cf. **2.2.2.**).

In casting film of membrane **M1.1**, additive $PMMA_{188}$-*co*-$PSPE_{16.5}$ was random copolymer composed of statistically distributed PMMA and PSPE segments in molecular chains. PMMA is capable of being thermodynamically compatible with matrix PVDF polymer by the well miscibility between them,[92] whereas zwitterionic PSPE is highly hydrophilic and capable of forming firm

hydration layer (hydrogen-bonding network of water molecules) via strong ionic solvation and electrostatic interaction between negative charged sulfo-betaine groups and positive charged ammonium groups in the pendent side chains of PSPE backbones.[57][58][93] The statistically dispersed PMMA and PSPE segments in copolymer chains behaved respectively as anchor region in matrix PVDF and functional region on the surface of membrane (pores). As aforementioned, after the instantaneous liquid-liquid demixing resulted from the thermodynamic instability of **M1.1** casting solution doping with additive in water coagulation bath, the hydrophilic PSPE-segment-dominated region in $PMMA_{188}$-*co*-$PSPE_{16.5}$ molecular chains were prone to migrate towards the boundary between polymer-rich phase and polymer-lean phase (nonsolvent-riched) via surface segregation which has a trend to minimize the interfacial energy.[40][51][94] Meanwhile, by means of the excellent thermodynamical compatibility with PVDF, the PMMA-segment-dominated region in $PMMA_{188}$-*co*-$PSPE_{16.5}$ molecular chains was still able to be entangled with PVDF chains in the region of polymer-rich phase with proximity to the phase boundary, and tethered the surface-segregated (boundary-segregated) PSPE-segment-dominated region in $PMMA_{188}$-*co*-$PSPE_{16.5}$. Within polymer-lean phase, when contacting with aqueous environment brought by in-flow of nonsolvent water, PSPE groups of PSPE-segment-dominated region which exposed along the boundary of phases, rapidly formed tight hydration shell between the cation and anion. The tightly bound hydration shell of hydrogen bonding network in the zwitterionic exert an negative effect on the mobility and flexibility of PSPE groups which exposed on the phase boundary.[57][75][95] Merely the PMMA segments which were irregularly arrayed in the PSPE-segment-dominated region on the phase boundary gained less effect on the mobility and flexibility. Consequently, as a comprehensive effect, the whole mobility and flexibility of PSPE-segment-dominated region was obviously decreased but remained partly due to the existence of PMMA segments. The each less mobile and flexible PSPE-segment-dominated region can further influence the whole mobility and flexibility of its complete $PMMA_{188}$-*co*-$PSPE_{16.5}$ molecular chains which migrated in the phase boundary. Thus, the formed stiffness of the whole random copolymer chains benefited the reorganization and collapse of PVDF chains of polymer-rich phase and thus the precipitation kinetics of PVDF chains to further result in the suppressed pore structure and macrovoids growth. The less flexibility and mobility of random copolymer chains also enlarged the difficulty of disentanglement between the molecular chains in interfacial region and sublayer to form pores.[83]

In the case of membrane **M1.2** casting film, additive $(PMMA)_{139}$-*b*-$(PSPE)_{12.5}$ was more regular block copolymer comprised relatively hydrophobic PMMA block and highly hydrophilic PSPE block. The PMMA block and PSPE block still played roles of anchor and surface hydrophilic function respectively, depending on their thermodynamic compatibility with PVDF and super

hydrophilicity. In contrast with $(PMMA)_{188}$-*co*-$(PSPE)_{16.5}$, more regularly ordered PMMA and PSPE block in $(PMMA)_{139}$-*b*-$(PSPE)_{12.5}$ were able to donate better stability on the surface, stronger surface migration and surface hydrophilicity during the liquid-liquid demixing process of casting film in coagulation. As aforementioned, after the rapid migration of block copolymer additive chains towards the boundary of polymer-rich phase, the exchange of nonsolvent and solvent gave rise to the rapid formation of tightly bound hydration shell of hydrogen bonding network in the zwitterionic PSPE block which was more compact and denser than hydration shell formed by random zwitterionic copolymer.[57][59] As a consequence, the stronger bound hydration shell of hydrogen bonding network was prone to contribute more powerful limitation on the chain mobility and flexibility of block copolymer chain which segregated on the boundary of polymer-rich phase after liquid-liquid demixing.[75][95][97][98] By the interaction between PMMA block and PVDF chains under boundary of polymer-rich phase, the stiffer block copolymer chains further led to the more facilitated reorganization and collapse of PVDF chains of polymer-rich phase and corresponding precipitation rate of PVDF polymer-rich phase.[83][99] In a word, the formation of interfacial pore structure and macrovoids growth should be more suppressed, compared with membrane **M1.1**.

From SEM, it is quite clear to see that the cross section of **Rf1**, **M1.1** and **M1.2** (**Fig. 47**, **Fig. 48** and **Fig. 49**) displayed the interconnected pores structure and continuous PVDF phase, which indicated that the continuous polymer-lean phase interconnected with continuous polymer-rich phase, and the nucleation and growth process dominated membrane formation after instantaneous liquid-liquid demixing. The top layer of **Rf1** (**Fig. 47**, Top surface, Mag.100k) with quite a few big pores surrounded by a little nodular morphology indicated that the rapid solidification (vitrification) of PVDF on the top layer, which was created by binodal demixing as well as partial spinodal demixing (created by PVP-induced highly in-flow of nonsolvent diffusion) and relatively retarded precipitation rate (PVP additive assistance) in the interfacial region of casting film (cf. **2.2.2.**). The top layer of **M1.1** in **Fig. 48** was smooth and originated fewer big pores, which evidenced the restrained pore-forming by the enhanced stiffness of ionic-solvated copolymer additive chains during the liquid-liquid demixing in the interfacial region of **M1.1** casting film. The top layer of **M1.2** (**Fig. 49**) showed much fewer big pores than **M1.1**, which signified the pore-forming suppression by the enhanced precipitation rate and harder disentanglement of chains due to the much stronger stiffness of ionic-hydrated block copolymer additive chains along the boundary of polymer-rich phase during the liquid-liquid demixing.[83] The wrinkles appeared on the **M1.2** top layer (**Fig. 49**) implied the occurrence of serious shrinkage during the skin layer region formation perhaps because of the relatively decreased amount of in-diffused nonsolvent

with respect to the increased amount of out-diffused solvent which caused by the barrier effect from rapidly solidified top surface of casting film.[83][100]

Strong macrovoids structure of **Rf1** (**Fig. 47**, Cross section) with full growth formed in sublayer underneath the top skin layer, clearly implied the nucleation growth induced by the interfacial instantaneous demixing and the largely decreased precipitation rate led by the involvement of PVP additive (cf. **2.2.2.**).[90] The pear-like shape of macrovoid in **Rf1** also meant, during nucleation period after rapid solidification of top skin layer, the limited amount of nuclei formed and expanded to macrovoids of membrane. The walls between macrovoids were porous (**Fig. 47**, Cross section), which revealed that, during the coarsening process, the coalescence of small droplets of polymer-lean phase for formation of lager macrovoid structure with interconnectivity was possible.[91] The macrovoids structure of **M1.1** (**Fig. 48**) was partly suppressed, which implied the slightly enhanced vitrification of PVDF polymer-rich phase due to the stiffness arisen from the ionic solvated additive chains during the nucleation growth. The porous walls between individual macrovoids structure also indicated the coarsening process the for coalescence of small droplets to form interconnective strucuture in sublayer of **M1.1**.[96] In **M1.2**, the obviously suppressed macrovoids structure underneath the skin layer (**Fig. 49**) strongly supported the highly facilitated precipitation rate of polymer-rich phase during liquid-liquid demixing and nucleation growth due to the largely enhancement of additive chains stiffness. Below the suppressed macrovoids, the apparent formation of a sponge-liked layer (**Fig. 49**) gave a response of the prior rapid precipitation of polymer-rich phase. The further enhanced resistance barrier from solidified thin top surface to the highly suppressed macrovoids (rapid precipitated polymer-rich phase) allowed sharply decreased nonsolvent in-flow to reach the region underneath the suppressed macrovoids.[87] Consequently, the underneath region which was close to the bottom was controlled by the typical delayed liquid-liquid demixing. Thus when the demixing occurred, the excess of polymer concentration led to the formation of sponge-liked layer finally. The porous walls between suppressed macrovoids cells in **M1.2** were more and thicker than ones in **M1.1**, because the better exposure of block copolymer along the polymer-rich phase boundary remarkably decreased the interfacial free energy between polymer-lean phase droplets and thus coalescence of polymer-lean phase droplets which was driven by the minimization of interfacial free energy were inhibited consequently.[81][96]

For **Rf1**, the distance from top of skin layer to the starting points of macrovoid structure was thin, which was strongly evidence that the instantaneous demixing in the interfacial region of casting film resulted in the barrier resistance for diffusion exchanging rate and thus the nucleation and growth of macrovoids (cf. **2.2.2.**). The skin layer of **M1.1** was thin and behaved as barrier

resistance to induce the nucleation formation and growth. Compared with membrane **Rf1** with additive PVP, the decreased water permeability of **M1.1** (cf. **6.1.7.1.**) was consistent in the slightly limited pore-forming and suppressed macrovoids growth resulted from the $PMMA_{188}$-*co*-$PSPE_{16.5}$ additive. Compared with membrane **Rf.1** and **M1.1** with additive PVP and $(PMMA)_{188}$-*co*-$(PSPE)_{16.5}$ respectively, the drastically decreased water permeability of **M1.2** (cf. **6.1.7.1.**) quite evidently verified the suppressed pore-forming as well as macrovoids growth resulted from the $(PMMA)_{139}$-*b*-$(PSPE)_{12.5}$ additive.

16 wt.% PVDF membranes which contained similar ratio of PMMA/PSPE (higher or lower) were prone to display similar morphology. Therefore the typical membrane morphologies with similar ratio of PMMA / PSPE were discussed respectively as following.

In dope solutions of membrane **M1.3** and **M1.6**, additive $PMMA_{300}$-*b*-$PSPE_{36.2}$ (0.5 wt.%) and $PMMA_{300}$-*b*-$PSPE_{45.6}$ (1 wt.%) which had similar and higher ratios of PMMA/PSPE were employed. The general cross section of **M1.3** and **M1.6** (**Fig. 50** and **Fig. 51**) showed the continuous PVDF phase and interconnected pore structures in sublayer as evidence of instantaneous liquid-liquid demixing and nucleation growth mechanism for macrovoids formation. The top surface of **M1.3** and **M1.6** (**Fig. 50** and **Fig. 51**) were smooth and had fewer big pores, and their cross sections both originated the suppressed macrovoids and sponge-liked region near the membrane bottom. The above morphological characters indicated that, in the case of decreased concentration of casting film (16 wt.% PVDF), block copolymer additive with shorter block of PSPE still was able to hamper the pore-forming and macrovoids growth via enough stiffness of block copolymer chains by ionic-hydration which were certified by the low water permeability of **M1.3** and **M1.6** (cf. **6.1.7.2.**). Compared with **M1.2**, **M1.3** and **M1.6** showed relatively enlarged macrovoids, which perhaps resulted from the longer molecular chains (bigger molecular weight) of block copolymer additive in **M1.3** and **M1.6**. With the purpose of minimization of interface (PVDF/water) free energy, the hydrophilic PSPE blocks, dragging the covalent-bound PMMA block, were strongly driven towards the interface of phases (polymer-rich/polymer-lean).[81][96] Even though the $PMMA_m$-*b*-$PSPE_n$ with different molecular weight have no apparent dissimilarity on the polymer surface free energy in casting film, when approaching the interface of phases, the $PMMA_m$-*b*-$PSPE_n$ with bigger molecular weight experienced the bigger conformational entropy penalty during the interface migration than in the bulk. Consequently, in the absence of enthalpic compensation, the $PMMA_m$-*b*-$PSPE_n$ with lower molecular weight gained preferential migration and enrichment on the interface of phases because of lower conformational entropy penalty.[51][101][102] Therefore, in contrast to **M1.2**, **M1.3**

and **M1.6** that contained block copolymer additives with bigger molecular weight presented the cross sections with slightly enhanced growth of macrovoids, which were verified by the apparently increased water permeability of **M1.3** and **M1.6** (cf. **6.1.7.2.**). The morphology of suppressed macrovods of **M1.3** indicated that, even 0.5wt.% block copolymer additive was sufficient to influence the PVDF membrane formation.

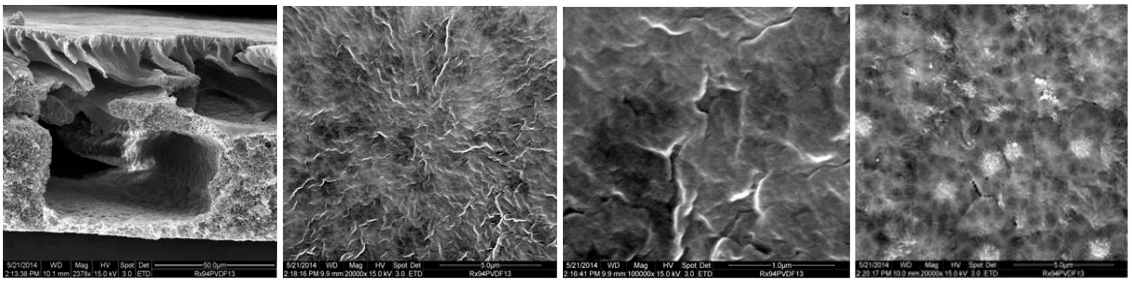

Fig. 50 Membrane **M1.3** ($PMMA_{300}$-*b*-$PSPE_{36.2}$ 0.5 wt.%, PVDF 16 wt.%). From left to right: Cross section (Mag.2k), top surface (Mag.20k), top surface (Mag.100k), back surface (Mag.20k).

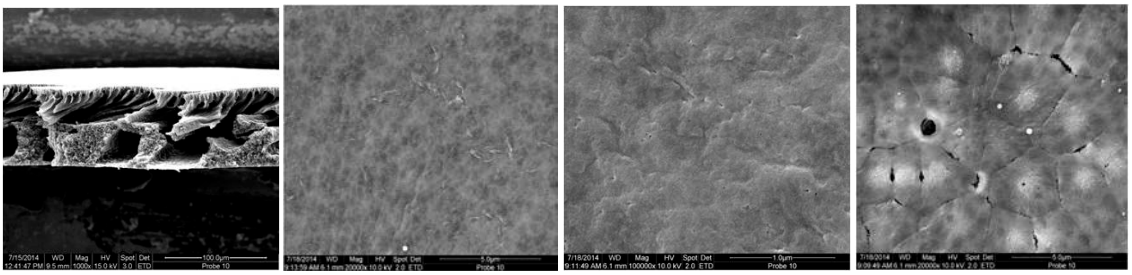

Fig. 51 Membrane **M1.6** ($PMMA_{300}$-*b*-$PSPE_{45.6}$ 1 wt.%, PVDF 16 wt.%). From left to right: Cross section (Mag.1k), top surface (Mag.20k), top surface (Mag.100k), back surface (Mag.20k).

Dope solutions of **M1.7** and **M1.8** contained additive $PMMA_{300}$-*b*-$PSPE_{291.3}$ (1.5 wt.%) and $PMMA_{300}$-*b*-$PSPE_{566}$ (1.5 wt.%) which were made up of same PMMA block as **M1.3** and **M1.6** and much longer PSPE block (bigger molecular weight). Because of the decreased solubility of $PMMA_m$-*b*-$PSPE_n$ with longer PSPE block, the concentration of additive were increased to 1.5 wt.% in order to achieve better exposure of PSPE on the membrane surface. The general cross section of **M1.7** and **M1.8** (**Fig. 52** and **Fig. 53**) were the continuous PVDF phase and presented interconnected pore structures in sublayer, which confirmed the instantaneous liquid-liquid demixing dominant in membrane formation and nucleation growth mechanism for macrovoids formation. The less suppressed macrovoids in the cross sections of **M1.7** and **M1.8** (**Fig. 52** and **Fig. 53**) supported that, additive $PMMA_m$-*b*-$PSPE_n$ with bigger molecular weight (longer PSPE block) was more difficult to migrate towards the phase boundary during liquid-liquid demixing due to the lager conformational entropy penalty and thus the precipitation rate of PVDF in polymer-

rich phase was less enhanced.[103][104] Additionally, the lower solubility of $PMMA_m$-*b*-$PSPE_n$ with bigger molecular weight (longer PSPE block) perhaps was considered as another factor responsible for the decreased additive in bulk and the resultant weakened suppressing effect on macrovoids in **M1.7** and **M1.8**. The top surface of **M1.7** and **M1.8** (**Fig. 52** and **Fig. 53**) generated a few big pores, which also can be regarded as an evidence for the insufficient influence of hydrated block copolymer on the disentanglement of PVDF chains that induced the pore-forming on the membrane surface. In contrast to **M1.2** and **M1.6**, the obviously enhanced water permeability of **M1.7** and **M1.8** (cf. **6.1.7.2.**) strongly supported the above explanations. The wrinkles appeared on the top surface (**Fig. 52** and **Fig. 53**) of **M1.3** and **M1.6** possibly arisen out of the relatively decreased amount of in-diffused nonsolvent versus the increased amount of out-diffused solvent from polymer-rich phase derived from the resistant barrier of rapidly solidified top surface of casting film due to the thermodynamically metastably instantaneous liquid-liquid demixing.[100] Compared with **M1.2**, **M1.3** and **M1.6**, The porous walls between the macrovoids in **M1.7** and **M1.8** became fewer and thinner, which indicated the enhanced coalescence of polymer-lean droplets arisen from increased interfacial free energy between polymer-lean phase droplets caused by the insufficient exposure of copolymer additive with bigger molecular weight.[81]

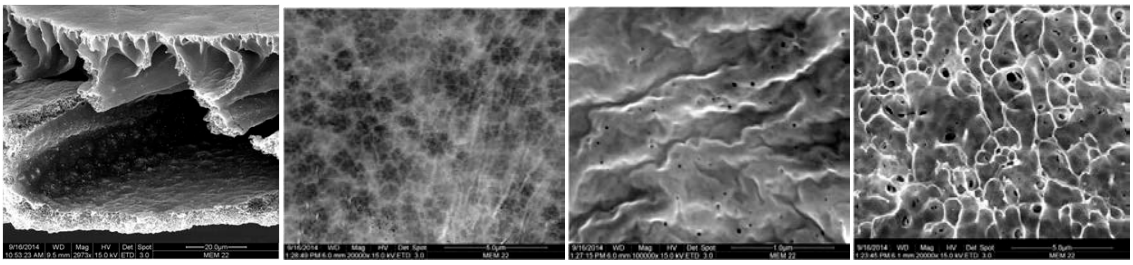

Fig. 52 Membrane **M1.7** ($PMMA_{300}$-*b*-$PSPE_{291.3}$ 1.5 wt.%, PVDF 16 wt.%). From left to right: Cross section (Mag.3k), top surface (Mag.20k), top surface (Mag.100k), back surface (Mag.20k).

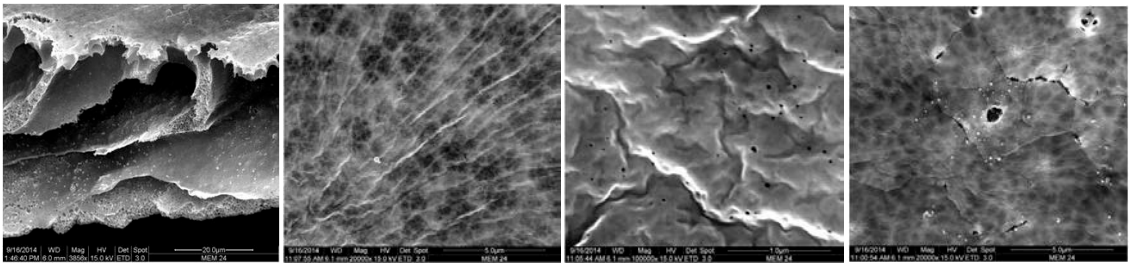

Fig. 53 Membrane **M1.8** ($PMMA_{300}$-*b*-$PSPE_{566}$ 1.5 wt.%, PVDF 16 wt.%). From left to right: Cross section (Mag.3k), top surface (Mag.20k), top surface (Mag.100k), back surface (Mag.20k).

M1.9 also showed the continuous PVDF phase and presented interconnected pore structures in the cross section region (**Fig. 54**) as a result of the instantaneous liquid-liquid demixing. The combined employment of $PMMA_{300}$-*b*-$PSPE_{291.3}$ (1.5 wt.%) and $PMMA_{300}$-*b*-$PSPE_{33.5}$ (1 wt.%) in **M1.9** brought about some apparent changes due to the introduced difference between PSPE block lengths. In contrast to **M1.7** and **M1.8**, the macrovoids of **M1.9** was suppressed and decreased with some sponge-liked formation underneath, whereas the top layer of **M1.9** originated no big pores. Clearly, the involvement of $PMMA_{300}$-*b*-$PSPE_{33.5}$ with lower molecular weight improved the migration of additive chains towards the boundary of polymer-rich phase and thus enhanced the precipitation kinetic of polymer-rich phase. The introduction of $PMMA_m$-*b*-$PSPE_n$ with different PSPE block lengths was capable of providing the stronger surface enrichment of block copolymer additive, which were directly supported by the largely reduced water permeability of **M1.9** (cf. **6.1.7.2.**), compared with **M1.3**, **M1.6**, **M1.7** and **M1.8**. The low molecular weight PSPE block enriched on the surface also can backfill the surface packing defects resulted from the high molecular weight PSPE block and yield better surface packing density of copolymer additives.[59][93] The wrinkles were still remained and signified thermodynamically metastably instantaneous liquid-liquid demixing of top skin layer. The porous walls between the decreased macrovoids cell became more and thicker, which gave a strong indication of neutralized interfacial free energy among polymer-lean phase droplets caused by the improved exposure of copolymer additive with different molecular weights.

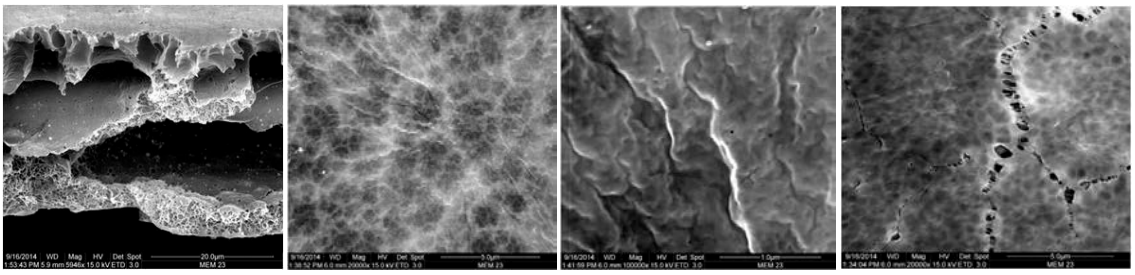

Fig. 54 Membrane **M1.9** ($PMMA_{300}$-*b*-$PSPE_{291.3}$ 1.5 wt.%, $PMMA_{300}$-*b*-$PSPE_{33.5}$ 1 wt.%, PVDF 16wt.%). From left to right: Cross section (Mag.6k), top surface (Mag.20k), top surface (Mag.100k), back surface (Mag.20k).

Dope solutions of **M1.10** and **M1.12** involved $PMMA_{94}$-*b*-$PSPE_{261}$(1 wt.%) and $PMMA_{98}$-*b*-$PSPE_{295}$ (1 wt.%) with long length PSPE block and much shorter PMMA block than block copolymer additives in aforementioned membrane dope solutions. The continuous polymer-lean phase interconnected with continuous polymer-rich phase in cross section of **M1.10** and **M1.12** (**Fig. 55** and **Fig. 56**) undoubtedly supported the nucleation and growth process dominated membrane formation after instantaneous liquid-liquid demixing. Additive for **M1.10** and **M1.12** had similar ratio of PMMA / PSPE, hence the morphology of **M1.10** and **M1.12** was also quite similar.

In the cross section of **M1.10** and **M1.12** (**Fig. 55** and **Fig. 56**), the remarkably suppressed development of macrovoids and appearance of sponge-liked layer near the bottom region potently certified the enhanced precipitation rate of polymer-rich phase as a consequence of adequate stiffness of block copolymer additive chains by ionic-hydration which migrated along the phase boundary.[83] The top layers without distinct big pores (**Fig. 55** and **Fig. 56**) also contributed a good support to the inability of PVDF chains disentanglement led by less flexibility of ionic-hydrated block copolymer chains along the phase boundary.[93] In **M1.10** and **M1.12**, the thickened porous walls between the cells of macrovoids also suggested the decreased interfacial free energy between polymer-lean phase droplets arisen from the sufficent exposure of copolymer additive along the phase boundary.[95] The still remained wrinkles on the top layer pointed out the thermodynamically metastably instantaneous liquid-liquid demixing of top skin layer at the beginning of coagulation and the following delayed demixing process. The greatly decreased water permeability of **M1.10** and **M1.12** (cf. **6.1.7.2.**) were consistent with the suppressed macrovoids and decreased pores in top layer. The $PMMA_{94}$-*b*-$PSPE_{261}$ and $PMMA_{98}$-*b*-$PSPE_{295}$ with much shorter PMMA block and relatively longer PSPE block showed quite typical negative influence on the macrovoid growth and pore formation, which indicated the better surface enrichment of the additives.

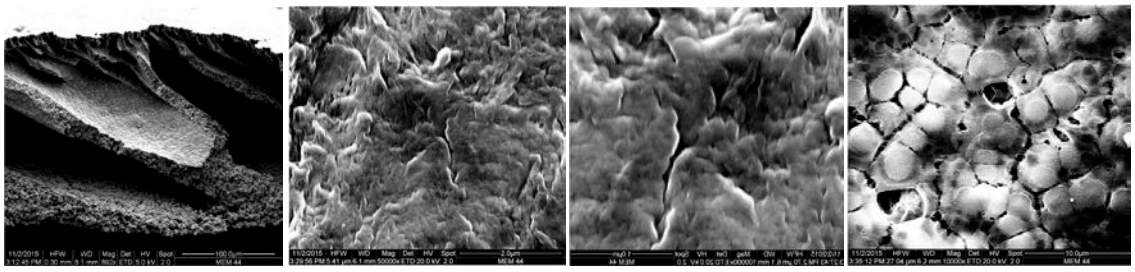

Fig. 55 Membrane **M1.10** ($PMMA_{94}$-*b*-$PSPE_{261}$ 1 wt.%, PVDF 16 wt.%). From left to right: Cross section (Mag.6k), top surface (Mag.50k), top surface (Mag.100k), back surface (Mag.50k).

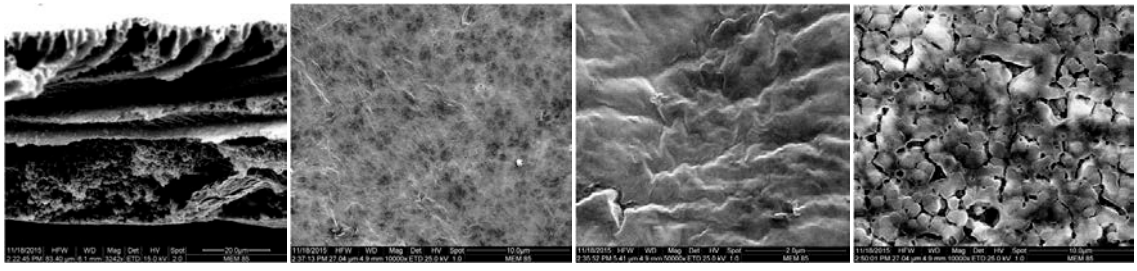

Fig. 56 Membrane **M1.12** ($PMMA_{98}$-*b*-$PSPE_{295}$ 1 wt.%, PVDF 16 wt.%). From left to right: Cross section (Mag.3k), top surface (Mag.10k), top surface (Mag.100k), back surface (Mag.10k).

As a comparable sample, membrane **Rf2** with another type of amphiphilic block copolymer additive $PMMA_{98}$-*b*-$PDMAEMA_{93}$ (1wt.%) also displayed the continuous PVDF phase and presented interconnected pore structures in the cross section region (**Fig. 57**) as a consequence of the instantaneous liquid-liquid demixing. The additive in **Rf2** had similar PMMA block and smaller hydrophilic PDMAEMA block, compared with **M1.10** and **M1.12**. Relying on the low entropy penalty from low molecular weight, $PMMA_{98}$-*b*-$PDMAEMA_{93}$ was able to migrate to the phase boundary favorably during the liquid-liquid demixing course. Consequently, not like $PMMA_m$-*b*-$PSPE_n$, when casting film of **Rf.2** in coagulation at r.t. (under the LCST of PDMAEMA), the hydrophiphilic and expanded PDMAEMA block was capable of remaining the mobility and flexibility of hydrated molecular chains,[105] but the extent of maintenance for chain flexibility and mobility was certainly less than the highly flexible PVP or PEG chains in aqueous environment. Logically, like PVP, the $PMMA_m$-*b*-$PDMAEMA_n$ chains also can behave to disturb re-organization and arrangement of PVDF molecular chains in polymer-rich phase on the top layer and in the sublayer of casting film **Rf.2**. Naturally, as a result of retarded precipitation, lots of distinct big pores on the top layer and less suppressed growth of macrovoids of **Rf.2** (**Fig. 57**) were formed finally. In contrast to **M1.10** and **M1.12**, the substantially enhanced water permeability of **Rf.2** (cf. **6.1.7.2.**) supported the above mentioned explanation on the mechanism of $PMMA_{98}$-*b*-$PDMAEMA_{93}$ influence. But what has to be mentioned is that, in the case of $PMMA_{98}$-*b*-$PDMAEMA_{93}$ with low molecular weight, its ability on improvement of membrane pore-forming and macrovoids growth was not comparable with PVP (K30). Contrary to the aforementioned membranes with various $PMMA_m$-*b*-$PSPE_n$ as additive, in the membrane **Rf.2**, nearly no apparent wrinkles presented on the top surface, which gave an indication of enhanced in-flow diffusion of nonsolvent due to the promoted porosity on the top surface.

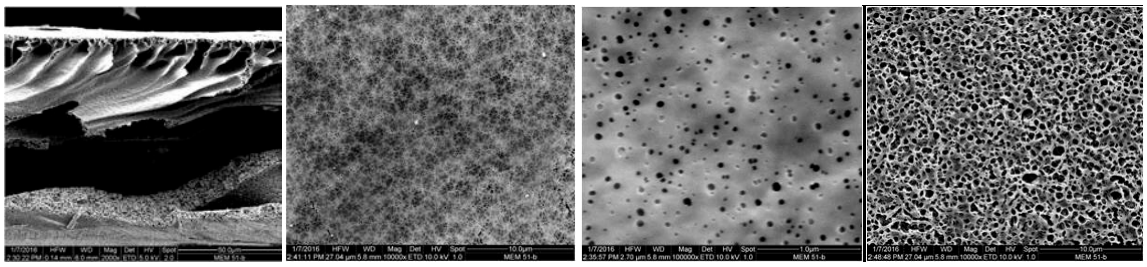

Fig. 57 Membrane **Rf2** ($PMMA_{98}$-*b*-$PDMAEMA_{93}$ 1 wt.%, PVDF 16 wt.%). From left to right: Cross section (Mag.2k), top surface (Mag.10k), top surface (Mag.100k), back surface (Mag.10k).

Dope solutions of control membranes **Rf4** and **Rf8** consisted of 1 wt.% and 3 wt.%PVP (K30) respectively with 16 wt.%PVDF. **Rf4** and **Rf8** both showed the continuous PVDF phase and interconnected pore structures in the regions of cross sections (**Fig. 58** and **Fig. 59**) as an

evidence of the instantaneous liquid-liquid demixing. In the cross section of **Rf.4** and **Rf.8**, the full growth of porous macrovoids (**Fig. 58** and **Fig. 59**) evidently indicated the nucleation growth induced by the interfacial instantaneous demixing and the largely decreased precipitation rate led by the involvement of PVP additive. The top skin layer of **Rf3** and **Rf4** (**Fig. 58** and **Fig. 59**, Top surface 100k) with numerous distinct big pores indicated the rapid solidification (vitrification) of PVDF on the top layer which was created by PVP additive assistance and the relatively retarded precipitation rate of PVDF-rich phase in the interfacial region of casting film. Particularly, the top surface of **Rf.8** (**Fig. 59**) showed the partly nodular morphology that arisen from the quite rapid spinodal demixing of interface region resulted from the higher interfacial polymer concentration due to the 3wt.% additional PVP additive.[81] The distance from the plane of top surface to the onset point of macrovoids in **Rf4** and **Rf8** were also remarkably elongated than the aforementioned membranes with $PMMA_m$-*b*-$PSPE_n$ additives, because the enhanced porosity of top layer in **Rf4** and **Rf8** allowed more in-flow of nonsolvent to diffuse in the deeper sublayer of casting film and thereafter the onset point for the growth of nuclei for polymer-lean phase droplets moved away from the solidified top layer.[86] The macrovoids structure of **Rf.8** was apparently more enlarged than that of **Rf.4**, which can be clearly attributed to the more doping amount of PVP in **Rf.8**. The larger water permeability of **Rf.4** (cf. **6.1.7.2.**) also strongly consistent in the above morphology explanation. In contrast to the aforementioned membranes with $PMMA_m$-*b*-$PSPE_n$, the absence of wrinkles on the top layer of **Rf.4** and **Rf.8** clearly illustrated the relation between the generation of wrinkles and porosity of top layer, the lower in-flow of nonsolvent caused by the higher porosity, the more wrinkles generated on the top surface. The thinner and fewer walls between macrovoids cells in **Rf.4** and **Rf.8** also signified the relatively increased interfacial free energy between the polymer-lean phase droplets due to the instability of entrapment of PVP chains along the phase boundary.

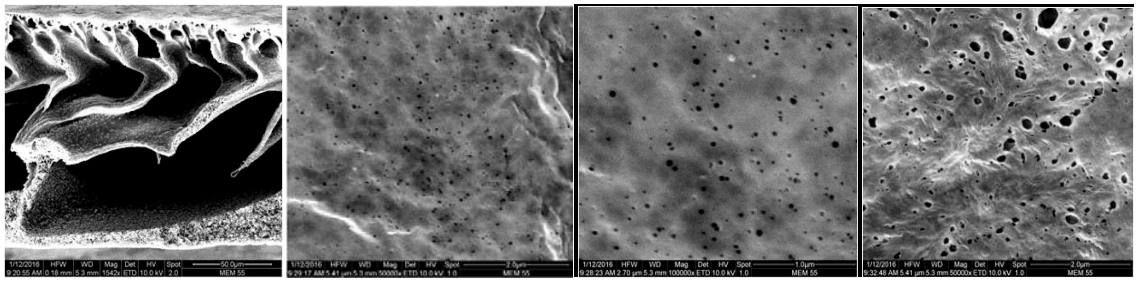

Fig. 58 Membrane **Rf4** (PVP K30 1 wt.%, PVDF 16 wt.%). From left to right: Cross section (Mag.2k), top surface (Mag.50k), top surface (Mag.100k), back surface (Mag.50k).

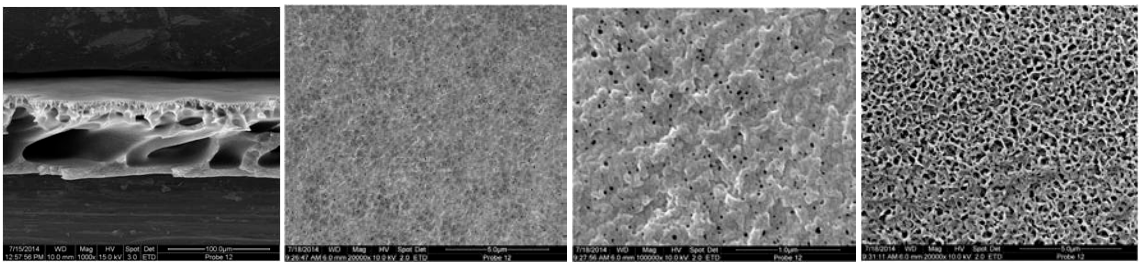

Fig. 59 Membrane **Rf8** (PVP K30 3 wt.%, PVDF 16 wt.%). From left to right: Cross section (Mag.1k), top surface (Mag.20k), top surface (Mag.100k), back surface (Mag.20k).

6.1.4. Contact angle

Water contact angle (CA) is an essential method to investigate the hydrophilicity and wetting nature of material surface. Even though it is difficult to judge the surface property of synthetic porous membrane merely by CA measurement, the relative hydrophilicity and hydrophobicity of polymer membrane samples were also easily available by the surface CA.[106]

Among the membranes that contained 17.5 wt.% PVDF in **Table 15**, **M1.2** that had 2 wt.% $(PMMA)_{139}$-*b*-$(PSPE)_{12.5}$ showed the lowest CA and indicated the strongest surface hydrophilicity, while **Rf1** with 2 wt.% PVP (K30) displayed the highest CA and accordingly the highest surface hydrophobicity. Obviously, depending on the conformational advantage from the regular arrangement of blocks, $(PMMA)_{139}$-*b*-$(PSPE)_{12.5}$ was capable to gain the more successful surface migration and enrichment than statistical copolymer $(PMMA)_{188}$-*co*-$(PSPE)_{16.5}$.[102] Therefore, the super hydrophilic PSPE blocks of $(PMMA)_{139}$-*b*-$(PSPE)_{12.5}$, which were entrapped by PMMA blocks along the surface and pore channel walls, highly improved the surface hydrophilicity of **M1.2** by means of the potent ionic-hydration network of PSPE blocks exposed on the surface.[57] During the membrane dope coagulation, due to the absence of anchor group (block), the surface migration of PVP driven by the low mixing entropy of PVP-PVDF blend brought about the separation of most PVP from PVDF and aggregation of PVP in polymer-lean phase, and finally the removal of PVP by the rinse of water. Therefore, the limited residue of PVP exposed on **Rf1** surface and pore channel walls resulted in the quite poor hydrophilicity.[78] Logically, in the case of **M1.1**, because the PSPE-segment-dominated region of $(PMMA)_{188}$-*co*-$(PSPE)_{16.5}$ chains were possibly exposed on the surface and pore walls, the consequent hydrophilicity brought by the statistically distributed PSPE units remarkably can't be comparable with that from regular PSPE block of $(PMMA)_{139}$-*b*-$(PSPE)_{12.5}$, but still surpassed that from PVP.

Code	Add. wt.%	Add. M_n(g/mol)	Ratio (PMMA/ PSPE)	PVDF Wt.%	[a]Top Contact angle (º)
M1.1	$(PMMA)_{188}$-*co*-$(PSPE)_{16.5}$ 2	23400	11.4	17.5	43±1.6
M1.2	$(PMMA)_{139}$-*b*-$(PSPE)_{12.5}$ 2	17000	11.1	17.5	24±1.0
Rf1	PVP(K30) 2	14000	N/A	17.5	59±1,4
M1.3	$(PMMA)_{300}$-*b*-$(PSPE)_{36.2}$ 0.5	40100	8.3	16	40.5±0.9
M1.4	$(PMMA)_{300}$-*b*-$(PSPE)_{36.4}$ 1	40200	8.3	16	40.4±0.6
M1.5	$(PMMA)_{317}$-*b*-($PSPE)_{25.3}$ 1	36900	12.5	16	36.8±2.4
M1.6	$(PMMA)_{300}$-*b*-$(PSPE)_{45.6}$ 1	42700	6.7	16	36.5±1.2
M1.7	$(PMMA)_{300}$-*b*-($PSPE)_{291.3}$ 1.5	111300	1.0	16	38±1.0
M1.8	$(PMMA)_{300}$-*b*-($PSPE)_{566}$ 1.5	188000	0.5	16	35.8±1.0
M1.9	$(PMMA)_{300}$-*b*-($PSPE)_{291.3}$ 1.5 $(PMMA)_{300}$-*b*-($PSPE)_{33.5}$ 1	111300 39300	1.0 9.1	16	32.8±0.4
M1.10	$(PMMA)_{94}$-*b*-$(PSPE)_{261}$ 1	82300	0.4	16	29.7±2.3
M1.11	$(PMMA)_{94}$-*b*-$(PSPE)_{261}$ 2	82300	0.4	16	30.1±1.6
M1.12	$(PMMA)_{98}$-*b*-$(PSPE)_{295}$ 1	92200	0.3	16	26.9±1.7
Rf2	$(PMMA)_{98}$-*b*-$(PDMAEMA)_{93}$ 1	24500	1.1	16	45.1±2.3
Rf3	PVP(K30) 0.5	14000	N/A	16	55.8±0.9
Rf4	PVP(K30) 1	14000	N/A	16	43.8±2.8
Rf5	PVP(K30) 1	14000	N/A	16	52.1±1.4
Rf6	PVP(K30) 1	14000	N/A	16	40.7±0.7
Rf7	PVP(K30) 1.5	14000	N/A	16	36.7±0.9
Rf8	PVP(K30) 3	14000	N/A	16	27.9±0.6

Table 15 Contact angle values (@r.t.) of PVDF membranes containing PVP, $PMMA_m$-*b*-$PDMAEMA_n$, $PMMA_m$-*co*-$PSPE_n$ or various $PMMA_m$-*b*-$PSPE_n$ with different doping concentrations (wt.%). Method was captive bubble. [a]Only contact angle value of PVDF membrane top surface (functional surface) were showed here.

Membranes **M1.3** to **M1.8** were prepared from the dope solutions that were composed of 16 wt.% PVDF, and respective 0.5 wt.%, 1 wt.%, 1.5 wt.% $PMMA_m$-*b*-$PSPE_n$ with PMMA 30 kg/mol and various ratios of blocks, and they basically presented similarly low CA (around or below 40º) regardless of the additive block ratios or the involving content. This also can be considered as the result of the high hydrophilicity created by the strongly preferential surface migration and exposure of $PMMA_m$-*b*-$PSPE_n$. Compared with **M1.3** to **M1.8**, **M1.9** that involved 16 wt.%PVDF and two different types of $PMMA_m$-*b*-$PSPE_n$ with short and long PSPE block respectively, showed a much lower CA, which can be explained by the reinforced packing density resulted from the

combination of additives with short and long PSPE block distributed along the membrane surface and pore walls.[59]

Membrane **M1.10** to **M1.13** involved 16 wt.%PVDF and respective 1 wt.% and 2 wt.% $PMMA_m$-*b*-$PSPE_n$ with short PMMA block (PMMA 10 kg/mol) and relatively long PSPE block and revealed even much lower CA than that of **M1.3** to **M1.9** which contained long PMMA block (PMMA 30 kg/mol) and relatively short PSPE block. The size of PMMA block might played key role on the surface migration and effective exposure for the enhancement of surface hydrophilicity.

Membranes **Rf2** to **Rf6**, which contained 16 wt.%PVDF and respective 1wt.% PVP (K30) or 1 wt.% $(PMMA)_{98}$-*b*-$(PDMAEMA)_{93}$, basically generated high CA (over 40º) and corresponding less hydrophilicity. In particular, by comparison of CA among **Rf4**, **Rf5** and **Rf6** which were prepared from dope solutions with the same additional content of PVP (K30) (1 wt.%), it can be found that the three membranes showed CA values with relatively large deviation, which apparently evidenced the aforementioned explanation on the loss of PVP during membrane coagulation. Following the increasing content of PVP in dope solution up to 2 wt.% to 3 wt.%, **Rf7** and **Rf8** also displayed the largely decreased CA and relatively enhanced surface hydrophilicity. In addition, the CA decline of **Rf7** and **Rf8** were also partly relative to the highly enhancement of pore size in these two membranes due to the increased content of PVP.[107]

It was also worthy to note that, all the membranes with single 1 wt.% $PMMA_m$-*b*-$PSPE_n$ (**M1.4** to **M1.6**, **M1.10**, **M1.12**) showed lower CA than that of membranes with 1 wt.%PVP (K30) (**Rf4**, **Rf5**, **Rf6**). Moreover, the membrane **M1.3** with single 0.5 wt.% $(PMMA)_{300}$-*b*-$(PSPE)_{36.2}$ also displayed a lower CA than membrane **Rf3** with 0.5 wt.% PVP (K30). It is quite evident that, $PMMA_m$-*b*-$PSPE_n$ was capable of creating higher hydrophilicity than frequently used commercial additive PVP (K30). The CA of all the membranes that contained $PMMA_m$-*b*-$PSPE_n$ with various molecular weight and ratios of PMMA / PSPE in **Table 15** reached or were below 40º, the target CA value of NANOPUR project.

6.1.5. ATR-FTIR spectra

ATR-FTIR is commonly utilized as a nondestructive method to study the chemical composition of membrane skin layer and matrix material for depth profile. Merely the selected typical ATR-FTIR spectra of PVDF membrane with one additive were presented and compared in **Fig. 60**.

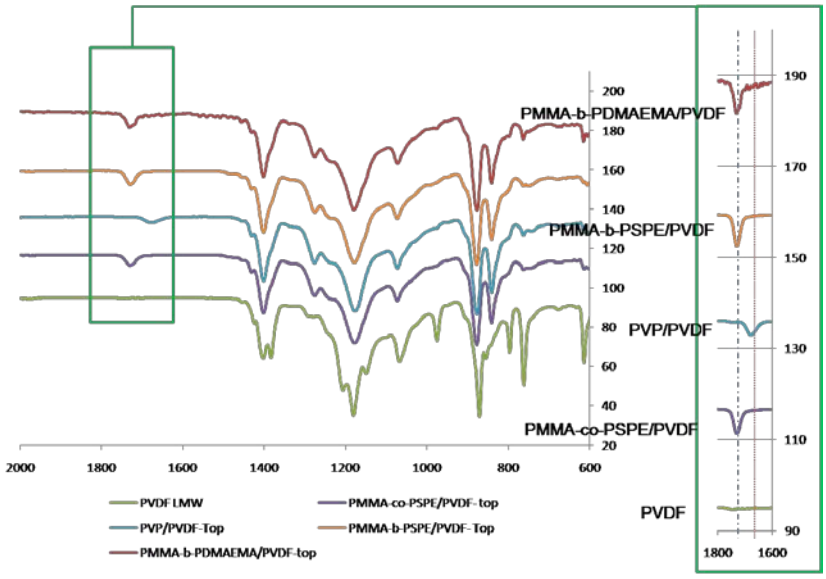

Fig. 60 Comparison of typical ATR-FTIR spectra from top side of pure PVDF membrane and PVDF membranes with $PMMA_m$-*b*-$PDMAEMA_n$, $PMMA_m$-*b*-$PSPE_n$, PVP and $PMMA_m$-*co*-$PSPE_n$. Selected ATR-FTIR spectra were from samples of **Rf2**, **M1.6**, **Rf4** and **M1.1**. The local spectrum between 1600 cm^{-1} and 1800 cm^{-1} was displayed in the frame on the right side.

Since the doping amount of respective additive (1 wt.% $PMMA_m$-*b*-$PSPE_n$, 2 wt.% $PMMA_m$-*co*-$PSPE_n$, 1 wt.% PVP, 1 wt.% $PMMA_m$-*b*-$PDMAEMA_n$) in dope solutions were quite limited compared with the whole content of matrix polymer, the characteristic peaks of their feature groups in additives were somewhat difficult to be identified from the normal ATR-FTIR spectra. In particular, the absorption of S=O (in SO_3^-; 1024-1034 cm^{-1}) from zwitterionic PSPE,[107] as a principal evidence of PSPE exposing on the membrane surface or in the matrix close to membrane surface, were too weak to identify. However, it was fortunate that, the C=O absorption from all the involved additives can be clearly characterized around ~1700 cm^{-1}. Moreover, the C=O absorption from the stretching vibration of carboxylate (1715-1730 cm^{-1}) in copolymer additives and stretching vibration of amide (1650-1660 cm^{-1}) in PVP presented distinctly recognizable difference on wavenumber by comparison of their ATR-FTIR spectra.

In **Fig. 60**, it was clear to see that, pure PVDF membrane showed no any absorption at ~1700 cm^{-1}, whereas the absorption around ~1700 cm^{-1} can be recognized clearly in the spectrum of rest PVDF membranes with various additives. In the further comparison of local spectrum at 1600-1800 cm^{-1}, PVDF membranes with $PMMA_m$-*b*-$PDMAEMA_n$, $PMMA_m$-*co*-$PSPE_n$ and $PMMA_m$-*b*-$PSPE_n$ showed absorption at same wavenumber, while PVDF membrane with PVP displayed absorption at relatively smaller wavenumber. This was completely in agreement with the aforementioned analysis on the different absorption between the stretching vibration of C=O from

carboxylate (1715-1730 cm^{-1}) and amide (1650-1660 cm^{-1}). Because the carboxylate groups were carried by the PMMA, PSPE and PDMAEMA, the successful surface exposure of $PMMA_m$-*b*-$PSPE_n$, $PMMA_m$-*co*-$PSPE_n$ and $PMMA_m$-*b*-$PDMAEMA_n$ in PVDF matrix membrane can be highly confirmed. In the same way, the substantial distribution of PVP on PVDF membrane surface also was verified positively.

6.1.6. XPS

The surface chemical composition of membranes can also be identified by use of XPS qualitatively and quantitatively.

Membrane **Rf4** (16 wt.% PVDF, 1 wt.% PVP) and **M1.6** (16 wt.% PVDF, 1 wt.% $PMMA_{300}$-*b*-$PSPE_{45.6}$) were selected as typical PVDF sample membranes with PVP and $PMMA_m$-*b*-$PSPE_n$ respectively for investigation of XPS. The curve-fitted core-level spectrum of C1s, O1s, F1s, N1s and S2p were identified and characterized respectively from XPS of the above two membranes to ascertain the surface chemical composition and the ratios of key element concentration (N/F, S/F).[109] To focus on the analysis of element concentration ratio, detailed core-level spectrum of C1s, F1s, N1s and S2p were showed in **Fig. 61** to **Fig. 64**.

In **Fig. 61** (left), besides the normal emission signals from PVDF, the emission peaks with binding energy (BE) of 286.2 eV (C-N) and 286.67 eV (C-O), which were not inherent in PVDF, were attributed to the blending additive PVP in PVDF matrix membrane. **Fig. 61** (right) displayed an extra emission peak of 286.63 eV (C-O) that undoubtedly came from the ester moiety of $PMMA_m$-*b*-$PSPE_n$ additive.[110]

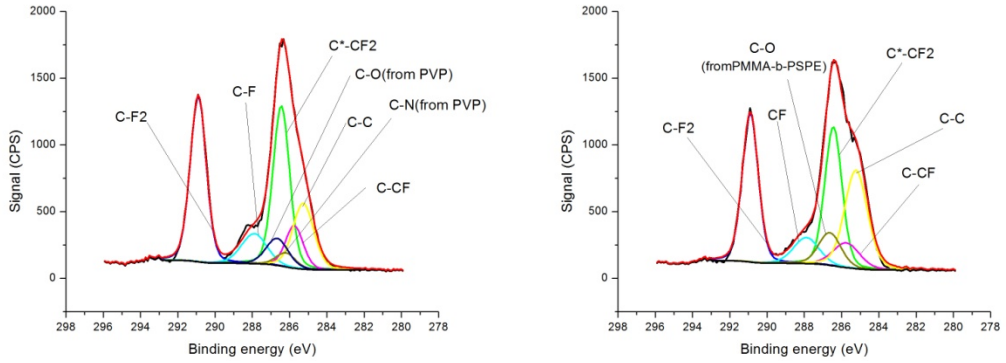

Fig. 61 XPS C1s core level spectrum of PVDF membrane with PVP (left) and PVDF membrane with $PMMA_m$-*b*-$PSPE_n$ (right).

In addition to the difference on the concentration (peak area), the F1s core-level that showed in **Fig. 62** (left and right) were similar and in agreement to F1s core-level of PVDF XPS. Therefore the concentration of fluorine can be considered as the common reference for the further calculation of element concentration ratio.[110]

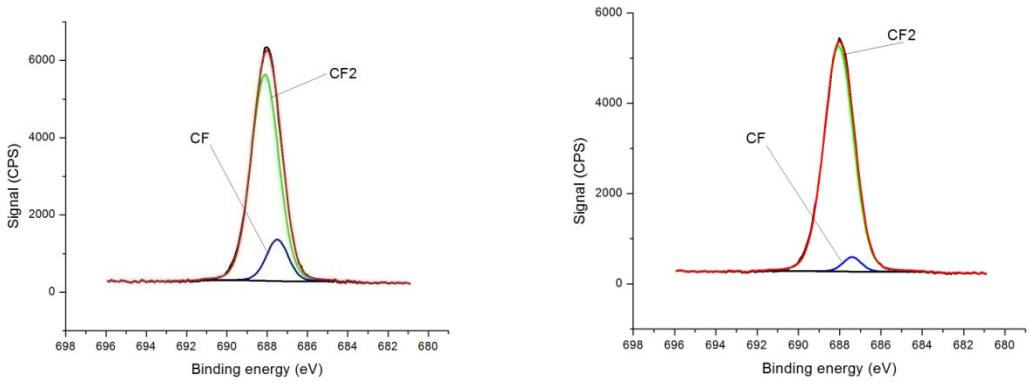

Fig. 62 XPS F1s core level spectrum of PVDF membrane with PVP (left) and PVDF membrane with $PMMA_m$-*b*-$PSPE_n$ (right).

The appearance of emission peak at 400.17 eV in **Fig. 63** (left) clearly indicated the tertiary amine group of PVP and served as strong evidence of surface-distributed PVP additive (residue of NMP solvent perhaps also gave some contribution to the emission peak). In **Fig. 63** (right), aside from emission signal at 400.19 eV, another emission peak at 402.86 eV can be distinctly recognized, which represented the involvement of the quaternary ammonium cation (N+). It can be absolutely affirmative that, the zwitterionic PSPE of $PMMA_m$-*b*-$PSPE_n$ successfully migrated and exposed on the membrane surface due to the identified quaternary ammonium cation (N+) of zwitterionic group. The tertiary amine that appeared in **Fig. 63** (right) was possibly the residue of NMP solvent.[109][110][111] Comparing with intensity of tertiary amine group in **Fig. 63** (left), the intensities of the quaternary ammonium cation (N+) and NMP residue in **Fig. 63** (right) were quite low (relative to the base line of noise), which also can indirectly support that the contribution of PVP to the intensity of tertiary amine group was much greater than NMP residue in **Fig. 63** (left).

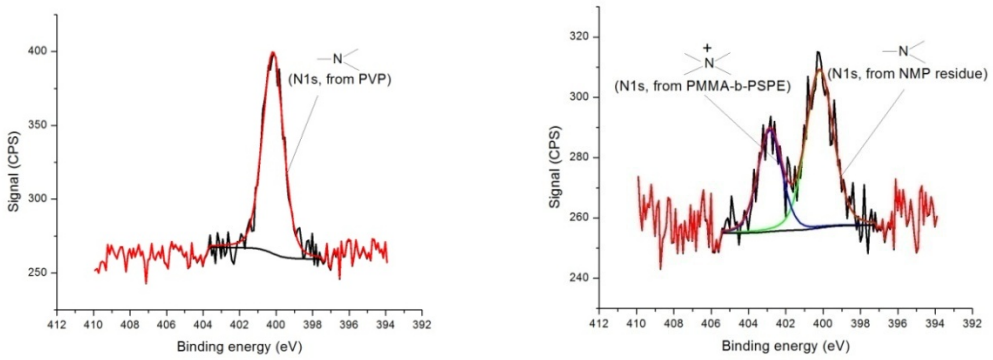

Fig. 63 XPS N1s core level spectrum of PVDF membrane with PVP (left) and PVDF membrane with $PMMA_m$-*b*-$PSPE_n$ (right).

The PVDF/PVP membrane showed no any emission signal of S2p on the surface in **Fig. 64** (left), whereas S2p emission peaks that belonged to zwitterionic PSPE and were evidently revealed at 167.95 eV and 169.15 eV in **Fig. 64** (right), further strongly supported the successful exposure of $PMMA_m$-*b*-$PSPE_n$ on the surface of PVDF matrix membrane.[111]

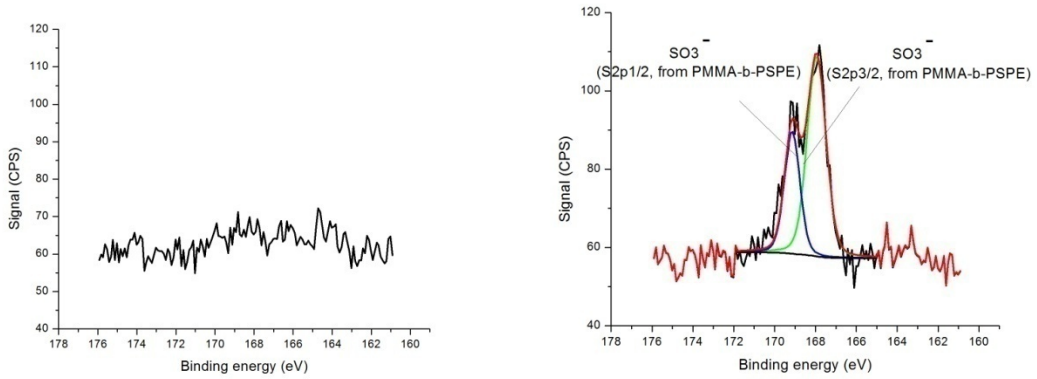

Fig. 64 XPS S2p core level spectrum of PVDF membrane with PVP (left) and PVDF membrane with $PMMA_m$-*b*-$PSPE_n$ (right).

As showed in **Table 16**, regarding the PVP/PVDF membrane, the actual N/F was higher than the theoretical N/F, which clearly signified that, during the demixing and migration towards polymer-lean phase, partial PVP can be entrapped on/along the phase interface and after solidification some PVP residue offered enrichment on the membrane surface, including pore channel interside. In the case of $PMMA_m$-*b*-$PSPE_n$/PVDF membrane, both the actual values of N/F and S/F were much higher, compared with theoretical ones, which firmly determined the remarkably preferential

surface migration of $PMMA_m$-*b*-$PSPE_n$ in PVDF matrix membrane. In order to minimize the interface energy between PVDF casting film and coagulation water bath, thermodynamically, the super hydrophilic PSPE block potently migrated toward the phase boundary from polymer-rich phase and anchored by the PMMA block along the phase boundary until the solidification occurred. Consequently, the following enrichment of PSPE on the membrane surface and pore channel interside was well realized and characterized.

Membrane samples	N/F (theory)	N/F (actual)	S/F (theory)	S/F (actual)
PVDF/PVP (**Rf4**)	0.018	0.052	N/A	N/A
PVDF/ PMMA-b-PSPE (**M1.6**)	0.005	0.013	0.005	0.014

Table 16 Element concentration ratios (theoretical and actual) of nitrogen / fluorine and sulfur / fluorine for PVDF membrane with PVP and PVDF membrane with $PMMA_m$-*b*-$PSPE_n$.

6.1.7. Membrane performance

6.1.7.1. PVDF membranes with 17.5 wt.% PVDF and 2 wt.% single additive

The internal capillary channels of porous membrane can be characterized by measurement of water flux through the membrane at a constant pressure.[6] The pure water permeability (PWP) of **M1.1**, **M1.2** and **Rf1** were firstly characterized as an evaluation of membrane porosity.

Code	Add. wt.%	Add. M_n(g/mol)	Ratio (PMMA/ PSPE)	PVDF wt.%	[a]Water permeability ($L \cdot h^{-1} \cdot m^{-2} \cdot bar^{-1}$)	BSA Rejection (%)
M1.1	$(PMMA)_{188}$-*co*-$(PSPE)_{16.5}$ 2	23400	11.4	17.5	412.9±13.4	85.3±0.1
M1.2	$(PMMA)_{139}$-*b*-$(PSPE)_{12.5}$ 2	17000	11.1	17.5	89.6±5.1	96.6±0
Rf1	PVP(K30) 2	14000	N/A	17.5	729.6±26.7	59.3±0.2

Table 17 Water permeability and BSA rejection at r.t. of PVDF (17.5 wt.%) membranes containing $PMMA_m$-*co*-$PSPE_n$, $PMMA_m$-*b*-$PSPE_n$ and PVP respectively. BSA concentration was 1 mg/ml; pH value of BSA buffer solution fixed at 7.0. [a]Water permeability and BSA rejection were measured after compaction process.

As seen in **Table 17**, **Rf1** with 2 wt.% PVP showed the highest PWP, whilst **M1.1** and **M1.2** which contained 2 wt.% zwitterionic copolymer additive displayed apparently decreased PWP. In contrast to **M1.1**, **M1.2** with block copolymer additive even revealed the much lower PWP. The above results were quite consistent in the aforementtioned analysis of SEM morphology for these

three membranes (cf. **6.1.3.**). The hydrophilic PVP had preferential motivation towards aqueous environment to the interphase boundary between the polymer-rich phase and polymer-lean phase during liquid-liquid demixing and retarded the precipitation kinetic of polymer-rich phase.[83] Consequently the relatively extended vitrification of polymer-rich phase allowed for the more coalescence and growth of polymer-lean phase on the top layer as well as sublayer and rendered the formation of porous surface and macrovoids structure which offered the highly enlarged water permeability of **Rf1**. The partially distributed PVP that entrapped on the surface of **Rf1** also was helpful to improve the hydrophilicity of PVDF matrix membrane and enhance the hydraulic affinity and thus PWP.[90] In the case of zwitterionic copolymer additives, as described in **6.1.3.**, the lack of mobility and flexibility in ionic-hydrated PSPE side chains after surface migration and exposure along the interphase boundary largely facilitated the rearrangement of polymer chains and therefore promoted the precipitation rate to suppress the growth of polymer-lean phase on the top layer and sublayer.[95] As a result, the PWP of **M1.2** was evidently decreased compared with **Rf1** and **M1.1**. The narrowing of internal pore channel that arisen from the swelling of hydrophilic PSPE after contacting with hydraulic flux also can be regarded as another factor for reduction of water permeability for **M1.2**.[80] Relying on the extra mobility and flexibility of chains brought by the randomly distributed PMMA segment in $PMMA_m$-*co*-$PSPE_n$ chains, the precipitation rate of matrix polymer wasn't promoted to a high extent. Hence the **M1.1** formed more porosity of surface and developed macrovoids than **M1.2**, which gave the contribution to the higher PWP.

Thanks to the strong relation between solute rejection and pore size distribution of membrane, solute rejection measurements is widely-applied to characterize membrane performance, especially for ultrafiltration membrane, in industrial assessment.[6][8] Herein Bovine serum albumin (BSA) was selected as macromolecular solute for sieving investigation in consideration of the excellent stability of BSA in buffer solution and its well-defined radius (M_w= 69 KDa, prolate ellipsoid dimensions: 140 × 40 × 40 Å) from the stable globular structure of molecule led by the strong intramolecular hydrogen bonding interactions.[6][112] In addition, considering the substantial adsorption between protein and hydrophobic PVDF matrix membrane,[113] filtration of BSA solution also can give some preliminary evaluation on the protein-fouling resistance of tested membranes. The pH value of BSA solution was remained at 7.0±0.05 and thus negative-charged (isoelectric point of BSA at r.t.: pH= 4.7) in order to avoid the electrostatic interaction because the matrix PVDF membranes surface normally was also negative-charged.[114] The initial flux for BSA filtration were set at 50 $L \cdot h^{-1} \cdot m^{-2}$ for the purpose of minimizing the concentration polarization (CP) at corresponding lower transmembrane pressure (TMP).[115] Moreover the increased extensional shear force from relative high TMP also can deform the BSA conformation and further reduce the hydrodynamic diameter of BSA molecules to cause more blocking of membrane intra channels

and sharp fouling by more penetration of BSA through the membrane pores.[112] Besides, the relative high stirrer rotation rate (e.g. 300 rpm used this work) also can offer strong turbulence in dead-end setting-up to further lessen the disturbance from CP phenomenon during filtration process.[8]

As clearly seen in **Table 17**, after BSA filtration at low TMP, **Rf1** with commercial PVP showed quite low BSA rejection, which indicated that, based on the size-sieving mechanism, the average surface pore size of **Rf1** was too big to sieve globular BSA molecules and displayed low selectivity towards BSA protein.[6] **M1.1** and **M1.2** respectively revealed high BSA rejection and signified the apparently narrowed pore size corresponding to the largely improved barrier selectivity for BSA protein.[6] In contrast to **M1.1**, the basically complete BSA rejection of **M1.2** implied that, the zwitterionic block copolymer additive exerted more control on the adjustment of pore formation on membrane top layer. The SEM morphology (cf. **6.1.3.**) of top layer for **M1.1**, **M1.2** and **Rf1** were also well in line with the observed BSA rejection results. Compared with **Rf1** that showed bigger pore size, pores with relatively smaller average size comparable to the BSA molecule diameter distributed in top layer of **M1.2** and **M1.1** effectively sieved most of the BSA protein under tested solution concentration (1 mg/ml). The improved hydrophilicity of membrane surface and internal pore walls also played an important role for achieving the high BSA rejection because protein molecules needed to overcome more energy barrier to expel the hydration layer in order to obtain contact with surface of membrane as well as internal pores for the following adsorption.[57][113][116] In view of the membrane surface property that characterized by aforementioned contact angle, XPS and ATR-FTIR, it is quite logic that the largely enhanced surface hydrophilicity of **M1.1** and **M1.2** also donated more positive effects on the higher BSA rejection due to the correspondingly improved fouling resistance, compared with **Rf1** that showed relatively lower surface hydrophilicity.

As seen in **Fig. 65**, regarding **M1.1**, **M1.2** and **Rf1**, a relationship of trade-off between water permeability and BSA rejection was clearly presented.[11][12] Membrane (**M1.2**) with high separation selectivity for BSA showed relatively low water permeability, whereas membrane (**Rf1**) with low separation selectivity for BSA yielded high water permeability. **M1.1** with moderate BSA retention corresponded to the water permeability in the middle. The minimization of trade-off between permeability and separation selectivity is regarded as a key factor for ideal UF membrane with high product retention and high filtration rate (proper pore size and improved permeability).[117]

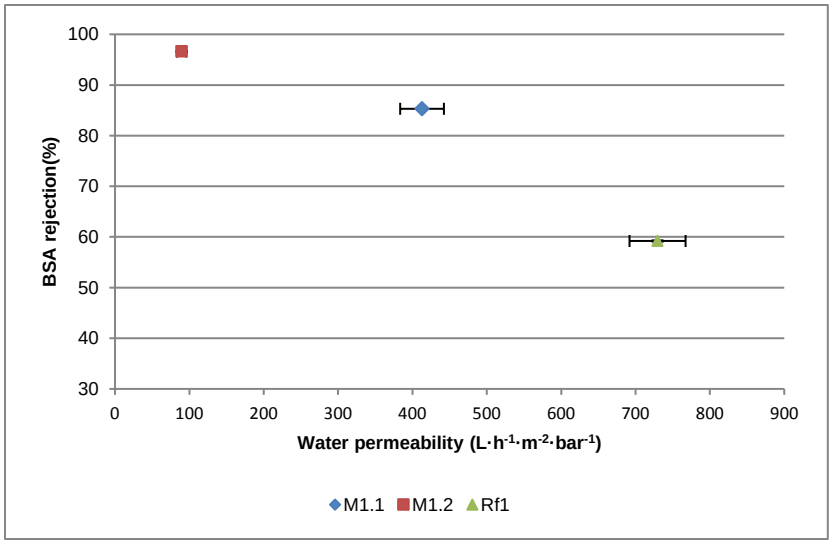

Fig. 65 BSA rejection as a function of water permeability for **M1.1**, **M1.2** and **Rf1**.

During ultrafiltration process, the increased UF membrane fouling caused by the adsorption of macromolecules (e.g. protein) on membrane surface and internal pore walls also can give considerable contribution to the high rejection of solute.[8][118] To further investigate the extent of membrane fouling during BSA filtration, the relative flux reduction (RFR) percentage and water permeability before and after BSA filtration for **Rf1**, **M1.1** and **M1.2** were compared in **Fig. 66**. All the UF membranes in **Fig. 66** showed decreased water permeability after BSA filtration to different extents, which clearly indicated that adsorptive fouling of BSA protein occurred in all the three types of membranes with different degree. It is can be seen clearly by comparison of RFR percentage that, **Rf1** displayed the biggest flux reduction (30.4%) whilst **M1.2** showed considerably small difference on flux decline (6.4%), **M1.1** exhibited the moderate flux reduction (17.3%) as aforementioned order of BSA rejection (all the ultrafiltration performed at initial flux 50 $L \cdot h^{-1} \cdot m^{-2}$). During the filtration, the adsorptive fouling normally occurred at the beginning of improved solute-membrane interaction dominated by the hydrophobicity of matrix membrane polymer,[119] including the deposition of solute molecules on membrane surface and internal pore walls, which incurred the drop of filtration flux.[118] The following formation of gel layer and even cake layer caused by the strong solute-solute interaction on the membrane surface and narrowing of internal pores created the further decline of filtration flux.[6][118][120] After BSA filtration, plenty of BSA molecules deposited on the surface and along the internal pore walls of **Rf1** due to the less hydrophilicity and big surface pores, which directly resulted in the formation of BSA gel layer on the **Rf1** surface and the narrowed internal pore channels, even pore-plugging to some extent.[117] The gel layer largely decreased porosity in top layer, while the narrowed pore channels also led to considerably change of the membrane surface hydrodynamic and highly decreased

water flux through membrane.[8][120] Consequently, **Rf1** showed the quite high RFR after BSA filtration.

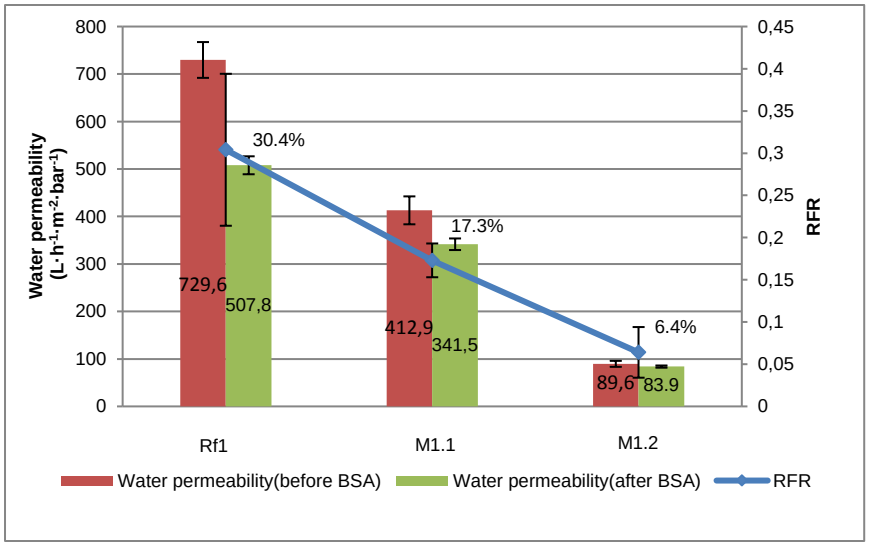

Fig. 66 Relative flux reduction (RFR) and comparison of water permeability (before & after BSA filtration) for **Rf1**, **M1.1** and **M1.2**.

Depending on the lower mean pore size, **M1.2** was capable of sieving almost completely BSA molecules basically out of the pore opening and prevented the BSA globular molecules from permeating into the pore channels. Last but not least, during BSA filtration, the ionic-hydrated PSPE blocks that enriched on **M1.2** surface and along the internal pore walls gave rise to the hydrogen-bonding network of water molecules similar to natural bulk water.[57] The hydration layer composed of overlapped hydrogen-bonding network of water functionalized as energy barrier against the invasion of protein molecules that approached the membrane surface or pore walls during filtration, because the disruption and replacement of this hydrogen-bonding network of water cost high free energy and loss of osmotic pressure entropy.[57][58] As a result, BSA protein that approached the **M1.2** surface (or internal wall of pores with bigger size comparable to BSA molecule diameter) met quite strong resistance arisen from the hydrophilic PSPE blocks on the surface as well as along the pore walls. Consequently the adsorptive fouling caused by BSA deposition on the **M1.2** surface and resultant pore blocking were diminished largely, which was reflected apparently in the low RFR of **M1.2**.

In comparison to **Rf1** and **M1.2**, **M1.1** showed moderate pore size that also can realize the sieving of the majority of BSA in feed as already showed high BSA rejection (85.3%). However the permeated flux through membrane still can carry part of BSA molecules to pass the bigger pores and form the deposition along the pore walls to some extent. Because the PSPE-segment-

dominated region that exposed on membrane surface and along internal pore walls inevitably had randomly distributed PMMA segments, the whole packing density of PSPE and conformation of hydrated PSPE layer were less optimized, compared with the integral PSPE block on **M1.2** surface and pore walls. Therefore the more amplified BSA deposition and adsorption was prone to occur on surface and internal pore walls of **M1.1** than that of **M1.2**, which resulted in slight gel layer on membrane surface and pore narrowing as evidenced finally by the higher RFR of **M1.1** than that of **M1.2**.

The behavior of BSA ultrafiltration for membrane **Rf1**, **M1.1** and **M1.2** were further investigated in term of normalized flux (ratio of BSA filtration flux / corresponding initial water flux), as shown in **Fig. 67**. It can be clearly seen that, during BSA ultrafiltration, filtration flux of **Rf1** showed a higher rate of flux decline than that of **M1.1** and **M1.2**. Particularly, in the period of 0-5 min and 25-30 min during BSA filtration, the drop rate of **Rf1** flux were much higher (steeper trendline) than that of **Rf1** flux in other time during BSA filtration. During the period of 0-5 min, the bigger pore size of **Rf1** relative to BSA molecule diameter created more contact between BSA and inner walls of pores when filtration flux passed through **Rf1** pores. Consequently, due to the less surface hydrophilicity of **Rf1**, the pore narrowing and even pore-plugging to some extent caused by the deposition and adsorption of BSA molecules via solute-membrane contact occurred in **Rf1** and led to the sharp decline of filtration flux rate.[118] Then from 5min to 25 min during BSA ultrafiltration, the filtration flux of **Rf1** still kept decreasing but the decline rate became lower than before. During the period of 25-30 min, due to pronounced reduction of permeating BSA arisen from pore narrowing and pore-plugging, the gradually magnified deposition and adsorption of BSA on **Rf1** surface and pore mouth yielded a gel layer, subsequently even slight cake layer, which behaved as a second membrane and further gave out another noticeable decline of filtration flux. Concentration polarization (CP) also offered some secondary contribution on the flux decline.[6]

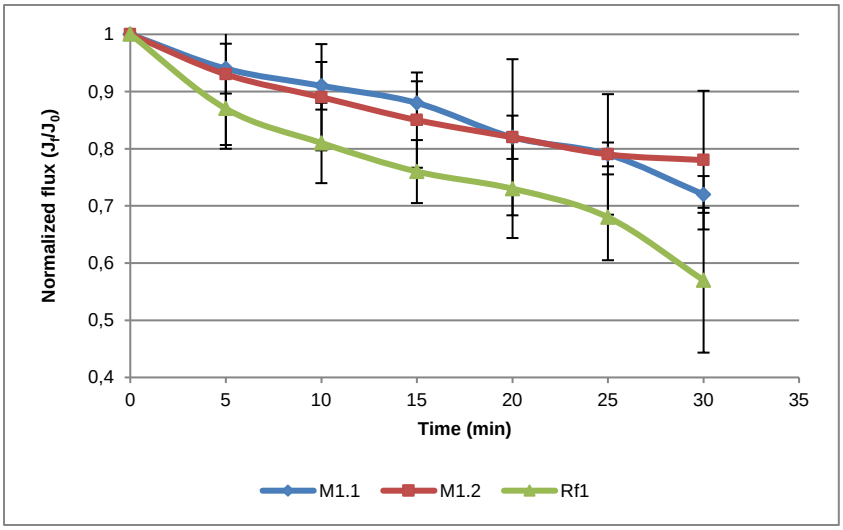

Fig. 67 Normalized flux during ultrafiltration of BSA solution (1 mg/ml in PBS buffer, pH= 7.0) for membrane **Rf1**, **M1.1** and **M1.2** during 30min period; $\mathbf{J_0}$ was at an initial flux of 50 $L \cdot h^{-1} \cdot m^{-2}$; $\mathbf{J_f}$ was BSA filtration flux calculated by the gravity of permeated solution every 5 min.

In general **M1.1** and **M1.2** showed much lower rate of filtration flux decline compared with **Rf1**, and in particular, **M1.2** remained the highest ratio of J_f/J_0 (~0.8) in the end of BSA ultrafiltration. As aforementioned, during BSA ultrafiltration, the smaller pore size of **M1.1** and **M1.2** relative to BSA molecule diameter offered high sieving on BSA molecules and kept most of BSA protein solute away from membrane inner pores. The rejected BSA molecules around membrane surface and pore mouth accumulated and largely enhanced the local BSA concentration and formed the boundary layer.[8] Consequently, the strong CP brought by the high BSA rejection dominated the initial flux decline of **M1.1** and **M1.2**.[121] Even though the super hydrophilic PSPE that exposed on surface of **M1.1** and **M1.2** offered strong resistance on BSA fouling, complete removal of BSA adsorption was still difficult and the local BSA adsorption on surface and slight pore narrowing as well as pore blocking should certainly occur, which formed the driven force to keep the further but slow decline of filtration flux of **M1.1** and **M1.2**. It is interesting to note that, during the period of 25-30 min, **M1.1** showed quite higher rate of flux decline (much steeper trendline) compared with that of **M1.2**. The difference on resistance of adsorptive between **M1.1** and **M1.2** perhaps can give an explanation. Because of the relatively decreased resistance for BSA adsorption, **M1.1** was more prone to accumulate a slight gel layer on the surface and in the same time had more occurrence of pore blocking in contrast to **M1.2**. Therefore, filtration flux of **M1.1** further dropped sharply from 25 min to 30 min during BSA filtration.

6.1.7.2. PVDF membranes with 16 wt.% PVDF and single additive

In general, all the 16 wt.% PVDF membranes with one additive in **Table 18** showed various water permeability and different BSA rejection. All the listed membranes with 0.5-3 wt.% PVP (**Rf3** to **Rf8**) displayed the quite high water permeability (WP) but decreased BSA rejection, while all the membranes with 1 wt.% $PMMA_m$-*b*-$PSPE_n$ demonstrated relatively low WP but basically complete separation of BSA (**M1.4** to **M1.12**, except **M1.3** that contained 0.5 wt% block copolymer additive). The different additives still played significant roles to determine the dissimilar properties of above membranes.[122]

Code	Add. wt.%	Add. M_n(g/mol)	Ratio (PMMA/ PSPE)	PVDF wt.%	[a]Water permeability ($L \cdot h^{-1} \cdot m^{-2} \cdot bar^{-1}$)	BSA rejection (%)
M1.3	$(PMMA)_{300}$-*b*-$(PSPE)_{36.2}$ 0.5	40100	8.3	16	197.2±16.8	76.0±0
M1.4	$(PMMA)_{300}$-*b*-$(PSPE)_{36.4}$ 1	40200	8.3	16	92.8±1.7	93.5±0
M1.5	$(PMMA)_{317}$-*b*-$(PSPE)_{25.3}$ 1	36900	12.5	16	85.1±7.6	95.3±3.4
M1.6	$(PMMA)_{300}$-*b*-$(PSPE)_{45.6}$ 1	42700	6.7	16	110.9±8.2	93.3±0.01
M1.7	$(PMMA)_{300}$-*b*-$(PSPE)_{291.3}$ 1.5	111300	1.0	16	145.7±0.8	91.5±0
M1.8	$(PMMA)_{300}$-*b*-$(PSPE)_{566}$ 1.5	188000	0.5	16	106.6±10.1	94.3±0
M1.9	$(PMMA)_{300}$-*b*-$(PSPE)_{291.3}$ 1.5 $(PMMA)_{300}$-*b*-$(PSPE)_{33.5}$ 1	111300 39300	1.0 9.1	16	46.5±16.8	94.0±0
M1.10	$(PMMA)_{94}$-*b*-$(PSPE)_{261}$ 1	82300	0.4	16	46.0±0	93±0.1
M1.11	$(PMMA)_{94}$-*b*-$(PSPE)_{261}$ 2	82300	0.4	16	52.8±8.1	92±0.1
M1.12	$(PMMA)_{98}$-*b*-$(PSPE)_{295}$ 1	92200	0.3	16	42.0±11.0	100±0
Rf2	$(PMMA)_{98}$-*b*-$(PDMAEMA)_{93}$ 1	24500	1.1	16	120.8±0.9	90±0.0
Rf3	PVP(K30) 0.5	14000	N/A	16	1030±23.9	17.3±0
Rf4	PVP(K30) 1	14000	N/A	16	562.2±91.4	76.5±0.5
Rf5	PVP(K30) 1	14000	N/A	16	506.4±37.2	80.7±0.2
Rf6	PVP(K30) 1	14000	N/A	16	305.3±2.4	82.9±0.1
Rf7	PVP(K30) 1.5	14000	N/A	16	1868.3±381.1	66.0±2.3
Rf8	PVP(K30) 3	14000	N/A	16	1941.3±486.0	52.1±0.2

Table 18 Water permeability and BSA rejection at r.t. of PVDF membranes containing PVP, $PMMA_m$-*b*-$PDMAEMA_n$ and various $PMMA_m$-*b*-$PSPE_n$ with different doping concentrations respectively. BSA concentration was 1mg/ml; pH value of BSA buffer solution fixed at 7.0. [a]Water permeability and BSA rejection were measured after compaction process.

To further effectively investigate the detailed mechanism of the different membrane performance, the relationship of viscosity vs. WP and WP vs. BSA rejection for all the examined membranes in **Table 18** were respectively plotted in **Fig. 68** and **Fig. 69**. Viscosity of dope solution normally is regarded as an critical parameter for the formation of membrane morphology and corresponding permeability prepared via nonsolvent induced phase inversion process (NIPS).[76] Highly increased viscosity of dope solution can apparently slow down the mutual diffusion rate between solvent and nonsolvent during coagulation and thus result in the delayed demixing as well as changed precipitation kinetics. Consequently, the top layer with decline of pore size as well as porosity and the suppressed growth of macrovoid with poor interconnectivity were finally originated.[124] As showed in **Fig. 68**, **Rf3**-**Rf6** with 0.5-1 wt.% PVP showed quite clear effect of increased dope solution viscosity on the formed WP. Following the increment of dope viscosity from 0.99 to 2.30 Pa.s (viscosity data, cf. **6.1.2.**), WP of **Rf3**-**Rf6** gradually decreased from 1030 to 305 $L \cdot h^{-1} \cdot m^{-2} \cdot bar^{-1}$. Nevertheless, **Rf7** and **Rf8** with 1.5 wt.% and 3 wt.% PVP displayed quite high viscosity but still remarkably huge WP, which can be reasonably explained as the reinforced pore-forming effect of increased PVP content that prevailed over effect of enhanced viscosity.

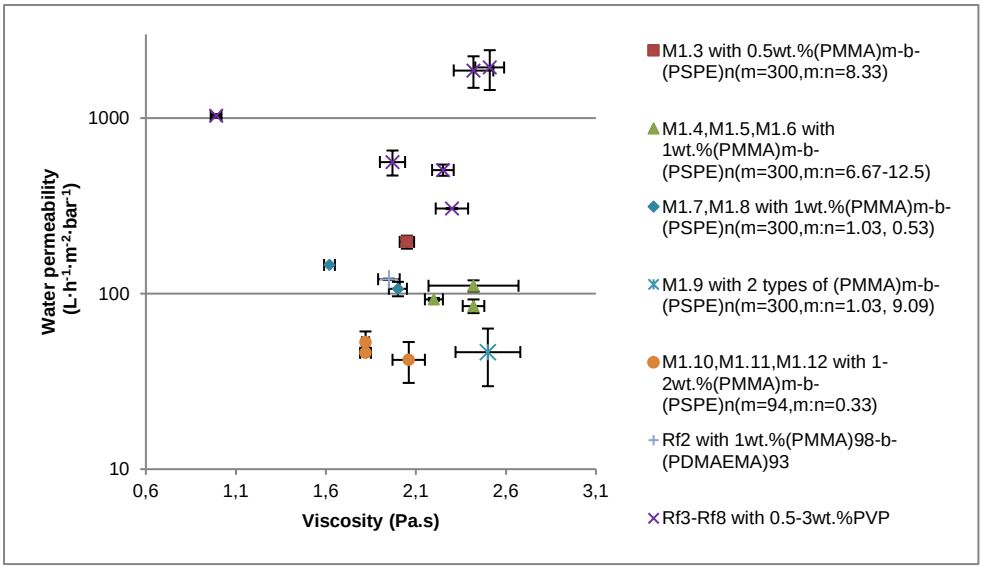

Fig. 68 Water permeability of 16 wt.% PVDF membranes with one additive as a function of corresponding viscosity.

Whole **M1.4**-**M1.6** that were doped 1 wt.% $PMMA_m$-*b*-$PSPE_n$ with long PMMA block (m= 300) and relatively short PSPE block (PMMA/PSPE= m/n= 6.7-12.5) showed higher viscosity than **M1.7** and **M1.8** that contained 1.5 wt.% $PMMA_m$-*b*-$PSPE_n$ with PMMA block (m= 300) but relatively long PSPE block (PMMA/PSPE= m/n= 1.0, 0.5), whereas the entire corresponding WP of **M1.4**-**M1.8** were still low and kept in a comparable range (85.1-145.7 $L \cdot h^{-1} \cdot m^{-2} \cdot bar^{-1}$), as shown in **Fig. 68**. The main reason should be attributed to the strong effect of additive $PMMA_m$-*b*-$PSPE_n$ that

escalated the precipitation kinetic and vitrification of matrix PVDF and predominated over viscosity difference during the morphology formation. It was interesting to noted that, due to the decreased effect of block copolymer additive and thus relatively more viscosity-dominated influence, **M1.3** with 0.5 wt.% $PMMA_m$-*b*-$PSPE_n$ showed apparently raised WP and slightly lower viscosity than **M1.4**-**M1.6**. By means of the more pronounced effect of block copolymer additive, **M1.10**-**M1.12** that contained additive 1-2 wt.% $PMMA_m$-*b*-$PSPE_n$ with shorter PMMA block (m= ~94) but relatively longer PSPE block (PMMA/PSPE= m/n= ~0.3) demonstrated even much lower WP, despite its lower viscosity compared with **M1.4**-**M1.6**. It should also be noticed that, **M1.9** that contained 1 wt.% $PMMA_{300}$-*b*-$PSPE_{33.5}$ and 1.5 wt.% $PMMA_{300}$-*b*-$PSPE_{291.3}$ revealed high viscosity and low WP, which seemed agree well with the viscosity-dominated mechanism of morphology formation, but indeed the intensified concurrent effect from the involved 2 types of block copolymer additives dominated **M1.9** morphology formation.

The whole of membranes **Rf3**-**Rf8** with 0.5-3 wt.% PVP showed quite enhanced WP (the minimum 305.3 $L \cdot h^{-1} \cdot m^{-2} \cdot bar^{-1}$ from **Rf6**) but evident trade-off relationship between WP and BSA rejection in **Fig. 69**. With the increment of WP, **Rf3**-**Rf8** basically displayed rapid decline of sieving performance on BSA protein (decreased BSA rejection). As aforementioned, presence of PVP retarded the precipitation kinetic of polymer-rich phase and consequently facilitated coalescence and growth of polymer-lean phase to form highly porous top skin layer and sublayer with macrovoids. However the extent of pore size increasing brought by different doping amount of PVP directly dominated the barrier selectivity of **Rf3**-**Rf8**. The enhancement of water permeability via doping PVP was achieved at the unfavorable cost of selectivity loss.

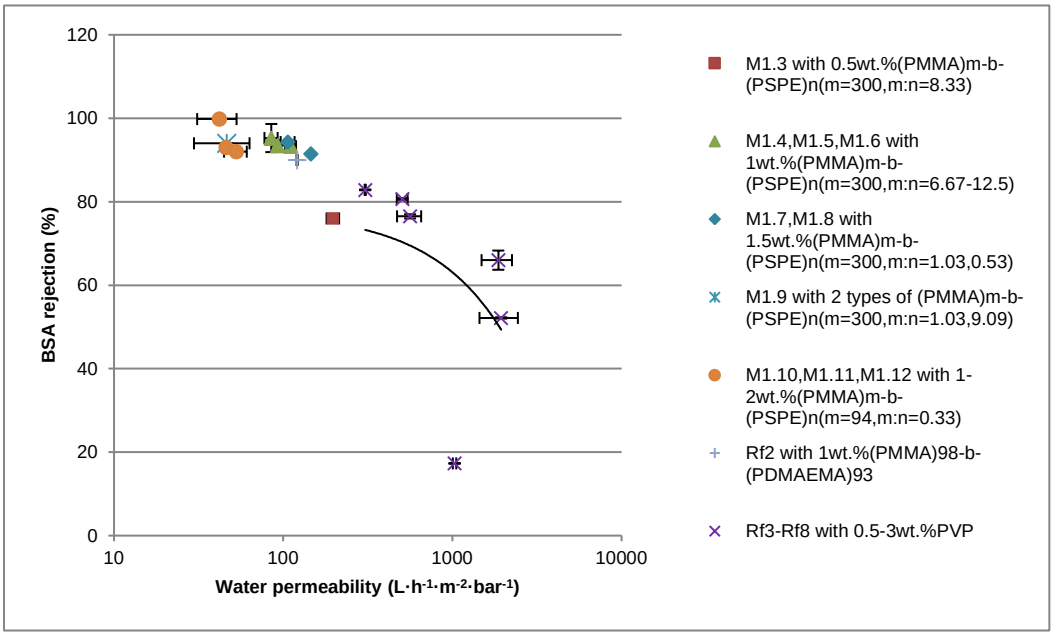

Fig. 69 BSA rejection of 16wt.% PVDF membranes with one additive as a function of corresponding water permeability. The trendline for **Rf3**-**Rf8** was presented.

Contrary to the case of membranes with PVP, as clearly seen in **Fig. 69**, the entire membranes with 1 wt.% $PMMA_m$-*b*-$PSPE_n$ (**M1.4** to **M1.12**) exhibited quite low water permeability (the maximum 145.7 $L \cdot h^{-1} \cdot m^{-2} \cdot bar^{-1}$ from **M1.7**) and remarkably high BSA retention (over 90%). Also as discussed before, the stiffness of block copolymer molecular chains arisen from the ionic-hydrated PSPE block that migrated and exposed along the interphase boundary during liquid-liquid demixing strongly facilitated the re-organization of matrix PVDF molecular chains and thus vitrification of polymer-rich phase in the top layer and sublayer.[82][95] As a result, the size of surface pores and porous structure in sublayer were largely suppressed by the effect of additional zweitterionic block copolymer additive, which directly led to the presented lower WP and high BSA sieving performance showed in **Fig. 69**. Furthermore, the super hydrophilicity brought by surface-enriched PSPE block also was another essential factor that governed the strong BSA rejection. But it should be noted that, compared with membranes with 1 wt.% $PMMA_m$-*b*-$PSPE_n$, **M1.3** with 0.5 wt.% $PMMA_m$-*b*-$PSPE_n$ demonstrated the apparently raised WP but a significant drop on BSA rejection (76%), which clearly indicated that the adequate content of zwitterionic block copolymer additive was quite crucial to the formation of the typical corresponding membrane property.

Through the detailed comparison, even though membranes **M1.4**-**M1.12** showed similarly high BSA rejection, their slightly different WP created by 1 wt.% $PMMA_m$-*b*-$PSPE_n$ with varied M_n and

ratios of blocks was apparently observed in **Fig. 69**. Compared with **M1.7** and **M1.8** that contained 1.5 wt.% $PMMA_m$-*b*-$PSPE_n$ with PMMA block (m= 300) but relatively long PSPE block (PMMA/PSPE= m/n= 1.0, 0.5), **M1.4**, **M1.5** and **M1.6** that were doped 1 wt.% $PMMA_m$-*b*-$PSPE_n$ with long PMMA block (m= 300) and relatively short PSPE block (PMMA/PSPE= m/n= 6.7-12.5) exhibited slightly decreased WP, which can be mainly attributed to not only the more favorable interphase boundary (surface) migration of $PMMA_m$-*b*-$PSPE_n$ with long PMMA block (m=300) and relatively short PSPE block driven by its smaller conformational entropy penalty arisen from the lower M_n but also the resultant positively enhanced precipitation kinetic of matrix PVDF. In addition, the better solubility of $PMMA_m$-*b*-$PSPE_n$ with long PMMA block (m= 300) and relatively short PSPE block also was quite helpful to reinforce the effect of block copolymer additive. In the case of **M1.10**-**M1.12** that contained additive 1-2 wt.% $PMMA_m$-*b*-$PSPE_n$ with shorter PMMA block (m= ~94) but relatively longer PSPE block (PMMA/PSPE= m/n= ~0.3), the WP were further decreased due to the strong facilitating effect of corresponding block copolymer additive on precipitation kinetics of matrix polymer. **M1.9** that contained 1wt.% $PMMA_{300}$-*b*-$PSPE_{33.5}$ and 1.5wt.% $PMMA_{300}$-*b*-$PSPE_{291.3}$ also showed quite low WP, which can be undoubtedly ascribed to the concurrent effect of 2 types of block copolymer additive on further intensified enhancement of rate of PVDF vitrification (cf. **Fig. 54** and discussion in **6.1.3.**). The higher BSA rejection of **Rf2** with $PMMA_{98}$-*b*-$PDMAEMA_{93}$ was highly relative to the strong BSA protein adsorption of hydrophilic PDMAEMA block that exposed on membrane **Rf2** surface and inner pore walls.[123]

The fouling phenomenon during BSA filtration for membranes **M1.4**, **M1.6**, **M1.7**, **M1.9**, **M1.10** and **Rf4** were further investigated as shown in **Fig. 70**. All the examined membrane samples showed decreased WP after BSA filtration, which evidently signified that, the adsorptive fouling of BSA protein took place in all the tested membranes to different extent. **Rf4** with 1wt.% PVP had higher porosity and bigger mean pore size relative to BSA diameter, which can be drawn from its much higher WP and relatively lower BSA rejection (76.5%). During the filtration, BSA protein that permeated through membrane deposited not only on the surface but also along the inner pore walls of **Rf4** via solute-membrane interaction due to the less hydrophilicity of **Rf4**.[118] Under the influence of following strong solute-solute interaction, gel layer formation on **Rf4** surface and pore narrowing, even partly pore-plugging occurred, which composed of the main fouling of membrane and directly resulted in the higher relative flux reduction (RFR) of **Rf4**.[125]

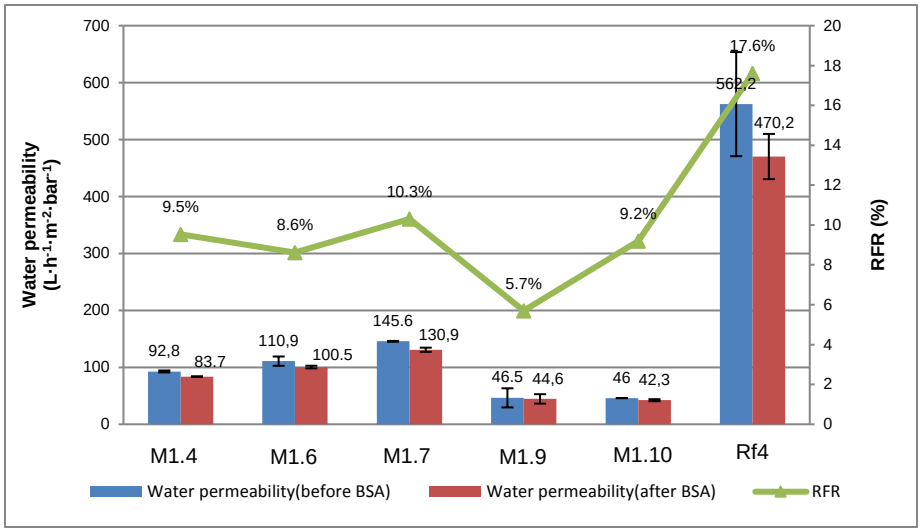

Fig. 70 Relative flux reduction (RFR) and comparison of water permeability (before and after BSA) for **M1.4**, **M1.6**, **M1.7**, **M1.9**, **M1.10** and **Rf4**.

All the tested membranes with various PMMA$_m$-*b*-PSPE$_n$ in **Fig. 70** showed quite lower RFR compared with **Rf4**. On one hand, the low surface porosity and smaller pore size relative to BSA diameter can remarkably decrease the BSA adsorption in inner pore walls and hence largely diminished the pore narrowing and pore-plugging in above membranes.[8][117] On the other hand, as aforementioned, the hydration layer that were composed of hydrogen-bonding network of water formed by zwitterionic PSPE block that exposed along membrane surface and inner pore walls, offered highly strong protein resistance to effectively reduce the adsorptive fouling of BSA protein during filtration.[57] It also can be seen from **Fig. 70** that, there was no significant difference on RFR among **M1.4**, **M1.6**, **M1.7** and **M1.10** which doped PMMA$_m$-*b*-PSPE$_n$ with different M_n and ratios of PMMA/PSPE. The slightly higher RFR of **M1.7** compared with **M1.4**, **M1.6** and **M1.10**, can be mainly attributed to the less dispersion of PSPE block on the surface arisen from the solubility of PMMA$_{300}$-*b*-PSPE$_{291.3}$ which contained relatively long PSPE block. It should be noted that, the apparently lowest RFR appeared in **M1.9** that doped 1 wt.% PMMA$_{300}$-*b*-PSPE$_{33.5}$ and 1.5 wt.% PMMA$_{300}$-*b*-PSPE$_{291.3}$, which undoubtedly indicated that the concurrent action of the two types of PMMA$_m$-*b*-PSPE$_n$ with different size of PSPE was capable of highly enhancing the packing density of PSPE on the membrane surface and inner pore walls.[93]

6.2. PVDF membranes with two types of additives

Considering the better solubility and homogeneity of dope solutions, PMMA$_m$-*b*-PSPE$_n$ with long PMMA block and relatively short PSPE block (M_n of PMMA block= 30 kg/mol, PMMA/PSPE = m/n =7.7-20) were combined with various types of second additives respectively to prepare PVDF

membrane in specific NIPS conditions. One extra additive, $(PMMA)_{94}$-*b*-$(PSPE)_{261}$ with short PMMA block but relatively long PSPE block, also was combined with PVP (K30) to prepare PVDF membrane for further characterization.

6.2.1. PVDF membranes with $PMMA_m$-*b*-$PSPE_n$ and PVP

All the dope solutions of PVDF membranes with combination of $PMMA_m$-*b*-$PSPE_n$ and PVP were shown in **Table 19**. In membranes **M2.1** to **M2.6**, different $PMMA_m$-*b*-$PSPE_n$ (M_n of PMMA= ~10 or 30 kg/mol) and PVP (K30 or K17) were doped with PVDF in membrane dope solutions. In the case of **M2.7**, three types of $PMMA_m$-*b*-$PSPE_n$ with similar M_n were doped together with PVP and PVDF in one dope solution. The dope solution of **M2.11** involved PVP and $(PMMA)_{94}$-*b*-$(PSPE)_{261}$ with shorter PMMA block but relatively long PSPE block. The procedure of NIPS for all the membrane here (**M2.1** to **M2.7**, **M2.11**) had same parameters of casting speed and humidity. All the detail of preparation of membranes can be seen in **4.3.3.**. The employed content (wt.%) for $PMMA_m$-*b*-$PSPE_n$ were different (1%, 1.5%, 2%). The employed content (wt.%) for PVP and PVDF were respectively fixed to 1% and 16%. The corresponding viscosity data for dope solutions were also tabulated in **Table 19** and further discussed in **6.2.1.1.**.

Code	ADD.I (wt.%)	ADD.I M_n(g/mol)	ADD.I Ratio (PMMA/ PSPE)	ADD.II (wt.%)	ADD.II M_w(g/mol)	PVDF LMW (wt.%)	[b]Viscosity (Pa.s)
M2.1	$(PMMA)_{317}$-*b*-$(PSPE)_{25.3}$ 1	38800	12.5	PVP(K30) 1	14000	16	2.85±0.07
M2.2	$(PMMA)_{317}$-*b*-$(PSPE)_{25.3}$ 1.5	38800	12.5	PVP(K30) 1	14000	16	2.75±0.07
M2.3	$(PMMA)_{300}$-*b*-$(PSPE)_{38.1}$ 1	40600	7.7	PVP(K30) 1	14000	16	2.72±0.05
M2.4	$(PMMA)_{300}$-*b*-$(PSPE)_{38.1}$ 2	40600	7.7	PVP(K30) 1	14000	16	4.23±0.01
M2.5	$(PMMA)_{300}$-*b*-$(PSPE)_{36.4}$ 2	40200	8.3	PVP(K30) 1	14000	16	3.28±0.07
M2.6	$(PMMA)_{300}$-*b*-$(PSPE)_{33.5}$ 2	39300	9.1	PVP(K17) 1	2000	16	1.99±0.12
[a]**M2.7**	$(PMMA)_{300}$-*b*-$(PSPE)_{15.8}$ 0.67 $(PMMA)_{300}$-*b*-$(PSPE)_{24.7}$ 0.67 $(PMMA)_{317}$-*b*-$(PSPE)_{25.3}$ 0.67	34400 36900 38800	20 12.5 12.5	PVP(K30) 1	14000	16	2.25±0.06
M2.11	$(PMMA)_{94}$-*b*-$(PSPE)_{261}$ 1	82300	0.4	PVP(K30) 1	14000	16	2.38±0.1

Table 19 Dope solutions of PVDF membranes containing PVP and $PMMA_m$-*b*-$PSPE_n$ (PMMA M_n= ~10 or 30 kg/mol) with different doping concentrations. Membrane matrix material was PVDF (M_w=48.1 kg/mol). Solvent was NMP. Coagulation bath was deionized water. Temperature of casting plate and coagulation were r.t.. The speed of casting knife were 5mm/s and humidity were less than 20.0% during casting process. [a]**M2.7** contained three types of $PMMA_m$-*b*-$PSPE_n$ in its dope solution. [b]Viscosity (@r.t.) of the listed PVDF membrane dope solutions with PVP and $PMMA_m$-*b*-$PSPE_n$ (PMMA M_n= ~10 or 30 kg/mol) with different doping concentrations were also tabulated. Shear rate fixed to 25 [1/s].

6.2.1.1. Rheology

As shown in **Table 19**, Dope solution of **M2.2** that contained 1 wt.% PVP (K30) and 1.5 wt.% $PMMA_{317}$-*b*-$PSPE_{25.3}$ (PMMA/PSPE= 12.5) showed similar viscosity to that of **M2.1** which involved 1 wt.% PVP (K30) and 1wt.% $PMMA_{317}$-*b*-$PSPE_{25.3}$ (PMMA/PSPE= m/n= 12.5). However, dope solution of **M2.4** that contained 1 wt.% PVP (K30) and 2 wt.% $PMMA_{300}$-*b*-$PSPE_{38.1}$ (PMMA/PSPE= 7.7) gained much higher viscosity than that of **M2.3** which involved 1 wt.% PVP (K30) and 1 wt.% $PMMA_{300}$-*b*-$PSPE_{38.1}$ (PMMA/PSPE= 7.7). Compared with $PMMA_{317}$-*b*-$PSPE_{25.3}$ (additive of **M2.3** and **M2.4**), the slightly longer PSPE block of $PMMA_{300}$-*b*-$PSPE_{38.1}$(additive of **M2.1** and **M2.2**) contributed more chances to originate more chains entanglement via non-covalent interactions and remarkably improved the viscosity with the increased content from 1 wt.% to 2 wt.%. Dope solution of **M2.5** contained 1 wt.% PVP (K30) and 2 wt.% $PMMA_{300}$-*b*-$PSPE_{36.4}$ (PMMA/PSPE= 8.3) that had basically same calculated amount of PMMA and PSPE as $PMMA_{300}$-*b*-$PSPE_{38.1}$ (PMMA/PSPE= 7.7) which was utilized in dope solution of **M2.4**, whereas the dope solution of **M2.5** showed apparently lower viscosity than dope of **M2.4**. The instrument errors during the measurements perhaps was a reasonable explanation for that. Dope solution of **M2.6** that contained 1 wt.% PVP (K17) and 2 wt.% $PMMA_{300}$-*b*-$PSPE_{33.5}$ (PMMA/PSPE= 9.1) displayed the lowest viscosity as a consequence of doping PVP (K17) which had a much smaller M_n than PVP (K30) that was utilized in most of dope solutions in **Table 19**. Dope solution of **M2.7** that contained rough 2 wt.% mixture of 3 types of $PMMA_m$-*b*-$PSPE_n$ with short PSPE block (PMMA/PSPE= m/n= 20, 12.5, 12.5) and 1 wt.% PVP (K30) also gave a lower viscosity compared with other rest membrane dope solutions aside from **M2.6** dope solution. The relatively too short PSPE block in $PMMA_m$-*b*-$PSPE_n$ (PMMA/PSPE= m/n= 20, 12.5, 12.5) that doped in **M2.7** perhaps should be mainly responsible for the originated lower viscosity. The viscosity of dope **M2.11**, which contained 1 wt.% PVP (K30) and $PMMA_{94}$-*b*-$PSPE_{261}$ with short PMMA block but relatively long PSPE block (PMMA= ~10 kg/mol, PMMA/PSPE= 0.4), was higher than that of **M2.6** mainly because of the involvement of PVP (K30) in dope of **M2.11**. The viscosity of **M2.7** and **M2.11** were similar. Generally, in contrast to viscosity of dopes **M1.5**, **M1.6** and **M1.10** respectively (cf. **Table 14**, 2.42±0.06, 2.42±0.06, 1.82±0.03), viscosity of dopes **M2.1**, **M2.3** and **M2.11**, which respectively contained 1 wt.% PVP (K30) and same 1 wt.% $PMMA_m$-*b*-$PSPE_n$ as that in **M2.1**, **M2.3** and **M2.11**, were highly enhanced by the additional PVP.

6.2.1.2. Typical SEM morphologies

Cross sections, top surface, detailed top surface of typical membranes were scanned with SEM and shown.

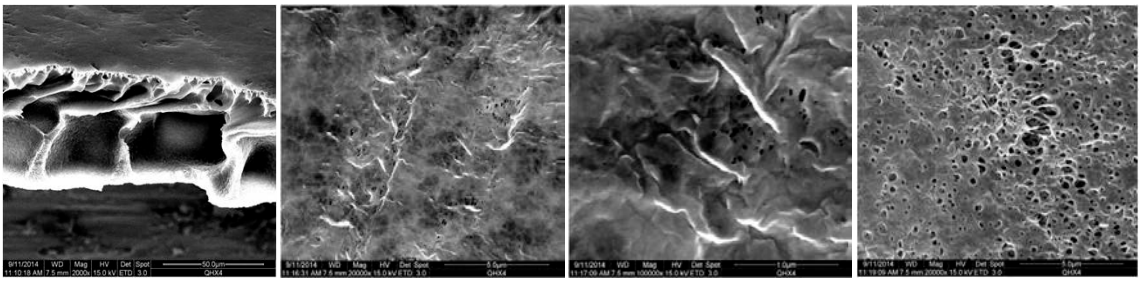

Fig. 71 Membrane **M2.1** ($PMMA_{317}$-*b*-$PSPE_{25.3}$ 1 wt.%, PVP (K30) 1 wt.%, PVDF 16wt.%). From left to right: Cross section (Mag.2k), top surface (Mag.20k), top surface (Mag.100k), back surface (Mag.20k).

As evidenced in aforementioned membranes with single $PMMA_m$-*b*-$PSPE_n$ additive, the strong influence on the morphology formation was gained from the utilization of $PMMA_m$-*b*-$PSPE_n$ with short PSPE block. The combination of two types of additives, PVP (K30) (1 wt.%) and $PMMA_{317}$-*b*-$PSPE_{25.3}$ (1 wt.%) with short PSPE block, were employed in dope solution of **M2.1**. The continuous polymer-lean phase interconnected with continuous polymer-rich phase in cross section of **M2.1** was strong evidence of the nucleation and growth process that dominated membrane formation after instantaneous liquid-liquid demixing. Different from **M1.2**, **M1.3** and **M1.6** which contained single additive $PMMA_m$-*b*-$PSPE_n$ with short block of PSPE, the full growth of pear-liked porous macrovoids were displayed in the cross section of **M2.1** (**Fig. 71**), which denoted another different mechanism resulted from the synergy of two additives. After the instantaneous liquid-liquid demixing, the facilitation of vitrification of PVDF-rich phase that arisen from the stiffness of ionic-hydrated $PMMA_m$-*b*-$PSPE_n$ chains along the phase boundary was offset by the flexible and hydrophiphilic PVP chains that also migrated towards the phase boundary. Contrary to the effect of stiff inonic-hydrated $PMMA_m$-*b*-$PSPE_n$, during the out-diffusion from polymer-rich phase, the flexible PVP chains in aqueous environment exerted disturbance on the re-arrangement and solidification of PVDF chains. Consequently, the precipitation kinetics of PVDF chains was balanced to the extent that the time for coalescence of polymer-lean phase in the top surface and sublayer were highly rationalized and allowed the optimized pore forming and nucleation growth for macrovoids. Unlike aforementioned PVP/PVDF membranes, on the top surface of **M2.1**, there was no distinct big pores except a few defects due to the operation conditions, which also indicated that, the pore size and porosity can be adjusted via the proper synergy of block copolymer additive and PVP. The highly enhanced water permeability of **M2.1**

(cf. **6.2.1.5.**) also strongly supported the morphology of top layer and sublayer of **M2.1**. The porous walls between macrovoids cell in **M2.1** was few and slightly thick as an integrative result of optimized energy difference between the polymer-lean droplets and the adjusted coalescence of the polymer-lean droplets via synergy of two types of additive.[81] The distance length from the top surface to the onset of macrovoids was relatively extended and gave an evidence to support the improved porosity in top layer of **M2.1** that needed adequate length of top layer to form the resistant barrier for initiation of nucleation growth to develop the macrovoids.[87]

In dope solutions of **M2.3** and **M2.4**, the two additives, PVP (K30) (1 wt.%) and $PMMA_{300}$-*b*-$PSPE_{38.1}$ (1 wt.% and 2 wt.%) with similar short PSPE block to additive in **M2.1**, were employed to investigate the influence of different using amounts of $PMMA_m$-*b*-$PSPE_n$ on the membrane morphology formation. **M2.3** and **M2.4** both showed the continuous PVDF phase and interconnected pore structures in the cross section region (**Fig. 72** and **Fig. 73**) as an evidence of the instantaneous liquid-liquid demixing and dominant nucleation growth mechanism. Similar to **M2.1**, the better growth of porous macrovoids in the cross section of **M2.3** and **M2.4** (**Fig. 72** and **Fig. 73**) also clearly demonstrated the optimization of pore-forming as well as nucleation growth and subsequent adjusted precipitation rate of polymer-rich phase due to the synergy of two additives. However, dissimilar to **M2.3** that contained 1 wt.% $PMMA_{300}$-*b*-$PSPE_{38.1}$, **M2.4** that had more (2 wt.%) $PMMA_{300}$-*b*-$PSPE_{38.1}$ originated an extral layer of sponge-liked structure near the bottom side. Perhaps in **M2.4**, the 2 wt.% employed copolymer additive exerted a little more suppression influence on the macrovoids development than 1 wt.% involved PVP, and thus the extra resistance caused by the slight suppression on macrovoids in front of bottom side limited the in-flow of nonsolvent and led to the formation of sponge-liked layer as membranes with single block copolymer additive that had short PSPE block. The surface of **M2.3** and **M2.4** showed no distinct big pores (**Fig. 72** and **Fig. 73**), which also can be regarded as a result of effective optimization on pore size control by synergy of two additives. Compared with aforementioned membranes with single $PMMA_m$-*b*-$PSPE_n$ additive, the absence of wrinkles on the surface of **M2.3** and **M2.4** signified that the enhanced porosity in top layer allowed the more nonslovent to in-diffuse in sublayer region and avoided the strong shrinkage of top surface. Like **M2.1**, in the case of **M2.3** and **M2.4**, the distance from the top surface to the onset of macrovoids was also relatively extended and effectively supported the improved porosity in top layer. The different using amount of $PMMA_m$-*b*-$PSPE_n$ in **M2.3** and **M2.4** can give significant influence on the formation of membrane morphology which were also consistent with the change of corresponding water permeability. (cf. **6.2.1.5.**)

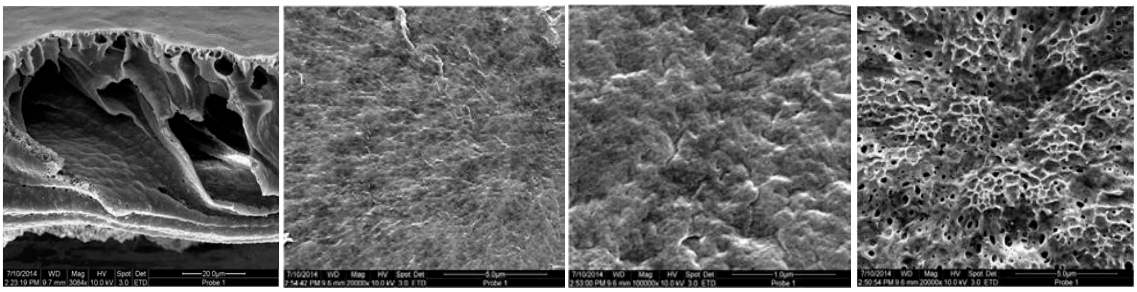

Fig. 72 Membrane **M2.3** ($PMMA_{300}$-*b*-$PSPE_{38.1}$ 1 wt.%, PVP (K30) 1 wt.%, PVDF 16 wt.%). From left to right: Cross section (Mag.3k), top surface (Mag.20k), top surface (Mag.100k), back surface (Mag.20k).

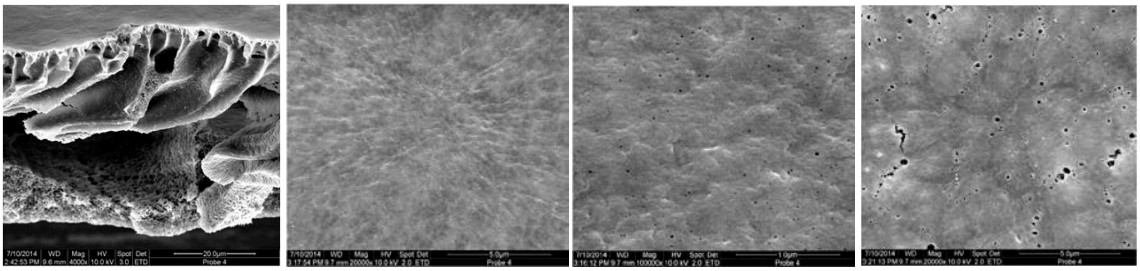

Fig. 73 Membrane **M2.4** ($PMMA_{300}$-*b*-$PSPE_{38.1}$ 2 wt.%, PVP (K30) 1 wt.%, PVDF 16 wt.%). From left to right: Cross section (Mag.4k), top surface (Mag.20k), top surface (Mag.100k), back surface (Mag.20k).

In dope solution of **M2.6**, $PMMA_{300}$-*b*-$PSPE_{33.5}$ (2 wt.%) and PVP (K17) 1 wt.%) were employed as two additives. $PMMA_{300}$-*b*-$PSPE_{33.5}$ displayed similar short block to the block copolymer additives which had been utilized in **M2.1**, **M2.3** and **M2.4**, whereas the PVP (K17) had much smaller molecular weights compared with PVP (K30). During the liquid-liquid demixing course, PVP (K17) more preferentially migrate and enrich on the phase boundary by means of the lower configurational entropy penalty when approaching boundary interface, in contrast to PVP (K30). Using amount of 2 wt.% block copolymer additive in **M2.6** also was expected to offer more control on the pore-forming as the case of **M2.4**. The continuous PVDF phase and interconnected pore structures were still persisted in the cross section region of **M2.6** (**Fig. 74**) and suggested the predominant instantaneous liquid-liquid demixing and the consequent nucleation as well as growth mechanism for membrane formation. The full developed macrovoids structure in cross section of **M2.6** apparently indicated that, 1 wt.% PVP (K17) with much smaller molecular weight was still able to balance the strong positive improvement on the precipitation rate of polymer-rich phase from the addition of 2 wt.% $PMMA_{300}$-*b*-$PSPE_{33.5}$. On one hand, unlike the top of **M2.4**, some distinct big pores can be identified on the top surface of **M2.6** (**Fig. 74**). On the other hand, in comparison with **Rf3** that had single utilization of 1 wt.% PVP (K30), the size of those distinct pores on top of **M2.6** was much smaller than ones presented on top of **Rf3**. The above interesting surface morphology of **M2.6** can be explained as the much stronger offsetting effect of

PVP (K17) than PVP (K30) on the precipitation rate of polymer-rich phase in top layer of **M2.6** in the case of synergy from block copolymer additive and PVP (K17) due to the relatively stronger surface migration and demixing tendency of PVP (K17) with much smaller molecular weight. The disappearance of surface wrinkles and elongated distance from top surface to the onset of macrovoids also contributed a persuasive clue for the enhanced porosity in the top layer of **M2.6**. The high water permeability of **M2.6** was consistent with the pronounced porous morphology. (cf. **6.2.1.5.**)

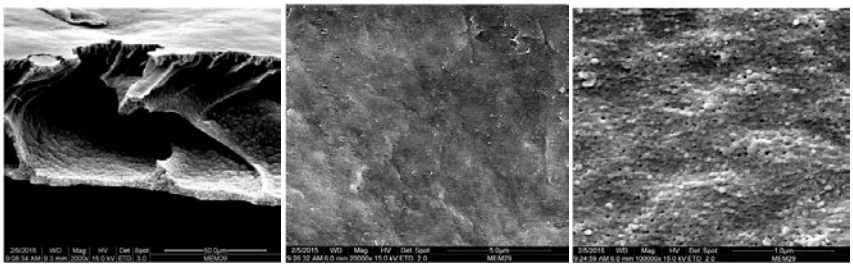

Fig. 74 Membrane **M2.6** ($PMMA_{300}$-*b*-$PSPE_{33.5}$ 2 wt.%, PVP (K17) 1 wt.%, PVDF 16 wt.%). From left to right: Cross section (Mag.4k), top surface (Mag.20k), top surface (Mag.100k).

In dope solution of **M2.7**, 1 wt.% PVP (K30) and the multi types of $PMMA_m$-*b*-$PSPE_n$ ($PMMA_{300}$-*b*-$PSPE_{15.8}$ 0.67 wt.%, $PMMA_{300}$-*b*-$PSPE_{24.7}$ 0.67 wt.%, $PMMA_{317}$-*b*-$PSPE_{25.3}$ 0.67 wt.%) were utilized as additives. All the three applied block copolymer additives had similar short PSPE block and the total amount of all the employed block copolymer additives in **M2.7** also approximately 2 wt.% as aforementioned membranes **M2.4** and **M2.6**. The instantaneous liquid-liquid demixing and according nucleation and growth process still governed the membrane morphology formation of **M2.7**, which can be supported by the continuous PVDF phase and interconnected pore structures originated in the cross section region of **M2.7** (**Fig. 75**). The well grown macrovoids of **M2.7** signified that the synergy of PVP (K30) and multi types of block copolymer additives was still available and pronounced. Similar to the top of membrane **M2.6**, on the top of **M2.7** (**Fig. 75**), some recognizable pores were still indentified but not big as ones on the top of **Rf3**. The reason perhaps can be ascribed to the detailed difference on the PSPE block of applied multi types of block copolymer additives. In general, all the three types of involved block copolymer additives had short PSPE block that was beneficial to the better exposure of additive on the phase boundary during liquid-liquid demixing, similar to the $PMMA_m$-*b*-$PSPE_n$ that were utilized in **M2.1**, **M2.3**, **M2.4** and **M2.6**. However, involvement of 0.67wt.% $PMMA_{300}$-*b*-$PSPE_{15.8}$ with much shorter PSPE block decreased the general content of PSPE block in the whole $PMMA_m$-*b*-$PSPE_n$ additives to much lower extent in contrast to the above discussed membranes that showed synergy effect from $PMMA_m$-*b*-$PSPE_n$ and PVP. Consequently the insufficient exposure of PSPE

block in the aqueous environment was unable to offer adequate stiffness in additive chains to offset the intervention effect of PVP on the vitrification of polymer-rich phase. As a result, the polymer-lean phase on the top layer gained relatively more time to grow and thus some recognizable pores formed finally on the top surface of **M2.7**. The disappearance of wrinkles on the top surface and the expanded length of top layer also strongly supported the enhanced porosity of top layer in **M2.7**. The porous walls between the macrovoids cell in **M2.7** thickened and became more, which also indicated the intensified coalescence of polymer-lean phase droplets due to the increased interfacial energy between polymer-lean phase droplets that was led by the insufficient exposure of PSPE block along the phase boundary during the liquid-liquid demixing in sublayer. The highly magnified water permeability of **M2.7** also substantiated the morphology explanation. (cf. **6.2.1.5.**)

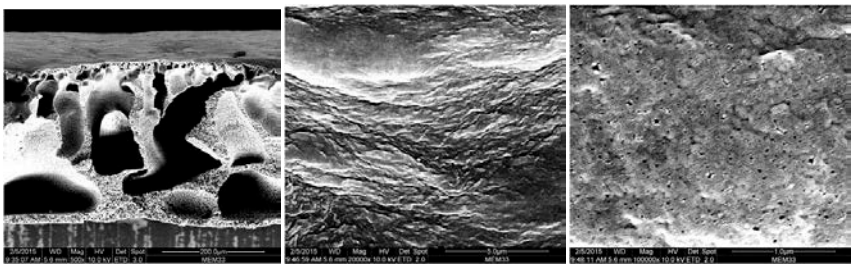

Fig. 75 Membrane **M2.7** ($PMMA_{300}$-*b*-$PSPE_{15.8}$ 0.67 wt.%, $PMMA_{300}$-*b*-$PSPE_{24.7}$ 0.67 wt.%, $PMMA_{317}$-*b*-$PSPE_{25.3}$ 0.67 wt.%, PVP (K30) 1 wt.%, PVDF 16 wt.%). From left to right: Cross section (Mag.4k), top surface (Mag.20k), top surface (Mag.100k).

M2.11 also showed the continuous PVDF phase and interconnected pore structures in the cross section region (**Fig. 76**) as an evidence of the instantaneous liquid-liquid demixing and dominant nucleation growth mechanism. Similar to above mentioned membranes with $PMMA_m$-*b*-$PSPE_n$ and PVP, **M2.11** presented surface where showed no distinct big pores and fully developed porous macrovoids without suppression, which offered strong evidence on the optimization of pore-forming as well as nucleation growth and subsequent adjusted precipitation kinetics of polymer-rich phase due to the synergy of two additives. Compared with morphology of **M1.10** (**Fig. 55**), the much more porous macrovoids in cross section of **M2.11** also clearly implied the positive influence on the pore-forming that created by the synergy interaction. The highly improved water permeability of **M2.11** was in agreement with the morphology explanation. (cf. **6.2.1.5.**)

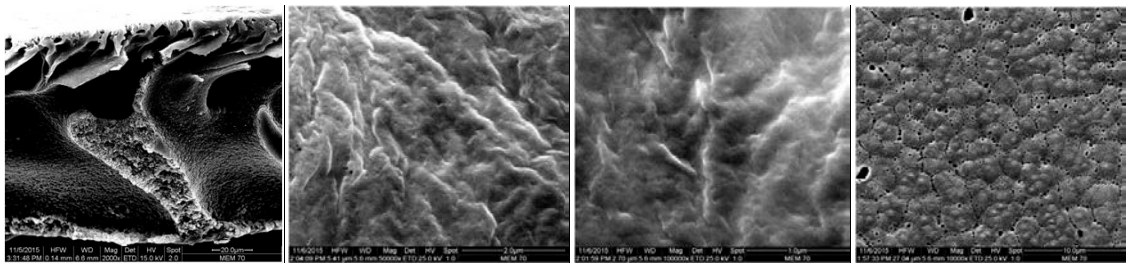

Fig. 76 Membrane **M2.11** ($PMMA_{94}$-*b*-$PSPE_{261}$ 1 wt.%, PVP K30 1 wt.%, PVDF 16 wt.%). From left to right: Cross section (Mag.5k), top surface (Mag.50k), top surface (Mag.100k), back surface (Mag.10k).

6.2.1.3. Contact angle

In general, all the membranes with combination of $PMMA_m$-*b*-$PSPE_n$ and PVP revealed low CA (around or below 40º, **Table 20**) and according high surface hydrophilicity and surface porosity. **M2.2** had more content of $PMMA_{317}$-*b*-$PSPE_{25.3}$ in dope solution than that of **M2.1**, but **M2.2** showed a little increased CA compared with **M2.1**. In comparison with **M1.5** that had single 1 wt.% $PMMA_{317}$-*b*-$PSPE_{25.3}$ as additive, **M2.1** also gave a higher CA. Perhaps the slight heterogeneity of **M2.1** and **M2.2** was the main reason for above occurrence.

Code	ADD.I (wt.%)	ADD.I M_n(g/mol)	ADD.I Ratio (PMMA/ PSPE)	ADD.II (wt.%)	ADD.II M_w(g/mol)	PVDF LMW (wt.%)	[a]Top Contact angle (º)
M2.1	$(PMMA)_{317}$-*b*-$(PSPE)_{25.3}$ 1	38800	12.5	PVP(K30) 1	14000	16	40.1±3.6
M2.2	$(PMMA)_{317}$-*b*-$(PSPE)_{25.3}$ 1.5	38800	12.5	PVP(K30) 1	14000	16	42.9±1.8
M2.3	$(PMMA)_{300}$-*b*-$(PSPE)_{38.1}$ 1	40600	7.7	PVP(K30) 1	14000	16	35.5±1.5
M2.4	$(PMMA)_{300}$-*b*-$(PSPE)_{38.1}$ 2	40600	7.7	PVP(K30) 1	14000	16	33.3±1.5
M2.5	$(PMMA)_{300}$-*b*-$(PSPE)_{36.4}$ 2	40200	8.3	PVP(k30) 1	14000	16	33.9±1.1
M2.6	$(PMMA)_{300}$-*b*-$(PSPE)_{33.5}$ 2	39300	9.1	PVP(K17) 1	2000	16	31.7±0.5
[b]**M2.7**	$(PMMA)_{300}$-*b*-$(PSPE)_{15.8}$ 0.67 $(PMMA)_{300}$-*b*-$(PSPE)_{24.7}$ 0.67 $(PMMA)_{317}$-*b*-$(PSPE)_{25.3}$ 0.67	34400 36900 38800	20 12.5 12.5	PVP(K30) 1	14000	16	33.9±0.8
M2.11	$(PMMA)_{94}$-*b*-$(PSPE)_{261}$ 1	82300	0.4	PVP(K30) 1	14000	16	28.7±0.9

Table 20 Contact angle values at r.t. of PVDF membranes containing PVP and $PMMA_m$-*b*-$PSPE_n$ (PMMA M_n= ~10 or 30 kg/mol) with different doping concentrations. Method was captive bubble. [a]Only contact angle value of PVDF membrane top surface (functional surface) were showed here. [b]**M2.7** contained 3 types of PMMA-*b*-PSPE in dope solutions.

M2.4 contained more $PMMA_{300}$-*b*-$PSPE_{38.1}$ in dope solution than that of **M2.3**, and accordingly, **M2.4** also presented lower CA than **M2.3**, which signified that $PMMA_{300}$-*b*-$PSPE_{38.1}$ was the main reason for the enhancement of surface hydrophilicity. Usually another prevailing reason for reduction of CA was the increased porosity and pore size of the measured surface except the nature of material. Compared with **M2.3**, **M2.4** had decreased surface porosity and macrovoids arisen from the more content of $PMMA_{300}$-*b*-$PSPE_{38.1}$ that created improved precipitation rate of polymer as all the $PMMA_m$-*b*-$PSPE_n$ worked during coagulation. Therefore, it can be confirmed that the decreased CA of **M2.4** undoubtedly came from the enlargement of surface hydrophilicity. $PMMA_{300}$-*b*-$PSPE_{36.4}$ that was additive in **M2.5** had basically same ratio of PMMA / PSPE as $PMMA_{300}$-*b*-$PSPE_{38.1}$ which was additive in **M2.4**, whereas **M2.5** and **M2.4** had totally same additive contents. As expected, **M2.5** also showed approximately same CA as **M2.4**, which exhibited the perfect reproducibility between **M2.4** and **M2.5** with basically same composition. In contrast to **M1.4** that contained single 1 wt.% $PMMA_{300}$-*b*-$PSPE_{36.4}$, **M2.3** that had 1wt.% $PMMA_{300}$-*b*-$PSPE_{38.1}$ and 1wt.% additional PVP (K30) revealed evidently decreased CA, which more possibly resulted from the enhanced surface porosity of **M2.3** with the aid of additional PVP (K30). **M2.6** contained 2wt.% $PMMA_{300}$-*b*-$PSPE_{33.5}$, which had similar ratio of PMMA / PSPE to $PMMA_m$-*b*-$PSPE_n$ in **M2.4** and **M2.5**, and 1wt.% PVP(K17) that had much smaller molecular weight than PVP (K30) which was applied in **M2.4** and **M2.5**, while the CA of **M2.6** was lower than that of **M2.4** and **M2.5**. Perhaps the PVP (K17) created more pores distributed on the surface by means of the more facilitated surface migration due to smaller molecular weight, and thus gave rise to the further decreased CA. **M2.7** with approximately 2 wt.% coalition of 3 types of $PMMA_m$-*b*-$PSPE_n$ also demonstrated a low CA that can be comparable to CA of **M2.4** and **M2.5** due to the largely enhancement of the surface porosity (high water permeability, cf. **6.2.1.5.**). $PMMA_{94}$-*b*-$PSPE_{261}$ had shorter PMMA block and relatively longer PSPE block compared with other $PMMA_m$-*b*-$PSPE_n$ which were used in most of membranes in **Table 20**. **M2.11** that contained $PMMA_{94}$-*b*-$PSPE_{261}$ and PVP (K30) showed the lowest CA. This value was slightly lower than CA of **M1.10** that contained single 1wt.% $PMMA_{94}$-*b*-$PSPE_{261}$, which can be attributed to the enhancement of surface porosity of **M2.11** due to the additional PVP (K30).

6.2.1.4. ATR-FTIR spectra

As aforementioned in discussion of **Fig. 60**, stretching vibration of C=O respectively from carboxylate and amide of different additives displayed different absorption wavenumber. The PVDF membrane that contained combination of $PMMA_m$-*b*-$PSPE_n$ and PVP was included in **Fig. 77** and was compared with other aforementioned membranes with different related additives. It is quite evident to see that, after addition of $PMMA_m$-*b*-$PSPE_n$ and PVP in dope solution of PVDF

membrane, the stretching vibration of C=O at ~1730 cm^{-1} and ~1660 cm^{-1} were both distinctly identified in ATR-FTIR spectrum top surface. Therefore, undoubtedly, the exposure of $PMMA_m$-*b*-$PSPE_n$ and PVP on the PVDF matrix membrane surface via surface migration mechanism during NIPS can be strongly substantiated by the above ATR-FTIR spectrum in **Fig. 77**.

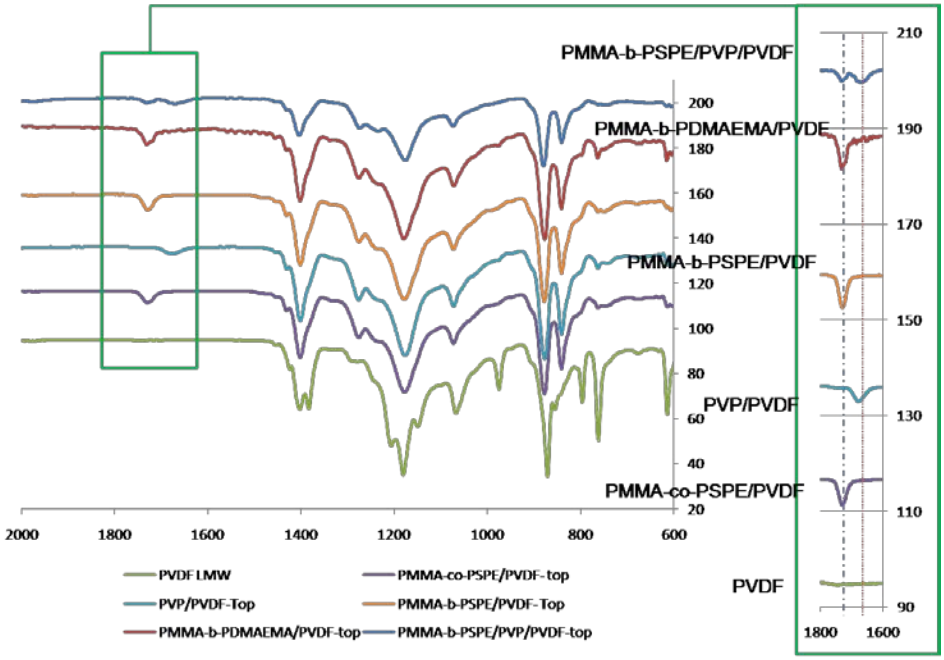

Fig. 77 Comparison of typical ATR-FTIR spectra respectively from pure PVDF membrane and PVDF membranes with combination of $PMMA_m$-*b*-$PSPE_n$ and PVP, $PMMA_m$-*b*-$PDMAEMA_n$, $PMMA_m$-*b*-$PSPE_n$, PVP, $PMMA_m$-*co*-$PSPE_n$. Selected ATR-FTIR spectra were from samples of **M2.4**, **Rf2**, **M1.6**, **Rf4** and **M1.1**. The local spectra between 1600 cm^{-1} and 1800 cm^{-1} wavenumber were displayed in the frame on the right side.

6.2.1.5. Membrane performance

On the whole, all the examined 16 wt.%PVDF membranes that were doped $PMMA_m$-*b*-$PSPE_n$ and PVP in **Table 21** showed remarkably pronounced enhancement of water permeability (WP) and remained high BSA retention in contrast to aforementioned 16 wt.% PVDF membranes with similar single $PMMA_m$-*b*-$PSPE_n$ (cf. **6.1.7.2.**). The combined utilization of PVP and $PMMA_m$-*b*-$PSPE_n$ as two additives played a key role to promote the membrane performance. The further investigation on the respectively plotted relationship of viscosity vs. WP and WP vs. BSA rejection for the listed membranes with two additives and part of aforementioned membranes with one additive (in **Fig. 78**-**Fig. 80**) gave some clues to preliminarily clarify the mechanism on improved membrane performance.

Code	ADD.I (wt.%)	ADD.I M_n (g/mol)	ADD.I Ratio (PMMA/ PSPE)	ADD.II (wt.%)	ADD.II M_w (g/mol)	PVDF LMW (wt.%)	Water permeability ($L \cdot h^{-1} \cdot m^{-2} \cdot bar^{-1}$)	BSA Rejection (%)
M2.1	$(PMMA)_{317}$-*b*-$(PSPE)_{25.3}$ 1	38800	12.5	PVP(K30) 1	14000	16	405.6±23.8	92.6±1.9
M2.2	$(PMMA)_{317}$-*b*-$(PSPE)_{25.3}$ 1.5	38800	12.5	PVP(K30) 1	14000	16	383.0±22.6	93.2±2.8
M2.3	$(PMMA)_{300}$-*b*-$(PSPE)_{38.1}$ 1	40600	7.7	PVP(K30) 1	14000	16	981.4±34.5	85.7±0
M2.4	$(PMMA)_{300}$-*b*-$(PSPE)_{38.1}$ 2	40600	7.7	PVP(K30) 1	14000	16	611.5±7.8	93.5±0
M2.5	$(PMMA)_{300}$-*b*-$(PSPE)_{36.4}$ 2	40200	8.3	PVP(K30) 1	14000	16	633.7±52.2	93.6±1.2
M2.6	$(PMMA)_{300}$-*b*-$(PSPE)_{33.5}$ 2	39300	9.1	PVP(K17) 1	2000	16	457.8±69.2	88.0±4.1
[a]M2.7	$(PMMA)_{300}$-*b*-$(PSPE)_{15.8}$ 0.67 $(PMMA)_{300}$-*b*-$(PSPE)_{24.7}$ 0.67 $(PMMA)_{317}$-*b*-$(PSPE)_{25.3}$ 0.67	34400 36900 38800	20 12.5 12.5	PVP(K30) 1	14000	16	1439.5±100.4	89.0±5.6
M2.11	$(PMMA)_{94}$-*b*-$(PSPE)_{261}$ 1	82300	0.4	PVP(K30) 1	14000	16	539.6±25.8	83.2±7.1

Table 21 Water permeability and BSA rejection at r.t. of PVDF membranes containing PVP and $PMMA_m$-*b*-$PSPE_n$ (PMMA M_n= ~10 or 30 kg/mol) with different doping concentrations. BSA concentration was 1mg/ml; pH value of BSA buffer solution fixed at 7.0. [a]**M2.7** contained 3 types of $PMMA_m$-*b*-$PSPE_n$ in dope solution. Water permeability and BSA rejection were measured after compaction process.

To investigate the viscosity effect of dope solutions on the membrane performance in **Table 21**, the relationship between viscosity of dope solutions and water permeability for above listed membranes with two additives and part of foregoing membranes with one additive was plotted in **Fig. 78**. As aforementioned, regarding **Rf3**-**Rf8** with single PVP (K30) additive, **Rf3**-**Rf6** with 0.5-1 wt.% PVP displayed apparently decreased WP following the decline of viscosity, which was quite in line with the normal effect of viscosity on membrane performance that high viscosity brought membranes with denser morphology due to the changed mutual diffusion rate.[75] However **Rf7** and **Rf8** showed highly enlarged WP that was led by the increased involvement of 1.5 wt.% and 3 wt.% PVP. **M1.4**-**M1.6** and **M1.10** entirely showed quite low WP regardless of different viscosity due to the strong influence of $PMMA_m$-*b*-$PSPE_n$ on facilitation of matrix PVDF precipitation kinetics.

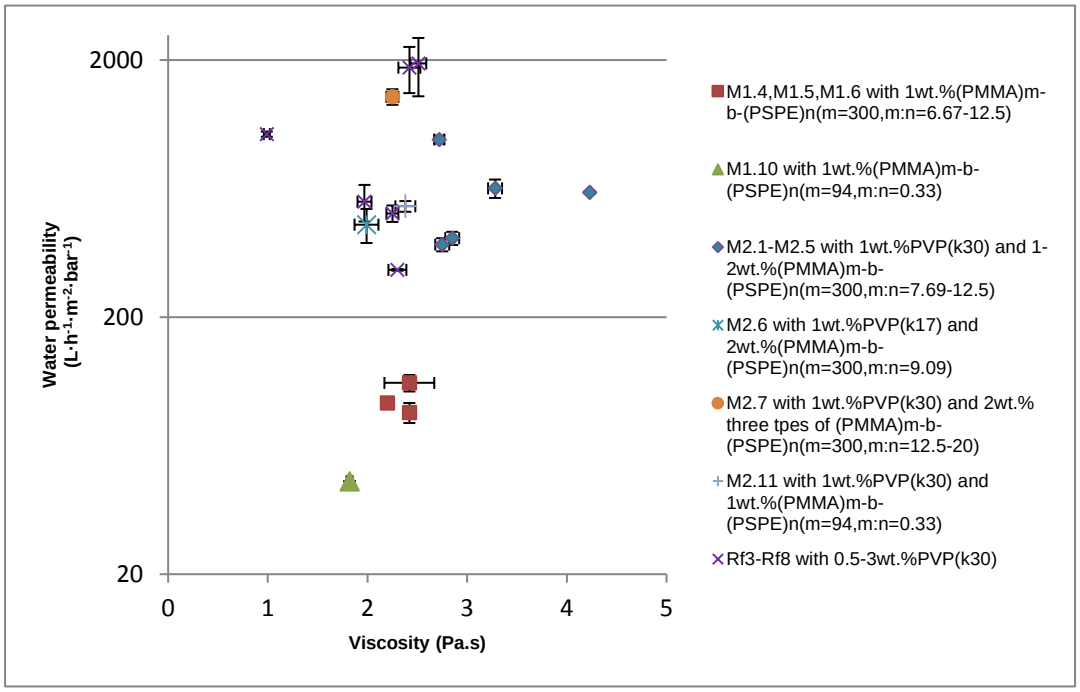

Fig. 78 Water permeability of 16 wt.% PVDF membranes with two additives (**M2.1**-**M2.11**) and part of aforementioned 16 wt.% PVDF membranes with one additive (**M1.4**-**M1.6**, **Rf3**-**Rf8**) as a function of viscosity of corresponding dope solution.

When $PMMA_m$-*b*-$PSPE_n$ and PVP were both utilized as additives together, some surprising phenomenon were observed between viscosity and WP. As shown in **Fig. 78**, all the membranes **M2.1**-**M2.7** and **M2.11** presented not only largely enhanced viscosity but much increased WP to different extent, which was quite dissimilar to above discussed membranes with sing PVP or single $PMMA_m$-*b*-$PSPE_n$. Compared with **M1.5** with 1 wt.% $PMMA_{317}$-*b*-$PSPE_{25.3}$, **M2.1** and **M2.2** that doped 1 wt.% PVP (K30) and 1-1.5 wt.% $PMMA_{317}$-*b*-$PSPE_{25.3}$ gained the obviously higher viscosity and WP. In contrast to **M1.4** and **M1.6** that respectively contained 1 wt.% $PMMA_{300}$-*b*-$PSPE_{36.4}$ and $PMMA_{300}$-*b*-$PSPE_{45.6}$, **M2.3** and **M2.4** that had 1-2 wt.% $PMMA_{300}$-*b*-$PSPE_{38.1}$ (basically similar to additive in **M1.4** and **M1.6**) and 1 wt.% PVP (K30) showed also much higher viscosity and more increased WP. **M2.5** that contained 2 wt.% $PMMA_{300}$-*b*-$PSPE_{36.4}$ (basically similar to additive in **M2.3** and **M2.4**) and 1 wt.% PVP (K30) reproduced the similarly increased viscosity and WP to **M2.4**. The raised viscosity in **M2.1**-**M2.5** apparently arose from the more additional PVP (K30) or $PMMA_m$-*b*-$PSPE_n$ that intensified the entanglement of polymer chains in dope solution. However the enhanced WP of **M2.1**-**M2.5** with increasing viscosity disobeyed the normal empirical rule. This should be mainly attributed to the additive PVP because additional PVP further elevated the hydrophilicity of dope solution on the basis of additional $PMMA_m$-*b*-$PSPE_n$ and offset part of the facilitation effect on precipitation rate from $PMMA_m$-*b*-$PSPE_n$. Regardless of the high viscosity, the strong hydrophilicity still can resulted in the quite favorable

diffusion rate between solvent and coagulant water during the liquid-liquid demixing,[126] and consequently played an important role in the formation of high WP with the assistance of synergy. It is also quite interesting to note that, compared with **M2.1** and **M2.2**, **M2.3** and **M2.4** offered more pronounced extent of increment on viscosity and WP, which should be ascribed to the different ratios of PMMA / PSPE in $PMMA_m$-*b*-$PSPE_n$ that were applied in **M2.1**-**M2.4** respectively. Combination of PVP and $PMMA_{300}$-*b*-$PSPE_{38.1}$ with slightly longer PSPE block in **M2.3** and **M2.4** yielded more pronounced synergy than combination of PVP with $PMMA_{317}$-*b*-$PSPE_{25.3}$ with relatively shorter PSPE block.

In comparison to **M1.10** with single 1 wt.% $PMMA_{94}$-*b*-$PSPE_{261}$, **M2.11** that contained 1 wt.% PVP (K30) and 1 wt.% $PMMA_{94}$-*b*-$PSPE_{261}$ also originated increased viscosity and highly enhanced WP relying on the strong synergy of combined additives and improved hydrophilicity of dope solution, which clearly signified that $PMMA_{94}$-*b*-$PSPE_{261}$ with quite short PMMA block and relatively long PSPE block also yielded similar synergy effect in agreement with $PMMA_{317}$-*b*-$PSPE_{25.3}$ and $PMMA_{300}$-*b*-$PSPE_{38.1}$ which had long PMMA block and relatively quite short PSPE block.

M2.6 with 1 wt.% PVP (K17) and 2 wt.% $PMMA_{300}$-*b*-$PSPE_{33.5}$ showed low viscosity and incrased WP mainly because of the low molecular weight of PVP (K17). However the remained synergy of PVP (K17) and $PMMA_{300}$-*b*-$PSPE_{33.5}$ still offered the improved WP. Due to the involved $PMMA_m$-*b*-$PSPE_n$ with much short PSPE block, **M2.7** also showed low viscosity. However thanks to the insufficient influence on facilitation of matrix polymer precipitation kinetics, relatively strengthened PVP effect rendered a quite enlarged WP for **M2.7**.

As seen in **Fig. 79**, as a result of effects from the two different additives PVP (K30) and $PMMA_m$-*b*-$PSPE_n$ respectively, **Rf3**-**Rf8** with 0.5-3 wt.% PVP (K30) showed apparent trade-off relationship between WP and BSA rejection, while **M1.4**-**M1.6**, and **M1.10** that doped various 1 wt.% $PMMA_m$-*b*-$PSPE_n$ respectively with different M_n and ratios of PMMA / PSPE displayed much lower WP but remained higher BSA retention all along. During the liquid-liquid demixing, PVP strongly retarded the precipitation rate of matrix PVDF polymer, whereas $PMMA_m$-*b*-$PSPE_n$ showed remarkable facilitation influence on the precipitation rate and the following vitrification of matrix PVDF polymer, as discussed previously in **6.1.7.2.**. In the case of **M2.1**-**M2.7** and **M2.11**, by means of the combination of PVP and $PMMA_m$-*b*-$PSPE_n$, the strong enhancement effect on surface pore-forming and macrovoids growth which was brought by interphase boundary (surface) migration of PVP and following resultant disturbance as well as hindrance on matrix PVDF precipitation kinetics, was effectively offset by the contrary facilitation influence on precipitation rate of matrix

PVDF as a consequence of the reinforced re-arrangement and collapse of PVDF chains led by stiffness of ionic-hydrated $PMMA_m$-*b*-$PSPE_n$ that also migrated towards interphase boundary (surface) after instantaneous liquid-liquid demxing of membrane dope solutions. The results of balanced effects from the combined two additives were the finally optimized pore size and porosity in membrane top layer and the developed porous sublayer with unsuppressed macrovoids in membrane sublayer, namely the high solute sieving performance (BSA rejection) and the high water permeability can be gained at the same time. In other words, the employment of PVP and $PMMA_m$-*b*-$PSPE_n$ as combined additives can offer strong synergy to overcome the trade-off relationship between WP and BSA retention that was inevitable in most of asymmetric membranes.

As clearly seen in **Fig. 79**, compared with **M1.5** that contained 1 wt.% $PMMA_{317}$-*b*-$PSPE_{25.3}$ and showed WP: 85.1 $L \cdot h^{-1} \cdot m^{-2} \cdot bar^{-1}$, BSA rejection: 95.3% (cf. **6.1.7.2.**), **M2.1** and **M2.2** that contained 1-1.5 wt.% $PMMA_{317}$-*b*-$PSPE_{25.3}$ (same as additive in **M1.5**) and 1 wt.% PVP (K30) displayed much higher WP and similarly high BSA rejection as a consequence of synergy from the combined additives. In contrast to **M1.4** and **M1.6** that respectively contained 1 wt.% $PMMA_{300}$-*b*-$PSPE_{36.4}$ and $PMMA_{300}$-*b*-$PSPE_{45.6}$, **M2.3** and **M2.4** that had 1-2 wt.% $PMMA_{300}$-*b*-$PSPE_{38.1}$ (basically similar to additive in **M1.4** and **M1.6**) and 1 wt.% PVP (K30) also exhibited highly enlarged WP and still remained high BSA rejection. It was interesting to mention that, even though there was no apparent difference on WP of **M1.5**, **M1.4** and **M1.6** that contained 1wt.% $PMMA_m$-*b*-$PSPE_n$ with slight different ratios of PMMA/PSPE, the WP of **M2.3**, **M2.4** that contained 1 wt.% PVP and 1-2 wt.% $PMMA_{300}$-*b*-$PSPE_{38.1}$ was enhanced to a quite larger extent than that of **M2.1** and **M2.2** that contained 1 wt.% PVP and 1-1.5 wt.% $PMMA_{317}$-*b*-$PSPE_{25.3}$. The main reason should be mainly attributed to the relatively longer PSPE block of $PMMA_{300}$-*b*-$PSPE_{38.1}$ in **M2.3** and **M2.4**, compared with $PMMA_{317}$-*b*-$PSPE_{25.3}$ that were utilized in **M2.1** and **M2.2**. The relatively longer PSPE block rendered more pronounced synergy in **M2.3** and **M2.4** than that in **M2.1** and **M2.2**.

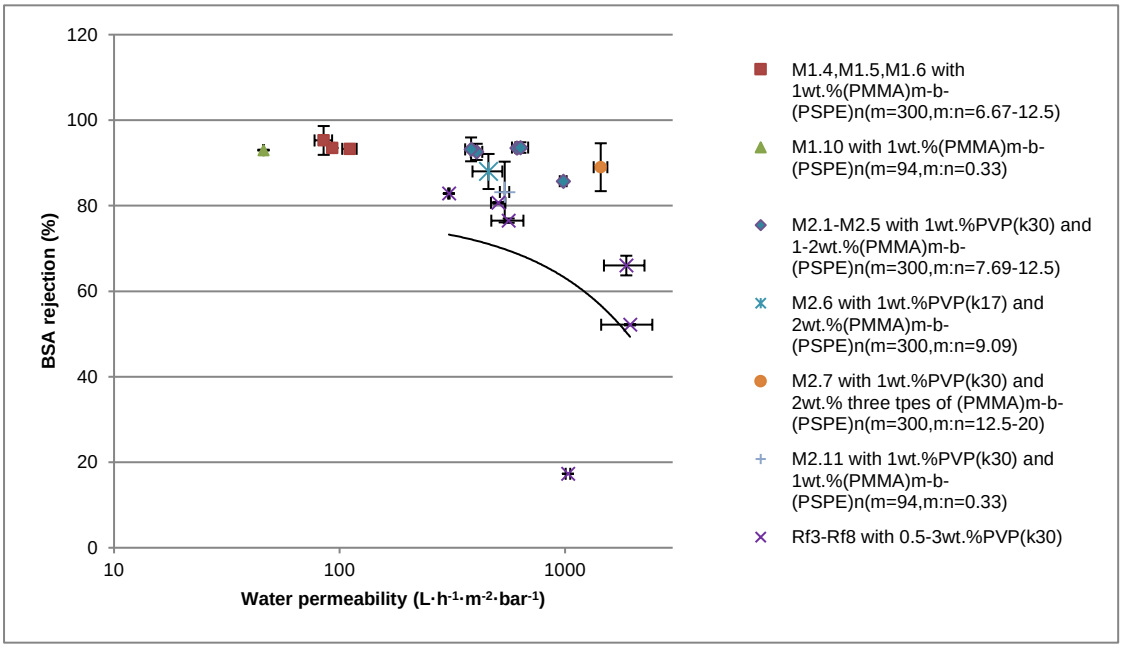

Fig. 79 BSA rejection of 16 wt.% PVDF membranes with two additives (**M2.1**-**M2.11**) and part of aforementioned 16 wt.% PVDF membranes with one additive (**M1.4**-**M1.6**, **Rf3**-**Rf8**) as a function of corresponding water permeability. The trendline for **Rf3**-**Rf8** was presented. (cf. **Fig. 68**)

As shown in **Fig. 80**, it should be noted that, **M2.4** that contained 2wt.% $PMMA_{300}$-*b*-$PSPE_{38.1}$ and 1 wt.% PVP demonstrated apparently decreased WP and higher BSA rejection in comparison to **M2.3** that had 1 wt.% $PMMA_{300}$-*b*-$PSPE_{38.1}$ and 1 wt.% PVP, which significantly implied that the stronger control can be exerted on the pore size and porosity in top layer and macrovoids development in sublayer by use of more content of $PMMA_m$-*b*-$PSPE_n$. As can be also seen in **Fig.80**, **M2.2** that contained 1.5 wt.% $PMMA_{317}$-*b*-$PSPE_{25.3}$ and 1 wt.% PVP also displayed reduced WP and slightly raised BSA rejection compared with **M2.1** that doped 1 wt.% $PMMA_{317}$-*b*-$PSPE_{25.3}$ and 1 wt.% PVP, which definitely supported the conclusions from comparison of **M2.3** and **M2.4**. Furthermore, **M2.5** that contained 2 wt.% $PMMA_{300}$-*b*-$PSPE_{36.4}$ (basically similar to additive in **M2.3** and **M2.4**) and 1 wt.% PVP still exhibited quite similar WP and BSA rejection to **M2.4**, which offered the strong reproducibility to further confirm the reinforced influence from more content of zwitterionic block copolymer additive.

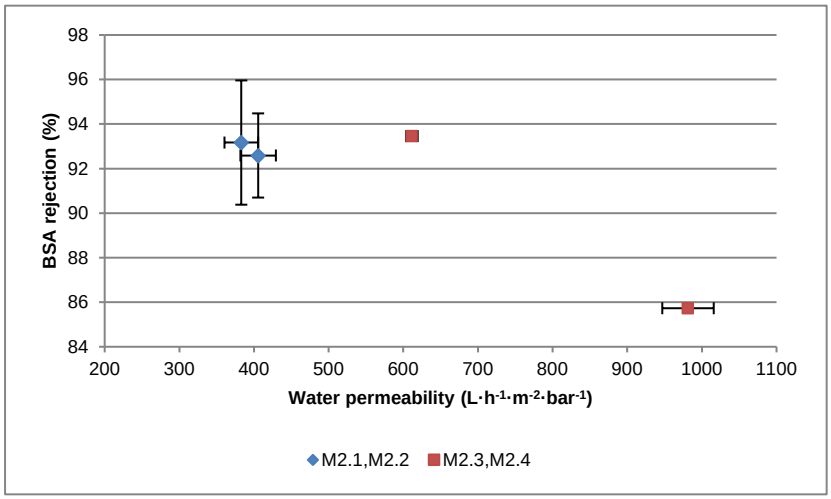

Fig. 80 Comparison of relationship between BSA rejection and water permeability for **M2.1**&**M2.2**, **M2.3**&**M2.4**.

Molecular weight of PVP (K17) (2 kg/mol) is much lower than that of PVP (K30) (14 kg/mol), therefore theoretically during the liquid-lquid demixing the interphase boundary (surface) migration of PVP (K17) should be more favorable than PVP (K30) due to the smaller conformational entropy penalty of the former. **M2.6** with 1wt.% PVP (K17) and 2 wt.% $PMMA_{300}$-*b*-$PSPE_{33.5}$ also showed quite obvious synergy effect on enhanced WP and maintenance of high BSA rejection in **Fig. 79**. Moreover it is interesting to note that WP of **M2.6** was lower than **M2.4** and **M2.5** that contained $PMMA_m$-*b*-$PSPE_n$ with similar M_n and ratio of PMMA / PSPE, which clearly signified that, unlike PVP (K30), during the liquid-liquid demixing PVP (K17) with lower molecular weight was more favorable to migrate out of polymer-rich phase into polymer-lean phase instead of entrapment and thus gave relatively less disturbance on precipitation rate. Consequently, the **M2.6** gained relatively lower WP compared with **M2.4** and **M2.5** that contained PVP (K30).

M2.7 that contained 1 wt.% PVP (K30) and 2 wt.% three types of $PMMA_m$-*b*-$PSPE_n$ with quite short PSPE block displayed a much pronounced WP(1439.5 $L \cdot h^{-1} \cdot m^{-2} \cdot bar^{-1}$) and still kept high BSA rejection. Generally, the size of PSPE block of all doped $PMMA_m$-*b*-$PSPE_n$ in **M2.7** were less than above discussed membranes with proper synergy. During the liquid-liquid demixing process, the quite shorter PSPE block offered insufficient influence on facilitation of matrix polymer precipitation kinetics to offset PVP effect on the retarding precipitation rate of matrix polymer. As a result, the PVP effect mainly strengthened and dominated the morphology formation of **M2.7** and originated the largely enhanced WP. Anyway, the high BSA rejection was remained, which perhaps was relative to the more enrichment of $PMMA_m$-*b*-$PSPE_n$ in the top layer.

Compared with **M1.10** that contained 1 wt.% $PMMA_{94}$-*b*-$PSPE_{261}$, **M2.11** that contained 1 wt.% PVP (K30) and 1 wt.% $PMMA_{94}$-*b*-$PSPE_{261}$ also revealed much increased WP and still can kept 83.2% BSA rejection, which also presented the apparent synergy effect from combined 2 additives. It should be mentioned that, different from $PMMA_m$-*b*-$PSPE_n$ that were involved in **M2.1**-**M2.7**, $PMMA_{94}$-*b*-$PSPE_{261}$ in **M2.11** had much smaller PMMA block and relatively long PSPE block but still can behave well to exhibited the synergy effect when it combined with PVP (K30) in **M2.11**. This significantly suggested that $PMMA_m$-*b*-$PSPE_n$ with quite different M_n and ratios of PMMA versus PSPE were quite potential to be applied for elevate membrane performance via combination with PVP.

In addition, excellent hydrophilicity of membrane surface and inner pore walls should be another essential factor to remain the high BSA rejection for above examined membranes with synergy of $PMMA_m$-*b*-$PSPE_n$ and PVP in **Table 23**.

To further discuss the extent of membrane fouling, relative flux reduction (RFR) and water permeability before and after BSA filtration (rejection) were compared in **Fig. 81** and **Fig. 82** for some selected PVDF membranes with two additives (**M2.3**-**M2.5**, **M2.11**) and some comparable PVDF membranes with one additive (**M1.4**, **M1.6**, **M1.10** and **Rf4**). All the plotted membranes showed suppressed water permeability after BSA filtration test and signified the occurrence of membrane fouling to different degree.

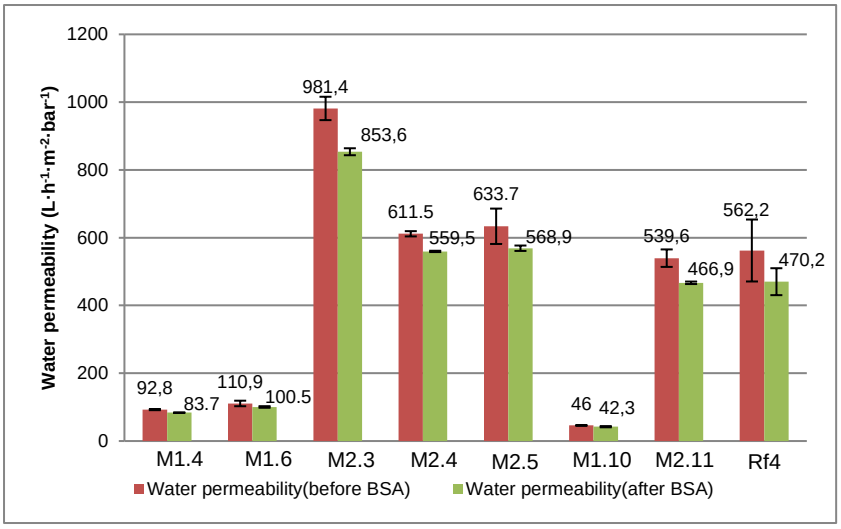

Fig. 81 Comparison of water permeability before and after BSA filtration for **M1.4**, **M1.6**, **M2.3**-**M2.5**, **M1.10**, **M2.11** and **Rf4**.

By comparison of RFR in **Fig. 82**, it is quite clear to see that **Rf4** with 1 wt.% PVP showed stronger fouling than rest membranes with single $PMMA_m$-*b*-$PSPE_n$ or combination of $PMMA_m$-*b*-$PSPE_n$ and PVP due to its less surface hydrophilicity and bigger mean pore size relative to BSA diameter, as detailed analyzed previously in **6.1.7.2.**.

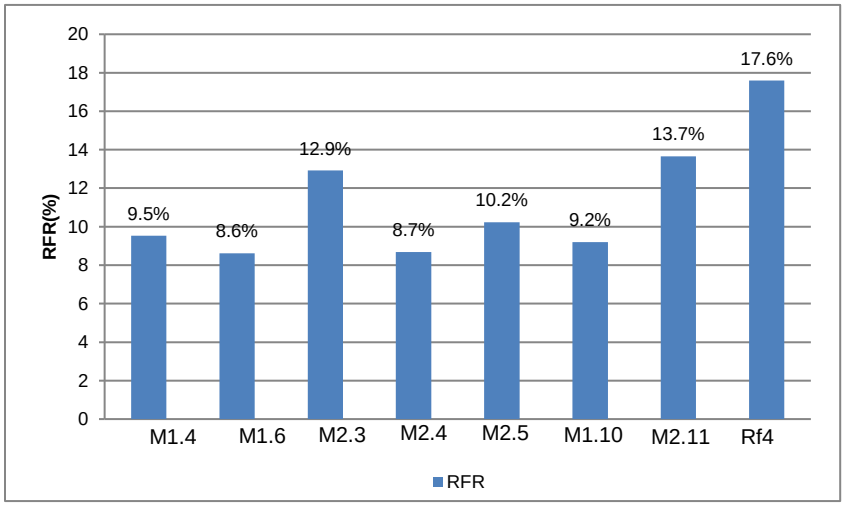

Fig. 82 Comparison of relative flux reduction (RFR) for **M1.4**, **M1.6**, **M2.3**-**M2.5**, **M1.10**, **M2.11** and **Rf4**.

M1.4, **M1.6** and **M1.10** that contained 1 wt.% $PMMA_m$-*b*-$PSPE_n$ with various M_n and ratios of PMMA / PSPE showed lower RFR because the doped $PMMA_m$-*b*-$PSPE_n$ improved the formation of smaller pore size relative to BSA diameter and highly enhanced the surface hydrophilicity and protein resistance by means of exposed PSPE block on the surface and inner pore walls (the detailed discussion, cf. **6.1.7.2.**).

Since the doped $PMMA_m$-*b*-$PSPE_n$ respectively in **M1.4**, **M1.6**, **M2.3**, **M2.4** and **M2.5** had similar M_n and ratio of PMMA / PSPE, it was more reasonable to compare and discuss the RFR difference for these membranes firstly. It can be clearly concluded that **M2.3** that contained 1 wt.% $PMMA_{300}$-*b*-$PSPE_{38.1}$ (similar to ones involved in **M1.4** and **M1.6**) and 1 wt.%PVP originated relatively bigger mean pore size and higher porosity than **M1.4** and **M1.6** due to the above discussed synergy effect from $PMMA_m$-*b*-$PSPE_n$ and PVP, which also can be verified by the enhanced WP and relatively slightly lower BSA rejection of **M2.3**. Consequently, the higher RFR of **M2.3** relative to **M1.4** and **M1.6** can be mainly attributed to the BSA deposition and adsorption in inner pores and the following pore narrowing or slight pore-plugging brought by the relatively bigger pore size of **M2.3**, in spite of the high surface protein resistance brought by surface-exposed PSPE block. 1 wt.% $PMMA_{300}$-*b*-$PSPE_{38.1}$ in **M2.3** can not offer sufficient offsetting influence against 1 wt.%PVP effect to form the proper pore size for sieving BSA protein

molecules. In **M2.4**, involvement of $PMMA_{300}$-*b*-$PSPE_{38.1}$ was raised to 2 wt.% in order to further balance the pore-forming effect of 1 wt.%PVP and pursue the optimized pore size and porosity. The resultant RFR of **M2.4** was quite low and comparable to that of **M1.4** and **M1.6**, which strongly implied that the smaller pore size relative to BSA diameter was realized and the strong fouling brought by pore narrowing and pore-plugging was further relieved also considering the high BSA rejection of **M2.4**. It is reasonable to ascribe the RFR of **M2.4** mainly to the slightly formed gel layer on membrane surface. **M2.5** that contained similar content and types of additives to **M2.4** showed slightly more RFR than **M2.4**, **M1.4** and **M1.6**, which perhaps can be explained as some operational error or membrane heterogeneity. But anyway, the **M2.5** still showed quite apparently lower RFR compared with **M2.3**, which rationally indicated the 2 wt.% $PMMA_{300}$-*b*-$PSPE_{36.4}$ and 1 wt.PVP performed well to bring about optimized synergy and support better resistance on protein fouling.

M1.10 and **M2.11** contained the same zwitterionic additive, 1 wt.% $PMMA_{94}$-*b*-$PSPE_{261}$. However the synergy of 1 wt.% $PMMA_{94}$-*b*-$PSPE_{261}$ and 1 wt.%PVP in **M2.11** can not well balance the pore-forming effect of PVP and thus created the relatively bigger mean pore size, which can be evidenced by the higher RFR and relatively low BSA rejection of **M2.11** in contrast to **M1.10** that contained single 1 wt.% $PMMA_{94}$-*b*-$PSPE_{261}$. This was well in agreement with above RFR result of **M2.3** and strongly supported the above discussion of synergy effect on fouling resistance.

In general, all the tested membranes with single or combined $PMMA_m$-*b*-$PSPE_n$ showed lower RFR and better protein fouling resistance than **Rf4** with merely PVP additive due to the better protein resistance from exposed zwitterionic PSPE block on membrane surface and inner pore walls. **M2.3** and **M2.11** that contained 1 wt.% $PMMA_m$-*b*-$PSPE_n$ and 1 wt.%PVP displayed higher fouling than **M1.4**, **M1.6** and **M1.10** with single 1 wt.% $PMMA_m$-*b*-$PSPE_n$ that respectively had similar or same M_n and ratios of PMMA/ PSPE to that involved in **M2.3** and **M2.11**. **M2.4** that contained 2 wt.% $PMMA_{300}$-*b*-$PSPE_{38.1}$ and 1 wt.%PVP (K30) showed the best fouling resistance on BSA protein.

6.2.2. PVDF membranes with other combination of two additives

In order to further study the synergy effect of combinaed additives, three dope solutions of PVDF membranes with combinations of two additives different from their counterparts in **6.2.1.** were prepared, as shown in **Table 22**. In membrane **M2.8**, 1.5 wt.% $PMMA_{300}$-*b*-$PSPE_{566}$ with quite long PSPE block and 2 wt.% small molecule additive glycol were doped with PVDF as casting solution. Glycol is helpful to improve solubility of PSPE block in organic solvent. 2 wt.% $PMMA_{300}$-

b-$PSPE_{38.1}$ with short PSPE block and 1 wt.% PEG as second additive were employed in membrane **M2.9** dope solution. 2wt.% PMMA and 1wt.% PVP (K30) were combined as additives utilized in membrane **M2.10** dope solution. The procedure of NIPS for all the membrane here (**M2.8** to **M2.10**) had same parameters of casting speed and humidity. The corresponding viscosity data for dope solutions were also tabulated in **Table 22** and further discussed in **6.2.2.1.**.

Code	ADD.I (wt.%)	ADD.I M_n(g/mol)	ADD.I Ratio (PMMA/ PSPE)	ADD.II (wt.%)	ADD.II M_w(g/mol)	PVDF LMW (wt.%)	[b]Viscosity (Pa.s)
M2.8	$(PMMA)_{300}$-*b*-($PSPE)_{566}$ 1.5	188000	0.5	Glycol 2	62	16	2.12±0.05
M2.9	$(PMMA)_{300}$-*b*-$(PSPE)_{38.1}$ 2	40600	7.7	PEG 1	12000	16	3.56±0.01
M2.10	$(PMMA)_{682}$ 2	68200	N/A	PVP(K30) 1	14000	16	4.04±0.12

Table 22 Dope solutions of PVDF membranes containing $PMMA_m$-*b*-$PSPE_n$ (M_n of PMMA= 30 kg/mol) or PMMA (M_n= 68 kg/mol) combined with different doping concentrations, and glycol, PEG or PVP which were respectively employed as second additives. Membrane matrix material was PVDF (M_w= 48.1 kg/mol). Solvent were NMP. Coagulation bath were deionized water. Temperature of casting plate and coagulation were r.t.. The speed of casting knife were 5mm/s and humidity were less than 20.0% during casting. [a]**M2.10** contained PMMA and PVP in dope solution without $PMMA_m$-*b*-$PSPE_n$. [b]Viscosity (@r.t.) of the listed PVDF membrane dope solutions were also tabulated. Shear rate fixed to 25 [1/s]..

6.2.2.1. Rheology

At r.t. membrane **M2.8** dope solution which contained 1.5 wt.% $PMMA_{300}$-*b*-$PSPE_{566}$ with quite long PSPE block and 2wt.% small molecule additive glycol showed the lowest viscosity in **Table 22**. But compared with viscosity of dope **M1.8** that contained single additive of 1.5 wt.% $PMMA_{300}$-*b*-$PSPE_{566}$ (cf. **6.1.2.**, 2.00±0.05), the viscosity of **M2.8** was apparently enhanced due to the addition of nonsolvent glycol that perhaps slightly improved the solubility of $PMMA_{300}$-*b*-$PSPE_{566}$ or maybe formed hydrogen bond with $PMMA_{300}$-*b*-$PSPE_{566}$ to bring increasing viscosity of dope **M2.8**. Dope solution of **M2.9** which contained 2 wt.% $PMMA_{300}$-*b*-$PSPE_{38.1}$ (PMMA/PSPE= 7.7) with short PSPE block and 1 wt.% PEG exhibited improved viscosity, like the dope solutions of **M2.4** and **M2.5** which had similar $PMMA_m$-*b*-$PSPE_n$ (PMMA/PSPE= m/n= 7.7 and 8.3) to **M2.9**. Compared with **M2.8** and **M2.9**, the highest viscosity was obtained in dope solution of **M2.10** which had 2 wt.% PMMA with a higher M_n and 1 wt.% PVP (K30). The high molecular weight PMMA apparently increased the viscosity of **M2.10** dope solution.

6.2.2.2. Typical SEM morphologies

Cross sections, top surface, detailed top surface of typical membranes were scanned with SEM and shown.

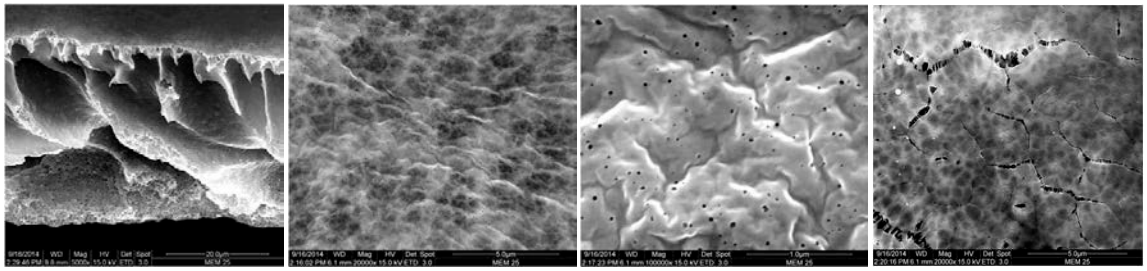

Fig. 83 Membrane **M2.8** ($PMMA_{300}$-*b*-$PSPE_{566}$ 1.5 wt.%, glycol 2 wt.%, PVDF 16 wt.%). From left to right: Cross section (Mag.5k), top surface (Mag.20k), top surface (Mag.100k), back surface (Mag.20k).

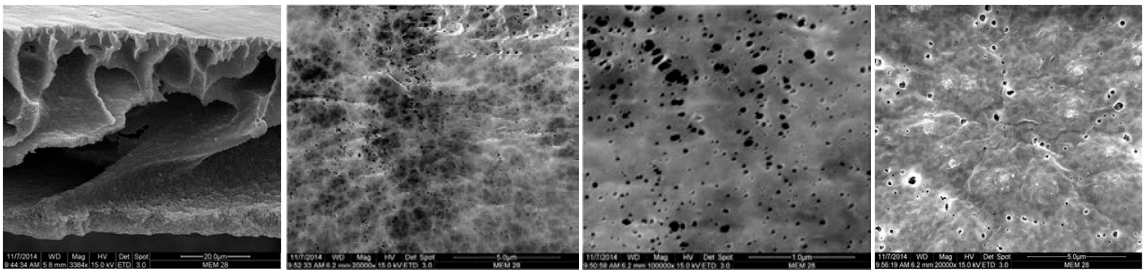

Fig. 84 Membrane **M2.9** ($PMMA_{300}$-*b*-$PSPE_{38.1}$ 2 wt.%, PEG 1 wt.%, PVDF 16 wt.%). From left to right: Cross section (Mag.3k), top surface (Mag.20k), top surface (Mag.100k), back surface (Mag.20k).

Glycol was widely employed as nonsolvent additive of small molecules to enhance membrane porosity. In dope solution of **M2.8**, 2 wt.% glycol and 1.5 wt.% $PMMA_{300}$-*b*-$PSPE_{566}$ were applied as additives to explore the effect on membrane formation. The continuous PVDF phase and interconnected pore structures still originated in the cross section region of **M2.8** (**Fig. 83**) and evidenced the dominant instantaneous liquid-liquid demixing and the following nucleation as well as growth during the membrane formation. The glycol was able to form strong hydrogen bond with $PMMA_{300}$-*b*-$PSPE_{566}$ and further increased the cost for surface migration of $PMMA_{300}$-*b*-$PSPE_{566}$ that had already experienced big conformational entropy penalty for surface migration in casting film due to the relatively big molecular weight. Hence the facilitated influence of $PMMA_{300}$-*b*-$PSPE_{566}$ on the precipitation rate of polymer-rich phase was relatively neutralized to some extent. However, due to the lower additional amount and fact of small molecules, glycol contributed limited effect on the precipitation kinetics, in comparison with polymer PVP. The less suppressed macrovoids and some distinct big pores can more or less support the above

deduction. The wrinkles on the top surface of **M2.8** also indicated the still relatively low porosity in top layer and relatively increased out-flow of solvent due to insufficient offsetting effect of glycol on the $PMMA_{300}$-*b*-$PSPE_{566}$. Compared with **M1.8**, water permeability showed no apparent enhancement and also can offer another illustration for above discussion.

In dope solution of **M2.9**, 1 wt.%PEG was applied as additive to be combined with 2 wt.% $PMMA_{300}$-*b*-$PSPE_{38.1}$ that had short PSPE block. Similar to PVP, PEG also prevailed as strong pore-forming and hydrophilic agents in preparation of membrane.[126] **M2.9** also retained the continuous PVDF phase and interconnected pore structures still originated in the cross section region of **M2.9** (**Fig. 84**) and indicated the dominant instantaneous liquid-liquid demixing and the following nucleation as well as growth during the membrane formation. The open porous macrovoids in cross section of **M2.9** signified the PEG performed the similar influence on the precipitation kinetics of polymer-rich phase and nucleation growth to PVP. However the numerous apparent big defects on the top surface pointed out the limitation of PEG utilization, the excessive flexibility of PEG molecular chains in aqueous environment donated too much interference on the vitrification process of PVDF and resulted in the generation of defects on the top surface of **M2.9**.[90] The absence of wrinkles on the top surface also substantiated the above speculation. The highly enhanced water permeability of **M2.9** was in agreement with the explanation of morphology.

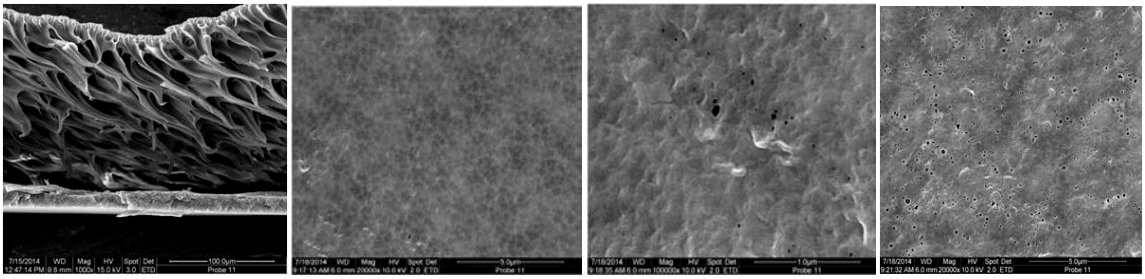

Fig. 85 Membrane **M2.10** ($PMMA_{682}$ 2 wt.%, PVP k30 1 wt.%, PVDF 16 wt.%). From left to right: Cross section (Mag.3k), top surface (Mag.20k), top surface (Mag.100k), back surface (Mag.20k).

2 wt.% $PMMA_{682}$ and 1 wt.%PVP were employed in dope solution of **M2.10** to examine the influence of combined homopolymer PMMA and PVP on the membrane formation. The cross section of **M2.10** showed the continuous PVDF phase with infrequent layers. The top surface of **M2.10** originated numerous large defects (the SEM of **Fig. 85** showed some selected smooth region) that almost resulted in the uselessness of **M2.10**. Perhaps the migration and entanglement of $PMMA_{682}$ that had relatively large molecular weight plus rapid out-diffusion of PVP made the rearrangement and thus solidification of PVDF molecular chains highly intervened

and therefore the excessively retarded precipitation rate led to the morphology of **M2.10** with too much defects and irregular cross section. The water permeability examined from a few region of **M2.10** without defects was high.

6.2.2.3. Contact angle

M2.8 displayed low CA (below 40º), but this value was still higher than **M1.8** that contained 1 wt.% single $PMMA_{300}$-*b*-$PSPE_{566}$. Perhaps the formation of hydrogen bond between $PMMA_{300}$-*b*-$PSPE_{566}$ and glycol offered some slight inhibition on the surface migration and thus led to a little decreased surface hydrophilicity. **M2.9** contained same 2 wt.% $PMMA_{300}$-*b*-$PSPE_{38.1}$ as **M2.4**, however the CA of **M2.9** was much higher than **M2.4**, which might be attributed to the difference between PVP and PEG. PEG molecular chains were more flexible than PVP and thus more PEG were prone to migrate out of surface instead of entrapment along the surface. As a result, the fewer residue of PEG on the surface gave less contribution to the hydrophilicity compared with PVP that showed slightly more surface residue. **M2.10** that had combination of large molecular weight PMMA and PVP showed a CA over 40º and indicated a less surface hydrophilicity than membranes with $PMMA_m$-*b*-$PSPE_n$ and PVP.

Code	ADD.I (wt.%)	ADD.I M_n(g/mol)	ADD.I Ratio (PMMA/ PSPE)	ADD.II (wt.%)	ADD.II M_w(g/mol)	PVDF LMW (wt.%)	[a]Top Contact angle (º)
M2.8	$(PMMA)_{300}$-*b*-($PSPE)_{566}$ 1.5	188000	0.5	Glycol 2	62	16	39.5±0.5
M2.9	$(PMMA)_{300}$-*b*-$(PSPE)_{38.1}$ 2	40600	7.7	PEG 1	12000	16	43.6±0.7
M2.10	$(PMMA)_{682}$ 2	68200	N/A	PVP(K30) 1	14000	16	42.4±1.4

Table 23 Contact angle values at r.t. of PVDF membranes containing $PMMA_m$-*b*-$PSPE_n$ ($M_{n\ PMMA}$= 30 kg/mol) or PMMA (M_n=68 kg/mol) combined with other second additives. Method was captive bubble. [a]Only contact angle value of PVDF membrane top surface (functional surface) were showed here.

6.2.2.4. Membrane performance

As shown in **Table 24**, Membrane **M2.8** which contained 1.5 wt.% $PMMA_{300}$-*b*-$PSPE_{566}$ with quite long PSPE block and 2wt.% small molecule additive glycol demonstrated the quite low water permeability (WP) and high BSA rejection. The sieving performance of **M2.8** was similar to aforementioned membranes **M1.8** that had single additive 1.5wt.% $PMMA_{300}$-*b*-$PSPE_{566}$, whereas the WP of **M2.8** was decreased compared with **M1.8**. The small molecule hydrophilic additive glycol failed to form synergy with $PMMA_{300}$-*b*-$PSPE_{566}$ in **M2.8**, perhaps partly because the strong

hydrogen bonding interaction between glycol and zwitterionic block copolymer that limited the synergy. **M2.9** which doped 1 wt.% PEG and 2wt.% $PMMA_{300}$-*b*-$PSPE_{38.1}$ with short PSPE block originated quite high water permeability but a BSA rejection less than 90%. The water permeability of **M2.9** was even slightly higher than **M2.4** that contained same 2 wt.% $PMMA_{300}$-*b*-$PSPE_{38.1}$ but 1 wt.% PVP (K30), whereas the BSA rejection of **M2.9** was much lower than **M2.4** as a result of involving PEG instead of PVP as second additive. Apparently, the synergy effect also occurred in the case of **M2.9**. Nevertheless, in the presence of the stronger pore-forming effect of PEG than PVP, 2 wt.% $PMMA_{300}$-*b*-$PSPE_{38.1}$ obviously was not adequate to offset the PEG effect and supply a satisfied control on the mean pore size of **M2.9**. Consequently, bigger mean pore size and more defects on membrane surface generated as shown in **6.2.2.2.**, and the sieving performance was decreased. **M2.10** which contained 2 wt.% PMMA with high M_n and 1 wt.% PVP (K30) also obtained improved water permeability and high BSA rejection. However, too much defects were yielded on **M2.10** surface that meant uselessness of this membrane.

Code	ADD.I (wt.%)	ADD.I M_n(g/mol)	ADD.I Ratio (PMMA/ PSPE)	ADD.II (wt.%)	ADD.II M_w(g/mol)	PVDF LMW (wt.%)	Water permeability ($L \cdot h^{-1} \cdot m^{-2} \cdot bar^{-1}$)	BSA Rejection (%)
M2.8	$(PMMA)_{300}$-*b*-($PSPE)_{566}$ 1.5	188000	0.5	Glycol 2	62	16	93.0±26.3	93.0±0.7
M2.9	$(PMMA)_{300}$-*b*-$(PSPE)_{38.1}$ 2	40600	7.7	PEG 1	12000	16	698.6±55.3	85.0±0
M2.10	$(PMMA)_{682}$ 2	68200	N/A	PVP(K30) 1	14000	16	585.3±10.1	90.0±2.3

Table 24 Water permeability and BSA rejection at r.t. of PVDF membranes containing $PMMA_m$-*b*-$PSPE_n$ ($M_{n\ PMMA}$ = 30 kg/mol) or PMMA (M_n= 68 kg/mol) combined with other second additives. BSA concentration was 1 mg/mL; pH value of BSA buffer solution was fixed at 7.0..

6.2.3. Optimized prototype of PVDF membrane with $PMMA_m$-*b*-$PSPE_n$ and PVP

M2.4 was selected as optimized prototype membrane in view of its outstanding performance parameters that reached the corresponding target value of NANOPUR project, as shown in **Table 25**. The main targets of NANOPUR projects for prepared ultrafiltration membrane included the water permeability $\geqq$ 500$L \cdot m^{-2} \cdot h^{-1} \cdot bar^{-1}$, MWCO $\leqq$ 100kDa, and contact angle $\leqq$ 40º. By comparison to the performance parameter of **M2.4** in **Table 25**, it is quite clear to find that **M2.4** showed much higher water permeability and quite lower contact angle. The MWCO of **M2.4** was merely higher than 100 KDa, but the measured value of 120±20kDa was quite close to the target. The pretty high BSA rejection (93% for $M_{w\ BSA}$= 67 kg/mol) and low RFR for dynamic fouling tests displayed the strong membrane resistance of **M2.4** for BSA protein fouling during the BSA filtration conditions. In particular it should be noted that, under the high TMP 0.2bar

(corresponding to 120 $L \cdot m^{-2} \cdot h^{-1}$ initial flux), 16.8% RFR of **M2.4** was still can be available. On one hand, this strongly indicated that the mean pore size of **M2.4** was quite smaller relative to BSA diameter and prevented most of BSA solute from permeating through pore channels of membrane even under the relative high TMP (0.2 bar) that perhaps led to the deformation of BSA globular molecules to smaller size. On the other hand, in presence of surface-exposed zwitterionic PSPE with highly protein resistance, the BSA adsorptive fouling on the surface and inner pore walls of **M2.4** was remarkably minimized.

Composition of M2.4	**Water permeability ($L \cdot m^{-2} \cdot h^{-1} \cdot bar^{-1}$) (@0.5bar)**	**BSA rejection (%)**	**MWCO (kDa)**	**Contact angle [°]**	**RFR(%) of dynamic BSA fouling test @0.03bar, J=20 $L \cdot m^{-2} \cdot h^{-1}$**	**RFR(%) of dynamic BSA fouling test @0.2bar, J=120 $L \cdot m^{-2} \cdot h^{-1}$**
PVDF (16wt.%); $PMMA_{300}$-*b*-$PSPE_{38.1}$ (M_n= 40.6 kg/mol, PMMA:PSPE=7.7) (2wt.%) ; PVP (K30) (1wt.%)	611.5±7.8	93.5±0	120±20	33.3±1.5	8.7	16.8

Table 25 Membrane performance of **M2.4**. BSA solution concentration was 1 mg/ml; pH value of BSA buffer solution fixed at 7.0. Concentration of dextran solution for molecular weight cut-off (MW-CO) was 1mg/ml. The method for contact angle measurement was captive bubble. The dynamic fouling was tested respectively at initial flux 20 and 120 $L \cdot m^{-2} \cdot h^{-1}$ under TMP 0.03 and 0.2bar.

7. PVDF membranes with $PMMA_m$-*b*-$PDMAEMA_n$ and their surface modification

Membrane **MS.1** and **MS.2** contained respectively 2 wt.% $PMMA_{539}$-*b*-$PDMAEMA_{350}$ or 2 wt.% $PMMA_{539}$-*b*-$PDMAEMA_{173}$ and 17.5 wt.% PVDF. $PMMA_m$-*b*-$PDMAEMA_n$ was also amphiphilic block copolymer with property of surface segregation during NIPS.[64] The PDMAEMA block which exposed on the surface of PVDF membranes can be further converted to PSPE groups via heterogeneous surface modification.[110]

Code	Add. (wt.%)	Add. M_n (g/mol)	Ratio PMMA:PDMAEMA	PVDF (wt.%)	Coagulation bath T(ºC)
MS.1	$(PMMA)_{539}$-*b*-$(PDMAEMA)_{350}$ 2	108200	1.5	17.5	DI water r.t.
MS.2	$(PMMA)_{539}$-*b*-$(PDMAEMA)_{173}$ 2	80700	3.1	17.5	DI water r.t.

Table 26 PVDF membrane dope solutions with $PMMA_m$-*b*-$PDMAEMA_n$ ($M_{n\ PMMA}$ = 53.9 kg/mol). Temperature of casting plate was r.t.. Solvent for dope solutions were NMP.

7.1. SEM morphologies

Cross sections, top surface, detailed top surface of typical membranes were scanned with SEM and shown.

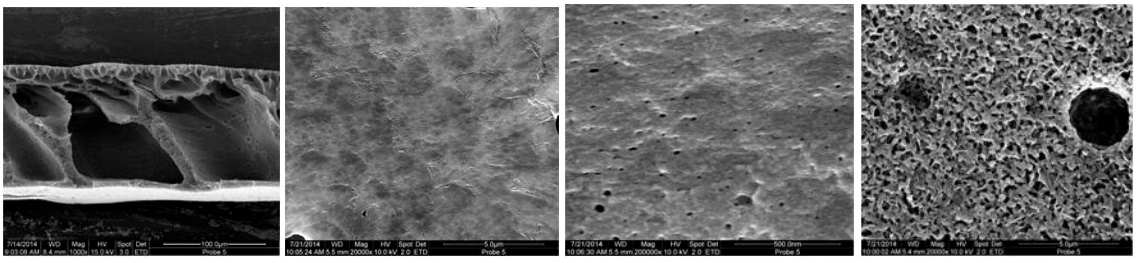

Fig. 86 Membrane **MS.1** ($PMMA_{539}$-*b*-$PDMAEMA_{350}$ 2 wt.%, PVDF 17.5 wt.%). From left to right: Cross section (Mag.1k), top surface (Mag.20k), top surface (Mag.200k), back surface (Mag.20k).

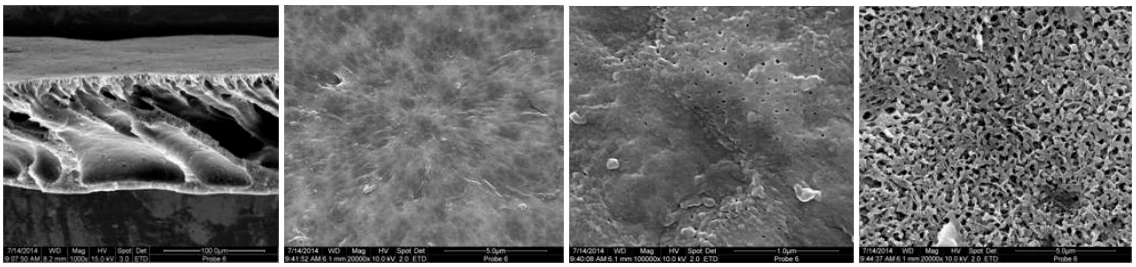

Fig. 87 Membrane **MS.1** after surface modification. From left to right: Cross section (Mag.1k), top surface (Mag.20k), top surface (Mag.100k), back surface (Mag.20k).

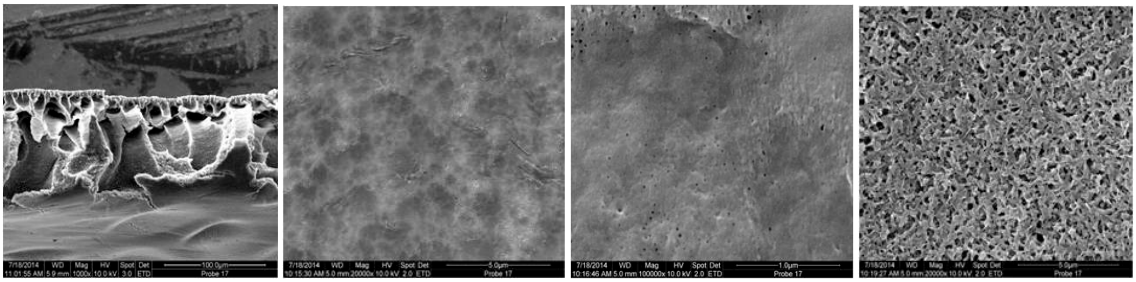

Fig. 88 Membrane **MS.2** ($PMMA_{539}$-*b*-$PDMAEMA_{173}$ 2 wt.%, PVDF 17.5 wt.%). From left to right: Cross section (Mag.1k), top surface (Mag.20k), top surface (Mag.200k), back surface (Mag.20k).

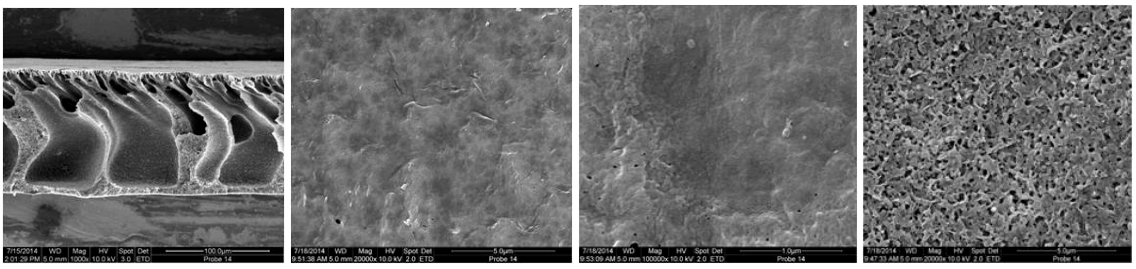

Fig. 89 Membrane **MS.2** after surface modification. From left to right: Cross section (Mag.1k), top surface (Mag.20k), top surface (Mag.100k), back surface (Mag.20k).

In dope solutions of **MS.1** and **MS.2**, 2 wt.% $PMMA_{539}$-*b*-$PDMAEMA_{350}$ and 2 wt.% $PMMA_{539}$-*b*-$PDMAEMA_{173}$, as single additive repectively, were employed. The continuous PVDF phase and interconnected pore structures still generated in the cross section region of **MS.1** and **MS.2** (**Fig. 86** and **Fig. 88**) and implied the dominant instantaneous liquid-liquid demixing and the following nucleation as well as growth during the membrane formation. The macrovoids of **MS.1** and **MS.2** gained full development in the width and length, while the top surface of **MS.1** and **MS.2** were basically smooth except for several limited distinct big pores. Due to the surface migration of flexible $PMMA_m$-*b*-$PDMAEMA_n$ chains as well as resultant strong diffusion exchanging rate by raised hydrophilicity matrix polymer and relatively large molecular weight of $PMMA_{539}$-*b*-

$PDMAEMA_{350}$ and $PMMA_{539}$-*b*-$PDMAEMA_{173}$, the precipitation rate of polymer-rich phase was largely disturbed and retarded, which rendered more time to the formation of porous structure (nucleation and growth) in the top layer and sublayer of casting film. The relatively extended distance from the top surface to the onset of macrovoids also contributed some support to the enhancement of porosity in top layer. The huge water permeability of **MS.1** and **MS.2** also agreed with the morphology analysis. In contrast to **MS.1** and **MS.2**, **MS.1** after surface modification and **MS.2** after modification showed slightly fewer big pores on the top surface and virtually unchanged macrovoids structure.

7.2. ATR-FTIR spectra

There is no absorption signals of stretching vibration from C=O (of carboxylate) or S=O (of SO_3^-) in ATR-FTIR spectrum of pure PVDF membrane. The characteristic absorption peak of C=O stretching vibration around 1719 cm^{-1} from carboxylate side chains of PMMA and PDMAEMA can be clearly identified in ATR-FTIR spectrum of PVDF membrane with $PMMA_m$-*b*-$PDMAEMA_n$, which evidenced the exposure of PDMAEMA block on the top surface of PVDF membrane. The characteristic absorption peaks of C=O stretching vibration (~1719 cm^{-1}) and S=O stretching vibration (1024-1034 cm^{-1}) from side chains of PMMA and zwittterionic PSPE block (betainized PDMAEMA block) appeared in ATR-FTIR spectrum of PVDF membrane with $PMMA_m$-*b*-$PDMAEMA_n$ after surface modification. Appearance of S=O (SO_3^-) strongly designated that, the PDMAEMA that exposed on the PVDF matrix membrane surface were successfully betainized to zwitterionic PSPE by means of surface modification process.

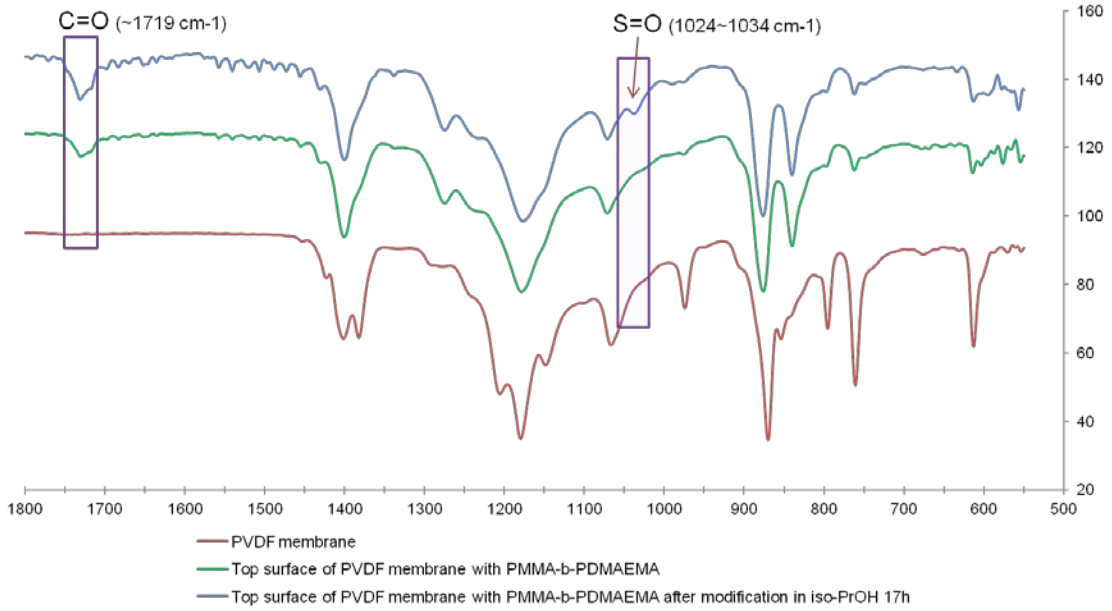

Fig. 90 Comparison of typical ATR-FTIR of top surfaces from pure PVDF membrane and PVDF membranes with $PMMA_m$-*b*-$PDMAEMA_n$ ($M_{n\ PMMA}$= 53.9 kg/mol) before and after surface modification. The selected membrane sample was from **MS.1** before and after surface modification.

7.3. Membrane performance

As shown in **Table 27**, membrane **MS.1** that doped 2 wt.% $PMMA_{539}$-*b*-$PDMAEMA_{350}$ with long PDMAEMA block generated quite huge water permeability and pretty low BSA rejection before surface modification, which can be attributed to the enhanced diffusion exchanging rate and strong interference on matrix polymer precipitation rate arisen from $PMMA_{539}$-*b*-$PDMAEMA_{350}$ with high molecular weight and long hydrophilic PDMAEMA block. The water permeability of **MS.1** after surface modification was decreased apparently although indeed it was still quite large, and the BSA rejection of **MS.1** also showed trivial increment after surface modification, which indicated that PDMAEMA block exposed on **MS.1** surface were exactly sulfo-betainized. Nevertheless partly due to the too big initial pore size and the limitation of surface modification as a post-treatment method, the sieving performance after surface modification merely gained slight enhancement as shown in **Fig. 91**.

Code	Add.(wt.%)	Add. M_n (g/mol)	Ratio PMMA/ PDMAEMA	PVDF (wt.%)	Coagulation bath T(°C)	Water permeability ($L \cdot h^{-1} \cdot m^{-2} \cdot bar^{-1}$) (before)	Water permeability ($L \cdot h^{-1} \cdot m^{-2} \cdot bar^{-1}$) (after)	BSA Rejection (%) (before)	BSA Rejection (%) (after)
MS.1	$(PMMA)_{539}$-*b*-$(PDMAEMA)_{350}$ 2	108200	1.5	17.5	DI water r.t.	5608.6±192.2	3123.9±276.3	12.2±0	16.9±0
MS.2	$(PMMA)_{539}$-*b*-$(PDMAEMA)_{173}$ 2	80700	3.1	17.5	DI water r.t.	1645.9±152.7	613.7±98.1	44.7±0	75.2±0

Table 27 Comparison of water permeability and BSA rejection at r.t. of PVDF membranes with $PMMA_m$-*b*-$PDMAEMA_n$ ($M_{n\ PMMA}$ = 53.9 kg/mol) before and after surface modification. BSA concentration was 1 mg/ml; pH value of BSA buffer solution fixed at 7.0.

Membrane **MS.2** that contained 2 wt.% $PMMA_{539}$-*b*-$PDMAEMA_{173}$ with relatively shorter PDMAEMA block showed decreased water permeability and enhanced BSA rejection compared with **MS.1** due to the lessened effect from the shorter PDMAEMA block of $PMMA_{539}$-*b*-$PDMAEMA_{173}$. After surface modification the water permeability of **MS.2** was sharply decreased, whereas the BSA rejection of **MS.2** was largely raised to 75%, which significantly indicated the $PMMA_{539}$-*b*-$PDMAEMA_{173}$ with relatively short PDMAEMA block brought about the more effective surface modification than **MS.1** as can be clearly seen in **Fig. 91**. The relatively smaller pore size of **MS.2** should be one of the key factor for the better modified performance. In addition, the strong protein adsorption of PDMAEMA also gave some contribution to the BSA retention results from **MS.1** and **MS.2**,[123] and this limited the accuracy of investigation for the surface modification (betainization) of membranes with $PMMA_m$-*b*-$PDMAEMA_n$.

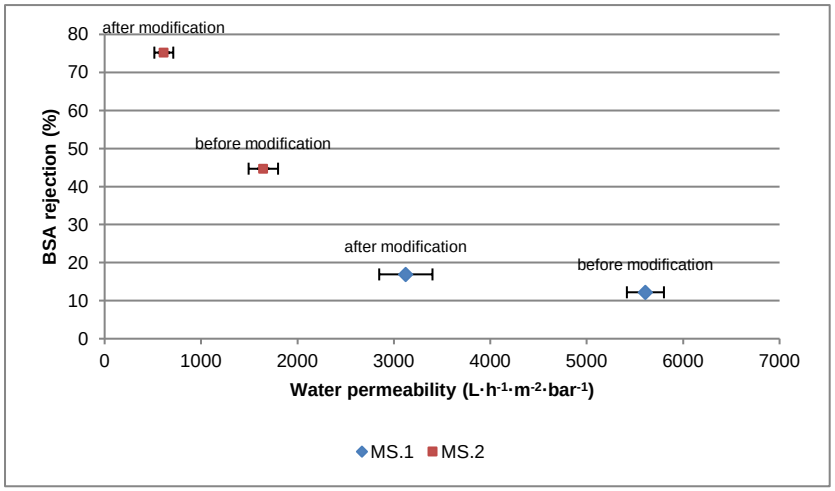

Fig. 91 BSA rejection before and after surface modification for **MS.1** and **MS.2** as a function of corresponding water permeability.

8. Conclusions

The method of free radical copolymerization for synthesis of $PMMA_m$-*co*-$PSPE_n$ was build up and $PMMA_{188}$-*co*-$PSPE_{16.5}$ was successfully synthesized with monomer of MMA and SPE in DMSO solvent. The two-steps sequential ATRP procedures for synthesis of precursor $PMMA_m$-*b*-$PDMAEMA_n$ with different M_n and various ratios of PMMA / PDMAEMA were also established. And via the following sulfo-betainization, various $PMMA_m$-*b*-$PDMAEMA_n$ were successfully converted to corresponding $PMMA_m$-*b*-$PSPE_n$. The prepared $PMMA_m$-*co*-$PSPE_n$ and $PMMA_m$-*b*-$PSPE_n$ were well characterized and their structures were confirmed via ^{1}H-NMR, ATR-FTIR, GPC and elemental analysis. Three types of ATRP catalyst systems with different ligands, i.e. Cu(I)Br/PMDETA, Cu(I)Br/$(Bipyridine)_2$ and Cu(I)Br/$(dN\text{-}Bipyridine)_2$, were compared and applied for synthesis of PMMA-Br macro initiator with various molecular weights. The end-functional bromine of PMMA-Br was well preserved through application of Cu(I)Br/$(Bipyridine)_2$ and Cu(I)Br/$(dN\text{-}Bipyridine)_2$ with finely adjusted ATRP parameters. The methods for synthesis of different $PMMA_m$-*b*-$PDMAEMA_n$ and the following sulfo-betainization showed excellent reliability and reproducibility. The finally synthesized $PMMA_m$-*b*-$PSPE_n$ (m= 139, 300, 94, 539; m/n= 0.3-20) with proper control of molecular weight and PDI met the requirement as diverse additives for the further general examination of their influences on PVDF membrane.

Dope solutions that contained 17.5 wt.% PVDF and respectively 2 wt.% $PMMA_{188}$-*co*-$PSPE_{16.5}$, 2 wt.% $PMMA_{139}$-*b*-$PSPE_{12.5}$, 2 wt.% PVP (K30) were successfully applied to prepare asymmetric UF membranes **M1.1**, **M1.2** and **Rf1** via nonsolvent induced phase separation (NIPS). Largely improved surface hydrophilicity were observed through the low contact angle values (CA) of **M1.1** and **M1.2** (CA below 40º). PSPE block of $PMMA_{188}$-*co*-$PSPE_{16.5}$ as well as $PMMA_{139}$-*b*-$PSPE_{12.5}$ and PVP that respectively enriched on the membrane top surface of **M1.1**, **M1.2** and **Rf1** by preferential surface migration were firmly verified via ATR-FTIR. Involvement of $PMMA_{139}$-*b*-$PSPE_{12.5}$ largely facilitated the precipitation kinetics of PVDF matrix polymer during coagulation of **M1.2**, and thus created the lowest water permeability and the highest BSA rejection of **M1.2** due to the resultant reduced pore size and remarkably decreased porosity. **M1.1** showed lower water permeability but higher BSA rejection compared with **Rf1**. **M1.2** also displayed the lowest RFR after BSA filtration and slow rate of flux decline during BSA filtration, which indicated the strong BSA fouling resistance of **M1.2**. The zwitterionic groups of PSPE block in $PMMA_{139}$-*b*-$PSPE_{12.5}$ that exposed on **M1.2** membrane surface gave rise to hydrogen-bonding network of water molecules resembling natural bulk water and further piled to form hydration shell as energy barrier against adsorption of BSA protein molecules and thus supplied improved anti-fouling ability. **M1.1** showed higher RFR and **Rf1** displayed the most serious BSA fouling. Generally,

involved zwitterionic $PMMA_{139}$-*b*-$PSPE_{12.5}$, contributed distinct positive influences, i.e. higher sieving and protein fouling resistance, to improve the performance of the corresponding PVDF membrane, whereas traditionally commercial PVP additive showed quite limited enhancement on PVDF membrane performance. Due to the architectural difference on arrangement of PSPE, random copolymer $PMMA_{188}$-*co*-$PSPE_{16.5}$ promoted less membrane performance than block copolymer $PMMA_{139}$-*b*-$PSPE_{12.5}$ except the higher water permeability.

Asymmetric membranes **M1.3**-**M1.12** were successfully prepared respectively with blends of 0.5-1.5 wt.% $PMMA_m$-*b*-$PSPE_n$ (m= 94, 300; m/n= 0.3-12.5) and 16 wt.% PVDF via NIPS. Membranes **Rf3**-**Rf8** were also prepared respectively with blends of 0.5-3 wt.% PVP (K30) and 16 wt.% PVDF via NIPS. All the membranes with single $PMMA_m$-*b*-$PSPE_n$ (**M1.3**-**M1.12**) showed strongly improved top surface hydrophilicity (CA below 40º). Bigger CA caused by less hydrophilicity was observed for membranes **Rf3**-**Rf8** with PVP (K30). The apparent surface segregation (exposure) of PSPE block from $PMMA_m$-*b*-$PSPE_n$ and PVP was strongly confirmed via ATR-FTIR and XPS. All the membranes involved single $PMMA_m$-*b*-$PSPE_n$ with different M_n and various PMMA / PSPE (**M1.3**-**M1.12**) exhibited relatively low water permeability and high BSA rejection (≧90%) compared with membranes with PVP (K30), which were in well agreement with performance of **M1.2** and strongly supported the facilitated the precipitation kinetics of PVDF matrix polymer driven by additive $PMMA_m$-*b*-$PSPE_n$ during coagulation as mechanism explanation of membrane performance. The selected membranes (**M1.4**, **M1.6**, **M1.7**, **M1.9** and **M1.10**) with various single $PMMA_m$-*b*-$PSPE_n$ entirely showed much lower RFR in contrast to membrane **Rf4** with PVP, which significantly certified again the strong anti-fouling potential of zwitterionic PSPE block distributing on the membrane surface and inner pore walls. In particular, **M1.9** that contained 2 types of $PMMA_m$-*b*-$PSPE_n$ with different PMMA versus PSPE showed the strongest BSA resistance but the lowest water permeability, which clearly signified that the compacting density of PSPE block on membrane surface was the essential factor for achieving ideal antifouling performance. By the detailed comparison of characterization results, it can be seen clearly that, involvement of zwitterionic $PMMA_m$-*b*-$PSPE_n$ indeed largely improved the sieving performance and protein fouling resistance of PVDF membranes in contrast to commercial PVP. In particular, the $PMMA_m$-*b*-$PSPE_n$ with high ratio of PMMA/PSPE tended gave rise to higher anti-fouling ability in PVDF membrane. However, the suppressed the membrane porosity (water permeability) largely limited the application of additive $PMMA_m$-*b*-$PSPE_n$ on improvement of PVDF UF membranes.

Asymmetric membranes **M2.1**-**M2.7** and **M2.11** were successfully prepared respectively with dope solutions that contained 16 wt.% PVDF and combination of 1 wt.% PVP and 1-2 wt.%

$PMMA_m$-*b*-$PSPE_n$ (m= 94, 300; m/n= 0.4-12.5) via NIPS. The low CA (below 40º) were observed for all the membranes and implied that the quite hydrophilic membrane surface can be achieved. ATR-FTIR of **M2.1**-**M2.7** and **M2.11** cerfitied the apparent surface enrichment of hydrophilic PSPE block in $PMMA_m$-*b*-$PSPE_n$ and PVP. The collaboration of $PMMA_m$-*b*-$PSPE_n$ and PVP together as combined additives showed quite strong synergy effect to not only highly enhance the water permeability of **M2.1**-**M2.7** and **M2.11** but basically retained their quite high BSA rejection. The trade-off relationship which most of ultrafiltration membranes suffered was successfully overcome by synergy effect of $PMMA_m$-*b*-$PSPE_n$ and PVP in **M2.1**-**M2.7** and **M2.11**. The strong facilitation effect of $PMMA_m$-*b*-$PSPE_n$ on precipitation kinetics of PVDF matrix polymer can be properly balanced by the retarding influence of additional PVP on the PVDF precipitation rate during coagulation process. All the membrans **M2.1**-**M2.7** and **M2.11** still showed much lower RFR than membrane **Rf4** with commercial PVP additive. Among **M2.1**-**M2.7** and **M2.11**, membranes with 2 wt.% $PMMA_m$-*b*-$PSPE_n$ and 1 wt.% PVP exhibited remarkably decreased RFR in contrast to membrans with 1 wt.% $PMMA_m$-*b*-$PSPE_n$ and 1 wt.% PVP due to the stronger control on pore-forming by more additional $PMMA_m$-*b*-$PSPE_n$. **M2.4** showed the lowest RFR. The collaboration of $PMMA_m$-*b*-$PSPE_n$ and PVP still served excellent BSA fouling resistance relying on the distributed zwitterionic PSPE and entrapped PVP residue on the membrane surface and inner pore walls. **M2.4** that contained 2 wt.% $PMMA_{300}$-*b*-$PSPE_{38.1}$ and 1 wt.% PVP (K30) was selected as the most optimized prototype membrane for NANOPUR project due to its relatively prominent performance parameters that can reach the target values of NANOPUR projects.

Glycol and PEG were also respectively combined with $PMMA_m$-*b*-$PSPE_n$ as additives in preparation of asymmetric PVDF membrane **M2.8**, **M2.9** via NIPS. The improved surface hydrophilicity of **M2.8** and **M2.9** were verified with the observed CA around 40º. The apparent synergy of PEG and $PMMA_m$-*b*-$PSPE_n$ was also shown in **M2.8**. Perhaps due to the too strong retarding influence of PEG on PVDF precipitation, the BSA rejection of **M2.8** was not high as membranes with synergy of PVP and zwitterionic copolymers.

Two types of 2 wt.% $PMMA_m$-*b*-$PDMAEMA_n$ (m= 539, m/n= 1.5, 3.1) were respectively blended with 17.5 wt.% PVDF and applied to prepare membrane **MS.1** and **MS.2** via NIPS. The hydrophilic PDMAEMA block also enriched on the surface of **MS.1** and **MS.2** via preferential surface migration during coagulation like $PMMA_m$-*b*-$PSPE_n$. After surface modification the exposed PDMAEMA block were successfully converted to PSPE. The comparison of ATR-FTIR before and after surface modification showed strong evidence of conversion from PDMAEMA to PSPE on the top surface of **MS.1** and **MS.2**. **MS.1** and **MS.2** showed the quite large water permeability and low BSA rejection due to the additive $PMMA_m$-*b*-$PDMAEMA_n$ with relatively

bigger Mn and pronounced disturbance on precipitation rate of matrix PVDF. After surface modification **MS.2** displayed more improved sieving performance than **MS.1**. In general, the difficulty of complete conversion of PDMAEMA block to PSPE block that exposed on membrane surface was still challenging the improvement of membrane performance. Obviously the direct blending of zwitterionic copolymer additives was more advantageous in contrast.

Overall, combination of commercial PVP and zwitterionic $PMMA_m$-*b*-$PSPE_n$ with high ratio of PMMA/PSPE showed promising potential for application on modification of PVDF membrane performace. Through simple NIPS of the direct blends of $PMMA_m$-*b*-$PSPE_n$, PVP and PVDF, the proper strong protein fouling resistance of zwitterionic groups and well controlled pore-forming and porosity can be readily integrated at the same time in PVDF membrane without any extral procedure. Based on these preliminarily results, the manufacture of PVDF UF membrane with high throughput, proper sieving performance and strong anti-fouling ability in industrilized scale can be highly expected through further exploration.

9. References

[1] Human development report 2006, United Nations development programme (UNDP), 2006.

[2] Coping with water scarcity. Challenge of the twenty-first century, United Nations (UN) Water. Food and agricultural association (FAO), 2007.

[3] Urban urgency, Water caucus summary, World water council (WWC), Marseille, France, 2007.

[4] Progress on sanitation and drinking-water, World health organization(WHO)/United Nations international children's fund (UNICEF) joint monitoring programme for water supply and sanitation, 2010.

[5] S. Judd, B. Jefferson, Membranes for industrial wastewater recovery and re-use, Elsevier, New York, 2003, pp. 2-66.

[6] M. Mulder, Basic principles of membrane technology, KLUWER ACADEMIC, London, 1996, pp. 1-457.

[7] B. Bruggen, C. Vandecasteele, T. Gestel, W. Doyenb, R. Leysenb, A review of pressure-driven membrane processes in wastewater treatment and drinking water production, Environ. Prog. Sustainable Energy 22 (2003) 46-56.

[8] R. Baker, Membrane technology and applications, John Wiley & sons Ltd., Chichester, 2004, pp. 1-272.

[9] L. Fiksdal, T. Leiknes, The effect of coagulation with MF/UF membrane filtration for the removal of virus in drinking water, J. Membr. Sci. 279 (2006) 364–371.

[10] Http://www.marketsandmarkets.com/PressReleases/membranes.asp

[11] M. Ulbricht, Editorial special issue of polymer on polymer membranes, Polymer 55 (2014) 1293-1295.

[12] A. Mehta, A. Zydney, Permeability and selectivity analysis for ultrafiltration membranes, J. Membr. Sci. 249 (2005) 245–249.

[13] G. Odian, Principles of polymerization, John Wiley & sons Ltd., New York, 2004, pp. 1-332.

[14] R.Z. Pan, Polymer chemistry, Chemical Industry Publisher, Beijing, 2007, pp. 163-169.

[15] J.W. Nicholson, The Chemistry of Polymers, RSC, Chatham, 2006, pp. 226-523.

[16] C.Y. Zhu, M. Zhang, Polymer chemistry, Nankai University, Tianjin, 2003, pp.18-116.

[17] K. Matyjaszewski, T.P. Davis, Handbook of radical polymerization, John Wiley & sons Ltd., New York, 2002, pp. 187-300.

[18] W.A. Braunecker, K. Matyjaszewski, Controlled/living radical polymerizaiton: features, developments, and perspectives, Prog. Polym. Sci. 32 (2007) 93-146.

[19] K. Matyjaszewski, J. Xia, Atom transfer radical polymerization, Chem. Rev. 101 (2001) 2921-2990.

[20] M. Kamigaito, T. Ando, M. Sawamoto, Metal-Catalyzed Living Radical Polymerization, Chem. Rev. 101 (2001) 3689-3745.

[21] K. Matyjaszewski, Atom transfer radical polymerization (ATRP): current status and future perspectives, Macromolecules 45 (2012) 4015-4039.

[22] M. Ulbricht, Advanced functional polymer membranes, Polymer 47 (2006) 2217-2262.

[23] R.D. Noble, S.A. Stern, Membrane and technology series 2, Membrane separations and technology, principles and applications, Elsevier, Amsterdam, 2003, pp. 16-30.

[24] M. Ulbricht, Porous Polymers, John Wiley & sons Ltd., Hoboken, 2011, pp. 277-322.

[25] I. Pinnau, B.D. Freeman, Membrane formation and modification, American Chemical Society, Washington DC, 2000, pp. 1-36.

[26] N.N. Li, A.G. Fane, W.S. Ho, T. Matsuura, Advanced membrane technology and applications, John Wiley & sons Ltd., Hoboken, 2008, pp. 101-165.

[27] E. Drioli, L. Giorno, Membrane operations, Innovative separations and transformations, Wiley-VCH, Weiheim, 2009, pp. 19-79.

[28] J.G.S. Marcano, T.T. Tsotsis, Catalytic membranes and membrane reactors, Wiley-VCH, Weiheim, 2002, pp. 15-80.

[29] S.P. Nunes, K.V. Peinemann, Membrane technology in the chemical industry, Wiley-VCH, Weiheim, 2001, pp. 3-38.

[30] B.S. Lalia, V. Kochkodan, R. Hashaikeh, N. Hilal, A review on membrane fabrication: Structure, properties and performance relationship, Desalination 326 (2013) 77-95.

[31] A.J. Reuvers, F.W. Altena, C.A. Smolders, Demixing and gelation behavior of ternary cellulose acetate solutions, J. Polym. Sci., Part B: Polym. Phys. 24 (1986) 793-805.

[32] L. Broens, F.W. Altena, C.A. Smolders, Asymmetric membrane structures as a result of phase separation phenomena, Desalinaiton 32 (1980) 33-45.

[33] M.H.V. Mulder, J.O. Hendrikman, J.G. Wijmans, C.A. Smolders, A rationale for the preparation of asymmetric pervaporation membranes, J. Appl. Polym. Sci. 30 (1985) 2805-2820.

[34] S.L. Madorsky, Fluorocarbon and chlorocarbon polymers, in: Thermal degradation of organic polymers, John Wiley & Sons Inc., New York, 1964, pp. 23-76.

[35] Z.L. Cui, E. Drioli, Y.M. Lee, Recent progress in fluoropolymers for membranes, Prog. Polym. Sci. 39 (2014) 164-198.

[36] F. Liu, B.K. Zhu, Y.Y. Xu, Improving the hydrophilicity of poly(vinylidene fluoride) porous membranes by electron beam initiated surface grafting of AA/SSS binary monomers, Appl. Surf. Sci. 253 (2006) 2096-2101.

[37] S. Salgin, Effects of ionic environments on bovine serum albumin fouling in a cross-flox ultrafiltration system. Chem. Eng. Technol. 30 (2007) 255-260.

[38] A.R. Costa, M.N. Pinho, M. Elimelech, Mechamisms of colloidal natural organic matter fouling in ultrafiltration. J. Membr. Sci. 281 (2006) 716-726.

[39] E.A. Vogler, Water and acute biological response to surfaces, J. Biomater. Sci., Polym. Ed. 10 (1999) 1015-1046.

[40] D. Rana, T. Matsuura, Surface modifications for antifouling membranes, Chem. Rev. 110 (2010) 2448-2471.

[41] H. Susanto, M. Ulbricht, Photografted thin polymer hydrogel layers on PES ultrafiltration membranes: characterization, stability, and influence on separation performance, Langmuir 23 (2007) 7818-7830.

[42] G. Kang, Y. Cao, Application and modification of poly(vinylidene fluoride) (PVDF) membranes – a review, J. Membr. Sci. 463 (2014) 145-165.

[43] A. Venault, Y. Chang, H.S. Yang, P.Y. Lin, Y.J. Shih, A. Higuchi, Surface self-assembled zwitterionization of poly (vinylidene fluoride) microfiltration membranes via hydrophobic-driven coating for improved blood compatibility, J. Membr. Sci. 454 (2014) 253–263.

[44] F. Liu, N.A. Hashim, Y.T. Liu, M.R. Abed, K. Li, Progress in the production and modification of PVDF membranes, 375 (2011) 1–27.

[45] J.F. Hester, P. Banerjee, A.M. Mayes, Preparation of protein-resistant surfaces on poly(vinylidene fluoride) membranes via surface segregation, Macromolecules 32 (5) (1999) 1643–1650.

[46] A.A. Yousefi, Influence of polymer blending on crystalline structure of polyvinylidene fluoride, Iranian Polym. J. 20 (2011) 109-121.

[47] N. Moussaif, R. Jerome, Miscibility of poly(vinylidene fluoride) and poly(methyl methacrylate-co-zinc polyacrylate) ionomers, Polymer 40 (1999) 6831-6839.

[48] W. Ma, J. Zhang, X. Wang, S. Wang, Effect of PMMA on crystallization behavior and hydrophilicity of poly(vinylidene fluoride)/poly(methyl methacrylate) blend prepared in semi-dilute solutions, Appl. Surf. Sci. 253 (2007) 8377–8388.

[49] N. Pezeshk, D. Rana, R.M. Narbaitz, T. Matsuura, Novel modified PVDF ultrafiltration flat-sheet membranes, J. Membr. Sci. 389 (2012) 280–286.

[50] F. Ran, S. Nie, W. Zhao, J. Li, B. Su, S. Sun, C. Zhao, Biocompatibility of modified polyethersulfone membranes by blending an amphiphilic triblock copolymer of poly(vinylpyrrolidone)-*b*-poly(methylmethacrylate)-*b*-poly(vinylpyrrolidone), ActaBiomater. 7 (2011) 3370–3381.

[51] I. Luzinov, S. Minko,V. Tsukruk, Adaptive and responsive surface through controlled reorganization of interfacial polymer layers, Prog. Polym. Sci. 29 (2004) 635-698.

[52] X. Liu, Y. Peng, S. Ji, A new method to prepare organic–inorganic hybrid membranes, Desalination 221 (2008) 376–382.

[53] A. Bottino, G. Capannelli, A. Comite, Preparation and characterization of novel porous PVDF-ZrO2 composite membranes, Desalination 146 (1–3) (2002) 35–40.

[54] S. Chen, L. Li, C. Zhao, J. Zheng, Surface hydration: Principles and applications toward low-fouling/nonfouling biomaterials, Polymer 51 (2010) 5283-5293.

[55] D. A. Herold, K. Keil, D. E. Bruns, Oxidation of polyethylene glycols by alcohol dehydrogenase, Biochem. Pharmacol. 38 (1989) 73-76.

[56] M.C. Shen, L. Martinson, M.S. Wagner, D.G. Castner, B.D. Ratner, T. A. J. Horbett, PEO-like plasma polymerized tetraglyme surface interactions with leukocytes and proteins: in vitro and in vivo studies, Biomater. Sci., Polym. Ed. 13 (2002) 367–390.

[57] J.B. Schlenoff, Zwitteration: coating surfaces with zwitterionic functionality to reduce nonspecific adsorption, Langmuir 30 (2014) 9625−9636.

[58] J. Ladd, Z. Zhang, S. Chen, J. C. Hower, S.Y. Jiang, Zwitterionic polymers exhibiting high resistance to nonspecific protein adsorption from human serum and plasma, Biomacromolecules 9 (2008) 1357-1361.

[59] M. Sin, S. Chen, Y. Chang, Hemocompatibility of zwitterionic interfaces and membranes, Polym. J. (Tokyo, Jpn.) 46 (2014) 436–443.

[60] H. Kitano, K. Sudo, K. Ichikawa, M. Ide, K. Ishihara, Raman Spectroscopic study on the structure of water in aqueous polyelectrolyte solutions. J. Phys. Chem. B 104 (2000) 11425−11429.

[61] J. D. Andrade, V. Hlady, Protein adsorption and materials biocompatibility - a tutorial review and suggested hypotheses. Adv. Polym. Sci. 79 (1986) 1−63.

[62] Y. Ikada, Blood-compatible polymers, Adv. Polym. Sci. 57 (1984) 103−140.

[63] N. T. Southall, K. A. Dill, A. D. J. Haymet, A view of the hydrophobic effect, J. Phys. Chem. B 106 (2002) 521−533.

[64] E. Berndt, S. Behnke, A. Dannehl, A. Gajda, J. Wingender, M. Ulbricht, Functional coatings for anti-biofouling applications by surface segregation of block copolymer additives, Polymer 51 (2010) 5910-5920.

[65] M. Horn, K. Matyjaszewski, Solvent effects on the activation rate constant in atom transfer radical polymerization, Macromolecules 46 (2013) 3350−3357.

[66] X.S. Wang, S.P. Armes, Facile atom transfer radical polymerization of methoxy-capped oligo(ethylene glycol) methacrylate in aqueous media at ambient temperature, Macromolecules 33 (2000) 6640-6647.

[67] S. Kitagawa, M. Munakata, Binuclear copper(1) complexes which reversibly react with CO. 1. di-p-halogeno-bis(2,2'-bipyridine)dicopper(I) and its derivatives, Inorg. Chem. 20 (1981) 2261-2267.

[68] X. Wang, N. Luo, S. Ying, Controlled/living polymerization of MMA promoted by heterogeneous initiation system (EPN-X–CuX–bpy), J. Polym. Sci., Part A: Polym. Chem. 37 (1999) 1255-1263.

[69] A. Lowe, N. Billingham, S. Armes, Synthesis and properties of low-polydispersity poly(sulfopropylbetaine)s and their block copolymers, Macromolecules 32 (1999) 2141-2148.

[70] F.L. Baines, N.C. Billingham, S.P. Armes, Synthesis and solution propierties of water-soluble hydrophilic-hydrophobic block copolymers, Macromolecules 29 (1996) 3416-3420.

[71] A. Lowe, C. McCormick, Synthesis and solution properties of zwitterionic polymers, Chem. Rev. 102 (2002) 4177-4189.

[72] X. Zhang, K. Matyjaszewski, Synthesis of well-defined amphiphilic block copolymers with 2-(dimethylamino)ethyl methacrylate by controlled radical polymerization, Macromolecules, 32 (1999) 1763-1766.

[73] V. Coessens, K. Matyjaszewski, Synthesis of polymers with amino end groups by atom transfer radical polymerization, J. Macromol. Sci., Part A: Pure Appl. Chem. 36 (1999) 811-826.

[74] V. Coessens, K. Matyjaszewski, Synthesis of polymers with phosphonium end groups by atom transfer radical polymerization, J. Macromol. Sci., Part A: Pure Appl. Chem. 36 (1999) 653-666.

[75] L. Shi, R. Wang, Y. Cao, Effect of the rheology of poly(vinylidene fluoride-co-hexafluropropylene) (PVDF-HFP) dope solutions on the formation of microporous hollow fibers used as membrane contactors, J. Membr. Sci. 344 (2009) 112-122.

[76] Z. Zhang, Q. An, Y. Ji, J. Qian, C. Gao, Effect of zero shear viscosity of the casting solution on the morphology and permeability of polysulfone membrane prepared via the phase-inversion process, Desalination 260 (2010) 43-50.

[77] S. Kudaibergenov, W. Jaeger, A. Laschewsky, Polymeric betaines: synthesis, characterization, and application, Adv. Polym. Sci. 201 (2006) 157-224.

[78] Q. Yang, T. Chung, M. Weber, Microscopics behavior of polyvinylpyrrolidone hydropphilizing agents on phase inversion polyethersulfone hollow fiber membranes for hemofiltration, J. Membr. Sci. 326 (2009) 322-331.

[79] R.M. Boom, T. van den Boomgaard, C.A. Smolders, Mass transfer and thermodynamics during immersion precipitation for a two-polymer system evaluation with the system PES-PVP-NMP-water, J. Membr. Sci. 90 (1994) 231-249.

[80] B. Chakrabarty, A.K. Ghoshal, M.K. Purkait, Preparation, characterization and performance studies of polysulfone membranes using PVP as an additive, J. Membr. Sci. 315 (2008) 36-47.

[81] P. van de Witte, P.J. Dijkstra, J.W.A. van den Berg, J. Feijen, Phase separation processes in polymer solutions in relation to membrane formation, J. Membr. Sci. 117 (1996) 1-31.

[82] T. Miyano, T. Matsuura, S. Sourirajan, Effect of polymer molecular weight, solvent and casting solution composition on the pore size and the pore size distribution of polyethersulfone(victres) membrane, Chem. Eng. Commun. 95 (1990) 11-26.

[83] I.M. Wienk, R.M. Boom, M.A.M. Beerlage, A.M.W. Bulte, C.A. Smolders, H. Strathmann, Recent advances in the formation of phase inversion membranes made from amorphous or semi-crystalline polymers, J. Membr. Sci. 113 (1996) 361-371.

[84] R.M. Boom, I.M. Wienk, T. Van den Boomgaard, C.A. Smolders, Microstructures in phase inversion membranes. Part 2. The role of a polymeric additive, J. Membr. Sci. 73 (1992) 277-292.

[85] M. Han, S. Nam, Thermodynamic and rheological variation in polysulfone solution by PVP and its effect in the preparation of phase inversion membrane, J. Membr. Sci. 202 (2002) 55-61.

[86] A.J. Reuvers, F.W. Altena, C.A. Smolders, Demixing and gelation behavior of ternary cellulose acetate solutions, J. Polym. Sci., Part B: Polym. Phys. 24 (1986) 793-804.

[87] P.S.T. Machado, A.C. Habert, C.P. Borges, Membrane formation mechanism based on precipitation kinetics and membrane morphology: flat and hollow fiber polysulfone membranes, J. Membr. Sci. 155 (1999) 171-183.

[88] D. Zuo, Y. Xu, W. Xu, H. Zou, The influence of PEG molecular weight on morphologies and properties of PVDF asymmetric membranes, Chin. J. Polym. Sci. 26 (2008) 405-414.

[89] C.A. Smolders, A.J. Reuvers, R.M. Boom, I.M. Wienk, Microstructures in phase-inversion membranes. Part 1. Formation of macrovoids, J. Membr. Sci. 73 (1992) 259-275.

[90] J. Kim, K. Lee, Effect of PEG additive on membrane formation by phase inversion, J. Membr. Sci. 138 (1998) 153-163.

[91] A. Venault, Y. Liu, J. Wu, H. Yang, Y. Chang, J. Lai, P. Aimar, Low-biofouling membranes prepared by liquid-induced phase separation of the PVDF/polystyrene-*b*-poly (ethylene glycol) methacrylate blend, J. Membr. Sci. 450 (2014) 340-350.

[92] H. Yoshida, Structure formation of PVDF/PMMA blends studied Simultaneous DSC/FI-IR measurement, J. Therm. Anal. Calorim. Vol. 49 (1997) 101-105.

[93] Y. Chang, S. Chen, Z. Zhang, S. Jiang, Highly protein-resistant coatings from well-defined diblock copolymers containing sulfobetaines, Langmuir 22 (2006) 2222-2226.

[94] M. Khayet, C.Y. Feng, T. Matsuura, Morphological study of fluorinated asymmetric polyetherimide ultrafiltration membranes by surface modifying macromolecules, J. Membr. Sci. 213 (2003) 159–180.

[95] C.H. Loh, R. Wang, Insight into the role of amphiphilic pluronic block copolymer as pore-forming additive in PVDF membrane formation, J. Membr. Sci. 446 (2013) 492-503.

[96] B. Crist, A. Nesarikar, Coarsening in polyethylene-copolymer blends, Macromolecules 28 (1995) 890-896.

[97] S.A. McKelvey, W.J. Koros, Phase separation, vitrification, and the manifestation of macrovoids in polymeric asymmetric membranes. J. Membr. Sci. 112 (1996) 29-39.

[98] J. Barzin, B. Sadatnia, Correlation between macrovoid formation and the ternary phase diagram for polyethersulfone membranes prepared from two nearly similar solvents, J. Membr. Sci. 325 (2008) 92-97.

[99] M.A.M. Beerlage, Polyimide ultrafiltration membranes for non-aqeous systems, PhD thesis University of Twente, Enschede, 1994, pp. 57-76.

[100] M.A.M. Beerlage, Polyimide ultrafiltration membranes for non-aqeous systems, PhD thesis University of Twente, Enschede, 1994, pp. 79-101.

[101] H. Lee, L.A. Archer, Functionalizing polymer surfaces by field-induced migration of copolymer additives. 1. Role of surface energy gradients, Macromolecules 34 (2001) 4572-4579.

[102] M. Khayet, M.V. Alvarez, K.C. Khulbe, T. Matsuura, Preferential surface segregation of homopolymer and copolymer blend films, Surf. Sci. 601 (2007) 885-895.

[103] H. Lee, L.A. Archer, Functionalizing polymer surfaces by surface migration of copolymer additives: role of additive molecular weight, Polymer 43 (2002) 2721-2728.

[104] J. Tan, J.L. Brash, Nonfouling biomaterials based on polyethylene oxide-containing amphiphilic triblock copolymer as surface modifying additives: synthesis and characterization of copolymers and surface properties of copolymer-polyurethane blends, J. Appl. Polym. Sci. 108 (2008) 1617-1628.

[105] Y. Kotsuchibashi, M. Ebara, T. Aoyagi, R. Narain, Recent advances in dual temperature responsive block copolymers and their potential as biomedical applications, Polymers 8 (2016) 380.

[106] G.R. Guillen, Y.Pan, M. Li, E.M.V. Hoek, Preparation and characterization of membranes formed by nonsolvent induced phase separation: a review, Ind. Eng. Chem. Res. 50 (2011) 3798-3817.

[107] Y. Zhao, B. Zhu, L. Kong, Y. Xu, Improving hydrophilicity and protein resistance of poly(vinylidene fluoride) membranes by blending with amphiphilic hyperbranched-star polymer, Langmuir 23 (2007) 5779-5786.

[108] C. Lu, B. Li, N. Liu, G. Wu, H. Gao, J. Ma, A hydrazone crosslinked zwitterionic polypeptide nanogel as a platform for controlled drug delivery, RSC Adv. 4 (2014) 50301–50311.

[109] T. Wang, Y. Wang, Y. Su, Z. Jiang, Antifouling ultrafiltration membrane composed of polyethersulfone and sulfobetaine copolymer, J. Membr. Sci. 280 (2006) 343-350.

[110] Q. Li, Q. Bi, B. Zhou, X. Wang, Zwitterionic sulfobetaine-grafted poly(vinylidene fluoride) membrane surface with stably anti-protein-fouling performance via a two-step surface polymerization, Appl. Surf. Sci. 258 (2012) 4707-4717.

[111] J. Li, M. Li, J. Miao, J. Wang, X. Shao, Q. Zhang, Improved surface property of PVDF membrane with amphiphilic zwitterionic copolymer as membrane additive, Appl. Surf. Sci. 258 (2012) 6398-6405.

[112] J.A. Howell, D. Wu, R.W. Field, Transmission of bovine albumin under controlled flux ultrafiltration, J. Membr. Sci. 153 (1999) 117-127.

[113] I.H. Huisman, P. Prádanos, A. Hernández, The effect of protein–protein and protein–membrane interactions on membrane fouling in ultrafiltration, J. Membr. Sci. 179 (2000) 79–90.

[114] D.B. Burns, A.L. Zydney, Effect of Solution pH on Protein Transport Through Ultrafiltration Membranes, Biotechnol. Bioeng. 641 (1999) 27-37.

[115] P.D. Peeva, A.E. Palupi, M. Ulbricht, Ultrafiltration of humic acid solutions through unmodified and surface functionalized low-fouling polyethersulfone membranes – effect of feed properties, molecular weight cut-off and membrane chemistry on fouling behavior and cleanability, Sep. Purif. Technol. 81 (2011) 124-133.

[116] J.A. Koehler, M. Ulbricht, G. Belfort, Intermolecular forces between a protein and a hydrophilic modified polysulfone film with relevance to filtration, Langmuir 16 (2000) 10419–10427.

[117] P.D. Peeva, N. Million, M. Ulbricht, Factors affecting the sieving behavior of anti-fouling thin-layer cross-linked hydrogel polyethersulfone composite ultrafiltration membranes, J. Membr. Sci. 390–391 (2012) 99–112.

[118] P.D. Peeva, T. Knoche, T. Pieper, M. Ulbricht, Performance of thin-layer hydrogel polythersulfone composite membranes during dead-end ultrafiltration of various protein solutions, Ind. Eng. Chem. Res. 51 (2012) 7231-7241.

[119] G. Belfort, J.M. Pimbley, A. Greiner, K.Y. Chung, Diagnosis of membrane fouling using a rotating annular filter. 1. Cell culture media, J. Membr. Sci. 77 (1993) 1-22.

[120] A. Martin, F. Martinez, J.I. Calvo, P. Pradanos, L. Palacio, A. Hernandez, Protein adsorption onto an inorganic microfiltration membrane: solute-solid interactions and surface coverage, J. Membr. Sci. 207 (2002) 199-207.

[121] G. Schock, A. Miquel, R. Birkenberger, Characterization of ultrafiltration membranes: cut-off determination by gel permeation chromatography, J. Membr. Sci. 41 (1989) 55–67.

[122] H. Susanto, M. Ulbricht, Characteristics, performance and stability of polyethersulfone ultrafiltration membranes prepared by phase separation method using different macromolucular additives, J. Membr. Sci. 327 (2009) 125-135.

[123] S. Kalasin, M. Santore, Non-specific adhesion on biomaterial surfaces driven by small amounts of protein adsorption, Colloids Surf., B 73 (2009) 229–236

[124] M.J. Han, S.T. Nam, Thermodynamic and rheological variation in polysulfone solution by PVP and its effect in the preparation of phase inversion membrane, J. Membr. Sci. 202 (2002) 55-61.

[125] I.H. Huisman, P. Pradanos, A. Hernandez, The effect of protein-protein and protein-membrane interactions on membrane fouling in ultrafiltration, J. Membr. Sci. 179 (2000) 79-90.

[126] J.F. Hester, A.M. Mayes, Design and performance of foul-resistant poly(vinylidene fluoride) membranes prepared in a single-step by surface segregation, J. Membr. Sci. 202 (2002) 119-135.

10. Appendix

10.1. List of abbreviations

ATRP	Atom transfer radical polymerization
ATR-FTIR	Attenuated total reflection infrared spectroscopy
BSA	Bovine serum albumin
CA	Contact angle
CAGR	Compound annual growth rate
CP	Concentration polarization
D	Dialysis
DMAc	Dimethylacetamid
DMF	N,N-Dimethylformamide
DMSO	Dimethyl sulfoxide
FRP	Free radical polymerization
GS	Gas separation
GPC	Gel permeation chromatography
^{1}H-NMR	^{1}Hydrogen nuclear magnetic resonance spectroscopy
LCST	Lower critical solution temperature
LiBr	Lithium bromide
MW	Molecular weight
MF	Microfiltration
ME	Membrane electrolysis
MD	Membrane distillation
MeHQ	Hydro-quinone monomethyl ether
MWCO	Molecular weight cut-off
Mag.	Magnification
MC	Membrane contactor
NIPS	Nonsolvent induced phase separation
NF	Nanofiltration
NMP	N-Methyl-2-pyrrolidon
PAN	Polyacrylonitrile
PA	Polyamide
PES	Poly(ether- sulfone)
PI	Polyimide
PEG	Poly(ethylene glycol)

PSF	Polysulfone
PV	Pervaporation
PVA	Poly(vinyl acetate)
PVDF	Polyvinylidenfluorid
PVP	Polyvinylpyrrolidon
PWP	Pure water permeability
RFR	Relative flux reduction
RO	Reverse osmosis
SEM	Scanning Electron Microscope
TMP	Transmembrane pressure
UF	Ultrafiltration
VP	Vapour permeation
XPS	X-ray Photoelectron Spectroscopy

10.2. Supplementary information

10.2.1. ^{1}H-NMR of PMMA-Br (M_n= 13.9 kg/mol)

The chemical structure of synthesized $PMMA_m$-Br can be confirmed as shown in **Fig. A1**. The proton signals at 0.73 ppm, 0.93 ppm (d) corresponded to $–CH_3$ from **1**. The proton signal at 1.75 ppm (b) corresponded to $–CH_2–$ from **2**. The proton signal at 3.55 ppm (s) can be distinctly identified and attributed to $O–CH_3$ from **3**.

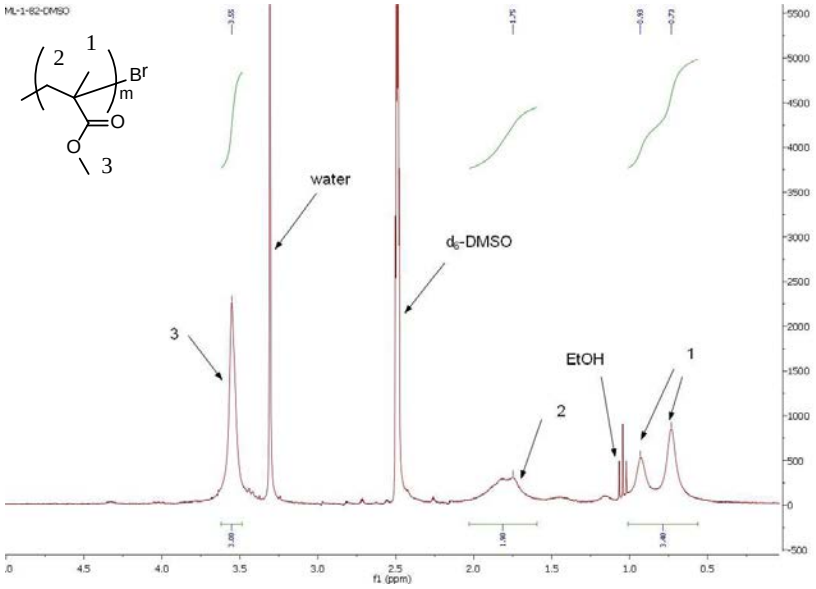

Fig. A1 ^{1}H-NMR (300 MHz) of PMMA-Br (M_n=13.9 kg/mol) microinitiator. Solvent: d_6-DMSO@298K (r.t.).

10.2.2. ^{1}H-NMR of PMMA-Br (M_n= 30 kg/mol)

The chemical structure of synthesized $PMMA_m$-*b*-$PSPE_n$ can be confirmed as shown in **Fig. A2**. The proton signals at 0.85 ppm, 1.02 ppm (d) corresponded to $–CH_3$ from **1**. The proton signal at 1.81 ppm, 1.90 ppm (d) corresponded to $–CH_2–$ from **2**. The proton signal at 3.60 ppm (s) can be distinctly identified and attributed to $O–CH_3$ from **3**.

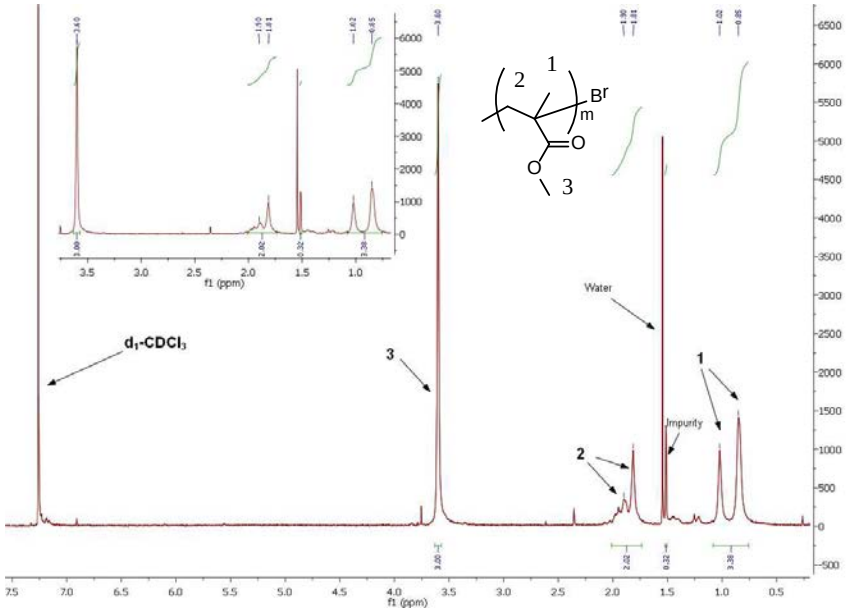

Fig. A2 ^{1}H-NMR (300 MHz) of PMMA-Br (M_n=30 kg/mol) microinitiator. Solvent: d_1-$CDCl_3$@298K (r.t.)

10.2.3. Evolution of M_n and PDI in reaction BlockP.13 and BlockP.14

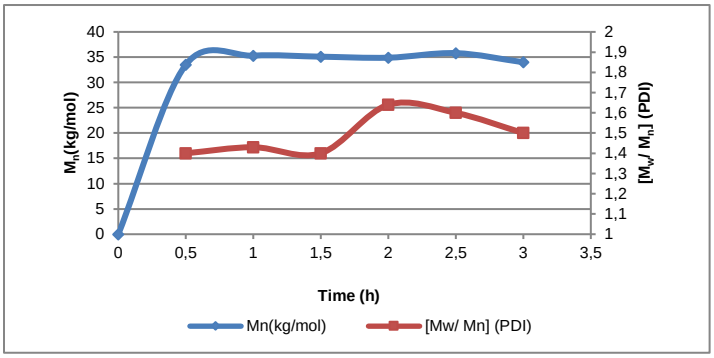

Fig. A3 Evolution of M_n and PDI as functions of time for synthesis of $PMMA_m$-*b*-$PDMAEMA_n$ in reaction **BlockP.13**. (**BlockP.13**) [DMAEMA]:[PMMA-Br]:[Cu(I)Br]:[PMDETA] =1600:1:1.5:1.5 in toluene for 3h at 50ºC, $C_{(DMAEMA)}$= 1.46 mol/L, M_n of PMMA-Br=30 kg/mol;

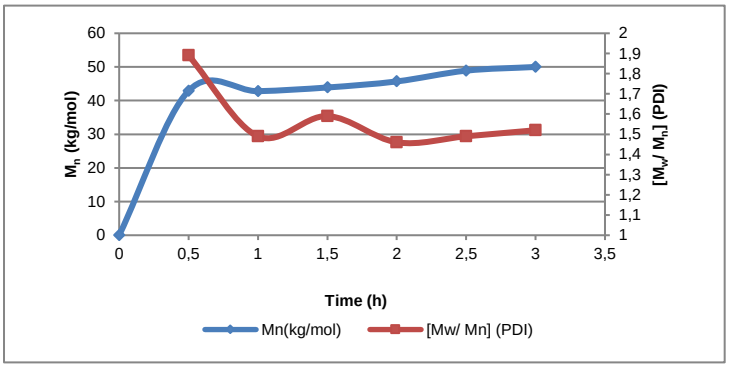

Fig. A4 Evolution of M_n and PDI as functions of time for synthesis of $PMMA_m$-*b*-$PDMAEMA_n$ in reaction **BlockP.14**. (**BlockP.14**) [DMAEMA]:[PMMA-Br]:[Cu(I)Br]:[PMDETA] =1600:1:10:10 in toluene for 3h at 50ºC, $C_{(DMAEMA)}$= 1.46 mol/L, M_n of PMMA-Br=30 kg/mol.

10.2.4. ^{1}H-NMR of PMMA-*b*-PDMAEMA ($M_{n\ PMMA}$= 30 kg/mol)

The chemical structure of all the synthesized $PMMA_m$-*b*-$PDMAEMA_n$ ($M_{n\ PMMA}$=30 kg/mol) can be confirmed as shown in **Fig. A5**. The proton signals at 0.85 ppm, 1.02 ppm (d) corresponded to –CH_3 from **1** and **a** collectively. The proton signals at 1.81 ppm, 1.90 ppm (d) corresponded to –CH_2– from **2** and **b** collectively. The proton signal at 4.05 ppm (s) can be attributed to O–CH_2– from **3**. The proton signal at 2.56 ppm (s) can be attributed to N–CH_2– from **4**. The proton signals at 2.28 ppm (s) corresponded to N–CH_3 from **5** and **6** collectively. The proton signals at 3.60 ppm (s) can be distinctly identified and attributed to O–CH_3 from **c**.

The integral area value of proton signals **c** (O–CH_3 from PMMA side chains, δ=3.60 ppm, s) and **3** (O–CH_2 – from PDMAEMA side chains, δ=4.05 ppm, s) were utilized to calculate the ratios of PMMA/PDMAEMA (m/n) in $PMMA_m$-*b*-$PDMAEMA_n$ with **Equation 6** (cf. **5.1.2.**). The calculated ratios of PMMA/PDMAEMA (m/n) in $PMMA_m$-*b*-$PDMAEMA_n$ were shown in **Table 7** (cf. **5.2.2.4.**).

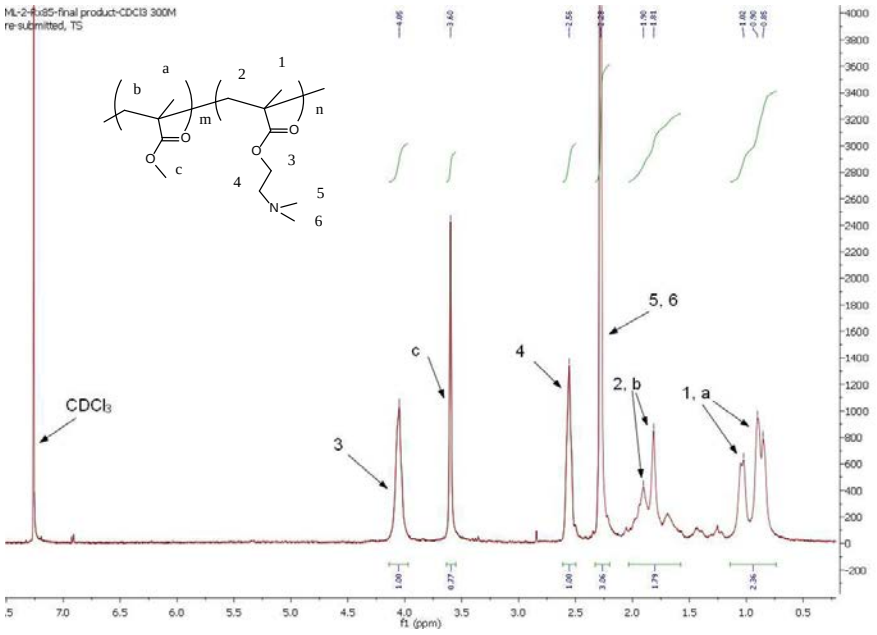

Fig. A5 ^{1}H-NMR (300 MHz) of a typical $PMMA_m$-*b*-$PDMAEMA_n$ (PMMA M_n=30 kg/mol). Solvent: d_1-$CDCl_3$ @298K (r.t.). The selected sample was **BP30k-12**.

10.2.5. Evolution of M_n and PDI in reaction MIni.14 and MIni.15

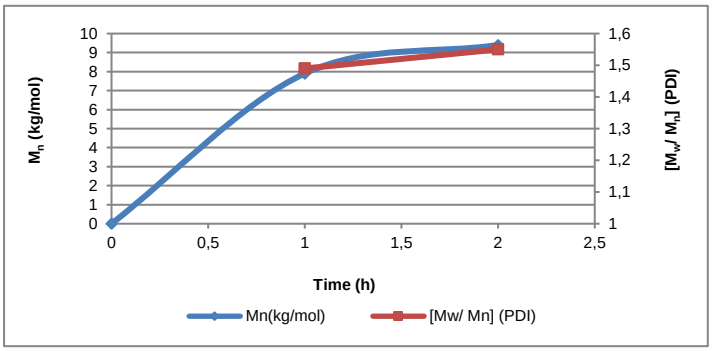

Fig. A6 Evolution of M_n and PDI with time for synthesis of PMMA-Br in reaction **MIni.14**.

(**MIni.14**) [MMA]:[EtBrP]:[Cu(I)Br]:[dinonyl bipyridine] =50:1:1:2 in toluene for 2h at 40ºC, $C_{(MMA)}$= 3 mol/L.

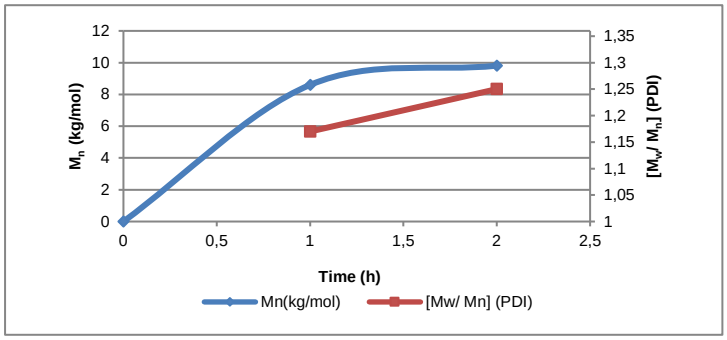

Fig. A7 Evolution of M_n and PDI with time for synthesis of PMMA-Br in reaction **MIni.15**. (**MIni.15**) [MMA]:[EtBrP]:[Cu(I)Br]:[dinonyl bipyridine]= 50:1:1:2 in toluene for 2h at 40ºC, $C_{(MMA)}$= 3 mol/L.

10.2.6. ^{1}H-NMR of PMMA-Br (M_n= ~10 kg/mol)

The chemical structure of synthesized $PMMA_m$-Br can be confirmed as shown in **Fig. A8**. The proton signals at 0.85 ppm, 1.02 ppm (d) corresponded to –CH_3 from **1**. The proton signal at 1.81 ppm, 1.90 ppm (d) corresponded to –CH_2– from **2**. The proton signal at 3.60 ppm (s) can be distinctly identified and attributed to O–CH_3 from **3**.

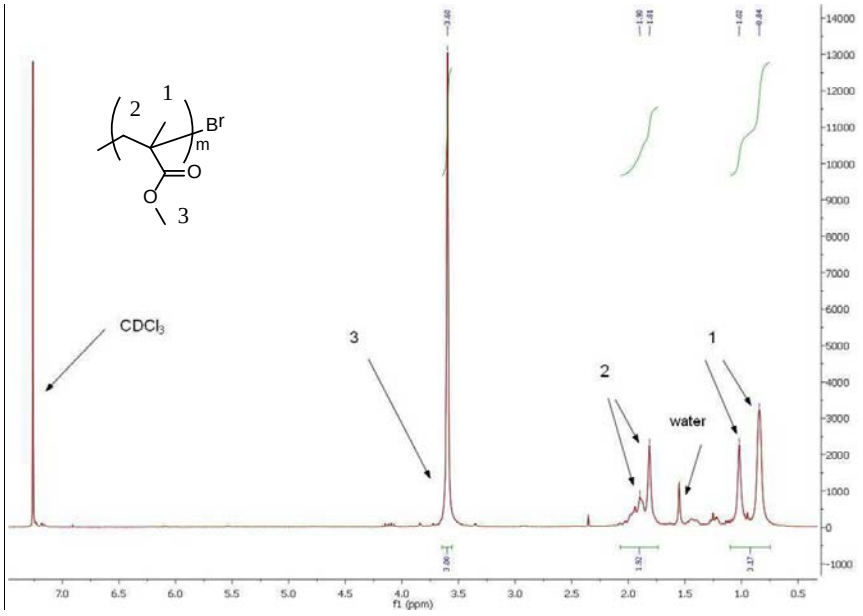

Fig. A8 ^{1}H-NMR (300 MHz) of PMMA-Br (M_n=~10 kg/mol) microinitiator. Solvent: d_1-$CDCl_3$@298K (r.t.). The selected sample was **MI10k-2**.

10.2.7. ^{1}H-NMR of PMMA-*b*-PDMAEMA ($M_{n\ PMMA}$ = ~10 kg/mol)

The chemical structure of all the synthesized $PMMA_m$-*b*-$PDMAEMA_n$ ($M_{n\ PMMA}$= ~10kDa) can be confirmed as shown in **Fig. A9**. The proton signals at 0.85 ppm (d), 1.02 ppm (s) corresponded to –CH_3 from **1** and **a** collectively. The proton signals at 1.80 ppm (s), 1.89 ppm (s) corresponded to –CH_2– from **2** and **b** collectively. The proton signal at 4.01 ppm (s) can be attributed to O–CH_2– from **3**. The proton signal at 2.52 ppm (s) can be attributed to N–CH_2– from **4**. The proton signals at 2.23 ppm (s) corresponded to N–CH_3 from **5** and **6** collectively. The proton signals at 3.59 ppm (s) can be distinctly identified and attributed to O–CH_3 from **c**.

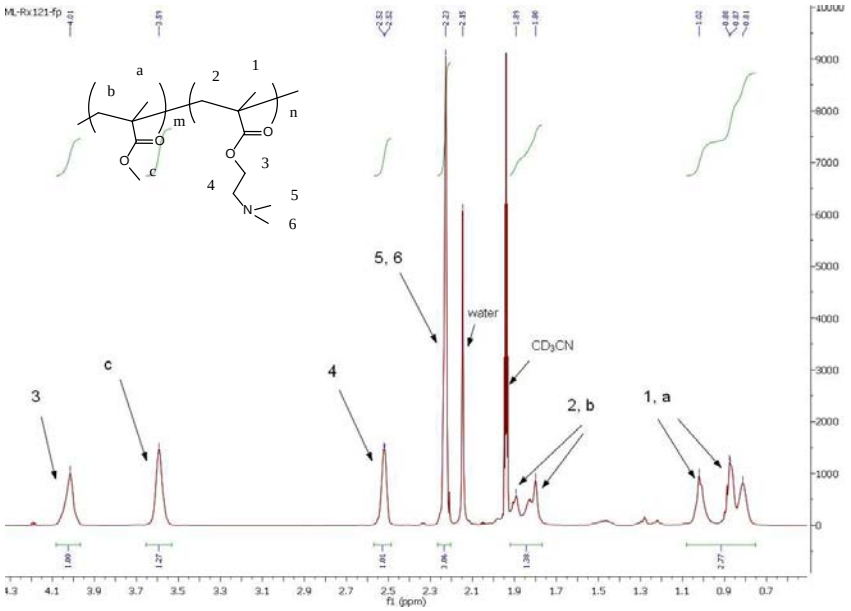

Fig. A9 ^{1}H-NMR (300 MHz) of a typical $PMMA_m$-*b*-$PDMAEMA_n$ (PMMA M_n= ~10 kg/mol). Solvent: d_1-CD_3CN @298K (r.t.). The selected sample was **BP10k-4**.

10.2.8. Synthesis of macroinitiator PMMA-Br (M_n=53.9 kg/mol)

As shown in **Fig. A10**, Cu(I)Br/Bipyriding$_2$ was adopted as catalyst system to synthesize PMMA-Br (M_n= 53.9 kg/mol). Higher MMA concentration and long reaction time were used, compared with the synthesis process for PMMA-Br (M_n= 30 kg/mol).

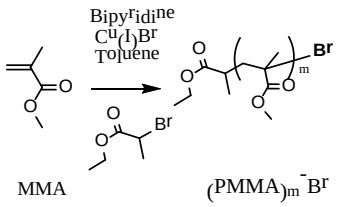

Fig. A10 Synthesis of macroinitiator PMMA-Br (M_n= 53.9 kg/mol). [MMA]:[EBrP]:[Cu(I)Br]:[Bipyridine] = 100:1:1:2 in toluene for 7h at 50ºC, $C_{(MMA)}$= 3 mol/L.

The chemical structure of synthesized $PMMA_m$-Br can be confirmed as shown in **Fig. A11**. The proton signals at 0.85 ppm, 1.02 ppm (d) corresponded to –CH_3 from **1**. The proton signal at 1.81 ppm, 1.90 ppm (d) corresponded to –CH_2– from **2**. The proton signal at 3.60 ppm (s) can be distinctly identified and attributed to O–CH_3 from **3**.

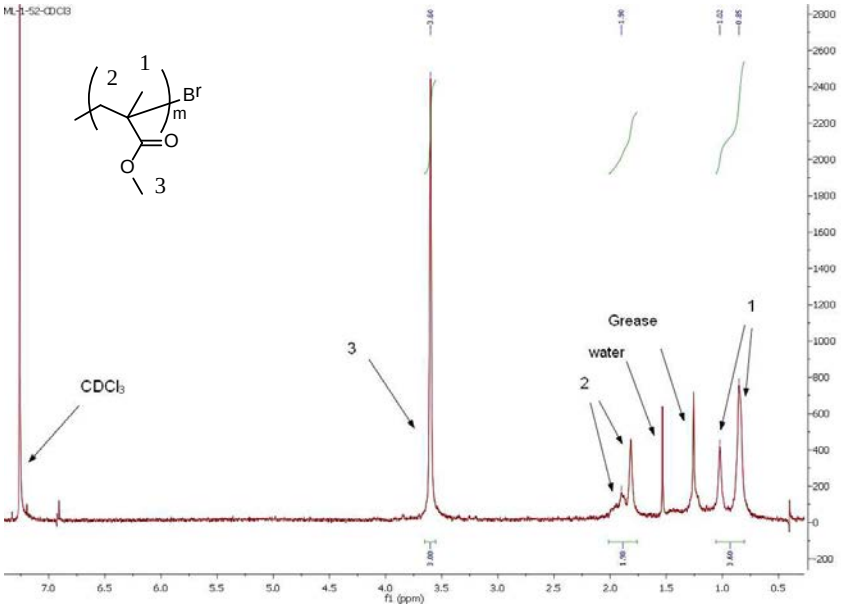

Fig. A11 ^{1}H-NMR (300 MHz) of PMMA-Br (M_n= 53.9 kg/mol) macroinitiator. Solvent: d_1-$CDCl_3$@298K (r.t.).

As shown in **Table A1**, the molecular weight (M_n) of synthesized $PMMA_m$-Br were determined by GPC. The PDI of PMMA-Br was broad due to the increased reaction time. The value for average number of repeating MMA units (m) in $PMMA_m$-Br was calculated as aforementioned description (cf. **5.2.2.2.**, **Equition 7**). The calculated m was 539.

Code	M_w/M_n (PDI)	M_n (g/mol) (GPC)	$(PMMA)_m$-Br (GPC)	Yield (%)
MI53k	1.61	53900	$(PMMA)_{539}$-Br	36

Table A1 Characterized PMMA-Br (M_n= 53.9 kg/mol) macroinitiator.

10.2.9. Synthesis of $PMMA_m$-*b*-$PDMAEMA_n$ with $M_{n\ PMMA}$=53.9 kg/mol

As shown in **Fig. A12**, Cu(I)Br/PMDETA catalyst system was still used to synthesize $PMMA_m$-*b*-$PDMAEMA_n$ with PMMA (M_n= 53.9 kg/mol). For the sake of preparation of $PMMA_m$-*b*-$PDMAEMA_n$ with diverse ratios of PMMA/PDMAEMA, the rate of ATRP for synthesis of second block PDMAEMA was regulated via different ATRP time.

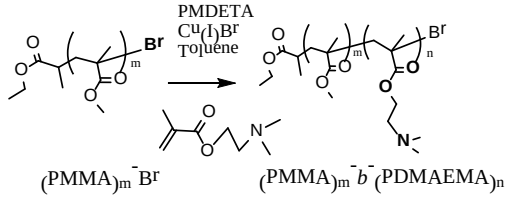

Fig. A12 Synthesis of precursor $PMMA_m$-*b*-$PDMAEMA_n$ ($M_{n\ PMMA}$ = 53.9 kg/mol). [DMAEMA]:[PMMA-Br]: [Cu(I)Br]:[PMDETA] =1600:1:10:10 in toluene at 50ºC, $C_{(MMA)}$= 3 mol/L. The reaction time was respectively 9h and 6h.

As shown in **Table A2**, the molecular weight (M_n) of $PMMA_m$-*b*-$PDMAEMA_n$ from GPC were less than the M_n that was calculated by m/n ratio from ^{1}H-NMR. All the $PMMA_m$-*b*-$PDMAEMA_n$ displayed high PDI due to the too long reaction time which brought about more terminations. The value of m (number of MMA repeatin units in PMMA block) was 539 as calculated before. Calculation processes for all the values of ratio (m/n, by ^{1}H-NMR) and n (number of DMAEMA repeating units in PDMAEMA block) were same as aforementioned description (cf. **5.2.2.2.**).

Code	$(PMMA)_m$-*b*-$(PDMAEMA)_n$ (^{1}H-NMR)	Ratio (PMMA/ PDMAEMA) (^{1}H-NMR)	M_n(g/mol) (^{1}H-NMR)	M_n(g/mol) (GPC)	M_w/M_n (PDI)	Yield (%)
BP53k-1	$(PMMA)_{539}$-*b*-$(PDMAEMA)_{350}$	1.5	108200	77100	1.93	67,7
BP53k-2	$(PMMA)_{539}$-*b*-$(PDMAEMA)_{173}$	3.1	80700	75000	1.53	72,9

Table A2 Characterizaed $PMMA_m$-*b*-$PDMAEMA_n$ ($M_{n\ PMMA}$= 53.9 kg/mol). The reaction time was respectively 9h and 6h for synthesis of **BP53k-1** and **BP53k-2**.

The chemical structure of all the synthesized $PMMA_m$-*b*-$PDMAEMA_n$ (PMMA M_n= 30 kg/mol) can be confirmed as shown in **Fig. A13**. The proton signals at 0.85 ppm, 1.02 ppm (d) corresponded to $-CH_3$ from **1** and **a** collectively. The proton signals at 1.81 ppm, 1.90 ppm (d) corresponded to $-CH_2-$ from **2** and **b** collectively. The proton signal at 4.05ppm (s) can be attributed to $O-CH_2-$ from **3**. The proton signal at 2.56 ppm (s) can be attributed to $N-CH_2-$ from **4**. The proton signals at 2.28 ppm (s) corresponded to $N-CH_3$ from **5** and **6** collectively. The proton signals at 3.60 ppm (s) can be distinctly identified and attributed to $O-CH_3$ from **c**.

The integral area value of proton signals **c** ($O-CH_3$ from PMMA side chains, δ=3.60 ppm, s) and **3** ($O-CH_2$ – from PDMAEMA side chains, δ=4.05 ppm, s) were utilized to calculate the ratios of PMMA/PDMAEMA (m/n) in $PMMA_m$-*b*-$PDMAEMA_n$ with **Equation 6** (cf. **5.1.2.**). The calculated ratios of PMMA versus PDMAEMA (m/n) in $PMMA_m$-*b*-$PDMAEMA_n$ were shown in **Table A2**.

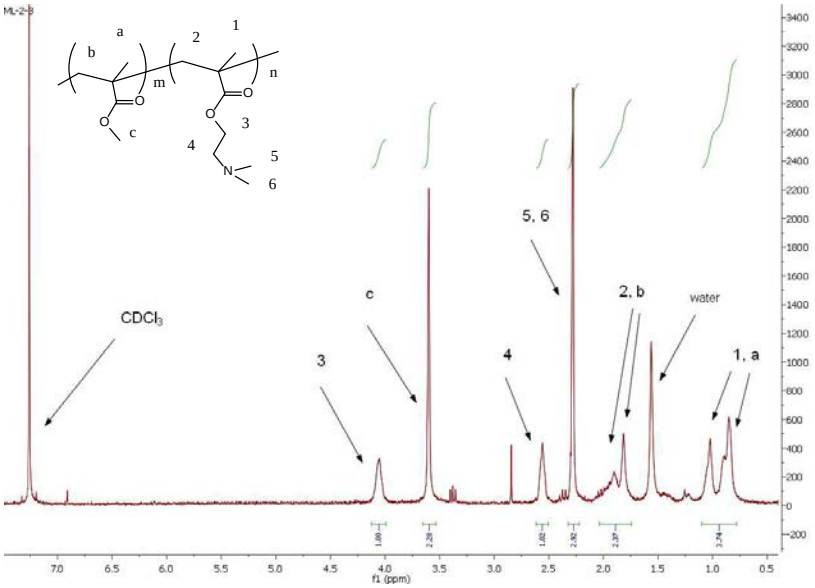

Fig. A13 ^{1}H-NMR (300 MHz) of selected $PMMA_m$-b-$PDMAEMA_n$ (M_n=53.9 kg/mol) macroinitiator. Solvent: d_1-$CDCl_3$@298K (r.t.).

As shown in **Fig. A14**, GPC distribution of PMMA-Br (M_n= 53.9 kg/mol) and the derived $PMMA_m$-*b*-$PDMAEMA_n$ were different depending on the various corresponding molecular weights resulted from the different lengths of formed DMAEMA block, which also strongly evidenced the successfully formed PDMAEMA block under used ATRP conditions

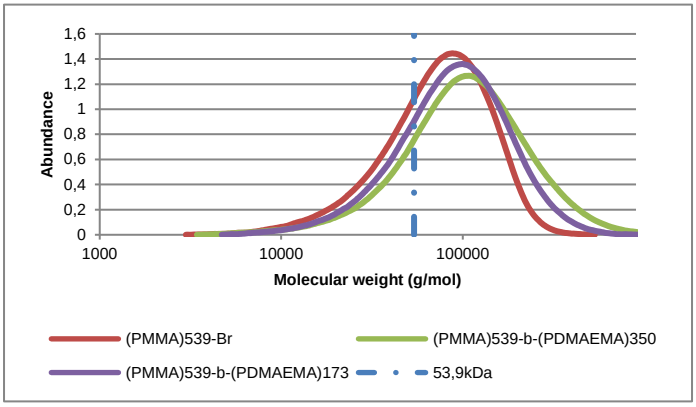

Fig. A14 GPC molecular weight distribution of PMMA-Br (M_n= 53.9 kg/mol) and corresponding $PMMA_m$-*b*-$PDMAEMA_n$ ($M_{n\ PMMA}$= 53.9 kg/mol).

10.3. Curriculum Vitae

The biography is not included in the online version for reasons of data protection.